ISSN 1580-2949
UDK 669+666+678+53 MTAEC9, 48(2)157–312(2014)

MATER. TEHNOL.	LETNIK VOLUME 48	ŠTEV. NO. 2	STR. P. 157–312	LJUBLJANA SLOVENIJA	MAR.–APR. 2014

VSEBINA – CONTENTS

STROKOVNI ČLANKI – PROFESSIONAL ARTICLES

UDK 669.14.018.252:621.793
Review article/Pregledni članek

ISSN 1580-2949
MTAEC9, 48(2)159(2014)

CHARACTERIZATION AND WEAR PERFORMANCE OF CrAgN THIN FILMS DEPOSITED ON Cr-V LEDEBURITIC TOOL STEEL

OCENA LASTNOSTI IN VEDENJE PRI OBRABI TANKIH PLASTI CrAgN, NANESENIH NA LEDEBURITNO ORODNO JEKLO Cr-V

Peter Jurči, Jana Bohovičová, Mária Hudáková, Pavel Bílek

Department of Materials, Faculty of Materials and Technology of the STU, Trnava, Paulínská 16, 917 24 Trnava, Slovak Republic
p.jurci@seznam.cz

Prejem rokopisa – received: 2013-02-14; sprejem za objavo – accepted for publication: 2013-05-28

Specimens made from Vanadis 6 cold-work tool steel were machined, ground, heat processed using a standard regime and finally mirror polished. After that they were layered with CrAgN. The Ag-content in the layers was chosen to be in mass fractions w = 3 % and 15 %. Microstructural analyses revealed that the CrN grew in a columnar manner. The addition of 3 % Ag did not influence the manner of growth of the films, but the addition of 15 % Ag made considerable changes to the film growth. Both the hardness and the Young's modulus were not influenced by the incorporation of 3 % Ag, but the addition of 15 % Ag reduced them. The layers with 3 % Ag had excellent adhesion on the steel substrate. On the other hand, the addition of 15 % Ag had a very negative impact on the coating adhesion. The films with the addition of 3 % Ag had superior tribological properties against hard material (alumina) as well as against a soft counterpart (CuSn6 as-cast bronze), while those with 15 % Ag were too soft and they underwent intensive wear.

Keywords: Vanadis 6 cold-work steel, PVD, chromium nitride, silver addition, tribological investigations

Vzorci, izdelani iz orodnega jekla Vanadis 6 za delo v hladnem, so bili obdelani, brušeni, toplotno obdelani po navadnem postopku in na koncu polirani do zrcalne površine. Nato je bil nanesen CrAgN. Količina v masnih deležih Ag v nanosu je bila izbrana 3 % in 15 %. Analize mikrostrukture so odkrile, da raste nanos v obliki stebrastih zrn. Dodatek 3 % Ag ni vplival na način rasti nanosa, dodatek 15 % Ag pa je povzročil občutne razlike v rasti nanosa. Oba, trdota in Youngov modul, nista bila odvisna od vnosa 3 % Ag, dodatek 15 % pa ju je zmanjšal. Nanosi s 3 % Ag so imeli dobro oprijemljivost na podlagi iz jekla. Po drugi strani pa je dodatek 15 % Ag močno poslabšal oprijemljivost nanosa. Nanosi s 3 % Ag so imeli boljše tribološke lastnosti pri trdem materialu (aluminijev oksid), kot tudi pri mehkem (liti bron CuSn), medtem ko so bili tisti s 15 % Ag premehki in so izkazovali veliko obrabo.

Ključne besede: jeklo za delo v hladnem Vanadis 6, PVD, kromov nitrid, dodatek srebra, tribološke preiskave

1 INTRODUCTION

Thin CrN-based films have been developed over the past three decades. They quickly gained a great deal of interest and popularity in a variety of industrial applications due to their wear- and corrosion resistance and good cutting properties.[1–10]

CrN films can be synthesized with a wide range of chemistries, phase constitutions and properties. A wide range of microhardness values of CrN-coatings, from 1500 HV for arc-vapour-deposited films[8,11–13] up to 2450–2600 HV for those prepared by magnetron sputtering techniques[14–17] can be obtained. In selected cases, for ultra-fine-grained films in particular, the microhardness of CrN-films can reach very high values, exceeding 3000 HV, as reported by Mayrhofer et al.[18] It should be noted that the phase constitution of the films also plays a role in their microhardness – the majority of authors established a slightly higher hardness for the Cr_2N than for the CrN,[19–23] while it was only Nouveau et al.[9] and Beger at al.[24] who reported the opposite tendency. The films prepared by high-power pulsed-magnetron sputtering (HIPIMS) also have a high hardness.[25] The Young's modulus E of CrN-based films can also be varied over a wide range, from 188 GPa to 400 GPa, depending on the negative substrate bias, the substrate temperature and the substrate nature (chemistry, phase constitution, hardness).[14,16,17,26] The formation of high internal stresses, mostly compressive, is one of the key problems connected with film growth on substrates. The stress intensity depends mainly on the substrate bias voltage – the application of low bias voltage produces internal stresses of around 2 GPa,[19,25] while the stresses can reach over 4 GPa when a negative substrate bias higher than 75 V is used for the deposition.[17,27] In any case, too high internal stresses influence the adhesion of the films negatively. The reduction of the stresses is possible through the post-deposition annealing of the films, which led to improved adhesion.[13,28] The difference in the mechanical (hardness) and physical (Young's modulus, thermal expansion coefficient, etc.) properties can cause serious problems with respect to the adhesion of the coatings to the substrate. Generally, a good adhesion can be achieved when ledeburitic steels or cemented carbides are used as a substrate,[10,13,27,29,30] due to their high hardness. The adhesion also increases as the portion of the phase CrN decreases and Cr_2N and/or (Cr) solid solution increases.[12,17,28]

The tribological properties of CrN-based films, however, cannot be changed over a sufficiently wide range. External lubrication is one of the possible ways how to improve the tribological behaviour of the films, but commercially available lubricants (oxides, molybdenum disulfide, graphite) exhibit considerable shortcomings. Graphite and molybdenum disulfide, for instance, undergo oxidation above 300 °C and, hence they degrade rapidly. Furthermore, metallic oxides, on the other hand, cannot be used at low temperatures since they exhibit an abrasive behaviour.

This is why self-lubricating composite films have been a subject of scientific interest in the past few years. These films combine a hard wear-resistant matrix (mostly formed by nitrides or carbo-nitrides) with soft lubricious phases that provide lubricious layer at room and elevated temperatures.

Silver is the most common addition used with transition-metal (TM) nitride thin films. It possesses a stable chemical behaviour and can exhibit self-lubricating properties due to its low shear strength. In addition it is known that silver is capable of migrating to the free surface, providing lubrication above 300 °C. Several investigations were focused on the TM-based ceramic films with the addition of silver, deposited on various substrates. The findings on the effect of Ag addition can be summarized as follows. The addition of silver can lead to an alteration in the growth of CrN-based films, as reported for instance by Mulligan et al.[31] There is a relatively good consensus on the lowering of the friction coefficient at operating temperatures in the range 300–500 °C.[31–37] The nature of this phenomenon is also well known. Silver is almost completely insoluble in CrN and forms nanoparticles in the basic CrN-compound. The Ag atoms can easily migrate to the free surface at elevated temperatures, form lubricious grains there, and thereby reduce the friction force significantly. On the other hand, the tribological properties of Ag-containing films differ significantly above 500 °C, whereas the nature of the TM nitride matrix is a key factor influencing their improvement[34] or deterioration.[32,33,35] The choice of an "optimal" silver addition, from point of view of tribological performance, into the basic film is not in doubt – many authors evaluated films with very high silver contents, e.g., above the mole fraction 20 % [31–33,35–37] although it seems that a much lower silver addition can lead to superior tribological parameters.[38,39] One can assume that silver, as a naturally soft metal, should reduce both the hardness and the Young's modulus of the films. However, some experimental works established either "no effect" of silver or a slight increase of the hardness.[38,39] The information on the effect of silver on the adhesion of films is lacking – one of the possible reasons is that various materials with completely different properties were used as substrates. Kostenbauer et al.[40] made very important observations. They investigated the stress development in multilayered TiN/Ag films with a different modulation period. The principal finding was that the stresses in all the multilayers decreased up to a temperature of 380 °C, followed by a plateau above this temperature. The authors attributed this behaviour to the fact that further stresses were relieved by the plastic deformation of silver interlayers. Based on these investigations, one can also assume that soft silver particles can also effectively relieve the internal residual stresses in the CrN-films, which can make a substantial contribution to the better adhesion of CrN-films and their improved wear behaviour.

Various materials (silicon wafers, carbon steels, nickel superalloys and stainless steels) have been used as substrates for CrAgN films, but not including ledeburitic steels. These materials, however, belong to the most important tool steels, which are used in many industrial operations, due to their good combination of structure and mechanical properties. Moreover, they can be changed using variations of heat-treatment parameters across a wide range.[41–43] The main challenge to perform the experimental works was thus to minimize the gap in knowledge, e.g., to evaluate what happens when P/M ledeburitic steels are coated with CrAgN. The current paper attempts to put together the experimental results on the development of adaptive nanocomposite CrAgN coatings on the Vanadis 6 Cr-V ledeburitic tool steel and to make a comprehensive report on the basic coating characteristics, like microstructure, hardness, Young's modulus, wear resistance, friction coefficient, as a function of the silver content and deposition temperature, with a small look into the near future at the end of the paper.

2 EXPERIMENTAL

2.1 Material and processing

The experimental material was the powder metallurgical ledeburitic steel Vanadis 6 with nominally mass fractions: w(C) = 2.1 %, w(Si) 1.0 %, w(Mn) = 0.4 %, w(Cr) = 6.8 %, w(Mo) = 1.5 %, w(V) = 5.4 % and Fe as balance. Two types of samples were made from the experimental material. The first ones were plates of 40 mm × 20 mm × 5 mm intended for the wear testing. The second samples were un-notched Charpy impact-test specimens (55 mm × 10 mm × 10 mm). After rough machining to the semi-final dimensions, the samples were subjected to a standard heat-treatment procedure consisting of the following steps: vacuum austenitizing up to the final temperature of 1050 °C, followed by nitrogen gas quenching (5 bar) and twice tempering. Each tempering cycle was conducted at 530 °C for 2 h. The resulting as-tempered hardness of the material was 724 HV (10). After the heat treatment, all the samples were fine ground and polished with a diamond suspension to a mirror finish.

The CrN- and CrAgN coatings were deposited in a magnetron sputter deposition system, in a pulse regime

with a frequency of 40 kHz. It should be noted that no adhesion inter-layer (like pure CrN) was deposited prior to the formation of either the CrN or CrAgN films, in order to highlight the differences in the adhesion of the films themselves. Two targets, positioned opposite to each other, were used. For the deposition of CrN, two targets from pure chromium (99.9 % Cr) were used. The target output power was adjusted to 2.9 kW for each cathode. For the deposition of the silver-containing films, one silver cathode (99.98 %) was inserted into the processing chamber instead of one chromium target. In these trials, the cathode output power was 5.8 kW on the chromium cathode. On the silver cathode, the output powers were 0.1 kW and 0.45 kW in order to produce the silver contents in the coating of 3 % and 15 % (mole fractions 1.3 % and 6 %), respectively. Two deposition temperatures were used. The first one was 250 °C. To achieve that, the samples were heated using resistive heaters during the sputter-cleaning step. Afterwards, the substrate temperature of 250 °C was kept constant by ion bombardment only. The second deposition temperature was 500 °C. It was achieved using resistive heaters placed on the internal walls of the processing chamber. The processes were carried out in a low-pressure atmosphere (0.15 mbar), containing pure nitrogen and argon (both of 99.999 % of purity), in a ratio of 1 : 4.5.

The specimens were ultrasonically degreased in acetone and loaded into the processing chamber. They were placed between the targets on rotating holders, with a rotation speed of 3 r/min. Just prior to the deposition, the substrates were sputter cleaned in an argon low-pressure atmosphere for 15 min. The substrate temperature was 250 °C for the cleaning. A negative substrate bias of 200 V was used for the sputter cleaning and that of 100 V for the deposition. The total deposition time was 6 h.

2.2 Investigation methods

The microstructure of the substrate material was documented using a light microscope ZEISS NEOPHOT 32 and a field-emission scanning electron microscope (SEM) JEOL JSM-7600F operated at an accelerating voltage of 15 kV. Metallographic samples were prepared using a standard preparation technique (rough and fine grinding, polishing by diamond suspension) and finally etched with Villela-Bain reagent.

The microstructure of the counterface materials was recorded using a light microscope ZEISS NEOPHOT 32 after a standard metallographic preparation.

Microstructural analyses of coatings were completed on the fracture surfaces of coated Charpy impact specimens. The material was immersed into liquid nitrogen for 20 min. and then broken down. The fracture surfaces were cleaned ultrasonically with acetone before observation, in order to remove any possible contamination of the material. A scanning electron microscope JEOL JSM-7600F operating with the same parameters was used for the analyses.

The nanohardness and the Young's modulus (E) of the coatings were determined using a nano-indenter under a normal load of 20 mN, for a NanoTest (Micro Materials Ltd) nanohardness tester equipped with a Berkovich indenter. Ten indentations were made for each coating applied and the mean value and the standard deviation were calculated from the measured values. The penetration depth (loading) of the indenter was chosen so as to not exceed one tenth of the total coating thickness, in order to avoid the influence of the substrate on the measured nanohardness.

The adhesion of the coatings on the substrate was evaluated using a CSM Revetest scratch-tester. The scratches were made under progressively increasing loads from 1 N to 100 N, with a loading rate of 50 N/min. A standard Rockwell diamond indenter with a tip radius of 200 μm was used. Five measurements were made on each specimen and the mean value of the adhesion, represented by the L_{c1} and L_{c2} critical loads, respectively, was calculated. The critical loads were determined by the recording of an acoustic emission signal as well as by viewing the scratches on the light micrographs. The L_{c1} critical load corresponded to the occurrence of the first inhomogeneities in the coating and the L_{c2} critical load was determined as the load when 50 % of the coating was removed from the substrate, unless otherwise discussed in the text.

The tribological properties of the coatings were measured using the CSM Pin-on-disc tribometer at ambient and elevated temperatures up to 500 °C. Balls of 6 mm in diameter, made from sintered alumina and CuSn6 bronze (as-cast structure, hardness of 149 HV (10)) were used for testing at all the temperatures. The balls made from heat-processed 100Cr6 ball-bearing steel (hardness of 700 HV (10)) were used, but for the testing at ambient temperature only. The experiments were conducted in laboratory air, at a relative humidity of 40–50 %. No external lubricant was added during the measurements. The normal loading used for the investigations was 1 N. For each measurement, the number of cycles was 5100, e.g., the total sliding distance was 100 m at the sliding radius of 5 mm. After the testing, the wear-track widths were measured on a light microscope ZEISS NEOPHOT 32 at a magnification of 50-times. Ten measurements were made on each track and the mean value, which was used for further evaluation, was calculated. The volume loss of the coated samples was calculated from the width of the wear tracks using the formula:[44]

$$V_1 = 2\pi R\left[\frac{r^2}{\sin\left(\frac{d}{2r}\right)}\right] - \frac{d}{4}\sqrt{4r^2 - d^2}$$

where R is the wear-scar radius, d is the mean value of the wear-track width, and r is the radius of the ball counterface.

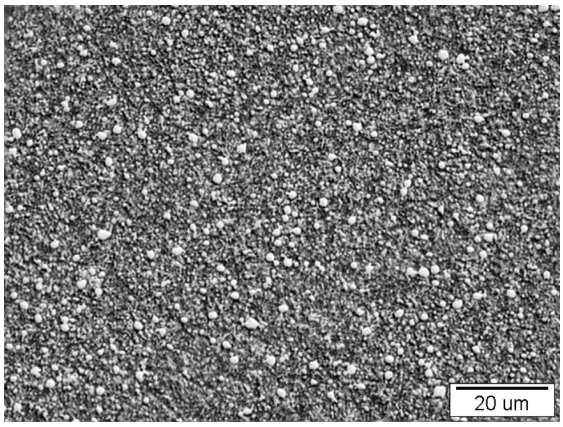

Figure 1: Light micrograph showing the microstructure of the PM ledeburitic steel Vanadis 6 substrate in the as-quenched and tempered state

Slika 1: Posnetek mikrostrukture kaljene in popuščene podlage iz PM ledeburitnega jekla Vanadis 6

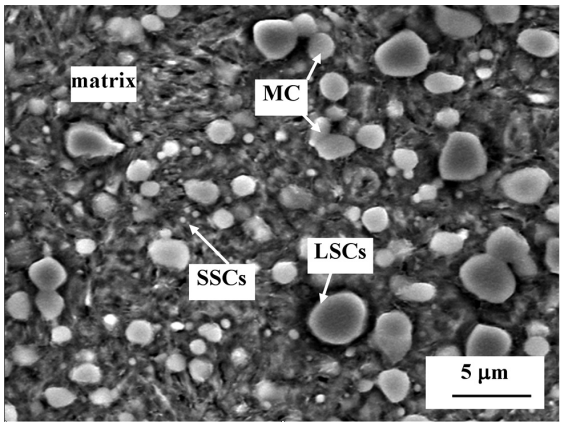

Figure 2: SEM micrograph showing detailed microstructure of PM ledeburitic steel Vanadis 6 substrate in the as-quenched and tempered state

Slika 2: SEM-posnetek detajla mikrostrukture kaljene in popuščene podlage iz PM ledeburitnega jekla Vanadis 6

The wear rate was then derived from the volume-loss calculation, using the formula:[44]

$$W = \frac{V_l}{l \times F_n}$$

where W is the wear rate, l is the sliding distance (m), F_n is the applied normal load and V_l is the volume loss.

3 RESULTS AND DISCUSSION

3.1 Substrate characterization

The microstructure of the substrate material after the heat treatment is shown in **Figures 1** and **2**, respectively. The light micrograph (**Figure 1**) shows that the material consists of a matrix, formed with tempered martensite and fine carbides, uniformly distributed throughout the matrix. The carbides are of two types (**Figure 2**). The MC-phase (medium-sized particles) mostly forms the eutectic part of the carbides. The second carbide type is the M_7C_3. The M_7C_3-phase underwent dissolution in the austenite during the heat processing, being responsible for the saturation of the austenite with the carbon and alloying elements.[45] The other part of the M_7C_3-carbides (designated as large secondary carbides (LSCs) and small secondary carbides (SSCs), and an almost complete amount of MC phase remained undissolved. After the heat treatment, the average hardness of the material was 724 HV (10).

3.2 Microstructure of the films

Figure 3 shows cross-sectional secondary-electron micrographs from all the developed films. The thickness of the CrN film without any silver addition was 4.3 µm (**Figure 3a**). This corresponds to a growth rate of 720 nm/h. The addition of 3 % of Ag did not change the

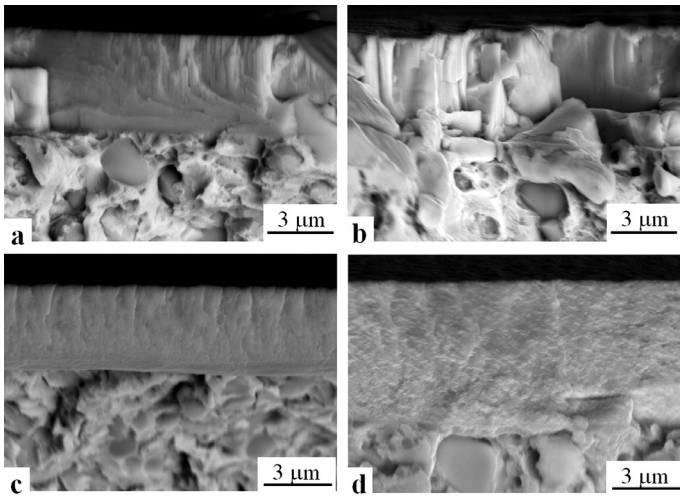

Figure 3: SEM micrographs showing the microstructure of developed films: a) CrN, deposition at 250 °C, b) CrAg3N, deposition temperature of 250 °C, c) CrAg3N, deposition temperature of 500 °C and d) CrAg15N, deposition temperature of 500 °C[47,48]

Slika 3: SEM-posnetki mikrostrukture razvoja plasti: a) nanos CrN pri 250 °C, b) CrAg3N, temperatura nanašanja 250 °C, c) CrAg3N, temperatura nanašanja 500 °C in d) CrAg15N, temperatura nanašanja 500 °C[47,48]

thickness (and the growth rate) of the films (**Figures 3b** and **3c**). On the other hand, the addition of 15 % Ag accelerated the growth rate of the film to 1050 nm/h and, as a result, this film had a thickness of 6.3 μm (**Figure 3d**). It should be noted that these results are inconsistent with other literature data. Yao et al.,[46] for instance, reported a decreased film thickness with a Ag addition. However, they have used completely different experimental setup for the coating deposition, which makes the results only roughly comparable. Our results, on the other hand, indicate that small addition of silver does not influence the growth rate of the films, which was confirmed recently.[47,48]

The pure CrN-based film, formed at 250 °C, grew in a columnar manner with clearly visible individual crystallites (**Figure 3a**). This type of layer growth is typical for magnetron sputtered CrN-films formed over a wide range of deposition parameters, as reported previously.[49] The addition of 3 % Ag into the CrN, formed at the same temperature, did not change the growth mechanism of the layer significantly (**Figure 3b**). The temperature effect on the layer growth for the films with 3 % Ag addition is visible on the micrograph in **Figure 3c**. It is clearly visible that the higher deposition temperature does not influence the growth manner. **Figure 3d** shows the microstructure of the film with 15 % Ag addition. The secondary-electron-mode detection yields clearly visible contrast between high atomic Ag (bright) and the surrounding CrN base. It is also clear that no individual crystals of CrN were formed. Therefore, it is clear that a small Ag addition does not change the growth manner of the film, while a higher Ag content incorporated into the CrN matrix has a considerable impact on that.

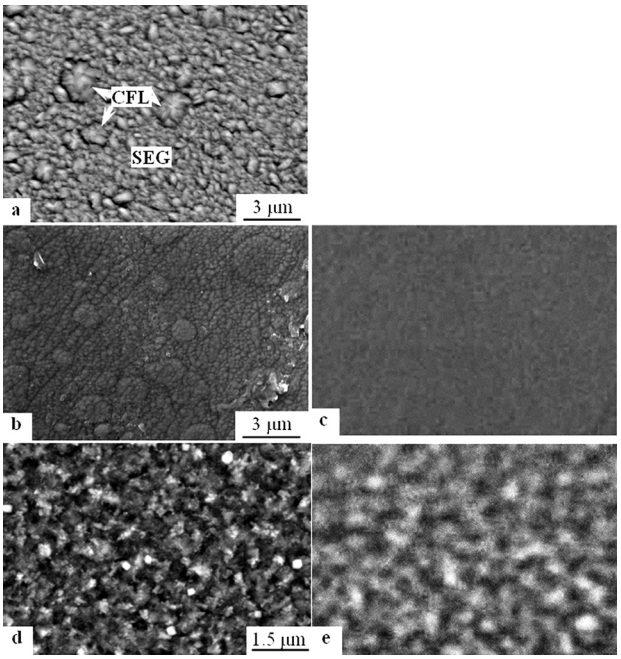

Figure 4: Plan-view SEM micrographs showing the surface microstructure of deposited films: a) CrN, deposition at 250 °C, b) CrAg3N, deposition temperature of 250 °C, c) corresponding EDS-map of silver, d) CrAg15N, deposition temperature of 500 °C and e) corresponding EDS-map of silver

Slika 4: SEM-posnetki površine, ki prikazuje mikrostrukturo nanesene plasti: a) CrN, nanešen pri 250 °C, b) CrAg3N, temperatura nanašanja 250 °C, c) EDS-razporeditev srebra, d) CrAg15N, temperatura nanašanja 500 °C in e) EDS-razporeditev srebra

Figure 4 brings representative SEM micrographs of the deposited films and corresponding EDS maps of silver. These pictures indicate that the surface microstructure is strongly influenced by introducing silver into the basic CrN-film. The surface of pure CrN (**Figure 4a**) exhibits a clearly visible, non-uniform structure, made up of two types of features. The first type of feature is the semi-equiaxed grains (SEG) with a size of 0.4–0.7 μm. This feature makes up around 90 % the surface and can be referred to as a "matrix". In this "matrix", several formations that can be described as a cauliflower-like (CFL) structure are embedded. Similar surface structure of chromium nitride films has already been reported and discussed by Zhao et al.[50] They established that the combination of "equiaxially grained" (or facetted) and CFL structures is typical for two-phase (CrN and Cr_2N) films.

The addition of 3 % Ag into the chromium nitride basic film causes a significant refinement in the grain size of the individual crystals (**Figure 4b**). No individual silver grains but inhomogeneities in the chemical composition throughout the micrograph became visible (**Figure 4c**).

The SEM micrograph in **Figure 4d** and the corresponding EDS mapping of Ag (**Figure 4e**), show that silver forms agglomerates (appearing in bright contrast due to their higher secondary-electron yield versus CrN) on the surface at a concentration of 15 %. The size of the silver agglomerates is well below 1 μm.

3.3 Mechanical properties of the films

The microhardness of pure CrN was (16.79 ± 1.49) GPa (**Table 1**). The microhardness of films containing 3 % Ag was only very slightly lower than that of the film that does not contain silver. Furthermore, the microhardness of these films was almost the same, e.g., the deposition temperature plays only a very minor role with respect to the coating hardness. The addition of 15 % Ag, on the contrary, led to a substantial hardness reduction, i.e., (11.43 ± 0.61) GPa. This may be explained by

Table 1: Mechanical properties of investigated films. The circled values (●) were obtained in a previous study[47]

Tabela 1: Mehanske lastnosti preiskovanih nanosov. Vrednosti, označene z (●), so iz vira[47]

Coating/deposition temperature	Hardness (GPa)	Young's modulus *E*/GPa
CrN/250 °C ●	16.79 ± 1.49	244 ± 15
CrAg3N/250 °C ●	15.97 ± 1.44	241 ± 9
CrAg3N/500 °C	16.13 ± 1.83	246 ± 17
CrAg15N/500 °C	11.43 ± 0.61	204 ± 6

the fact that silver is a very soft metal and its agglomerates embedded in the CrN matrix cause softening of the film. These observations are very consistent with other experimental works. Yao et al.[46] reported only a very slight Knoop hardness decrease for magnetron sputtered nanocomposite coatings with very small silver additions. Mulligan et al.[31] established a much more remarkable hardness decrease, but they added the mole fraction of Ag 22 % (e.g., a much larger amount than that used in this study).

The Young's modulus, *E*, of the CrN and CrAg3N films was of about 240 GPa (**Table 1**). The *E* value ranges, in addition, overlap considerably. The addition of 15 % of silver to the basic film, on the other hand, tends towards a decrease of the Young's modulus. The information on the impact of the silver addition on the Young's modulus is lacking in the literature. Only Aouadi and his co-workers[38] reported a decreased Young's modulus with an increased amount of silver in magnetron-sputtered YSZ-based films. The fact that the Young's modulus reduces with the addition of silver can be considered as natural, since silver had a much lower *E* (around 79 GPa) than chromium nitride (over 200 GPa in most cases[14,16,17]). However, at very small silver additions, there is almost no impact of silver on the Young's modulus, as indicated in **Table 1**. It seems that there is a threshold below which no impact of the silver on the Young's modulus can be expected and, above which the addition of silver leads to a substantial lowering of the *E*.

One can believe that the effect of the size and the distribution of silver particles can also play a role in the mechanical behaviour of the coatings. However, there is no relevant information on the impact of these structural parameters on the mechanical properties of the films yet. These investigations can be considered as a challenging factor for further investigations.

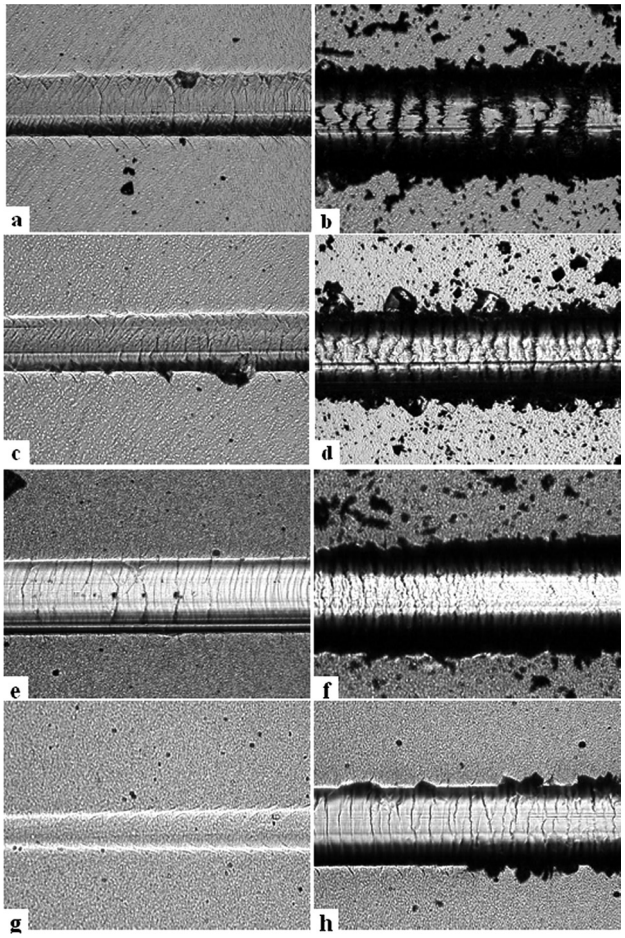

Figure 5: Light micrographs showing the failures after scratch testing: a) CrN, deposition temperature of 250 °C, L_{c1}, b) L_{c2}, c) CrAg3N, deposition temperature of 250 °C, L_{c1}, d) L_{c2}, e) CrAg3N, deposition temperature of 500 °C, L_{c1}, f) L_{c2}, g) CrAg15N, deposition temperature of 500 °C, L_{c1}, h) L_{c2} [47,48]

Slika 5: Svetlobni posnetki napak, nastalih pri preizkusu razenja: a) CrN, temperatura nanašanja 250 °C, L_{c1}, b) L_{c2}, c) CrAg3N, temperatura nanašanja 250 °C, L_{c1}, d) L_{c2}, e) CrAg3N, temperatura nanašanja 500 °C, L_{c1}, f) L_{c2}, g) CrAg15N, temperatura nanašanja 500 °C, L_{c1}, h) L_{c2} [47,48]

3.4 Adhesion of the films

After the scratch-test, the failure of the pure chromium nitride film begins with semi-circular tensile cracking (**Figure 5a**). The first cracks were observed at a normal load of around 24 N (L_{c1}). The "total" failure of the chromium nitride film is shown in **Figure 5b**. It is manifested by many parallel cracks visible in the scratch, where about 50 % of the coating is removed from the substrate. The typical load range when this phenomenon occurred was 40–45 N.

The slightly softer CrAg3N film deposited at 250 °C also failed due to the presence of semi-circular tensile cracks. However, the distance between the first cracks is larger than that in the pure chromium nitride and some of the cracks stopped their propagation through the scratch (**Figure 5c**). The critical load at which these phenomena first occurred was around 23 N (**Table 2**). **Figure 5d** shows the total failure of the CrAgN film grown at 250 °C. It is evident that some of the parallel cracks stopped their propagation through the film, which suggests that the coating can store a larger amount of plastic deformation energy preceding the failure. This assumption is supported by the fact that the "total" failure of the film was detected at a load higher than that of pure chromium nitride (**Table 2**).[47]

Table 2: Critical loads for a defined degree of coatings failure[47]
Tabela 2: Kritične obremenitve za opredeljeno stopnjo poškodbe nanosa[47]

Coating/deposition temperature	L_{c1}/N	L_{c2}/N
CrN/250 °C	24.5 ± 1.7	42.7 ± 4.4
CrAg3N/250 °C	23.4 ± 5.9	52.2 ± 5.9
CrAg3N/500 °C	46.9 ± 8.1	82.6 ± 8.4
CrAg15N/500 °C	6.4 ± 0.6	44.1 ± 6.3

For the film with 3 % Ag addition, grown at a substrate temperature of 500 °C, the first indication of

coating damage occurred at an average loading of around 47 N (L_{c1}). Coating damage begins with the appearance of semi-circular tensile cracks, e.g., it looks to be similar to that of the coating deposited at a lower temperature (**Figure 5e**). The "total" failure of the film is in **Figure 5f**. It is typical, with the occurrence of many parallel micro-cracks inside the scratch track. Some of them stopped their propagation during the testing. Also, it is shown that part of the track (the left-hand side of the micrograph) does not exhibit visible cracks. Here, no typical "coating damage" was observed (50 % of the coating removed). The typical load when this symptom occurred ranged between 74 N and 88 N (L_{c2}).

The beginning of the failure of the film containing 15 % Ag cannot easily be found. **Figure 5g** shows a scratch track at a relatively low loading range (around 6.4 N), where the critical load L_{c1} was determined. However, neither tensile cracking nor spallation of the film has been observed at low loading. What was determined was only that the film underwent a local plastic deformation with clearly visible, semi-circular deformation zones (arrow designated). These zones are widely spaced, which suggests that the film is capable of storing a relatively large amount of plastic energy before failing cohesively. Typical symptoms for the "total" failure of the coating have not been detected, in a similar way to the film with 3 % Ag (**Figure 5f**). The scratch track contained many parallel cracks and microcracks when subjected to higher loads (**Figure 5h**). Moreover, the first symptoms of chipping were detected as being adjacent to the scratch track at a normal load of 44.1 N.

The fact that a high silver content tends to worse adhesion of the film is consistent with Yao's findings,[46] where a very slight adhesion decrease with increasing silver content has been reported. However, the experimental setup used was different in this work, i.e., an M2-type high-speed steel with unknown hardness and heat treatment state was used as a substrate instead of Vanadis 6, another deposition system was applied for the coating growth and, finally, no details of the scratch testing were reported. All these facts make the results almost incomparable. What can be suggested is that the high silver content makes the coating too soft and very sensitive to the failure at higher loading.

Moreover, the addition of 3 % silver increased the adhesion of the films in our work, particularly when a temperature of 500 °C was used for the deposition. Here, Kostenbauer's findings,[40] that the intrinsic stresses in silver-containing multilayer coatings are relieved above 380 °C, can give a correct explanation. It is known that the deposition of chromium nitride films, which do not contain silver, leads to the formation of high intrinsic stresses, exceeding 4 GPa.[17,19,25,27] They can be lowered by several methods. One of them is a so-called "post-deposition annealing", which can result in the increased adhesion performance of the films.[13] The second suitable method is the incorporation of a soft and insoluble phase (pure silver for instance) into the chromium nitride. It can be assumed that such a phase would be capable of relaxing the stresses during the deposition of the films. Based on this assumption, a distinctively higher adhesion strength of the films that contain 3 % Ag seems to be logical.

3.5 Tribological investigations

Figure 6 gives an overview of the friction coefficients μ resulting from testing at room temperature for all the used counterparts. The pure CrN film has a μ = 0.378 when tested against alumina. The CrAg3N films formed at 250 °C and 500 °C had average friction coefficients of 0.389 and 0.373, respectively. The lowest average μ was recorded for the film containing 15 % Ag, i.e., 0.365. Therefore, one can conclude that almost no positive effect of the silver addition can be found when an alumina ball is used.

Generally, the testing against 100 Cr6 ball-bearing steel gave a slightly higher μ compared to the alumina. The pure CrN film had average of μ = 0.425. The silver containing-films had a slightly lowered friction coefficient, e.g., around 0.4, but it should be noted that the friction-coefficient value ranges overlap. Thus, one would conclude that no positive impact of the silver on the friction coefficient of CrN against 100 Cr6 steel has been found, in a similar way to the case of alumina ball counterpart.

Testing against a CuSn6 bronze ball gave a lower friction coefficient. The pure CrN film had a μ = 0.332. A silver addition of 3 % tended to lower the friction coefficient and the lowering of the friction coefficient became even more significant for the composite Ag-containing films grown at a temperature of 500 °C. The impact of silver incorporation into the basic CrN compound can be thus considered as slightly positive, when tested against bronze at room temperature.

Figure 7 shows an overview of the friction coefficients μ recorded while testing against alumina at a room and elevated temperatures. The normal load applied was

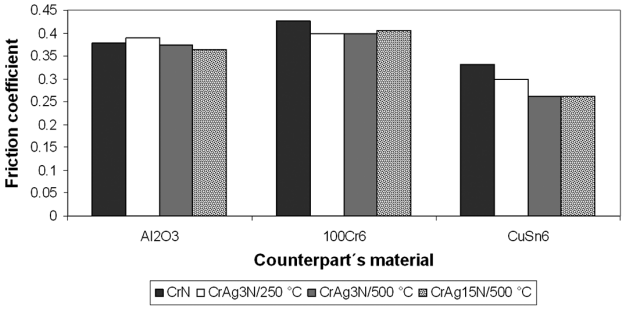

Figure 6: Average friction coefficient of investigated films against various counterpart materials, testing at room temperature, normal load applied of 1 N

Slika 6: Povprečni koeficient trenja za preiskovane nanose pri različnih materialih v paru, preizkušeno pri sobni temperaturi, normalna obremenitev 1 N

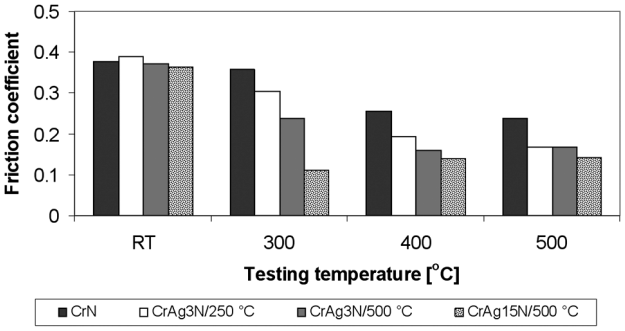

Figure 7: Average friction coefficient of investigated films against alumina at room (RT) and elevated temperatures, normal load applied of 1 N

Slika 7: Povprečni koeficient trenja za preiskovane nanose pri aluminijevem oksidu pri sobni temperaturi (RT) in povišanih temperaturah, normalna obremenitev 1 N

1 N. As stated above, almost no differences in μ were found when tested at room temperature. Testing at 300 °C, however, yields to a different behaviour of the coatings. The friction coefficients for the pure CrN, CrAg3N grown at 250 °C, CrAg3N grown at 500 °C and CrAg15N formed at 500 °C were 0.357, 0.304, 0.238 and 0.110, respectively. Higher testing temperatures lowered the difference in the μ for different coatings, for instance, the friction coefficients recorded by the testing at 400 °C were 0.256, 0.194, 0.160 and 0.139 for the pure CrN, CrAg3N formed at 250 °C, CrAg3N formed at 500 °C and CrAg15N formed at 500 °C, respectively. The measurement at 500 °C gave rather similar results.

Table 3 shows the wear rates calculated from the widths of the wear scares produced by the sliding of an alumina counterpart on the samples' surfaces. At room temperature the beneficial effect of the silver addition is evident only in the case of the CrAg3N film grown at 500 °C. Compared to pure CrN, the wear rate is lowered by two times. For the film containing 3 % Ag grown at 250 °C, a slight worsening of the wear rate was recorded and, for the film containing 15 % Ag the wear rate was higher by an order of magnitude.

The testing at elevated temperature led to a dramatic increase of the wear rate for the pure CrN film. The film with a 3 % Ag addition grown at 250 °C behaved in a very similar way from the qualitative point of view. The wear rate was minimal after the testing at an ambient temperature, which was followed by a steep increase at 300 °C and a decrease at 400 °C and 500 °C, respectively. However, it is clearly evident that the wear rates after the testing at these temperatures are considerably lower. This makes a distinct difference compared to the wear behaviour of the pure CrN film. The film with the same silver content, but grown at 500 °C, had lower wear rates than that grown at 250 °C at room temperature and 300 °C, respectively. However, the testing at higher temperatures brought a higher wear rate. The film that contains 15 % Ag had the lowest wear rate when tested at 300 °C. However, the wear rate of the film increased as the testing temperature increased, and the increase of the wear rate was found to be greater than those of other investigated films.

The results of wear-rate measurements at room temperature are very consistent with the obtained values of the friction coefficients – the wear rate decreased with a decrease of the μ.

In order to explain the temperature behaviour of both coatings, it should be noted that there was no lubricant added to the experimental setup. The fact that the wear rate was lower or higher can thus be attributed only to the self-lubricating effect of the silver. This effect is, however, prevalent only above the testing temperature of 400 °C, when the Ag-atoms are capable of being transported to the surface.

Below this temperature, but above the ambient temperature, only the effect of the softening of the coatings can be expected. It was reflected by a much higher wear rate at 300 °C than that at ambient temperature. Finally, it should also be noted that the softening of alumina could take place during the testing.[51] The behaviour of the film that contains 15 % Ag can be characterized as a special case. As we determined, the incorporation of 15 % Ag makes the film soft. This gives a natural explanation for the high wear rate measured at ambient temperature. At a temperature of 300 °C, the friction coefficient of the coating became extremely low and thereby the wear rate was lowered, also. Above this temperature, however, a softening of the coating can be expected, as reported for instance by Kostenbauer et al.[40] which gives a natural explanation for the high wear rate measured at 400 °C and 500 °C, respectively.

Figure 8 demonstrates the wear scars obtained by testing the CrAg3N and CrAg15N films developed at 500 °C, at ambient temperature. The testing gave very narrow tracks in the cases of CrN and CrAgN, respectively, see the representative micrograph in **Figure 8a**. The track developed on the CrAg15N film looks rather wider (**Figure 8b**), as a result of the lower hardness of

Table 3: Wear rate ($mm^3/(N\ m)$) at ambient and elevated temperatures, alumina used as a counterpart

Tabela 3: Hitrost obrabe ($mm^3/(N\ m)$) pri sobni in povišanih temperaturah; aluminijev oksid uporabljen kot par

Testing temperature coating (°C)	CrN	CrAg3N/ 250 °C	CrAg3N/ 500 °C	CrAg15N/ 500 °C
Room temperature	6.947×10^{-13}	7.399×10^{-13}	3.65×10^{-13}	1.031×10^{-12}
300	2.926×10^{-11}	2.894×10^{-11}	8.405×10^{-12}	7.053×10^{-12}
400	1.162×10^{-11}	4.329×10^{-12}	9.927×10^{-12}	1.925×10^{-11}
500	1.927×10^{-11}	6.208×10^{-12}	1.522×10^{-11}	4.802×10^{-11}

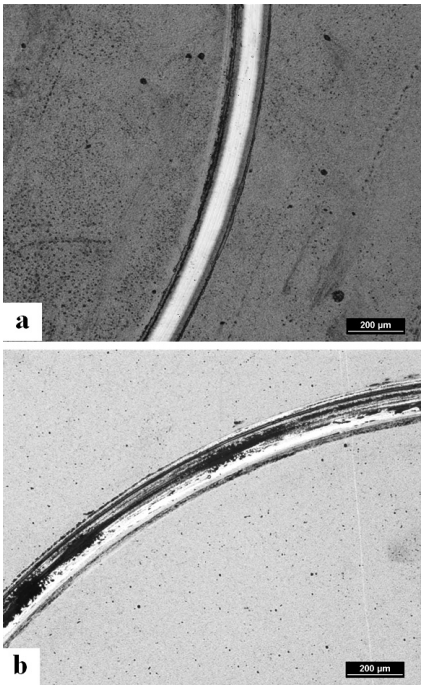

Figure 8: Light micrographs showing the wear tracks of: a) CrAg3N film grown at 500 °C, b) CrAg15N film grown at 500 °C, after sliding at room temperature, alumina used as a counterpart

Slika 8: Svetlobni posnetek prikazuje sledi obrabe: a) CrAg3N-nanos, nanesen pri 500 °C, b) CrAg15N-nanos, nanesen pri 500 °C, po drsenju pri sobni temperaturi, za par je bil uporabljen aluminijev oksid

the film. These results correspond well with the measured wear rates. The wear rates of the films formed with pure CrN and CrAg3N, respectively, were very low, while that of the CrAg15N film was considerably higher (**Table 3**).

Figure 9 shows representative optical images of the wear scars developed while testing the CrAg3N and CrAg15N films, respectively, against the alumina counterpart at various temperatures. Compared to the wear tracks obtained at ambient temperature, there is significant broadening visible. This can be due to the fact that the elevated temperature tends towards softening of the films. It should be noted that the softening of alumina could also be expected. However, the softening of the films probably became more remarkable.

The testing at 300 °C (**Figures 9a** and **9d**), gave wear tracks of similar width, e.g., 0.267 mm and 0.251 mm for the CrAg3N and CrAg15N films, respectively. This can be considered rather surprising because the CrAg15N film is much softer than the CrAg3N and, further softening can be expected at higher temperature. However, the friction coefficient was measured to be much lower for the CrAg15N; this can be referred to the higher silver content in the CrN and its better capability to facilitate lubrication at higher temperatures, in good agreement with previous investigations.[32,33,37]

The testing at 400 °C (**Figures 9b** and **9e**) induced significant broadening of the wear tracks. This is highlighted for the CrAg15N film much more than that for CrAg3N, compare **Figures 9b** and **9e**. Here, the effect of softening of CrAg15N became prevalent and the self-lubrication by Ag particles was insufficient to compensate for the softening of the film. It is worth noting that the opinions on the optimal silver content from the point of view of the self-lubricating effect facilitation are divergent. Hu et al.,[33] for instance, have reported that the minimal Ag amount in the coating was the mole fraction $x = 24$ % to ensure lubrication at higher temperatures. Mulligan et al.[52] have established that the optimal amount of silver incorporated into CrN is $x = 22$ %. This is quite enough for the formation of a lubricious film inside the wear tracks and for the achievement of an excellent tribological performance. In the current experiment, much lower silver additions were used. It is thus logical that this is the softening of the CrN through the Ag, which plays a dominant role in the tribological behaviour of the films.

The testing at 500 °C highlighted the differences between the tribological behaviour of the films containing 3 % and 15 % Ag, respectively (**Figures 9c** and **9f**). The width of the wear track on the CrAg3N film

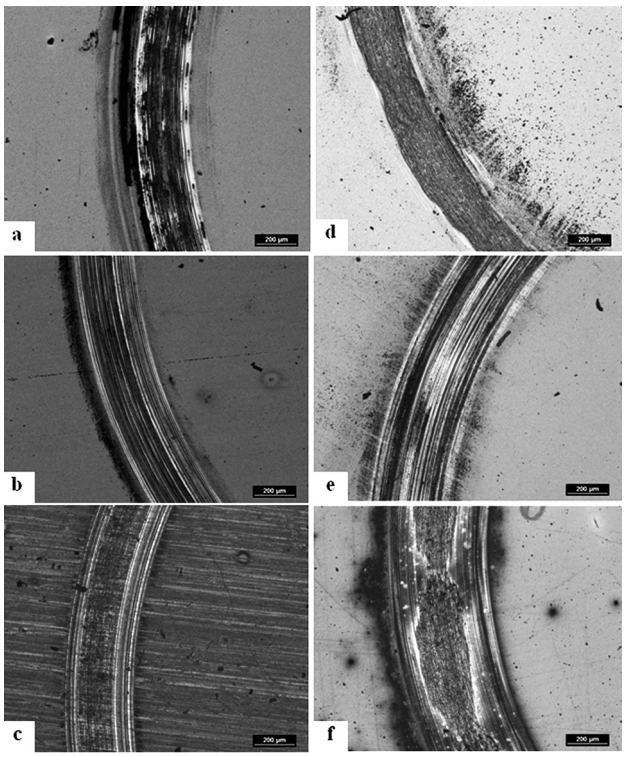

Figure 9: Plan-view optical images showing the wear tracks of the CrAg3N film grown at 500 °C: a) testing temperature of 300 °C, b) testing temperature of 400 °C, c) testing temperature of 500 °C and CrAg15N film grown at 500 °C, d) testing temperature of 300 °C, e) testing temperature of 400 °C, f) testing temperature of 500 °C

Slika 9: Svetlobni posnetki sledi obrabe na CrAg3N-nanosu, nanesenem pri 500 °C: a) temperatura preizkusa 300 °C, b) temperatura preizkusa 400 °C, c) temperatura preizkusa 500 °C in CrAg15N-nanos, nanesen pri 500 °C, d) temperatura preizkusa 300 °C, e) temperatura preizkusa 400 °C, f) temperatura preizkusa 500 °C

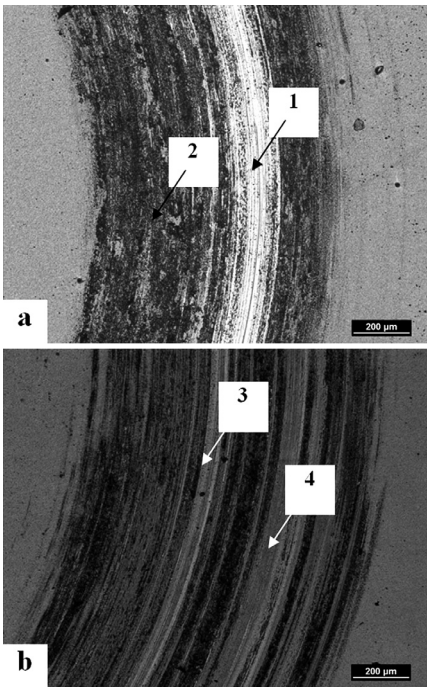

Figure 10: Plan view optical images showing the wear tracks of the CrAg3N film grown at 500 °C, developed during contact with CuSn6: a) testing at ambient temperature, b) testing temperature of 400 °C
Slika 10: Svetlobni posnetek sledov obrabe na CrAg3N-nanosu, nanesenem pri 500 °C, nastal med kontaktom s CuSn6: a) preizkus pri sobni temperaturi, b) temperatura preizkusa 400 °C

increased to 0.324 mm. Here, no indications of total failure of the film were observed. The width of the films that contain 15 % Ag was 0.477 mm. There are indications of total film failure clearly visible – the free substrate surface is shown inside the wear scars.

Figure 10 shows representative plan-view micrographs of the wear tracks obtained by testing of CrAg3N-film, grown at 500 °C, against the CuSn6 ball. The testing at ambient temperature gave wear tracks with a width of 0.89 mm (**Figure 10a**). There are two typical areas inside the wear track. The first one can be classified as almost unaffected by the sliding (1). The second part of the wear track exhibits clearly visible symptoms of scraping (2). However, no evidence of the counterpart's adhesion was recorded.

The testing at a temperature of 400 °C produced wear tracks with a width of 1.02 mm (**Figure 10b**). Here, two typical areas inside the track can also be found. The first one is, similar to the case of the testing at a room temperature, almost unaffected by the sliding (3). The dominant part of the wear track, however, shows indications of considerable counterpart material transfer (4). The counterpart's material exhibits evidence of surface oxidation, because of the elevated temperature used for the testing.

To explain the behaviour of the sliding couple CrAg3N deposited at 500 °C vs. CuSn6 bronze, various aspects should be considered. First of all it should be noted that the behaviour of the sliding couple is determined by the fact that the CuSn6 is soft in nature (149 HV 10) and it has a low shear strength, so that it can be easily smeared on the surface. This tendency is highlighted when a higher testing temperature is used. Moreover, the bronze does not contain any hard phases. **Figure 11** shows the microstructure of the CuSn6 ball. The bright particles are the α-phase formations with an average microhardness of 156 HV (0.1) and the dark places are formed by the eutectoid $\alpha + \varepsilon$, having an average microhardness of 196 HV (0.1). This is why no abrasive character of the interaction sample/counterpart has been detected. Moreover, the softness of the CuSn6 has made it impossible to determine the wear rate using the method.[44] The measurement of wear profiles using profilometers was not possible, also. Therefore it can only be concluded that the CrAg3N film exhibits good anti-sticking properties at low temperature, but that these properties are worsened at elevated temperatures.

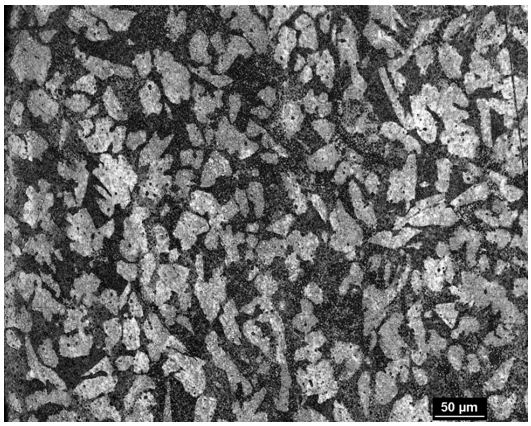

Figure 11: Light micrograph showing the microstructure of a CuSn6 ball
Slika 11: Svetlobni posnetek mikrostrukture kroglice CuSn6

4 CONCLUSIONS

Investigations of magnetron-sputtered CrN films with various Ag additions have brought the following findings:

The pure chromium nitride film grew in a typical columnar manner with clearly visible individual crystals. Its surface structure is a mixture of semi-equiaxed grains and cauliflower-like formations.

The addition of 3 % Ag tends mainly towards a refinement in the scale of the microstructural features, while the incorporation of 15 % Ag induced considerable changes in the growth manner, whereas no individual crystals of the CrN are more visible and nano-sized silver agglomerates are formed.

The pure CrN film as well as those with a 3 % Ag addition grew at a deposition rate of 720 nm/h, while the growth rate of the film with 15 % Ag was accelerated to 1050 nm/h. It is clear that the deposition temperature did not affect both the deposition rate and the final coating

thickness, but a higher Ag content led to a greater thickness of the film.

The nanohardness and the Young modulus of the pure CrN film were 16.79 GPa and 244 GPa, respectively. A small addition of silver has almost no impact on both the nanohardness and the Young's modulus. The incorporation of 15 % Ag into the film induced a reduction of both the nanohardness and the Young's modulus. There is probably a threshold of Ag content below which the impact of the silver on the mechanical properties of chromium nitride can be considered as negligible.

The addition of 3 % Ag improved the adhesion of the CrN film, whereas the improvement was considerably higher in the case of the film grown at 500 °C. The adhesion of the film with 15 % Ag was very poor.

It has been established that there is almost no effect of silver addition on the friction coefficient when tested at room temperature against alumina, but the testing against the same counterpart at higher temperature gave a positive effect of the silver addition on the μ.

The testing against 100Cr6 steel gave a higher friction coefficient than that against the alumina, while the testing against the CuSn6 bronze led to lower μ.

The addition of 3 % Ag to the CrN increased the wear performance at elevated temperatures, while the addition of 15 % Ag made the film too soft and sensitive to wear, which resulted in a partial removal of the film from the substrate inside the wear tracks.

Based on the obtained results, it seems that the optimal silver addition into the CrN film lies between 3 % and 15 %. Hence, silver concentrations of 7 % and 11 %, respectively, are going to be investigated (determination of the most important coating characteristics, i.e., microstructure, hardness, Young's modulus, wear resistance, friction coefficient) in the near future.

Acknowledgements

This paper is the result of the project implementation: CE for the development and application of diagnostic methods in the processing of metallic and non-metallic materials, ITMS: 26220120048.

5 REFERENCES

[1] R. Aubert, A. Gillet, J. Gaucher, P. Errat, Thin Solid Films, 108 (**1983**), 165
[2] R. Gahlin, M. Bromark, P. Hedenquist, S. Hogmark, G. Hakanson, Surf. Coat. Techn., 76–77 (**1995**), 174
[3] A. Tricoteaux, P. Y. Jouan, J. D. Guerin, J. Martinez, A. Djouadi, Surf. Coat. Techn., 174–175 (**2003**), 440
[4] G. Paller, B. Matthes, W. Herr, E. Broszeit, Mater. Sci. Eng. A, 140 (**1991**), 647
[5] L. Cunha, M. Andritshky, Surf. Coat Techn., 111 (**1999**), 158
[6] P. H. Mayrhofer, H. Willmann, C. Mitterer, Surf. Coat. Techn., 146–147 (**2001**), 222
[7] A. Lousa, J. Romero, E. Martinez, J. Esteve, F. Montala, L. Carreras, Surf. Coat. Techn., 146–147 (**2001**), 268
[8] A. Kondo, T. Oogami, K. Sato, Y. Tanaka, Surf. Coat. Techn., 177–178 (**2004**), 238
[9] C. Nouveau, E. Jorand, C. Deces-Petit, C. Labidi, M. A. Djouadi, Wear, 258 (**2005**), 157
[10] C. Nouveau, M. A. Djouadi, C. Deces-Petit, P. Beer, M. Lambertin, Surf. Coat. Techn., 142–144 (**2001**), 94
[11] O. Salas, K. Kearns, S. Carrera, J. J. Moore, Surf. Coat. Techn., 172 (**2003**), 117
[12] W. K. Grant, C. Loomis, J. J. Moore, D. L. Olson, B. Mishra, A. J. Perry, Surf. Coat. Techn., 86–87 (**1996**), 788
[13] M. Odén, J. Almer, G. Hakansson, M. Olsson, Thin Solid Films, 377–378 (**2000**), 407
[14] D. Mercs, N. Bonasso, S. Naamane, J. M. Bordes, C. Coddet, Surf. Coat. Techn., 200 (**2005**), 403
[15] E. Martinez, J. Romero, A. Lousa, J. Esteve, Surf. Coat. Techn., 163–164 (**2003**), 571
[16] S. M. Aouadi, D. M. Schultze, S. L. Rohde, K. C. Wong, K. A. R. Mitchell, Surf. Coat. Techn., 140 (**2001**), 269
[17] L. Cunha, M. Andritschky, K. Pischow, Z. Wang, Thin Solid Films, 355–356 (**1999**), 465
[18] P. H. Mayrhofer, G. Tischler, C. Mitterer, Surf. Coat. Techn., 142–144 (**2001**), 78
[19] M. A. Djouadi, C. Nouveau, P. Beer, M. Lambertin, Surf. Coat. Techn., 133–134 (**2000**), 478
[20] R. Wei, E. Langa, C. H. Rincon, J. H. Arps, Surf. Coat. Techn., 201 (**2006**), 4453
[21] J. Lin, Z. L. Wu, X. H. Zhang, B. Mishra, J. J. Moore, W. D. Sproul, Thin Solid Films, 517 (**2009**), 1887
[22] J. Lin, W. D. Sproul, J. J. Moore, S. Lee, S. Myers, Surf. Coat. Techn., 205 (**2011**), 3226
[23] B. Warcholinski, A. Gilewicz, Journal of Achievements in Materials and Manufacturing Engineering, 37 (**2009**) 2, 498
[24] M. Béger, P. Jurči, P. Grgač, S. Mečiar, M. Kusý, J. Horník, Kovove Materialy/Metallic Materiále, 51 (**2013**) 1, 1
[25] A. P. Ehiasarian, W. D. Munz, L. Hultman, U. Helmersson, I. Petrov, Surf. Coat. Techn., 163–164 (**2003**), 267
[26] J. W. Lee, S. K. Tien, Y. C. Kuo, C. M. Chen, Surf. Coat. Techn., 200 (**2006**), 3330
[27] F. R. Lamastra, F. Leonardi, P. Montanari, F. Casadei, T. Valente, G. Gusmano, Surf. Coat. Techn., 200 (**2006**), 6172
[28] E. Broszeit, C. Friedrich, G. Berg, Surf. Coat. Techn., 115 (**1999**), 9
[29] F. Attar, T. Johannesson, Thin Solid Films, 258 (**1995**), 205
[30] R. R. Aharonov, B. F. Coll, R. P. Fontana, Surf. Coat. Techn., 61 (**1993**), 223
[31] C. P. Mulligan, T. A. Blanchet, D. Gall, Surf. Coat. Techn., 203 (**2008**), 584
[32] C. Muratore, A. A. Voevodin, J. J. Hu, J. S. Zabinski, Wear, 261 (**2006**), 797
[33] J. J. Hu, C. Muratore, A. A. Vojvodin, Compos. Sci. Technol., 67 (**2007**), 336
[34] S. M. Aouadi, D. P. Singh, D. S. Stone, K. Polychronopoulou, F. Nahif, C. Rebholz, C. Muratore, A. A. Vojvodin, Acta Mater., 58 (**2010**), 5316
[35] C. P. Mulligan, T. A. Blanchet, D. Gall, Surf. Coat. Techn., 204 (**2010**), 1388
[36] C. P. Mulligan, D. Gall, Surf. Coat. Techn., 200 (**2005**), 1495
[37] C. P. Mulligan, T. A. Blanchet, D. Gall, Surf. Coat Techn., 205 (**2010**), 1350
[38] S. M. Aouadi, A. Bohnhoff, M. Sodergren, D. Mihut, S. L. Rohde, J. Xu, S. R. Mishra, Surf. Coat. Techn., 201 (**2006**), 418
[39] P. Basnyat, B. Luster, Z. Kertzman, S. Stadler, P. Kohli, S. Aouadi, J. Xu, S. R. Mishra, O. L. Eryilmaz, A. Erdemir, Surf. Coat. Techn., 202 (**2007**), 1011
[40] H. Kostenbauer, G. A. Fontalvo, J. Keckes, C. Mitterer, Thin Solid Films, 516 (**2008**), 1920

[41] P. Jurči, B. Šuštaršič, V. Leskovšek, Mater. Tehnol., 44 (**2010**) 2, 77–84
[42] A. I. Tyshchenko, W. Theisen, A. Oppenkowski, S. Siebert, O. N. Razumov, A. P. Skoblik, V. A. Sirosh, Y. N. Petrov, V. G. Gavriljuk, Mater. Sci. Eng., A, 527 (**2010**), 7027
[43] A. Oppenkowski, S. Weber, W. Theisen, J. Mater. Proc. Technol., 210 (**2010**), 1949
[44] ASTM G 99-95a Standard Test Method for Wear Testing with a Pin-on-Disk Apparatus, ASTM International, 2000
[45] P. Jurči, Mater. Tehnol., 45 (**2011**) 5, 383–394
[46] S. H. Yao, Y. L. Su, W. H. Kao, K. W. Cheb, Surf. Coat. Techn., 201 (**2006**), 2520
[47] P. Jurči, I. Dlouhý, Appl. Surf. Sci., 257 (**2011**) 24, 10581
[48] P. Jurči, S. Krum, Materiálové inžinierstvo/Materials Engineering, 19 (**2012**) 2, 64
[49] N. Schell, J. H. Petersen, J. Bottiger, M. Mucklich, J. Chevallier, K. P. Andreasen, F. Eichhorn, Thin Solid Films, 426 (**2003**), 100
[50] Z. B. Zhao, Z. U. Rek, S. M. Yalisove, J. C. Bilello, Surf. Coat. Techn., 185 (**2004**), 329
[51] R. G. Munro, J. Am. Ceram. Soc., 80 (**1997**), 1919
[52] C. P. Mulligan, T. A. Blanchet, D. Gall, Wear, 269 (**2010**), 125

UDK 621.762.5:666.3/.7
Original scientific article/Izvirni znanstveni članek

ISSN 1580-2949
MTAEC9, 48(2)171(2014)

SYNTHESIZING Si_3N_4 FROM A MIXTURE OF SiO_2-CaO

SINTEZA Si_3N_4 IN MEŠANICE SiO_2-CaO

Nuray Karakuş, Hüseyin Özkan Toplan

Sakarya University, Engineering Faculty, Dept. of Metallurgy and Materials Engineering, 54187 Sakarya, Turkey
nurayc@sakarya.edu.tr

Prejem rokopisa – received: 2012-08-16; sprejem za objavo – accepted for publication: 2013-07-05

In this study α-phase-rich Si_3N_4 powders were synthesized containing the sintering additive (CaO) using carbothermal reduction and nitridation. The starting agent for the silicon source was high-purity (99 %) synthetic silica. Carbon was added to the high-purity SiO_2 above the stoichiometric amount of oxygen. $CaCO_3$ (for the silicon nitride containing the mass fraction of CaO w = 10 %) was premixed in the starting reactants depending on the final powder composition and the type and amount of the secondary phases required for sintering. The synthesis was carried out in a tube furnace in different temperature ranges (1400 °C, 1450 °C and 1475 °C for 3h) under a nitrogen-gas atmosphere. Having completed the synthesis process, the powder properties were examined using standard characterization techniques (XRD, SEM, etc.).

Keywords: silicon nitride, carbothermal reduction, CaO, SiO_2

V tej študiji so bili sintetizirani s karbotermično redukcijo in nitridacijo z α-fazo bogati prahovi Si_3N_4 z dodatkom za sintranje (CaO). Začetni izvir silicija je bil zelo čisti (99 %) sintetični SiO_2. Ogljik je bil dodan zelo čistemu SiO_2 nad stehiometrično količino kisika. $CaCO_3$ (za silicijev nitrid je vseboval 10 % CaO) je bil primešan začetnim reaktantom, odvisno od končne sestave prahu in vrste ter količine sekundarnih faz, potrebne za sintranje. Sinteza je bila izvršena v cevni peči pri različnih temperaturah (1400 °C, 1450 °C in 1475 °C, 3 h) v atmosferi dušika. Po sintranju so bile lastnosti prahu ugotovljene z uporabo navadnih tehnik za karakterizacijo (XRD, SEM itd.).

Ključne besede: silicijev nitrid, karbotermična redukcija, CaO, SiO_2

1 INTRODUCTION

Silicon nitride (Si_3N_4) ceramics have a range of structural applications, such as engine components, heat exchangers, pump-seal materials, ball bearings, cutting tools, etc., owing to their excellent mechanical properties at both room and elevated temperatures.[1] The material properties of Si_3N_4 have led to speculation that it may also have a role in biomedical fields, since it is biocompatible and is visible on plain radiographs as a partially radiolucent material.[2]

The most common methods for silicon nitride preparation are the carbothermal reduction and nitridation (CRN) of silica, the direct nitridation of silicon and the thermal decomposition of silicon diimide. The carbothermal reduction used in this study takes place according to the following overall reaction:[3]

$$3SiO_2 + 6C + 2N_2 \rightarrow Si_3N_4 + 6CO \quad (1)$$

One of the difficulties found in the fabrication process is the sintering applied to attain high relative densities. Therefore, the use of additives to form a liquid phase is required.[4] Sintering aids such as MgO, Y_2O_3 and Al_2O_3 added to α-Si_3N_4 powders must be homogeneously distributed and possess the desired powder composition before shaping and sintering.[5] In this study α-phase-rich Si_3N_4 powders were synthesized containing a sintering additive using carbothermal reduction and nitridation. Thus, Si_3N_4 powder is ready for sintering and in addition is produced in a single step. Calcium oxide (CaO) was chosen as a metal oxide additive and it was mixed before synthesizing the Si_3N_4. Silicon nitride ceramic powders synthesized using this method might therefore be readily sintered because homogeneously distributed sintering additives were present in the starting materials. For this reason, the processing parameters are described in terms of the powder-synthesis conditions.

2 EXPERIMENTAL

For the CRN process, the raw material was high-purity synthetic silica of nearly colloidal range and it was supplied from EGE Kimya A. S. Activated charcoal was used as a reducing agent and it was supplied by TÜPRAŞ (Turkish Petroleum Refineries Co). The properties of the silica are given in **Table 1**. $CaCO_3$ was used as the CaO source; it was supplied by Çelvit Company. The $CaCO_3$ (for the silicon nitride containing w = 10 % CaO) was premixed in the starting reactants, depending on the final powder composition and the type and amount of the secondary phases desired for sintering. Carbon was added to the high-purity SiO_2 above the stoichiometric amount of oxygen (w(C)/w(SiO_2) ratio of 3). Dry mixing was performed by ball milling for 10 h with alumina

Table 1: Properties of silica (with firm data)
Tabela 1: Lastnosti SiO_2 (podatki dobavitelja)

Properties	SiO_2
Purity (%)	99
Grain size (μm)	14
Specific surface area (BET) ($m^2\ g^{-1}$)	139

balls for the composition. The nitrogen gas (99.99 % in purity) that was used for the nitridation process was supplied by BOS.

The carbothermal reduction and the nitridation process (CRN) were carried out in an atmosphere-controlled tube furnace. The synthesis was performed under a nitrogen gas flow (1 L/m) at 1400 °C, 1450 °C and 1475 °C for 3 h. After holding at these temperatures and this time, the furnace was allowed to cool to room temperature. The gas flow was stopped during cooling when the temperature reached 900 °C. After the CRN process, the products were heated in air for 1 h at 900 °C for residual carbon burning.

After the CRN process at different temperatures, the powder properties were examined by using standard characterization techniques (XRD, SEM, EDS).

3 RESULTS AND DISCUSSION

The silica was mixed with w(CaO) = 10 % (based on the final product) and carbon black for the CRN process. The prepared mixture was subjected to the CRN process for 3 h at 1400 °C, 1450 °C and 1475 °C. The XRD analyses of the produced powders are shown in **Figure 1**.

The α-Si_3N_4 was formed at a temperature of 1400 °C after 3h of reaction. In addition, small amounts of unconverted SiO_2 and CaN_2O_3 phase were found in the product powders. The temperature was increased to 1450 °C, but the β-Si_3N_4 formation was not completed at this temperature, which indicates that the holding time and/or temperature were not enough to complete the reaction. The best result was obtained at 1475 °C after a 3 h reaction. At this temperature (1475 °C), the produced powder was converted to α-Si_3N_4 and β-Si_3N_4, and in addition a minor amount of $CaSi_2N_2O_2$ was present. The formation of the $CaSi_2O_2N_2$ phase by a solid-state reaction was completed at 1300–1400 °C for 10 h.[6,7]

The complete formation of α-Si_3N_4 without using an additive (without CaO) was obtained at 1475 °C for a 6 h reaction, but the β-phase was not dedicated.[8] As seen from the XRD data, the carbothermal reduction and nitridation took place at 1475 °C. Comparing this with our previous work, the optimum temperature is the same for the product powders that used Y_2O_3 and Y_2O_3-Li_2O and 25 °C higher than the products that used MgO.[9] The powder produced at 1475 °C was fully converted to α and β-Si_3N_4, and a minor amount of $CaSi_2N_2O_2$ phase, as expected, were present. Different types of additives have been employed for the pressureless and pressure-assisted sintering of Si_3N_4 ceramics.

The melting temperature of the CaO-SiO_2 system is approximately 1436 °C, as indicated by the binary phase-equilibrium diagram.[10] However, the presence of N lowers these eutectic temperatures further. The alkali and alkaline-earth oxides have a low melting point and the viscosity of the resulting liquid is also low. The solution-diffusion-precipitation processes are enhanced.[11] Therefore, the $CaSi_2N_2O_2$ phase obtained after the CRN process can be desirable as the sintering aids for later use in sintering. Studies on the sintering of these synthesizing powders will be the focus of future work.

SEM micrographs of the powder synthesized from SiO_2 – w(CaO) = 10 % at 1400 °C and 1475 °C for 3 h are given in **Figure 2**. The micron-sized Si_3N_4 grains

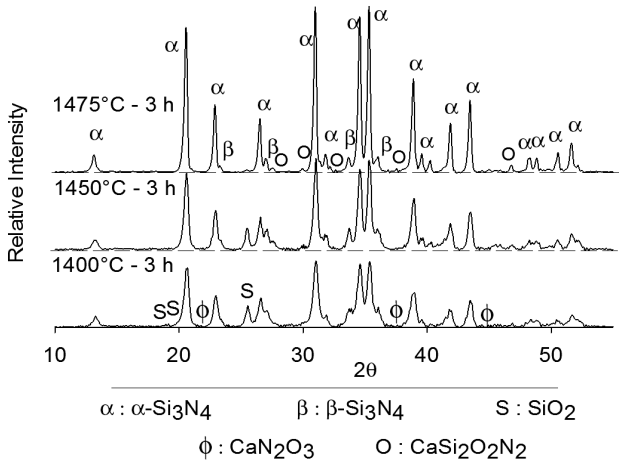

Figure 1: Phases formed at different temperatures (1400–1475 °C) after CRN of the SiO_2 – w(CaO) = 10 % mixture

Slika 1: Faze, ki nastajajo pri različnih temperaturah (1400–1475 °C) po CRN mešanice SiO_2 in w(CaO) = 10 %

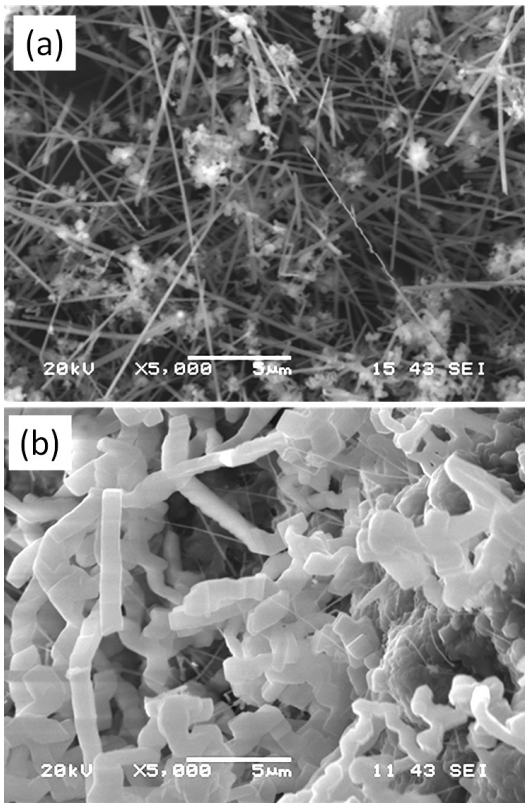

Figure 2: SEM micrographs of the product powder synthesized at: a) 1400 °C, 3 h and b) 1475 °C, 3 h

Slika 2: SEM-posnetka prašnatega produkta, sintetiziranega pri: a) 1400 °C, 3 h in b) 1475 °C, 3 h

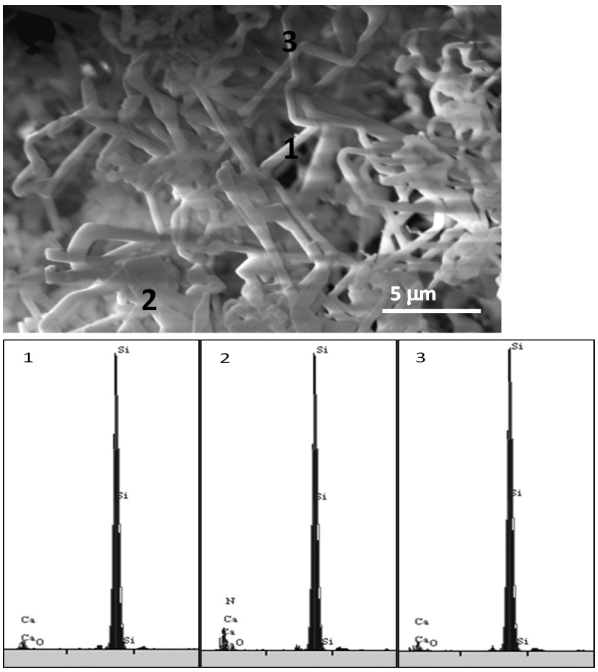

Figure 3: EDS analysis of the powders synthesized from SiO_2 – w(CaO) = 10 % at 1475 °C for 3 h

Slika 3: EDS-analiza prahov, sintetiziranih iz SiO_2 – w(CaO) = 10 % pri 1475 °C po 3 h

were formed after the CRN. SEM micrographs of the powder produced at 1400 °C for 3 h revealed different morphologies, ranging from irregular-shaped small particles to equiaxed small grains and long whiskers. The long whiskers had a cross-section of approximately 300 nm. SEM micrographs of the produced powder at 1475 °C for 3 h revealed the same morphologies as small particles and long whiskers.

It was clear that the grain size was increased with increasing temperature from 1400 °C to 1475 °C. The whiskers had a thickness of approximately 1 µm after the CRN process at 1475 °C. The EDS analysis of the powders synthesized from SiO_2 – w(CaO) = 10 % at 1475 °C for 3 h is showed in **Figure 3**. According to the EDS analysis, the Si, N, O, and Ca elements were detected from the particles in a manner consistent with the XRD analysis (**Figure 1**).

4 CONCLUSIONS

α-Si_3N_4 powders containing CaO as an oxide additive were successfully synthesized by carbothermal reduction and nitridation. The best result was obtained at 1475 °C after a 3 h reaction. The Si_3N_4 powders showed two major grain morphologies: submicron equiaxed and long whiskers. The advantage of using pre-additive oxide (CaO) in the CRN process is in terms of the reaction temperature and time.

5 REFERENCES

[1] X. Zhu, Y. Zhou, K. Hirao, Journal of the European Ceramic Society, 26 (**2006**), 711–718

[2] B. S. Bal, M. N. Rahaman, Acta Biomaterialia, 8 (**2012**), 2889–2898

[3] A. Ortega, M. D. Alcala, C. Real, Journal of Materials Processing Technology, 195 (**2008**), 224–231

[4] C. Santos, S. Ribeiro, K. Strecker, P. A. Suzuki, S. Kycia, C. R. M. Silva, Ceram. Inter., 35 (**2009**), 289–293

[5] M. Gopal, L. C. De Jonghe, G. Thomas, Scripta Mater., 36 (**1997**), 455–460

[6] Y. Gu, Q. Zhang, H. Wang, Y. Li, J. Mater. Chem., 21 (**2011**), 17790–17797

[7] Y. Gu, Q. Zhang, Y. Li, H. Wang, R. J. Xie, Materials Letters, 63 (**2009**), 1448–1450

[8] N. Karakuş, A. O. Kurt, H. Ö. Toplan, Materials and Manufacturing Processes, 27 (**2012**) 7, 797–801

[9] N. Karakuş, A. O. Kurt, H. Ö. Toplan, Ceramics International, 35 (**2009**), 2381–2385

[10] A. L. Brinkley, The Degree of Master of Science, MIT Virginia Military Institute, 1994

[11] B. Matovic, Ph.D. Dissertation, Max Planck Institut für Metallforschung, Stuttgart, 2003

UDK 621.74
Original scientific article/Izvirni znanstveni članek

ISSN 1580-2949
MTAEC9, 48(2)175(2014)

CAST CELLULAR METALS WITH REGULAR AND IRREGULAR STRUCTURES

ULITE KOVINE S PRAVILNO IN NEPRAVILNO CELIČNO STRUKTURO

Vlasta Bednářová, Petr Lichý, Tomáš Elbel, Aleš Hanus

Department of Metallurgy and Foundry Engineering, FMMI, VŠB - Technical University of Ostrava, 17. listopadu 15/2172, Ostrava – Poruba, Czech Republic
vlasta.bednarova@vsb.cz

Prejem rokopisa – received: 2012-09-03; sprejem za objavo – accepted for publication: 2013-06-10

An appropriate way to reduce the weight of manufactured parts without adversely affecting their strength is to use porous metallic materials with different internal arrangements of the intentionally created cavities. Porous metallic materials can be made from liquid metal, from powdered metal, metal vapours, or from metal ions. The aim of this research was to verify the possibilities of producing metallic foams by conventional foundry processes, to study the process conditions as well as the physical and mechanical properties of the metal foams produced. The experiments demonstrated the possibility of manufacturing castings with both a regular cellular structure and a solid skin in a single casting operation using different kinds of preform made from commonly used resin-bonded core mixtures. From the perspective of the need to destroy the preforms after the metal's solidification it seems a very interesting prospect to produce preforms from different salts.

Keywords: cellular metals, metal foams, casting

Primerna pot za zmanjšanje mase izdelanih delov, ne da bi občutno vplivali na njihovo trdnost, je uporaba poroznih kovinskih materialov z različno notranjo razporeditvijo namerno povzročenih praznih jamic. Porozne kovinske materiale se lahko izdela iz staljene kovine, kovinskih prahov, kovinskih par ali iz kovinskih ionov. Namen raziskave je bil preveriti možnost izdelave kovinskih pen po navadnem livarskem postopku, študij pogojev procesa, fizikalne in mehanske lastnosti izdelane kovinske pene. Izvršeni poskusi so pokazali možnost izdelave ulitkov z urejeno celično strukturo in čvrsto skorjo z eno livarsko operacijo z uporabo različnih predoblik, izdelanih iz navadnih mešanic za jedra. S stališča potrebne razgradnje predoblike, potem ko se kovina strdi, se zdi konkurenčna izdelava predoblike iz različnih soli.

Ključne besede: celične kovine, kovinske pene, ulivanje

1 INTRODUCTION

Cellular metals and metallic foams are metallic materials containing pores in their structure that are created intentionally. To properly identify the material, according to J. Banhart,[1] one has to distinguish the following: the term *cellular metal* is a general term describing a material in which any kind of gaseous voids are dispersed, in a *porous metal* the pores are usually round and isolated from each other, while the terms foam metal and metal foam are used for a porous metal produced by foaming a melt in which the pores are not interconnected ("structure with closed pores"). In addition, we have the term *metal sponge,* which is used for highly porous materials, in which the pores are connected in a complicated manner and the structure cannot be divided into individual cavities ("structure with open pores"). The term metallic foam is, however, very often used, even in the professional literature, as a general designation of porous materials.

Since the discovery of porous metallic materials numerous methods of production have been developed. According to the state in which the metal is processed the manufacturing processes can be divided into four groups. Porous metallic materials can be made from:[2]

- **liquid metal** (e.g., direct foaming with gas, blowing agents, powder compact melting, casting, spray forming),
- **powdered metal** (e.g., sintering of powders, fibres or hollow spheres, extrusion of polymer/metal mixtures, reaction sintering),
- **metal vapours** (vapour deposition),
- **metal ions** (electrochemical deposition).

Over the past two decades, opportunities for the use of porous metals have increased in many research and industrial applications. Growing interest is related to the specific characteristics of this material. Porous metals represent a new type of materials that fulfil current ecological requirements (particularly in the area of weight reduction) and have unique service properties thanks to a structure with low densities, large specific surfaces, and a useful combination of physical and mechanical properties (absorption of energy, absorption of sound and vibration, thermal insulation, and heat exchange).

Despite the uniqueness of the properties and the wide range of possibilities of use, the number of examples of practical, stable, industrial applications is not large. Nickel foam materials are mass-produced and used as electrodes in rechargeable batteries for portable devices (mobile phones, laptops), while titanium foams are used

as implants. At present, the most explored porous metal materials are aluminium foams, which can be documented by the development of prototypes as well as practical applications (small series for AUDI and Lamborghini crash zones).[3] The reasons for the limited use of cellular metals are primarily economic. This is why the current interest (as reflected in a growing number of new published studies and possibilities for industrial applications[4–7]) is focused mainly on the development of technologies enabling the production of foam materials at costs that would allow their widespread use.

The research work carried out at the Department of Metallurgy and Foundry Engineering of the VSB – Technical University aims to study a technique for manufacturing porous metals using the conventional principles of gravity casting in sand moulds. Our intention is to use procedures for liquid-metal processing, enabling the production of complex-shaped castings, not only a simple block of metal foam. The research focuses on two approaches that use the standard foundry technique of casting into disposable sand moulds or permanent metallic moulds with the use of precursors and ceramic prefabricated parts prepared by known methods for core making. These approaches bring low overall costs as well as the advantage of the direct production of parts from complex shapes without any necessary further forming, welding, machining and with use of traditional foundry procedures.

The production of metallic foams using conventional gravity casting into foundry moulds presupposes a more cost-efficient process than other known technologies such as powder metallurgy, metal evaporation and ionization. Cast metallic foams are not yet produced in the Czech Republic.

2 EXPERIMENTAL

The subject of the research was the testing of infiltration techniques for the manufacture of porous metals with both regular and irregular structures. The foundry methods used can be divided into two basic groups:

- two-stage investment casting
- infiltration of liquid metal into the mould cavity filled with different types of filling materials

Figure 1: Ceramic particles with fractions 8–18 mm
Slika 1: Keramični delci zrnatosti 8–18 mm

2.1 Two-stage investment casting

According to this process, a polymer foam, e.g. polyurethane foam, is used as a "lost foam pattern". The pattern is first infiltrated by a slurry of the plaster, to create a plaster "investment". This then undergoes a heat treatment that solidifies the "investment" and burns the polymer foam. Molten metal is poured into the prepared investment, and after the metal's solidification the investment must be removed to leave the internal cavities.

Plaster slurry composition:
100 mass parts of Goldstarpowders MO28 plaster
50 mass parts of water

The material used for the casting was the AlSi10MgMn alloy.

2.2 Infiltration techniques

Infiltration techniques are based on the infiltration of a liquid metal between various filler materials (called a preform or precursor) placed in the mould cavity. Since they do not occupy the entire volume, these precursors form a network of interconnected porosities. The preform must be made of a material that retains its shape during the liquid metal's infiltration (sufficient strength, low abrasion) and can be destroyed after the casting to leave the cavities. The preform must not contain a disconnected island of material so that it can be completely eliminated from the solidified metal.

2.2.1 Use of a precursor as a filler material

Material of precursors that were inserted into the green sand mould cavity:

- granules made of ceramic material with fractions of 8–16 mm and 3–4 mm (**Figure 1**).
- granules made of resin-bonded moulding mixtures (shell-mould, CO_2 resol), fractions 8–16 mm (**Figure 2**).

Apart from the different granulometry, several designs of gating system were used, and the temperature of the filler material was changed (in order to positively affect the castabily of the molten metal).

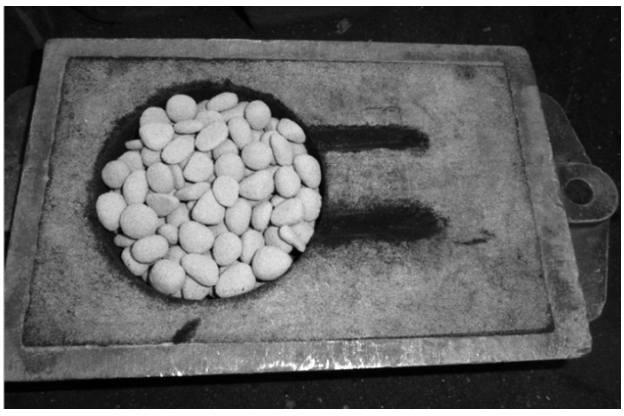

Figure 2: Shell-mould particles inserted into mould cavity
Slika 2: Lupinasti delci, vloženi v livno votlino

The materials used for the casting were the AlSi10MgMn alloy and cast iron with lamellar graphite – in accordance with EN GJL-200.

2.2.2 Use of preform as a filler material

A regular cellular structure can be achieved using different types of preforms that fill the mould cavity. Using a preform like a core not filling the whole mould cavity can make it possible to manufacture a casting with a solid surface layer and an internal porous structure with defined cell dimensions.

For the manufacturing of a sand preform/core it was necessary to prepare a core box. Fused Deposition Modelling technology was used to manufacture the core box. Due to the complex lattice shape of the core, a sectional core box was designed consisting of five parts, which allowed the easy removal of the core.

The materials used for the preform/core manufacturing were:

- CO_2 hardened alkaline phenolic process (the resin is an alkaline phenolic one, containing a linking substance stabilised at a high pH, curing occurs by gassing with carbon dioxide, which dissolves in the water solvent of the resin, so lowering its pH and activating the linking substance.)
- and KCl salt (**Figure 3**).

3 RESULTS AND DISCUSSION

3.1. Two-stage investment casting

The pattern was made of polyurethane foam, the cavities of which was first filled by plaster (100 mass parts of plaster, 50 mass parts of water). The plaster investment was then allowed to dry completely, by subsequently annealing at (100, 500, 640) °C for drying and evaporation of a polyurethane foam. Melting and pouring were made with an INDUTHERM MC 15 device. The equipment enables a combination of vacuum and high pressure to ensure full infiltration. Pouring off takes place using a 90° rotation of the casting unit. The AlSi10MgMn alloy was poured at a temperature 750 °C under a reduced pressure of 1 bar. After pouring, the INDUTHERM MC 15 device automatically switches to an overpressure of 2 bar in order to optimize the mould filling, even for delicate parts. The plaster was removed by dissolving out in water. In the case of a very fine metal foam there are sometimes problems with removing the ceramic without damaging the metal foam. The obtained castings are the exact replicates of the original polymer foam (**Figure 4**) and exhibit the highest porosities (80–97 %). This type of foam provides a very promising application, for example, in the filtration of liquid metals.

Figure 4: AlSiMg alloy near-net-shape metal foam, porosity 90 %
Slika 4: Drobna mreža kovinske pene iz zlitine AlSiMg s poroznostjo 90 %

Investment casting can also be used to obtain castings with both high porosities and a regular cellular structure.

The pattern was made from extruded polystyrene foam, forming regular structures made from elements bonded layer by layer, as shown in **Figure 5**. The pattern cavities were filled with a plaster slurry (100 mass parts of plaster, 35 mass parts of water). After solidification and sufficient drying of the matrix prepared in this way the pattern/investment was subjected to 8 h of gradual annealing (**Figure 6**) in order to remove the polystyrene

Figure 3: Test samples of KCl salt
Slika 3: Preizkušanci iz soli KCl

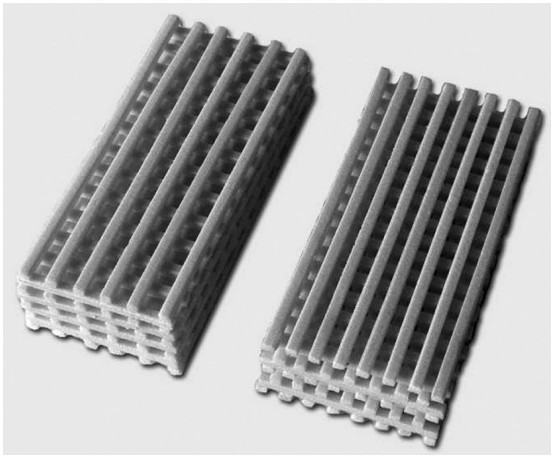

Figure 5: Polymer foam pattern with regular internal structure
Slika 5: Predoblika s pravilno notranjo strukturo iz polimerne pene

Figure 6: Thermal treatment of plaster investment to burn the polymer foam
Slika 6: Toplotna obdelava forme iz mavca, za odstranitev polimerne pene

foam and to achieve sufficient strength as the plaster matrix is subjected to large loads, both thermal and mechanical, during the pouring off.

The plaster pattern was inserted into the cavity of the commonly used green sand mould (bentonite bonded mixture) and then the AlSi10MgMn alloy was poured at a temperature of 750 °C. The plaster was removed by dissolving into a water bath and its residues were removed by a mechanical force in an ultrasonic bath.

The manufacture of castings with a regular cellular structure (**Figure 7**) by investment casting makes it possible to achieve internal cavities (cells) with a precisely defined shape, and thus predicable mechanical properties and reproducible results.[8,9] The main disadvantages of the production process are a high complexity and rather high costs.

3.2. Infiltration techniques

3.2.1 Use of a precursor as a filler material

The performed experiments using different types of precursors[10] proved the feasibility of this method for manufacturing porous metals. The condition of extraction of the precursors after solidification of the metal is an obstacle for the use of ceramic particles because it is generally difficult to remove the ceramic to leave the

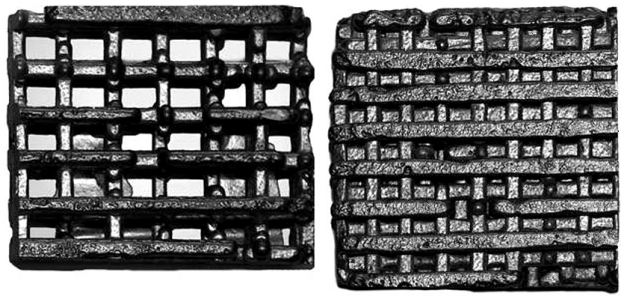

Figure 7: AlSiMg alloy castings with a regular cellular structure, porosities 60–68 %
Slika 7: Ulitek iz zlitine AlSiMg z enakomerno celično strukturo s poroznostjo 60–68 %

Figure 8: Casting made of AlSi10MgMn with remaining precursors
Slika 8: Ulitek, izdelan iz AlSi10MgMn s preostalo predobliko

cavities. More advantageous is the use of granules manufactured from the used resin-bonded core mixtures, which can be easily removed, depending on the pouring temperature and the core mixture collapsibility. In the case of the worse collapsibility the filler material may remain in the casting (**Figure 8**) and its removal would require an additional annealing of the castings (to destroy the resin), which would slightly increase the energy consumption of such production.

The main characteristic of the method using different kinds of precursors as a filler material is the irregular structure and the random distribution of pores throughout the volume of the casting, and therefore the impossibility of achieving reproducible results (**Figure 9**).

3.2.2 Use of a preform as a filler material

The performed experiments have demonstrated the possibility of manufacturing castings with both a regular cellular structure and solid skin in a single casting operation using different kinds of preform made from commonly used resin-bonded core mixtures. The specified resin-core mixture[11] has a sufficient strength and abrasion resistance enabling the handling operation and good collapsibility allows destroying it after solidification.

From the perspective of the necessity to destroy preforms after metal solidification (**Figures 10** and **11**) it seems a good strategy to produce preforms from

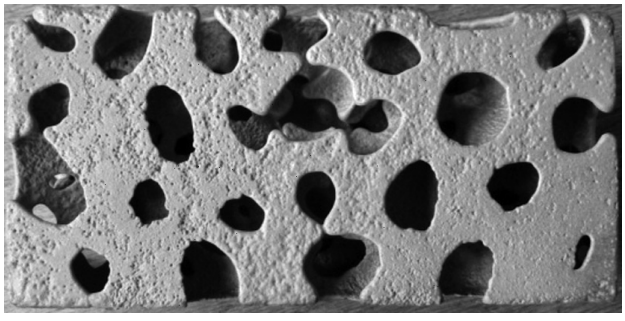

Figure 9: Clean cavities of cast iron EN GJL-200
Slika 9: Očiščene praznine v litem železu EN GJL-200

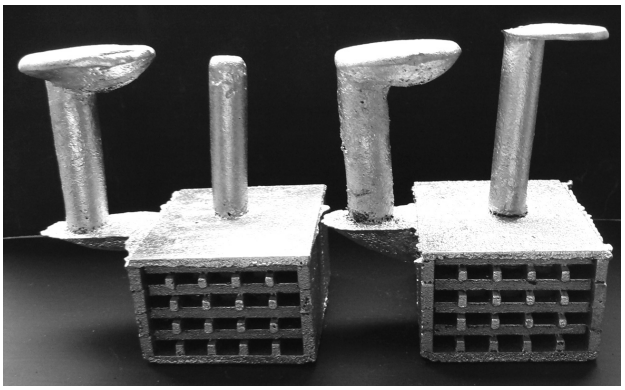

Figure 10: AlSiMg alloy castings with a regular cellular structure
Slika 10: Ulitki iz zlitine AlSiMg z enakomerno celično zgradbo

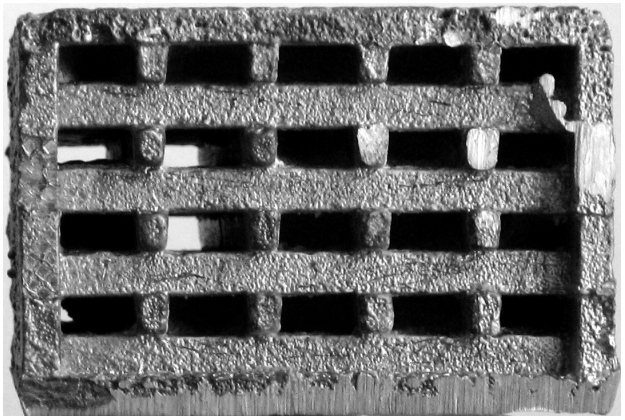

Figure 11: Detail of AlSiMg alloy casting with regular cellular structure
Slika 11: Detajl ulitka iz zlitine AlSiMg z enakomerno celično zgradbo

different salts. The tested salt was 100 % KCl, and the cores were prepared by stamping with a pressing force to 10 t.

The use of the KCl made destroying the preform very easy by dissolving out the water. But industrial implementation would require an extra waste-water treatment circuit, which would make the application more complicated.

4 CONCLUSIONS

Investment casting makes it possible to achieve the highest porosity (97 %) in both types of porous castings. In the case of very fine metal foams, problems may occur with removing the ceramic without the metal foam being damaged. Near-net-shape cast-metal foams provide a promising implementation, e.g., liquid-metal filtration. The manufacturing of castings with a regular cellular structure, using investment casting, makes it possible to achieve internal cavities (cells) with a precisely defined shape, and thus predicable mechanical properties and reproducible results. The main disadvantages of the investment-casting production process are its high complexity and thus rather high production costs. Using different types of precursors as a filler material results in porous castings with open pores in a stochastic arrangement. The main drawback of the method is the irregular structure and random distribution of the pores throughout the volume of the casting. The performed experiments have demonstrated the possibility of manufacturing castings with both a regular cellular structure and a solid skin in a single casting operation using different kinds of the preform made from commonly used resin-bonded core mixtures.

Mastering the production of metallic foams with a defined structure and properties using gravity casting into sand foundry moulds will contribute to an expansion of the assortment produced in foundries by a completely new type of material, which has unique service properties thanks to its structure, and which fulfils the current ecological requirements. The manufacture of foams with the aid of gravity casting in conventional foundry moulds is a cost-advantageous process that can be industrially used in foundries without high investment demands. Metal foams are progressive materials with continuously expanding use. Cast metallic foams are not yet produced in the Czech Republic.

Acknowledgements

This work was supported by the Technology Agency of the CR within the frame of the research project TA02011333.

5 REFERENCES

[1] J. Banhart, Manufacture, characterisation and application of cellular metals and metal foams, Progress in Materials Science, 46 (**2001**), 559–632
[2] J. Banhart, Manufacturing routes for metallic foams, Journal of Minerals, Metals and Materials, 52 (**2000**) 12, 22–27
[3] Y. Gaillard, J. Dairon, M. Fleuriot, B. W. Corson, Les materiaux cellulaires: une innovation aux applications multiples, Fonderie magazine, (**2010**) 1, 21–33
[4] Cellmet News: http://www.metalfoam.net/cellmet-news_2006-1_net.pdf
[5] I. Paulin, et. al., Synthesis of aluminium foams by the powder metallurgy process: compacting of precursors, Mater. Tehnol., 45 (**2011**) 1, 13–19
[6] MetFoam2009: http://www.metfoam2009.sav.sk/index.php?ID=2571
[7] J. Dairon, et al., Mousses métalliques: CTIF innove dans les matériaux cellulaires, Fonderie – Fondeur d'aujourd'hui, (**2009**) 295, 12–19
[8] M. Cholewa, M. Dziuba-Kaluža, Analysis of structural properties of skeleton castings regarding the crystallization kinetics, Archives of Materials Science and Engineering, 38 (**2009**) 2, 93–102
[9] I. Zyrjanova, Lité kovové pěny z Al slitin, diplomová práce, VŠB-TU Ostrava, 2011
[10] A. Hanus, P. Lichý, V. Bednářová, Production and properties of cast metals with porous structure, Metal 2012, 21st International Conference on Metallurgy and Materials, Conference proceedings, 1–6
[11] V. Bednářová, P. Lichý, T. Elbel, Casting routes for porous metals manufacturing, Proceedings book, 12th International Foundrymen Conference, Sustainable Development in Foundry Materials and Technologies, Opatija, 2012, 16–23

UDK 543
Original scientific article/Izvirni znanstveni članek

ISSN 1580-2949
MTAEC9, 48(2)181(2014)

SPIN-COATING FOR OPTICAL-OXYGEN-SENSOR PREPARATION

UPORABA SPINSKEGA NANOSA PRI IZDELAVI OPTIČNIH SENZORJEV ZA KISIK

Polonca Brglez[1,2], Andrej Holobar[1], Aleksandra Pivec[3], Mitja Kolar[2,4]

[1]ECHO, d. o. o., Stari trg 37, 3210 Slovenske Konjice, Slovenia
[2]University of Maribor, Faculty of Chemistry and Chemical Engineering, Smetanova 17, 2000 Maribor, Slovenia
[3]ZRS Bistra Ptuj, Slovenski trg 6, 2250 Ptuj, Slovenia
[4]Centre of Excellence PoliMaT, Tehnološki park 24, 1000 Ljubljana, Slovenia
mitja.kolar@um.si

Prejem rokopisa – received: 2012-09-27; sprejem za objavo – accepted for publication: 2013-06-18

Thin-film oxygen sensors were prepared using the spin-coating technique, where a tris (4,7-diphenyl-1,10-phenanthroline) ruthenium(II) dichloride complex (RuDPP) in various solvents and silicones deposited on different substrates was used for the sensor production. By changing the spin-coating set-up parameters, homogeneous sensor coatings and the optimum sensor response to oxygen were studied – the sensors were exposed to various concentrations of oxygen within the range from 0 % to 100 %. During the presented study, the optimum results were obtained when a 150 μL of sensor solution was applied to a Dataline foil using silicone E4 and a chloroform solvent. A spin coater with the following three rotation stages was used: 750/700 r/min for 3 s, 300 r/min for 3 s and 150 r/min for 4 s. The spin-coating technique has several benefits: it is fast, easy to use and appropriate for low-volume operations. It allows modifications and preparations of several sensor series using the minimum reagent consumption. However, the disadvantage of this technique also has to be mentioned, namely, an uneven film thickness in the radial direction. The film thickness mainly depends on the experimental set-up (volume, rotation time and speed, solvent viscosity and evaporation). Spin coating as an alternative and very flexible technique for an oxygen-sensor preparation is suggested for the laboratory-scale work, where the majority of experimental data could be used when other new coating methods are also researched and implemented.

Keywords: tris (4,7-diphenyl-1,10-phenanthroline) ruthenium(II) dichloride complex, spin coating, optical oxygen sensor, oxygen

Izdelani so bili tankoplastni optični senzorji za kisik s tehniko spinskega nanosa. Pri tem so bile uporabljene različne koncentracije tris (4,7-difenil-1,10-fenantrolin) rutenij(II) diklorid kompleksa (RuDPP), različna topila, polimerni nosilci, silikoni in parametri spinskega prekritja. Naš namen je bil pripraviti najbolj homogen nanos senzorske raztopine in tako dobiti najbolj optimalne lastnosti senzorjev. Preučevali smo tudi vpliv hitrosti in časa vrtenja spinske naprave za prekrivanje na odziv senzorjev, saj so bili le-ti po izdelavi izpostavljeni različnim koncentracijam kisika v območju od 0 % do 100 %. Najboljši nanos senzorske raztopine smo dobili s senzorsko raztopino v kloroformu 150 μL z uporabo silikona E4 z nanosom na folijo Dataline. Pri tem smo uporabili tri različne stopnje vrtenja: 3 s pri 750/700 r/min, 3 s pri 300 r/min in 4 s pri 150 r/min. Prednost uporabe spinskega prekrivanja je, da je ta tehnika zelo hitra, enostavna za uporabo in je primerna za nanos majhnih prostornin. Omogoča izdelavo več serij senzorjev z različnimi lastnostmi ob minimalni porabi reagentov. Nanos senzorske raztopine na polimernem nosilcu v radialni smeri je v veliki meri odvisen od eksperimentalnih razmer: prostornine nanosa, hitrosti vrtenja, viskoznosti in hlapnosti topil. Metoda spinskega prekritja se je izkazala kot učinkovita metoda za nanos senzorskih raztopin v laboratorijskem merilu, vendar je po celotni senzorski površini težko pripraviti popolnoma homogen nanos, zato je za pripravo večjih količin identičnih senzorjev – po optimiranju vseh drugih eksperimentalnih razmer – smiselno preučiti še alternativne metode nanašanja.

Ključne besede: tris (4,7-difenil-1,10-fenantrolin) rutenijev(II) diklorid kompleks, spinsko prekritje, optični kisikov senzor, kisik

1 INTRODUCTION

Oxygen (O_2) is considered to be one of the more important gases in our environment. The determination of O_2 concentrations in the air, especially at low levels, plays an important role in different areas ranging from environmental, biological, analytical and industrial monitoring. These are the reasons why there is still a growing interest in the construction and development of oxygen sensors.[1–4]

There has been a trend in the development of optical oxygen sensors over the last few decades because these sensors are more attractive than conventional amperometric sensors. Optical oxygen sensors have a lot of advantages such as: a faster response time, a high sensitivity and selectivity, no O_2 consumption, the inertness against sample flow rate or stirring speed, absence of poison, and no need for a reference electrode.[5–15] They are immune to exterior electromagnetic-field interference and can be produced as disposable sensors.[16,17] Optical oxygen sensors are cheap, easily miniaturized and simple to use; they mainly operate on the principle of oxygen quenching those dye molecules that have been entrapped within a porous support matrix. Ruthenium(II) complexes are, by far, the most widely used oxygen dyes, because they have relatively long fluorescent lifetimes determined by the metal-to-ligand charge-transfer (MLCT) excited state, fast response time, strong visible absorption, large Stokes shift, and high photochemical stability.[2,3,11,12,14,18–23] Ru(II) complexes exhibit a high

sensibility to luminescence quenching and the positions of their absorption and emission spectra permit an application of low-cost, solid-state optoelectronics for the detection of luminescence intensity. The dyes can be excited with blue or even blue-green light-emitting diodes (LEDs) exhibiting a large Stokes shift and resulting in the emission of orange-red light.[24]

The basic operational principle of a fluorescent optical sensor for measuring oxygen is based on reducing the intensity of the fluorescence (quenching) due to the involvement of oxygen within the dye structure. The calibration of the most luminescence quenching-based optical sensors relies, in essence, on the Stern-Volmer equation.

The immobilization of the Ru(II) complexes in sol-gel matrices has been recently investigated.[4,25–27] There have also been reports on optical oxygen sensors based on the luminescence change of the ruthenium(II) complex immobilized in organic and inorganic polymers (polystyrene, silicone polymer, sol-gel glass, etc.) and zeolite matrix.[28–30] The sol-gel process has been so far the most widely used method for the preparation of oxygen sensors.[5,31,32] It is an efficient immobilization technique due to its many desirable properties such as high thermal stability, good photostability and optical transparency within the visible region.[5]

The spin-coating technique is also used for the sensor preparation. Spin coating has been used for several decades for the application of thin films.[33,34] This is a technique that uses centrifugal forces created by a spinning substrate for spreading a coating solution evenly over a surface.[35] It can be controlled with a few parameters in order to yield a well-defined coating coverage.[36,37] The flow is governed by a balance between the centrifugal force against the viscosity and surface tension. It has been shown that the non-uniform distribution in the initial film profile tends to become uniform during spinning. Spin coating has been mainly used in the photoresist coating process because of its simplicity of operation, its uniformity and the thinness of the coated layers. The spin-coating process involves depositing a small puddle of fluid onto the center of a substrate, and then spinning the substrate at a high speed (typically around 3000 r/min). The centripetal acceleration then causes the solution to spread towards, and eventually off, the edge of the substrate leaving a thin film on the surface. The coat thickness is controlled with the rotational speed of the substrate; faster rotations result in thinner coating layers.

The spin-coating process needs to be reshaped and optimized because of the changes in the operational parameters and the wafer size.[38] There is scientific literature describing the spin-coating process, emphasizing the importance of rotational speed, time, acceleration, periods, liquid viscosity, density, polymer, temperature and humidity for the film thickness.[39]

There are four distinct stages in the spin-coating process (**Figure 1**):

- Deposition of a coating fluid onto a wafer or substrate.
- Acceleration of the substrate up to its final desired rotational speed.
- Spinning of the substrate at a constant rate; fluid viscous forces dominate the fluid thinning behavior.
- Spinning of the substrate at a constant rate; the solvent evaporation dominates the coating thinning behavior.

The final film thickness and other properties depend on the nature of the used polymer (viscosity, drying rate, percent of solids, surface tension) and the parameters chosen for the spin process (final rotational speed, acceleration). One of the more important factors in spin coating is the repeatability. Subtle variations in these parameters defining the spin process can result in drastic variations in the coated films.

The presented goal was a preparation of thin-film oxygen sensors using the spin-coating technique. In this work a spin coater was used for spreading different sensor solutions onto various polymer substrates. The substrates (polymer solid layers – foils) were optically transparent films. The most important function of the substrate was to act as a strong mechanical carrier with a high transparency, physical strength, and chemical resistance. Different amounts of RuDPP in various solvents were used for the sensor production and various transparent polymer substrates were used as the carriers. The goal was to obtain the most homogeneous sensor coating with the spin coater by changing the set-up parameters. After the sensor preparation the sensors were exposed to various concentrations of oxygen, ranging from 0 % to 100 %.

2 EXPERIMENTAL WORK

2.1 Chemicals and solutions

All the chemicals used were of analytical purity grade. All the solutions were prepared with deionized

Figure 1: Scheme of the spin-coating sensor preparation
Slika 1: Shematičen prikaz postopka spinskega nanosa pri izdelavi senzorjev

water. Silicon (Elastosil E4, Elastosil E41, Wacker), a polymer layer (foil DATALINE 57170, Dataline, EU; foil PLASTIBOR TOP COD 12530 12950, Lazertechas, UAB; foil ESSELTE 509700, Esselte, EU), a tris (4,7-diphenyl-1,10-phenanthroline) ruthenium(II) dichloride complex (Sigma-Aldrich), toluene (Sigma-Aldrich), chloroform (CHLO) (Sigma-Aldrich) and methyl ethyl ketone (ME) (Sigma-Aldrich) were used for the sensor preparation.

The following gases from Messer, d. o. o., Slovenia, were used for testing an optical oxygen sensor: nitrogen (N_2, 99.999 %) and oxygen (O_2, 99.9999 %).

2.2 Apparatus

Optical measurements were studied using an EOM-O_2 micro electro-optical module (PreSens) controlled by the EOM-O_2_v1_3_exe software, a gas-mixing device (Echo, d. o. o.) and a flow cell (Echo, d. o. o.). Additional equipment included: an AB54-S balance (Mettler Toledo), a spin-coater (Polos), a MST digital magnetic stirrer (Ika) and a SUPRA 35 VP (Carl Zeiss) scanning-electron microscope (SEM).

2.3 Preparation of RuDPP optical oxygen sensors

Different amounts of RuDPP within the range of 20 mg to 80 mg were diluted using different solvents (toluene, chloroform and methyl ethyl ketone).

An appropriate amount of RuDPP was weighted in a 10 mL flask and diluted using an appropriate solvent. The prepared sensor solution was then being stirred with a magnetic stirrer for 10 min. The sensor solution was then filtered through filter paper and a 4 mL sensor solution was added to 2 g of silicone. This sensor solution was mixed on a magnetic stirrer for about 1 h to become homogeneous and viscous. The sensor solution was protected from the external light with an aluminum foil, and was applied to the solid layers using the spin-coating technique. Different polymer solid layers (foils) were used for the substrate (ESSELTE, DATALINE and PLASTIBOR). Different amounts ((100, 150 and 200) μL) of the sensor solutions were applied using the spin-coating technique. The effects of changing the rotation speeds and times of spinning were also studied; the details are given in **Table 1**.

Table 1: Rotation speed and spinning time
Tabela 1: Hitrost vrtenja in čas vrtenja naprave za spinsko prekrivanje

Stage	Number of turns (r/min)	Time of spinning (s)
1st step	500 to 900	1–10
2nd step	300 to 700	1–10
3rd step	100 to 150	1–10

The sensor solution was mounted on a rotating platform. The substrate was rotated according to the selected rotation speed/spinning time and the sensor solution was dispensed directly onto it. The high-speed rotation threw off most of the solution, leaving behind a thin, uniform coating.

The prepared optical sensors were then dried; they were usually left to dry out for 24–48 h at a room temperature of (20 ± 2) C°. After drying, the optical sensors were cut to the diameter dimensions of 1.75 cm^2/15 mm. The sensors were stored in a dark and dry place before use.

2.4 Measurement procedures

The optical oxygen sensors were tested in a flow cell (**Figure 2**). They were excited with a blue LED and measured with an optical detector from PreSens. The gas mixtures (N_2/O_2) passed the active sensor surfaces at a constant flow rate of 1 L/min.

The changes of the signal were measured for different concentrations of oxygen. The gas mixtures were prepared with a gas mixing device (Echo, d. o. o.).[4] During the constant flow of the carrier gas, various concentrations of oxygen were added to obtain different concentrations within the range of $1 \cdot 10^{-6}$ to $1000 \cdot 10^{-6}$. The accuracy of the concentrations was $\pm 0.7 \cdot 10^{-6}$. The gas-mixing device provided a repeatability of ± 0.15 % and, within the full-scale mode, the temperature range was from 15 °C to 25 °C and the pressure varied from 70 kPa to 400 kPa. **Figure 3** schematically presents the system used for the optical measures. The measuring system consisted of: a gas-mixing device, a flow cell, an electro-optical module and a computer.

Surface analyses of the sensors were performed with a scanning electron microscope (SEM), Supra 35 VP

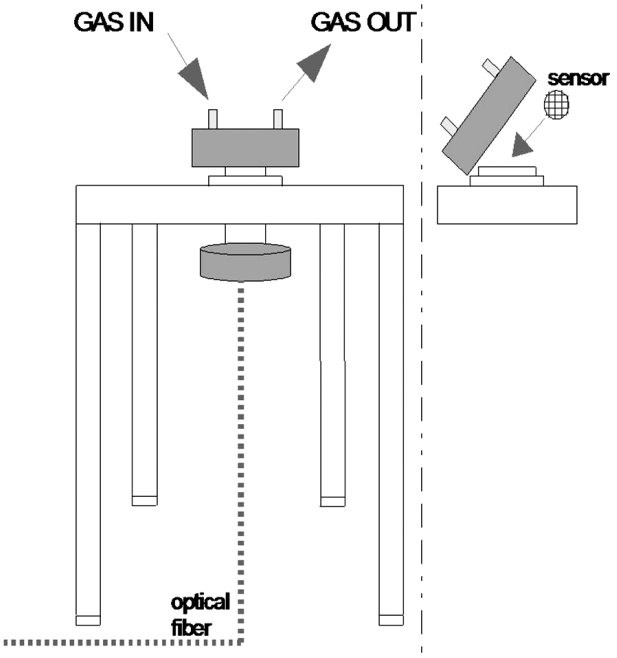

Figure 2: Scheme of the flow cell (left) and sensor positioning (right)
Slika 2: Shema pretočne celice (levo) in namestitev senzorja (desno)

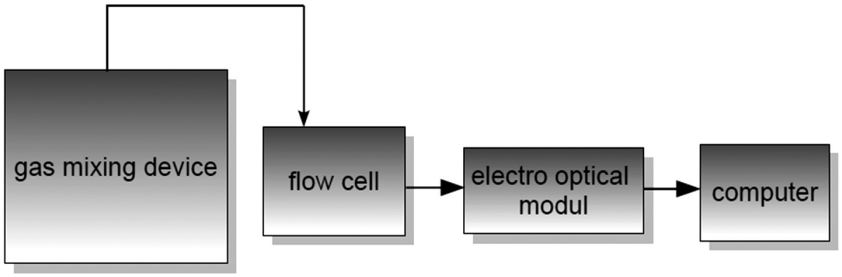

Figure 3: Scheme of the measuring system
Slika 3: Shema merilnega sistema

Carl Zeiss. All the pictures were recorded using a 30 μm scan window at the 1 kV electronic potential.

3 RESULTS AND DISCUSSION

The influences of the dye concentration, different polymer solid layers (foils), silicones, film thickness and different solvents on the sensor sensitivity were studied.

3.1 Influence of the RuDPP concentration vs. the sensor sensitivity

The Stern-Volmer equation describes the fluorescence intensity versus the measured concentration of oxygen.[4] A deviation from the linearity is connected with the heterogeneity of a polymer matrix; the fluorophore molecules are usually surrounded by voids and polymer particles, therefore, all the indicator molecules are non-equally accessible to oxygen. A decline in fluorescence is strongly dependent on the diffusion and adsorption of oxygen and on the dye solubility. The concentration of the indicator must be appropriately selected in order to obtain the optimum sensor sensitivity, and the dye concentration must be additionally optimized according to the measure range.

The sensors were prepared according to the procedure described in Section 2.3. The amounts of (20, 40, 60 and 80) mg of RuDPP were used for preparing the sensor solution (**Figure 4**), while the linearity (R^2) was tested within the range of 0 % to 100 % concentration of oxygen.

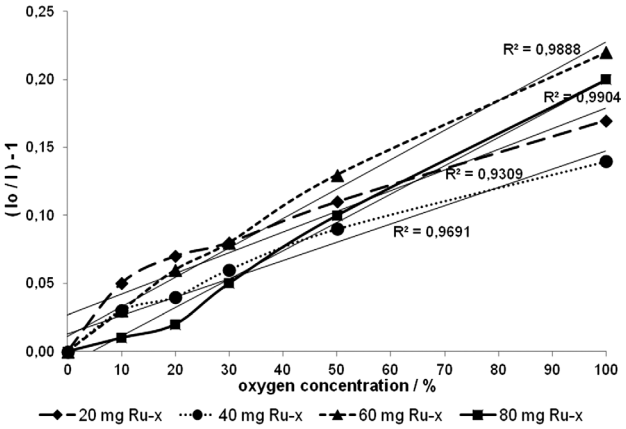

Figure 4: Influence of RuDPP concentration vs. sensor response
Slika 4: Vpliv koncentracije RuDPP na odziv senzorjev

The linearity of the sensors prepared from 20 mg of RuDPP was 0.9309, for 40 mg of RuDPP it was 0.9691, for 60 mg of RuDPP it was 0.9888, and 0.9904 for 80 mg of RuDPP. The optimum sensor was the one with 80 mg of RuDPP, therefore, it can be concluded that the concentration of RuDPP strongly influences the sensor response. In general, with higher concentrations of RuDPP, the sensor linearity, accuracy and precision are improved. In addition, a strong fluorescence signal was obtained and no additional amplification of the measuring signal was used. The electronic-optical noise usually increased with a higher amplification rate, which can also be a reason for a nonlinear sensor response. On the other hand, due to the high cost of RuDPP, it is important to incorporate low dye concentrations. In order to prepare sensors with different properties, typical amounts of (40, 60 and 80) mg of RuDPP were used for further studies.

3.2 Sensor preparation – modification of foils and silicones

In the next step different foils and silicones as the support matrices were tested. In order to optimize the sensors, different foils (Plastibor, Dataline, Esselte) and commercially available silicones (E4, E41) were used. The linearities and sensitivities (k) of different sensors were tested; **Table 2** presents all the major sensor characteristics. **Figure 5a** presents the changes in the measured signal versus the various concentrations of oxygen with different foils, and **Figure 5b** shows the change in the signal with different silicones. When using the Datalain foil a slightly better linear response was obtained, especially at low concentration ranges of oxygen, when compared to the Plastibor or Esselte foils, but the selection of the solid layers does not significantly improve or change the sensor properties. It is generally known that with the increasing roughness of a substrate foil the adhesion of the coatings on the surface is improved even in spin coating. Here, it is important to mention that rough surfaces cause a lower transparency with a significant back-scattering light effect, and for this reason we used low-roughness foils. Additionally, a compromise between the foil transparency and surface

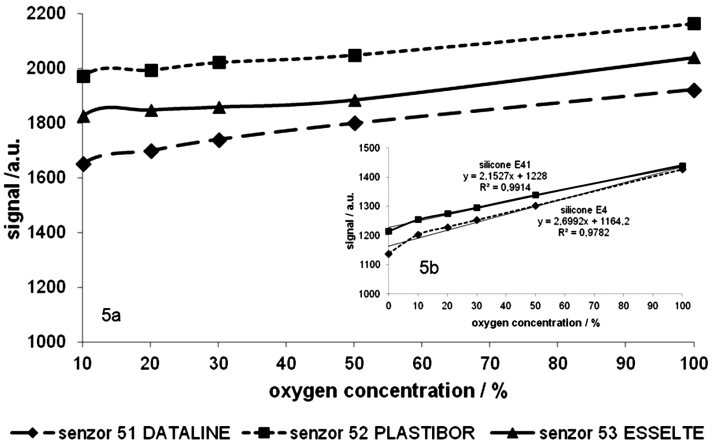

Figure 5: a) Impact of a solid layer (a foil) on sensor response (signal/a.u. – arbitrary units vs. concentration of O_2 in %), b) comparison of different silicones vs. sensor response

Slika 5: a) Vpliv trdnega nosilca (folije) na odziv senzorjev (izmerjen signal (a.u. enote) vs. koncentracija O_2 v %), b) vpliv silikona na občutljivost senzorja

Table 2: Influence of the solid layers on the sensor characteristics

Tabela 2: Vpliv trdnih plasti na lastnosti senzorjev

RuDPP/mg	FOIL	SILICONE	SOLVENT	*V*/μL	STAGES	*k*	R^2
60	DATALINE	E4	ME	150	1600 r/min → 3 s 2300 r/min → 3 s 3150 r/min → 4 s	2.699	0.978
60	PLASTIBOR	E4	ME	150	1600 r/min → 3 s 2300 r/min → 3 s 3150 r/min → 4 s	2.464	0.960
60	ESSELTE	E4	ME	150	1600 r/min → 3 s 2300 r/min → 3 s 3150 r/min → 4 s	2.684	0.886
60	DATALINE	E41	CHLO	200	1600 r/min → 3 s 2300 r/min → 3 s 3150 r/min → 4 s	4.141	0.964
60	PLASTIBOR	E41	CHLO	200	1600 r/min → 3 s 2300 r/min → 3 s 3150 r/min → 4 s	4.516	0.974
60	ESSELTE	E41	CHLO	200	1600 r/min → 3 s 2300 r/min → 3 s 3150 r/min → 4 s	4.531	0.957
80	DATALINE	E41	ME	200	1300 r/min → 3 s 2200 r/min → 5 s 3100 r/min → 2 s	–2.727	0.361
80	ESSELTE	E41	ME	150	1300 r /min → 3 s 2200 r/ min → 5 s 3100 r/ min → 2 s	–8.761	0.992
80	PLASTIBOR	E41	ME	150	1300 r/ min → 3 s 2200 r/min → 5 s 3100 r/min → 2 s	–5.709	0.834
80	DATALINE	E41	CHLO	150	1600 r/min → 3 s 2300 r/min → 3 s 3150 r/min → 4 s	5.106	0.975
80	PLASTIBOR	E41	CHLO	150	1600 r/min → 3 s 2300 r/min → 3 s 3150 r/min → 4 s	4.073	0.943
80	ESSELTE	E41	CHLO	150	1600 r/min → 3 s 2300 r/min → 3 s 3150 r/min → 4 s	4.787	0.966
20	DATALINE	E4	ME	150	1750 r/min → 3 s 2300 r/min → 3 s 3150 r/min → 4 s	4.277	0.735
20	PLASTIBOR	E4	ME	150	1750 r/min → 3 s 2300 r/min → 3 s 3150 r/min → 4 s	3.693	0.606

20	ESSELTE	E4	ME	150	1750 r/min → 3 s 2300 r/min → 3 s 3150 r/min → 4 s	3.962	0.635
20	DATALINE	E4	CHLO	150	1750 r/min → 3 s 2300 r/min → 3 s 3150 r/min → 4 s	2.545	0.946
20	PLASTIBOR	E4	CHLO	150	1750 r/min → 3 s 2300 r/min → 3 s 3150 r/min → 4 s	1.609	0.585
20	ESSELTE	E4	CHLO	150	1750 r/min → 3 s 2300 r/min → 3 s 3150 r/min → 4 s	1.94	0.845
40	DATALINE	E41	CHLO	200	1600 r/min → 3 s 2300 r/min → 3 s 3150 r/min → 4 s	4.531	0.957
40	PLASTIBOR	E41	CHLO	200	1600 r/min → 3 s 2300 r/min → 3 s 3150 r/min → 4 s	3.857	0.959
40	ESSELTE	E41	CHLO	200	1600 r/min → 3 s 2300 r/min → 3 s 3150 r/min → 4 s	4.077	0.865
40	DATALINE	E4	CHLO	200	1750 r/min → 3 s 2300 r/min → 3 s 3150 r/min → 4 s	6.468	0.528
40	PLASTIBOR	E4	CHLO	200	1750 r/min → 3 s 2300 r/min → 3 s 3150 r/min → 4 s	6.654	0.524
40	ESSELTE	E4	CHLO	200	1750 r/min → 3 s 2300 r/min → 3 s 3150 r/min → 4 s	7.003	0.524
40	DATALINE	E41	CHLO	200	1750 r/min → 3 s 2300 r/min → 3 s 3150 r/min → 4 s	2.166	0.555
40	PLASTIBOR	E41	CHLO	200	1750 r/min → 3 s 2300 r/min → 3 s 3150 r/min → 4 s	2.207	0.562
40	ESSELTE	E41	CHLO	200	1750 r/min → 3 s 2300 r/min → 3 s 3150 r/min → 4 s	1.806	0.405

Table 3: Variation of silicones vs. sensor sensitivity
Tabela 3: Vpliv silikona na odzivnost senzorjev

RuDPP/mg	FOIL	SILICONE	SOLVENT	*V*/µL	STAGES	*k*	R^2
40	DATALINE	E4	CHLO	200	1750 r/min → 3 s 2300 r/min → 3 s 3150 r/min → 4 s	6.468	0.528
40	DATALINE	E41	CHLO	200	1750 r/min → 3 s 2300 r/min → 3 s 3150 r/min → 4 s	2.166	0.555
40	PLASTIBOR	E4	CHLO	200	1750 r/min → 3 s 2300 r/min → 3 s 3150 r/min → 4 s	6.654	0.524
40	PLASTIBOR	E41	CHLO	200	1750 r/min → 3 s 2300 r/min → 3 s 3150 r/min → 4 s	2.207	0.562
40	ESSELTE	E4	CHLO	200	1750 r/min → 3 s 2300 r/min → 3 s 3150 r/min → 4 s	7.003	0.524
40	ESSELTE	E41	CHLO	200	1750 r/min → 3 s 2300 r/min → 3 s 3150 r/min → 4 s	1.806	0.405
60	DATALINE	E4	ME	150	1600 r/min → 3 s 2300 r/min → 3 s 3150 r/min → 4 s	2.699	0.978
60	DATALINE	E41	ME	150	1600 r/min → 3 s 2300 r/min → 3 s 3150 r/min → 4 s	2.152	0.991

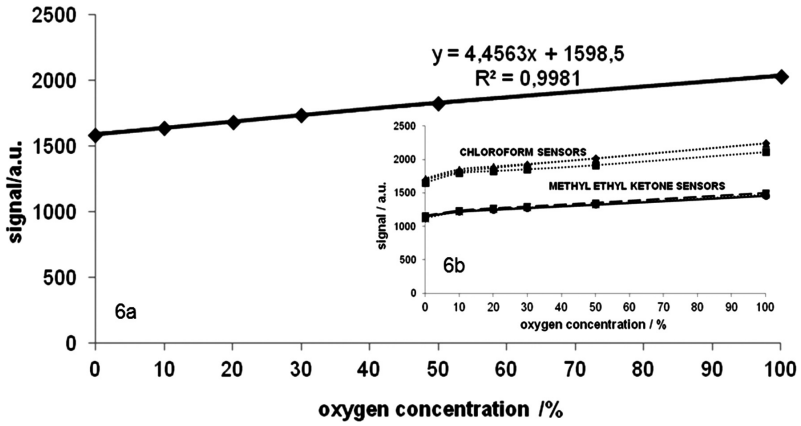

Figure 6: a) Sensor response under optimum conditions (signal/a.u. – arbitrary units vs. concentration of O_2 in %), b) sensitivity of the sensor using different solvents (chloroform and methyil ethyil ketone)

Slika 6: a) Odziv senzorja pri optimalnih pogojih (izmerjen signal (a.u. enote) vs. koncentracija O_2 v %), b) vpliv topil (kloroform, metil-etil keton) na odziv senzorjev

roughness was made by adding inert silicones to the sensor solution. **Table 3** presents the conditions for preparing the sensor solutions using different silicones. The optimum linearity (0.9914) was obtained using silicone E41, foil Dataline and 60 mg of RuDPP. The silicone adhesion of the sensor solution to the foils was significantly improved, while preserving the optimum light transparency.

3.3 Spin coating and sensor thickness

A lot of factors participated in the spin-coating sensor preparation[33,34] – one of these was also the selection of a suitable solvent. The sensors were prepared using chloroform, toluene, and methyl ethyl ketone. Toluene as a solvent proved to be unsuitable because it partially dissolved the surfaces of the foils. Other solvents were constantly evaporating, also during the spin-coating period, but the sensors prepared with chloroform presented better characteristics (linearity and sensitivity) than the sensors prepared with methyl ethyl ketone (**Figure 6a**). Chloroform had a lower evaporating rate than methyl ethyl ketone and the sensors prepared with chloroform had a uniform film thickness. **Figure 6b** demonstrates that the sensor prepared with chloroform also had a substantially higher signal (by approximately 30 %), while the other parameters remained constant.

Our further experimental work used different spin-coating stages (periods) and accelerations. The optimum results were obtained when a 150 µL sensor solution in chloroform containing 80 mg of RuDPP with silicone E41 (foil Dataline) was applied (**Figure 6a**) under the following spin-coating conditions:

1st step: 750/700 r/min → 3 s
2nd step: 300 r/min → 3 s
3rd step: 150 r/min → 4 s

This spin-coating technique had several benefits including a fast process time (only a few seconds) when using low volumes of reagents. A modification of the spin speeds or an increase in the spin time allowed a thin-film preparation (below 1 µm).

Using scanning electron microscopy, the irregularities in the sensor surface were searched. For the SEM analysis, the sensors with homogeneous surfaces (an optical selection) and optimum oxygen responses were selected. An optical selection means that the sensors with the most uniform coating and without any visible solid particles or air bubbles were scanned (**Figure 7**).

The coatings and thicknesses of the sensors were incompletely uniform throughout the sensor surfaces varying within the range of (3.5–5.0 ± 0.5) µm. Air bubbles were visible on individual parts, probably captured in the sensors during the polymerization step. This

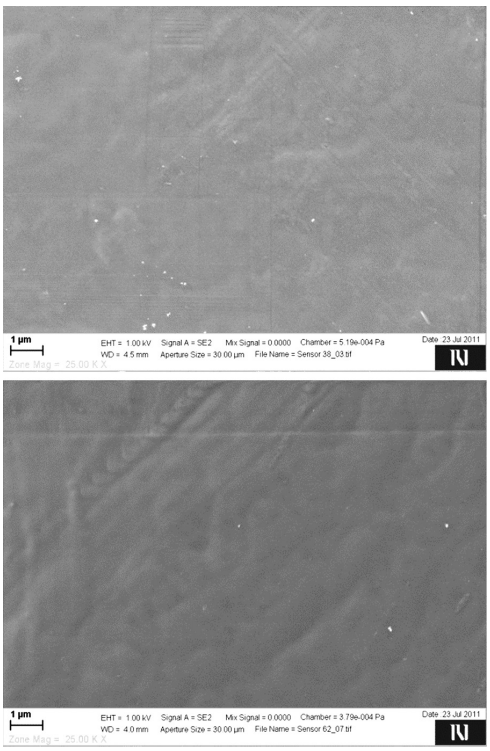

Figure 7: Optical-oxygen-sensor SEM images at 2500-times

Slika 7: SEM-posnetka površine optičnih senzorjev za kisik pri 2500-kratni povečavi

could be avoided, to some degree, by implementing a vacuum chamber over the treated surface. The main problem regarding the entrapped air bubbles was the fluctuation of the scattering light causing a lower fluorescence signal – the light was scattered in all directions. The entrapped air bubbles could also cause a longer response time – the measuring oxygen molecules can be trapped within the presented voids.

4 CONCLUSION

The spin-coating technique was studied while used for the optical-sensor preparation when different parameters directly affected the film thickness and, therefore, also the sensor response to oxygen. This paper primarily focuses on the influences of the rotation speed and spinning time on the film thickness, in addition to the acceleration, temperature, humidity, viscosity, solvents, silicones, foils and RuDPP concentration studied. The optimum results were obtained when 80 mg of RuDPP was dissolved in chloroform, silicone E41 was added and a 150 μL of sensor solution was applied to the Dataline foil under the following spin-coating conditions: 1st step: 750/700 r/min for 3 s, 2nd step: 300 r/min for 3 s, and 3rd step: 150 r/min for 4 s.

Spin coating is an alternative method for a sensor preparation. It is a very fast, simple method, consuming low volumes of reagents, but making it difficult to prepare completely homogeneous layers on the whole sensor surface. Therefore, it is suggested to be used for a laboratory-scale sensor preparation, where the majority of experimental data could be used later when new coating methods are researched.

Acknowledgements

The authors would like to thank the Slovenian Technology Agency (TIA) for the financial support through Grant P-MR-08/54. The authors acknowledge the financial support from the Ministry of Education, Science, Culture and Sport of the Republic of Slovenia through the contract No. 3211-10-000057 (Centre of Excellence for Polymer Materials and Technologies).

5 REFERENCES

[1] H. R. Zhang, B. Li, B. F. Lei, W. L. Li, Journal of Luminescence, 128 (**2008**) 8, 1331–1338

[2] K. Matsui, F. Momose, Chemistry of Materials, 9 (**1997**) 11, 2588–2591

[3] D. S. Tyson, J. Bialecki, F. N. Castellano, Chemical Communications, 23 (**2000**), 2355–2356

[4] P. Brglez, A. Holobar, A. Pivec, M. Kolar, N. Belsak, Acta Chimica Slovenica, 59 (**2012**) 1, 50–58

[5] H. R. Zhang, B. Li, B. F. Lei, W. L. Li, S. Z. Lu, Sensors and Actuators B-Chemical, 123 (**2007**) 1, 508–515

[6] L. Huynh, Z. U. Wang, J. Yang, V. Stoeva, A. Lough, I. Manners, M. A. Winnik, Chemistry of Materials, 17 (**2005**) 19, 4765–4773

[7] M. E. Kose, A. Omar, C. A. Virgin, B. F. Carroll, K. S. Schanze, Langmuir, 21 (**2005**) 20, 9110–9120

[8] B. H. Han, I. Manners, M. A. Winnik, Chemistry of Materials, 17 (**2005**) 12, 3160–3171

[9] M. E. Kose, B. F. Carroll, K. S. Schanze, Langmuir, 21 (**2005**) 20, 9121–9129

[10] H. D. Zhang, Y. H. Sun, K. Q. Ye, P. Zhang, Y. Wang, 15 (**2005**) 31, 3181–3186

[11] Z. J. Fuller, K. A. Kneas, W. Y. Xu, J. N. Demas, B. A. DeGraff, Analytical Chemistry, 75 (**2003**) 11, 2670–2677

[12] Y. Tang, E. C. Tehan, Z. Y. Tao, F. V. Bright, Analytical Chemistry, 75 (**2003**) 10, 2407–2413

[13] M. C. DeRosa, P. J. Mosher, G. P. A. Yap, K. S. Focsaneanu, R. J. Focsaneanu, C. E. B. Evans, Inorganic Chemistry, 42 (**2003**) 16, 4864–4872

[14] M. T. Murtagh, M. R. Shahriari, M. Krihak, Chemistry of Materials, 10 (**1998**) 12, 3862–3869

[15] C. McDonagh, B. D. MacCraith, A. K. McEvoy, Analytical Chemistry, 70 (**1998**) 1, 45–50

[16] J. F. Fernandez-Sanchez, T. Roth, R. Cannas, M. K. Nazeeruddin, S. Spichiger, M. Graetzel, U. E. Spichiger-Keller, Talanta, 71 (**2007**) 1, 242–250

[17] S. Arain, G. T. John, C. Krause, J. Gerlach, O. S. Wolfbeis, I. Klimant, Sensors and Actuators B-Chemical, 113 (**2006**) 2, 639–648

[18] C. McDonagh, P. Bowe, K. Mongey, B. D. MacCraith, Journal of Non-Crystalline Solids, 306 (**2002**) 2, 138–148

[19] K. Matsui, K. Sasaki, N. Takahashi, Langmuir, 7 (**1991**) 11, 2866–2868

[20] E. R. Carraway, J. N. Demas, B. A. Degraff, J. R. Bacon, Analytical Chemistry, 63 (**1991**) 4, 337–342

[21] P. Innocenzi, H. Kozuka, T. Yoko, Journal of Physical Chemistry B, 101 (**1997**) 13, 2285–2291

[22] M. M. F. Choi, D. Xiao, Analytica Chimica Acta, 403 (**2000**) 1–2, 57–65

[23] X. Chen, Z. M. Zhong, Z. Li, Y. Q. Jiang, X. R. Wang, K. Y. Wong, Sensors and Actuators B-Chemical, 87 (**2002**) 2, 233–238

[24] P. Hartmann, M. J. P. Leiner, M. E. Lippitsch, Sensors and Actuators B-Chemical, 29 (**1995**) 1–3, 251–257

[25] B. D. Maccraith, Analyst, 118 (**1993**) 4, 385–388

[26] P. Hartmann, M. J. P. Leiner, M. E. Lippitsch, Analytical Chemistry, 67 (**1995**) 1, 88–93

[27] H. J. Kim, Y. C. Jeong, J. I. Rhee, T. H. Kim, Bulletin of the Korean Chemical Society, 27 (**2006**) 12, 2084–2086

[28] Y. Amao, I. Okura, Sensors and Actuators B-Chemical, 88 (**2003**) 2, 162–167

[29] S. Draxler, M. E. Lippitsch, I. Klimant, H. Kraus, O. S. Wolfbeis, Journal of Physical Chemistry, 99 (**1995**) 10, 3162–3167

[30] B. Meier, T. Werner, I. Klimant, O. S. Wolfbeis, Sensors and Actuators B-Chemical, 29 (**1995**) 1–3, 240–245

[31] X. D. Wu, L. T. Song, B. Li, Y. H. Liu, Journal of Luminescence, 130 (**2010**) 3, 374–379

[32] B. F. Lei, B. Li, H. R. Zhang, S. Z. Lu, Z. H. Zheng, W. L. Li, Y. Wang, Advanced Functional Materials, 16 (**2006**) 14, 1883–1891

[33] A. Doliska, S. Strnad, J. Stana, E. Martinelli, V. Ribitsch, K. Stana-Kleinschek, Journal of Biomaterials Science-Polymer Edition, 23 (**2012**) 5, 697–714

[34] A. Doliska, M. Kolar, K. Stana-Kleinschek, M. Mozetic, Surface and Interface Analysis, 44 (**2012**) 1, 56–61

[35] M. C. Lin, C. K. Chen, Applied Mathematical Modelling, 36 (**2012**) 6, 2536–2549

[36] Y. K. Yang, T. C. Chang, Microelectronics Journal, 37 (**2006**) 8, 746–751

[37] Y. K. Kuo, C. G. Chao, Microelectronics Journal, 37 (**2006**) 8, 759–764

[38] J. Y. Jung, Y. T. Kang, J. Koo, International Journal of Heat and Mass Transfer, 53 (**2010**) 9–10, 1712–1717

[39] P. Yimsiri, M. R. Mackley, Chemical Engineering Science, 61 (**2006**) 11, 3496–3505

UDK 66.017:669.018.95
Original scientific article/Izvirni znanstveni članek

ISSN 1580-2949
MTAEC9, 48(2)189(2014)

ELECTROCHEMICAL SYNTHESIS AND CHARACTERIZATION OF POLY *O*-AMINOPHENOL – SiO_2 NANOCOMPOSITE

ELEKTROKEMIJSKA SINTEZA IN KARAKTERIZACIJA NANOKOMPOZITA POLI *O*-AMINOFENOL – SiO_2

Fatemeh Bagheralhashemi, Abdollah Omrani, Abbas Ali Rostami, Abbas Emamgholizadeh

Faculty of Chemistry, University of Mazandaran, P. O. Box 453, Babolsar, Iran
gholizadehabbas612@yahoo.com

Prejem rokopisa – received: 2012-10-08; sprejem za objavo – accepted for publication: 2013-06-07

We report on the influence of SiO_2 on the electropolymerization of *O*-aminophenol (OAP). A poly *O*-aminophenol (POAP) nanocomposite with different particle sizes was deposited on a glassy carbon (GC) electrode in a solution having OAP 0.01 M and sulfuric acid 0.5 M using cyclic voltammetry (CV). The surface morphologies of the POAP films were studied using scanning electron microscopy (SEM). The results indicated that a modified surface, having a high surface coverage and an improved specific capacitance with semiconducting properties, was obtained. The cyclic voltammetry and electrochemical impedance spectroscopy (EIS) studies confirmed that the nanocomposite films have a higher capacitance than the pure POAP films. The presence of SiO_2 led to an obvious improvement in the overall electrochemical performance of the GC surface covered by POAP films.

Keywords: poly (*O*-aminophenol), glassy carbon electrode, electropolymerization

Poročilo obravnava vpliv SiO_2 na elektropolimerizacijo *O*-aminofenola (OAP). Nanokompozit poli *O*-aminofenol (POAP) z različno velikostjo delcev je bil nanesen na elektrodo iz svetlečega ogljika (GC) s ciklično voltametrijo (CV) v raztopini z OAP 0,01 M in žvepleno kislino 0,5 M. Morfologija površine POAP-nanosa je bila pregledana z vrstičnim elektronskim mikroskopom (SEM). Rezultati so pokazali, da ima spremenjena površina visoko pokritost površine, izboljšano specifično kapacitivnost in izkazuje polprevodniške lastnosti. Študije ciklične voltametrije in elektrokemijske impedančne spektroskopije (EIS) so potrdile, da ima nanokompozitni nanos višjo kapacitivnost kot čisti POAP-nanos. Prisotnost SiO_2 je pokazala občutno izboljšanje splošnih elektrokemijskih zmogljivosti površine GC, pokrite s POAP-nanosom.

Ključne besede: poli (*O*-aminofenol), elektroda iz svetlečega ogljika, elektropolimerizacija

1 INTRODUCTION

Nanotechnology is a rapidly growing area of nanostructured material science because of its huge number of applications in various fields, such as catalysis,[1,2] sensors,[3,4] electronics,[5] optics,[6,7] and medical sciences.[8–10] Nanometer silicon dioxide (nano-SiO_2) is one of the most popular nanomaterials that are being employed in different areas, like industrial manufacturing, packaging, composite materials, disease labeling, drug delivery, cancer therapy, and biosensors. The modified silica is low-price, esuriently oxide with a high chemical and thermal stability.[11] The development of chemically modified electrodes (CMEs) is an area of great interest. CMEs can be broadly divided into two main categories: as (a) surface-modified and (b) bulk-modified electrodes. Methods of surface modification include adsorption, covalent bonding, attachment of polymer films, etc.[12] Polymer-coated electrodes can be differentiated using other modification methods, like adsorption and covalent grafting on the surface. Depending on the surface properties and the experimental conditions, films with a different morphology, such as multilayer or monolayer, will be deposited. A conducting polymer provides an excellent opportunity for the preparation of composites having desirable mechanical properties. These include their applications in storage batteries,[13] electrochemical devices,[14,15] light-emitting diodes,[16] corrosion inhibitors,[17] and sensors.[18,19] Understanding the nature of these polymers is of great importance for developing electrochemical devices. Among the conducting polymers, polyaniline (PANI) and its derivatives have been studied extensively due to the commercial availability of the monomer, an easy protocol for synthesis, a well-behaved electrochemical response, a high environmental stability, and a high conductivity. In recent years, various composites of PANI and inorganic compounds have been fabricated with improved characteristics.[20,21] Although silica is an insulating material, some of its composites showed conductivity at the level of conducting PANI.[22] However, some of silica composites displayed enhanced conductivity, which may be due to the change in morphology of the conductive films in the hybrid materials.[23] Electrochemical polymerization offers the advantage of a reproducible deposition in terms of film thickness and loading level, making the immobilization procedure of a metal-based electrocatalyst very simple and reliable. By considering this point that the nature of the working-electrode surface is a key factor in observing the electrochemical response of a deposited polymeric film,

the electropolymerization of an OAP monomer in a suspension of silica nanoparticles is investigated in the present research for the first time. The silica nanoparticle is selected because of its good stability in common aqueous acidic solutions such as H_2SO_4, HCl and $HClO_4$. Accordingly, a poly (*O*-aminophenol)/SiO_2 nanocomposite as a novel organic matrix was fabricated and characterized.

2 EXPERIMENTAL

2.1 Materials

The solvent used in this work was bi-distilled water. Sulfuric acid (purity 99 % from Merck) was used as a supporting electrolyte. The OAP (purity 98 % from Merck) was utilized as the monomer and distilled prior to be used. Silica nanoparticles (purity 99 % with average size of 10 nm and a surface area of 600 $m^2 g^{-1}$) were purchased from Aldrich and used as an additive. Buffer solutions with various pHs between 5 and 12 were prepared using *O*-phosphoric acid and its salts (purity 99 % from Fluka).

2.2 Instruments

Cyclic voltammetery experiments were carried out using a Potentiostat/Galvanostat EG&G Model 263 (USA) that was well controlled and operated using M 270 software. Impedance spectroscopy measurements were performed using a potentiostat/galvanostat (model Autolab, PGSTAT30, Eco Chemie, Netherlands) with FRA software. All the measurements were conducted using a three-electrode cell configuration system. The utilized three-electrode system was composed of Ag/AgCl · KCl (saturated) as the reference electrode, a platinum wire as the auxiliary electrode and GCE as the working electrode substrate. The surface morphology of the deposited films was characterized by scanning electron microscopy (model VEGA-TESCAN). A pH meter (model 3030, JENWAY) was used to read the pH of the buffer solutions. The pH values for the solution of phosphate were adjusted by either a solution of sulfuric acid or sodium hydroxide depending on the pH needed.

2.3 Electrode modification

Prior to the modification of the GCE, it was polished with alumina slurries on a polishing cloth to a mirror finish and then ultrasonically cleaned for 2.0 min in ethanol. Then, the electrode was rinsed thoroughly with distilled water.

3 RESULTS AND DISCUSSION

3.1 Electrochemical polymerization

The POAP film and POAP/SiO_2 nanocomposite were prepared at the surface of the GCE in the absence and presence of nanoparticles SiO_2 (w = 2 %) in 0.5 mol L^{-1} H_2SO_4/0.1 M OAP using the potentiostatic method at E = 0.6 V.

3.2 Surface morphology

The morphology of POAP film and its blend with SiO_2 nanoparticles was characterized using scanning electron microscopy (**Figure 1**). The SEM image of the pristine POAP film on the GCE (**Figure 1a**) shows a composed morphology of elongated globules (densely smooth film). **Figure 1b** shows the structure of the nanocomposite (POAP/SiO_2) surface. The surface of the POAP film prepared in the presence of SiO_2 nanoparticles exhibited discretely shaped agglomerates due to the influence of the SiO_2 nanoparticles. The clusters of small SiO_2 nanoparticles are not uniformly adhered on the surface of POAP globules. This structure allows the electrolyte constituent better access to the interior of the nanocomposite. Certainly, the high dispersion of SiO_2 nanoparticles on the surface of the POAP spheres might have improved the surface area and the stability of the

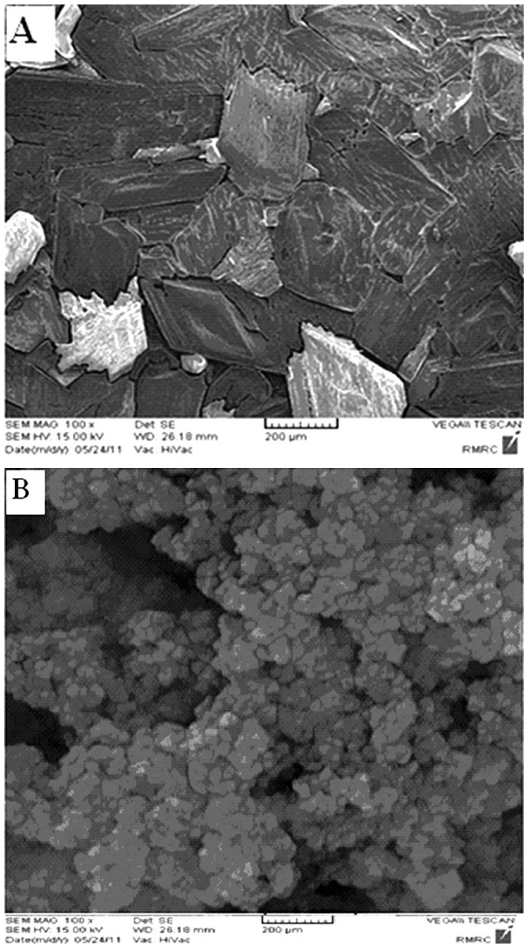

Figure 1: SEM images of: a) POAP film and b) POAP/SiO_2 synthesized in H_2SO_4 solution 0.5 mol L^{-1}

Slika 1: SEM-posnetka: a) POAP-nanosa in b) POAP/SiO_2, sintetiziran v raztopini H_2SO_4 0,5 mol L^{-1}

nanocomposite. This may be attributed to possible interactions via the hydrogen bonding between the imine (-NH) group of POAP and the hydroxyl (-OH) group on the surface of the nano-silica.

3.3 Cyclic voltammetry of POAP/SiO$_2$ and POAP films

Figure 2 shows 15 consecutive voltammograms, from 0 V to 1.3 V, to deposit the POAP/SiO_2 film in a phosphate solution at pH = 3 at a scan speed of 0.2 V/s. By the 5th cycle the anodic peak could not be observed. When the number of scans increased over 5, an anodic peak current (I_a) was observed clearly at +0.65 V.

The charge measured by the integration of the anodic peak area was found to be 12.02 mC cm^{-2} for the 15th cycle, and oxidation of the POAP film occurred at 0.65 V. The voltammetric behavior of the POAP film in the same electrolyte solution and in the same potential range is shown in **Figure 3**.

Although a similar polymerization charge was used to synthesize both of the films (POAP/SiO_2 and POAP), the voltammetric behavior of the POAP film was significantly different. During the 1st to the 5th cycle, the cyclic voltammogram did not show any change. The shift of the anodic peak potential to higher currents was continued until the 10th cycle. The reached anodic peak charge for the POAP/SiO_2 film after the 15th cycle was not similar to the charge measured for the pure POAP film until the same cycle. It seems that a transition from the so-called POAP(II) structure to the POAP(I) structure occurred. The changes in the POAP(II) structure during the voltammetry traces could be related to the nature of the transporting species like counter ions and/or nanoparticles.[24] The increase in the anodic peak current of the POAP/SiO_2 film can be attributed to the re-structuring of the POAP during cycling, where the polymer forms a more incompact structure, which required the lower overall potential to be flattened.

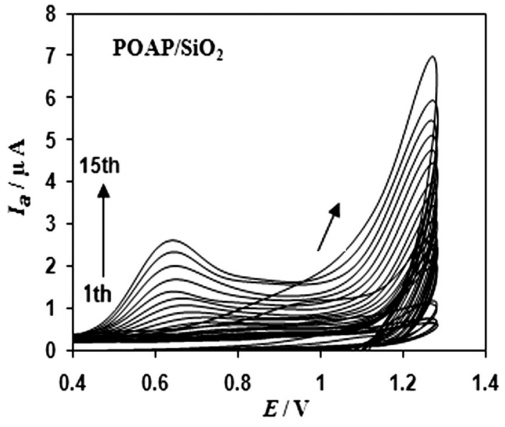

Figure 2: Cyclic voltammograms of the POAP/SiO_2 nanocomposite in a phosphate solution at pH = 3, scan rate: v = 0.2 V s^{-1}. The 15 cycles are shown (E_i = 0 to E_f = +1.5 V).

Slika 2: Ciklični voltamogrami nanokompozita POAP/SiO_2 v fosfatni raztopini pri pH = 3, hitrost skeniranja v = 0,2 V s^{-1}. Prikazanih je 15 ciklov (E_i = 0 do E_f = +1,5 V).

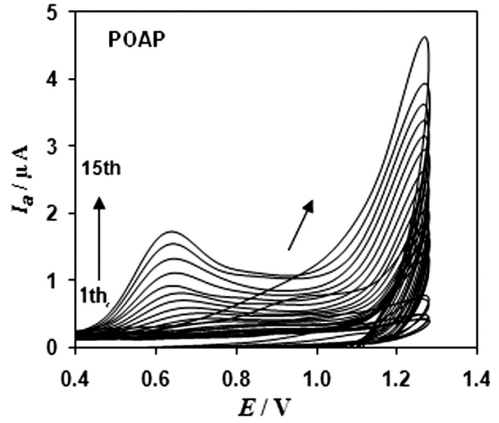

Figure 3: Cyclic voltammograms of the POAP in a phosphate solution at pH = 3, scan rate: v = 0.2 V s^{-1}. The 15 cycles are shown (E_i = 0 to E_f = +1.5 V).

Slika 3: Ciklični voltamogrami POAP v fosfatni raztopini pri pH = 3, hitrost skeniranja v = 0,2 V s^{-1}. Prikazanih je 15 ciklov (E_i = 0 do E_f = +1,5 V).

The silanol groups of SiO_2 could be adsorbed onto the GC surface. This changes the interfacial structure and the property of the GC/electrolyte solution, which benefits the electropolymerization process. However, the organic-inorganic interactions between the POAP and SiO_2 involved in the electropolymerization process pushed the polymer chains and so facilitated the growth of the polymer chains. The anodic peak current increased by increasing the number of cycles for both of the systems, but its values were higher for the nanocomposite than for the pure POAP system.

3.4 Effect of the scan rate

The effect of the scan rate (v) was investigated in a phosphate solution at pH = 3 in order to compare the electrochemical behavior of the deposited polymeric films. The results of this investigation are shown in **Figure 4**.

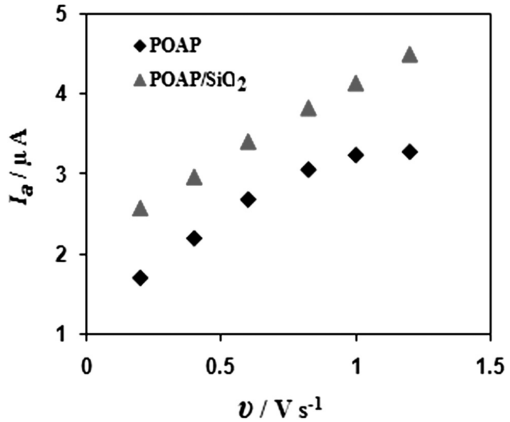

Figure 4: The anodic peak current (I_a) of POAP/SiO_2 and POAP films at various scan rates v = 0.2–1.2 V s^{-1}

Slika 4: Vrh anodnega toka (I_a) pri POAP/SiO_2- in POAP-nanosu pri različnih hitrostih skeniranja v = 0,2–1,2 V s^{-1}

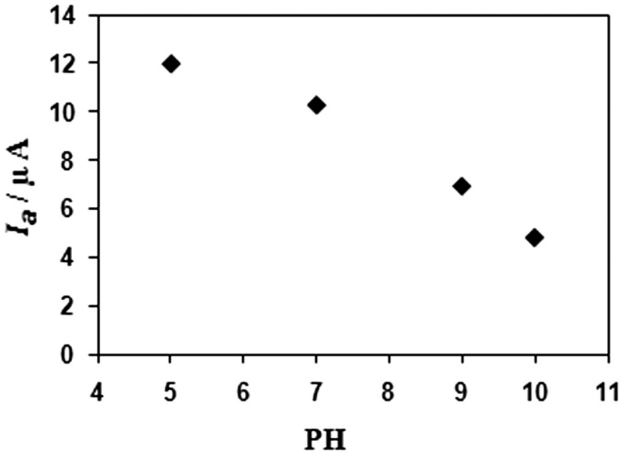

Figure 5: The anodic current (I_a) of POAP in different buffer solutions of *O*-phosphoric acid at pH = (5, 7, 9 and 10)
Slika 5: Anodni tok (I_a) POAP v različnih puferskih raztopinah *O*-fosforne kisline pri pH = (5, 7, 9 in 10)

The oxidation current clearly increased as the scan rate increased. An increase in the scan rate is likely due to an enhancement of the electron flow. It appears that the increased collision of electrons resulted in a reduction in the velocity of the electrons leading to a saturation of the current. The oxidation current for the POAP/SiO_2 system increases linearly with the square of the scan rate. The above result indicated that the redox process was confined to the surface of the GCE, confirming the immobilized state of the POAP/SiO_2. The differences in the redox currents reflect the effective active surface areas that are accessible to the electrolytes for the POAP/SiO_2. It seems that the porous POAP/SiO_2 film has a higher effective surface area. This improvement of the doping/undoping rate is a result of the increase in the surface area and the porous structure, which are of benefit to the ion diffusion and migration.

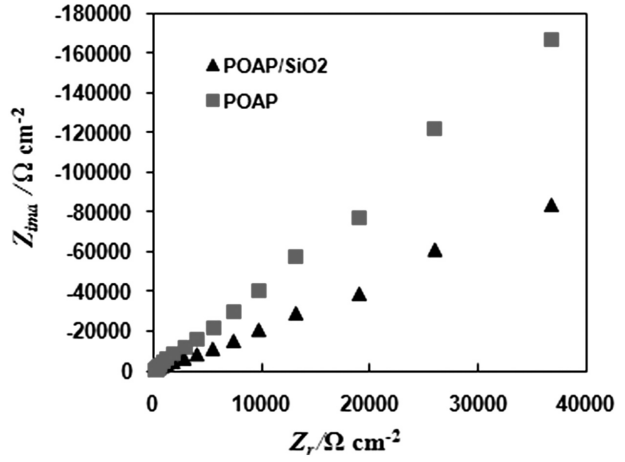

Figure 6: Impedance profiles of the produced films in phosphate electrolyte solution 0.1 M for: a) the POAP and b) the POAP/SiO_2 nanocomposite
Slika 6: Profil impedance nanosov v raztopini fosfata 0,1 M za: a) POAP- in b) POAP/SiO_2-nanokompozit

3.5 The influence of pH on the electropolymerization of POAP

It is well known that the electrochemical process involving aniline-type polymers requires the exchange of electrons and protons.[25] Accordingly, the solution pH has a significant effect on the electrochemical behavior of the polymeric films. **Figure 5** shows the cyclic voltammograms of POAP films deposited at various pH values. The results indicated that the current intensity increased as the pH of the electrolyte solution became more acidic. From this it can be implied that the doping/undoping rates in acidic media are more facilitated. In the other situation the POAP film becomes more electro-inactive in basic media.

3.6 EIS measurements

EIS experiments were conducted to provide some insights into the electrode/polymeric film/electrolyte interface. **Figure 6** displays typical impedance spectra of the POAP/SiO_2 and pure POAP in a phosphate solution 0.1 M recorded at a dc potential of 0.65 V for the frequency range 40 mHz to 60 kHz. The semicircle obtained from the high-frequency region was ascribed to the blocking properties of a single electrode, which can be related to the faradic process of an ion exchange that is extremely slow at the polymer/electrolyte interface.

The charge-transfer resistance (R_{ct}) for the POAP/SiO_2 was determined to be 2×10^2 kΩ cm^{-2}, which is smaller than the value found for the pure POAP (2.52×10^3 kΩ cm^{-2}). In other words, the pure POAP film presents a higher electrochemical charge-transfer resistance than the nanocomposite film. This could be assigned to the compact structure of the chains in POAP film and its less active sites for faradic reactions. These results were also confirmed by the cyclic voltammetry observations, where the peak current values increased in the presence of silica nanoparticles.

4 CONCLUSIONS

In this work, a new nanocomposite based on OAP was prepared by the electropolymerization of OAP at the surface of GCE, as a low-cost substrate, in the presence of SiO_2 nanoparticles. Apart from the higher electropolymerization rate, the POAP/SiO_2 nanocomposite showed good electrochemical behavior, which can be due to the different morphology of the POAP in the presence silica nanoparticles. A discrete agglomerated morphology of the prepared composite was observed owing to the influence of the SiO_2 nanoparticles. The nanoparticles can reduce the possible interactions between the POAP chains and, hence, have an important role in the dynamics of the polymeric chain. Impedance spectroscopy results confirmed that the POAP film is more resistive toward charge transfer than the POAP/SiO_2 nanocomposite. Therefore, the presence of SiO_2 nano-

particles results in the improved conductivity of the POAP films.

5 REFERENCES

[1] S. Scalzullo, K. Mondal, M. Witcomb, A. Deshmukh, M. Scurrell, K. Mallick, Nanotechnol., 19 (**2008**), 75708

[2] G. Wei, W. Zhang, F. Wen, Y. Wang, M. Zhang, J. Phys. Chem. C, 112 (**2008**), 10827

[3] F. Osterloh, H. Hiramatsu, R. Porter, T. Guo, Langmuir, 20 (**2004**), 5553

[4] X. Zheng, D. Guo, Y. Shao, S. Jia, S. Xu, Langmuir, 24 (**2008**), 4394

[5] J. Ouyang, C. W. Chu, C. R. Szmanda, L. Ma, Y. Yang, Nat. Mater., 3 (**2004**), 918

[6] A. J. Haes, S. Zou, G. C. Schatz, R. P. Van Duyne, J. Phys. Chem. B, 108 (**2004**), 109

[7] Y. Wang, X. Xie, T. Goodson, Nano Lett., 5 (**2005**), 2379

[8] L. R. Hirsch, R. J. Stafford, J. A. Bankson, S. R. Sershen, B. Rivera, R. E. Price, J. D. Hazle, N. J. Halas, J. L. West, Proc. Natl Acad. Sci., 1000 (**2003**), 13549

[9] C. Loo, A. Lowery, N. Halas, J. West, R. Drezek, Nano Lett., 5 (**2005**), 709

[10] X. Yang, J. Liu, H. He, L. Zhu, C. Gong, X. Wang, L. Yang, H. Huang, L. He, B. Zhang, Z. Zhuang, Particles fiber toxicology, 7 (**2010**), 1

[11] G. Dagan, S. Sampath, O. Leu, Chem. Mater., 7 (**1995**), 446

[12] R. W. Murray, Chemically modified electrodes in electroanalytical chemistry, volume 13, In: A. J. Bard (Ed), Marcel Decker, New York 1984, 191

[13] K. Gurunathan, D. P. Amalnekar, D. C. Trivedi, Mater. Lett., 57 (**2003**), 1642

[14] P. Somani, A. B. Mandale, S. Radhakrishnan, Acta Mater., 48 (**2000**), 2859

[15] J. P. Ferraris, C. Henderson, D. Torres, D. Meeker, Synth. Met., 72 (**1995**), 147

[16] D. Chinn, M. Delong, A. Fujii, S. Frolov, K. Yoshino, Z. V. Vardeny, Synth. Met., 120 (**1999**), 930

[17] S. Koul, S. K. Dahwan, R. Chandra, Synth. Met., 124 (**2001**), 295

[18] J. Cha, J. I. Han, Y. Choi, D. S. Yoon, K. W. Oh, G. Lim, Biosens. Bioelectron, 18 (**2003**), 1241

[19] N. F. Atta, A. Galal, H. B. Mark, T. Yu, P. Bishop, Talanta, 47 (**1998**), 987

[20] E. Granto, B. Basnar, Z. Cheglakov, E. Katz, I. Willner, Electroanalysis, 18 (**2006**), 26

[21] E. Granto, E. Katz, B. Basnar, I. Willner, Chem. Mater., 17 (**2005**), 4600

[22] Z. Niu, Z. Yang, Z. Hu, Y. Lu, C. C. Han, Adv. Funct. Mater., 13 (**2003**), 949

[23] Y. Wang, X. Wang, J. Li, Z. Mo, X. Zhao, X. Jing, F. Wang, Adv. Mater., 13 (**2001**), 1582

[24] M. Zhou, M. Geschke, B. Heinze, J. Phys. Chem. B, 106 (**2002**), 10065

[25] E. M. Genies, M. Labkowski, J. Electroanal. Chem., 236 (**1987**), 199

UDK 669.715:621.74.046
Original scientific article/Izvirni znanstveni članek

ISSN 1580-2949
MTAEC9, 48(2)195(2014)

DEVELOPMENT OF LOW-Si ALUMINUM CASTING ALLOYS WITH AN IMPROVED THERMAL CONDUCTIVITY

RAZVOJ ALUMINIJEVE LIVARSKE ZLITINE Z MAJHNO VSEBNOSTJO Si IN IZBOLJŠANO TOPLOTNO PREVODNOSTJO

Jesik Shin, Sehyun Ko, Kitae Kim

Production Technology R/D Div., Korea Institute of Industrial Technology, Incheon, South Korea
jsshin@kitech.re.kr

Prejem rokopisa – received: 2012-10-12; sprejem za objavo – accepted for publication: 2013-05-28

To develop an aluminum alloy that can combine a high thermal conductivity with a good castability and anodizability, low Si-containing aluminum alloys, Al-(0.5–1.5)Mg-1Fe-0.5Si and Al-(1.0–1.5)Si-1Fe-1Zn alloys were assessed as potential candidates. The developed alloys exhibited a thermal conductivity of 170–190 % level (160–180 W/(m K)), a fluidity of 60–85 % level, and an equal or higher ultimate tensile strength compared to those of an ADC12 alloy. In each developed alloy system, the thermal conductivity and the strength decreased and increased, respectively, as the content of the major alloying elements, Mg and Si, increased. The fluidity was inversely proportional to the Mg content and directly proportional to the Si content. The Al-(1.0–1.5)Si-1Fe-1Zn alloys showed better thin-wall castability due to their lower surface energy. In the experimental aluminum alloys with a low Si content, the fluidity was mainly dependent on the melt surface energy, the Al dendrite coherency point (DCP), and the first intermetallic crystallization point (FICP), rather than on the solidification interval, latent heat, or the viscosity.

Keywords: alloy design, low-Si aluminum casting alloy, thermal conductivity, castability

Za razvoj aluminijeve zlitine, ki združuje dobro toplotno prevodnost z dobro livnostjo in možnostjo eloksiranja, se predvideva, da sta dobro izhodišče aluminijevi zlitini z majhno vsebnostjo Si, kot sta Al-(0,5–1,5)Mg-1Fe-0,5Si in Al-(1,0–1,5)Si-1Fe-1Zn. Razvite zlitine so pokazale, da je toplotna prevodnost med 170–190 % (160–180 W/(m K)), livnost med 60–85 % in enaka natezna trdnost, kot jo ima primerjalna zlitina ADC12. V vsakem razvitem sistemu je toplotna prevodnost naraščala in trdnost padala, ko je naraščala vsebnost glavnih legirnih elementov Mg in Si. Tekočnost je bila obratno sorazmerna z vsebnostjo Mg in sorazmerna z vsebnostjo Si. Zlitina Al-(1,0–1,5)Si-1Fe-1Zn je pokazala boljšo livno sposobnost pri tankih stenah zaradi manjše površinske energije. Pri preizkusnih aluminijevih zlitinah z majhno vsebnostjo Si je bila tekočnost predvsem odvisna od površinske energije taline, koherenčne točke Al-dendritov (DCP) in prve točke strjevanja (FICP) intermetalne zlitine in manj od intervala strjevanja, latentne toplote ali viskoznosti.

Ključne besede: oblikovanje zlitine, aluminijeva livna zlitina z majhno vsebnostjo Si, toplotna prevodnost, livna sposobnost

1 INTRODUCTION

As the amount of heat that needs to be removed from electric devices such as LED lighting increases rapidly with the tendency towards higher outputs, the development of heat-dissipating components has recently become a subject of special interest. Aluminum, the most common heat-sink material, has inherent disadvantages that need to be overcome. Although high-purity aluminum possesses excellent thermal conductivity, it is extremely difficult to diecast; thus, alloying elements must be added, despite the thermal conductivity loss that occurs as a result of adding these alloying elements. The ADC12 alloy, a commercial Al–Si-based aluminum alloy, has been the most common aluminum alloy for heat-sinks. A heat-sink with a three-dimensional complex shape that is favorable to heat dissipation can be fabricated in a net shape, with a high productivity and without the cost penalty that comes with using a high-pressure diecasting process, like with the ADC12 alloy. However, a low thermal conductivity below 100 W/(m K) and the poor anodizing characteristics of the ADC12 alloy, caused by its high Si content, are becoming serious problems with the increasing power requirements of electric devices. Other commercial aluminum alloys are also difficult to diecast or exhibit a conductivity that is too low for them to be used as heat-dissipating components for high-power electric devices.[1–4]

Therefore, the aim of this study was to develop a novel, low-Si-containing anodizable aluminum alloy that possesses both a good thermal conductivity and castability. To achieve this goal, the elements known to have advantages in improving castability, strengthening the matrix, and preventing die sticking as well as to have a minimal effect on the resistivity increment of aluminum, such as Mg, Si, Zn, and Fe, were chosen and alloyed. The amounts of the total alloying elements and Si were kept between mass fractions 2 % and 3.5 %, and below 1.5 %, respectively. The thermal conductivity, fluidity, and mechanical strength of the newly designed Al-*x*Mg-1Fe-0.5Si and Al-*x*Si-1Fe-1Zn alloys were investigated as functions of the Mg and Si content and compared to those of the ADC12 alloy.

2 EXPERIMENTAL

2.1 Alloy design

To achieve the combination of a high thermal conductivity and good castability and anodizability, two low-Si quaternary aluminum alloys were designed as follows. First, in terms of the effects of the alloying elements on the electrical resistivity,[5] energy release for solidification,[6] and viscosity[5,7] of aluminum, as shown in **Table 1**, Mg and Si were chosen as the major alloying elements. The energy release for solidification was obtained by summing the latent heat and the superheating energy calculated for a superheat of 100 °C using the specific heat of each element according to the simple mixture rule. A low electrical resistivity and viscosity, and a high-energy release for the solidification are preferred because the decreasing electrical resistivity tends to increase the thermal conductivity, while increasing the energy release for solidification and decreasing the viscosity, both of which tend to increase the requirements for good castability, such as melt fluidity. The elements marked with an asterisk (*) in **Table 1** are those that are considered favorable to thermal conductivity and castability. Thus, it can be seen that only two elements, Mg and Si, meet all the required conditions. Secondly, Fe was included to prevent mold-sticking problems. Lastly, Si and Zn were utilized as supplementary alloying elements, as described below.

In **Table 2**, the constituent elements of the two low-Si quaternary aluminum alloy systems, Al-*x*Mg-Fe-Si (Alloy 1 series) and Al-*x*Si-Fe-Zn (Alloy 2 series), and their chemical compositions are summarized. The total amounts of alloying elements were kept between mass fractions 2 % and 3.5 % to achieve a good balance of thermal conductivity and castability. The amounts of Mg and Si were varied from 0.5 % to 1.5 % in order to systematically investigate the effects of these major alloying elements on the thermal conductivity and castability. If the alloying levels are too high or too low, the thermal conductivity and castability may deteriorate, respectively. Because the Si particles decrease the anodizability, the level of Si in particular was kept below 1.5 %, which is the maximum amount of Si in commercial wrought Al alloys known to have good anodizability. The amount of Fe was 1 %, the same as in the ADC12 alloy. In the Al-*x*Mg-Fe-Si alloys, 0.5 % Si was added as a supplementary element to effectively increase the energy

Table 1: Effects of alloying elements on electrical resistivity,[5] energy release for solidification,[6] and viscosity of aluminum[5,7] (calculation was made for ΔT of 100 °C)

Tabela 1: Vpliv legirnih elementov na električno upornost,[5] energijo, sproščeno pri strjevanju,[6] in viskoznost aluminija[5,7] (izračun je bil izdelan za ΔT 100 °C)

Element	Resistivity			Energy release for solidification			Viscosity variation of Al with alloying
	Maximum solubility in Al (w/%)	Resistivity increment of Al per w/% (μΩ cm)		Latent heat, H of pure elements (kJ/kg)	Specific heat, c' of pure elements (kJ/kg)	$H + c'\Delta T$ increment of Al per w/% (kJ/kg)	
		In solution	Out of solution				
Cr	0.77	4.00	0.180	402	0.66	–0.3	(+)
Cu	5.65	*0.34	0.030	205	0.45	–2.5	(+)
Fe	*0.05	2.56	0.058	272	0.78	–1.5	(+)
Li	4.00	3.31	0.680	422	4.46	*3.7	
Mg	14.90	*0.54	0.220	362	1.34	*0.0	*(–)
Mn	1.82	2.94	0.340	268	0.70	–1.6	(+)
Ni	*0.05	*0.81	0.061	292	0.56	–1.5	(+)
Si	1.65	*1.02	0.088	1804	0.93	*14.0	*(–)
Ti	1.00	2.88	0.120	366	0.68	–0.6	(+)
V	0.50	3.58	0.280	329	0.62	–1.1	
Zn	82.80	*0.09	0.023	111	0.48	–3.4	*(0)
Zr	0.28	1.74	0.044	212	0.37	–2.5	

Table 2: Chemical composition in mass fractions (w/%) of the developed low-Si aluminum alloys Al-*x*Mg-Fe-Si (alloy 1 series) and Al-*x*Si-Fe-Zn (alloy 2 series)

Tabela 2: Kemijska sestava v masnih deležih (w/%) razvitih aluminijevih zlitin z majhno vsebnostjo Si, Al-*x*Mg-Fe-Si (zlitina 1. serije) in Al-*x*Si-Fe-Zn (zlitina 2. serije)

Alloy		Major Element		Anti-die-sticking element	Supplementary element		Base element	Thermal conductivity (W/(m K))
		Mg	Si	Fe	Zn	Si	Al	
1	1-1	0.5	–	1.0	–	0.5	98.0	186
	1-2	1.0	–	1.0	–	0.5	97.5	175
	1-3	1.5	–	1.0	–	0.5	97.0	160
2	2-1	–	1.0	1.0	1.0	–	97.0	171
	2-2	–	1.2	1.0	1.0	–	96.8	163
	2-3	–	1.5	1.0	1.0	–	96.5	153

release for solidification. Because Si has been reported to be less effective in strengthening the Al matrix than Mg,[5] 1 % Zn was added as a supplementary element in the Al-*x*Si-Fe-Zn alloys. Although heat-sinks are not structural components that need a very high strength, proper strength is imperative in order to eject the castings from molds safely. Moreover, Zn has the lowest resistivity increment, as shown in **Table 1**. The thermal conductivities of the alloys were calculated by a simple rule-of-mixture and the Wiedemann-Franz law using the data of **Table 1** in order to predict the effects of the elements on the resistivity of Al.

2.2 Evaluation and analyses

The fluidity test was conducted using a ceramic-coated steel mold with multiple channels on a low-pressure casting machine under an inert-gas atmosphere in order to prevent melt oxidation. **Figure 1a** shows the parting plane of the metal mold for the fluidity test. The flow channels were 100 mm long and open to the air at the end, and their diameters were (8, 4, 2, and 1) mm. **Figure 1b** shows the fluidity test casting after solidification. The average flow lengths for each channel diameter were taken as the fluidity values, and 10 experiments were performed to confirm the reproducibility. To evaluate the fluidity only as a function of alloy composition, the mold temperature, the superheat temperature, and the pressure during pouring were kept constant: 190 °C, 100 °C, and 15 kPa, respectively. The melting points of the alloys were determined by a thermal analyzer TG/DTA, model SDT Q600, applying a heating rate of 10 °C/min up to 700 °C in an Ar atmosphere (flow rate: 0.1 L/min).

The thermal conductivities of the alloys were drawn from their electrical resistivities as measured by an eddy-current technique, utilizing the Wiedemann-Franz law to determine the relation between the electrical resistivity and the thermal conductivity. The tensile strength evaluation was carried out according to ASTM B 557M using specimens taken from a Y-block casting with dimensions of 200 mm × 150 mm × 25 mm. The ADC12 alloy (Al-10 % Si-2.5 % Cu-1 % Fe-0.2 % Mg) was used as a comparative material for the properties evaluation of the developed alloys.

Thermophysical modeling using the commercial software JMatPro 5.0 was performed to obtain the thermophysical properties relating to castability and the phase-equilibria information. For microstructural analysis, including phase characterization, the cross-sections of the fluidity test channels were examined using a field-emission scanning electron microscope (FESEM), model FEI Quanta 200F, equipped with an energy-dispersive spectroscopy (EDS) probe. To understand the solidification paths, cooling curve analyses (CCA) were carried out based on the two-thermocouple method.[8,9] Two K-type thermocouples, one at the center (TC) of the graphite mold and one near the wall (TW), were positioned to record the solidification history, as shown in **Figure 2**. Then the graphite mold was dipped into the melt for about 30 s to fill it up and allow its temperature to equilibrate with the melt temperature. According to Farahany's method,[8] the temperature at which the first maximum difference between the thermocouples TC and TW occurred is regarded as the dendrite coherency point (DCP).

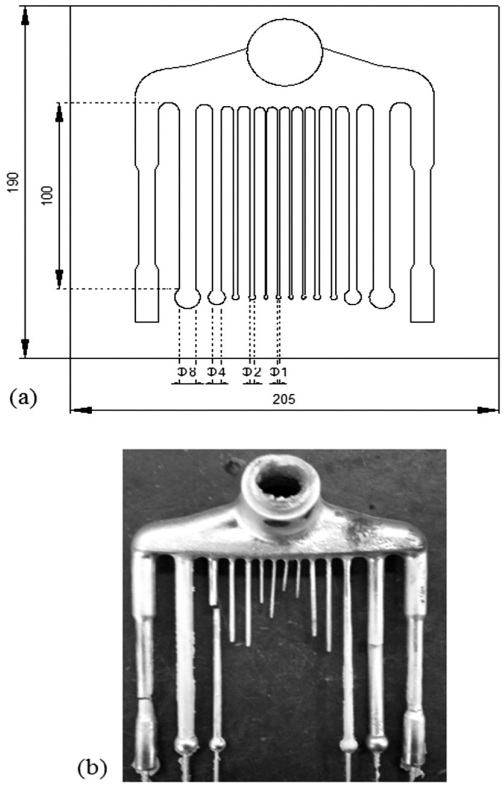

Figure 1: a) Parting plane of the metal mold for fluidity test and b) fluidity test casting

Slika 1: a) Načrt debeline delov pri preizkusu tekočnosti in b) ulitek po preizkusu tekočnosti

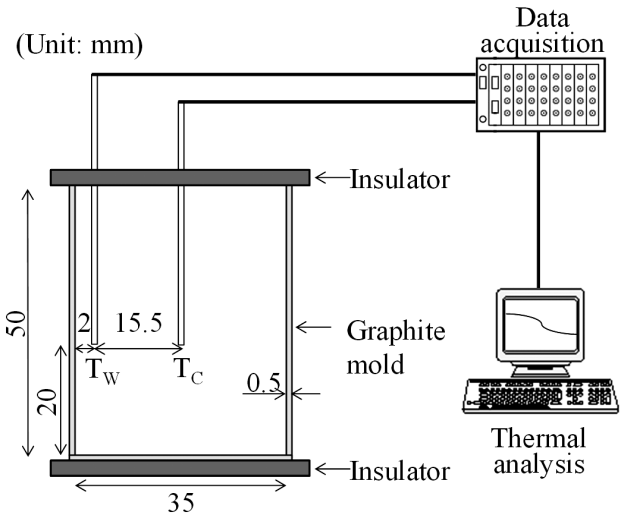

Figure 2: Cooling-curve analysis, set-up with a graphite mold and two K-type thermocouples

Slika 2: Sestav za analizo ohlajevalnih krivulj z grafitno kokilo in dvema termoelementoma vrste K

3 RESULTS AND DISCUSSION

The measured thermal conductivity, fluidity, and ultimate tensile strength of the developed Al-*x*Mg-1Fe-0.5Si and Al-*x*Si-1Fe-1Zn alloys were compared to those of the ADC12 alloy and the results are summarized in **Figure 3**. The developed alloys showed a higher thermal conductivity of 160–180 W/(m K), which is approximately 70–90 % higher than that of the ADC12 alloy, as shown in **Figure 3a**. The thermal conductivity of the alloys decreased with the increment of Mg and Si, the major alloying elements. The difference in the thermal conductivity between the two alloy systems was fairly insignificant. The average flow lengths for the diameter channels 1 mm and 2 mm are summarized in **Figure 3b**. The channels larger than 2 mm in diameter were completely filled for both alloy melts. The fluidity of the developed alloys reached 60–85 % that of the ADC12 alloy, which was obtained by averaging the flow length for the diameter channels 2 mm. It was found that the fluidity of the Al-*x*Mg-1Fe-0.5Si alloys decreased with increasing Mg content, whereas that of the Al-*x*Si-1Fe-1Zn alloys increased with increasing Si content. Interestingly, the opposite tendency was observed between the two alloy systems with a changing channel diameter, i.e., for the diameter channels 2 mm, the Al-*x*Mg-1Fe-0.5Si alloys showed a higher fluidity than the Al-*x*Si-1Fe-1Zn alloys, but this tendency was reversed for the diameter channels 1 mm. The tensile strength of the two alloy systems increased with increasing Mg and Si contents, reaching an equal or higher tensile strength than the ADC12 alloy, as shown in **Figure 3c**. The strength of the Al-*x*Mg-1Fe-0.5Si alloys was higher than that of the Al-*x*Si-1Fe-1Zn alloys.

To understand the fluidity behavior, which is more complex than understanding the thermal conductivity or strength, important thermophysical properties relating to the castability were calculated by JMatPro software and are summarized in **Figure 4**. **Figure 4a** shows the variation of the energy release for solidification as a function of the contents of Mg and Si. From a higher perspective, the two alloy systems showed similar levels of energy release for solidification. However, looking within each alloy system, the energy release of solidification for the Al-*x*Mg-1Fe-0.5Si alloys did not change until reaching a mass fraction 1.0 % Mg and then it decreased. Considering that Mg is an element with almost the same energy release for solidification as Al, the solidification path and crystallization phases seemed to change as the Mg content increased from 1.0 % to 1.5 %. In the Al-*x*Si-1Fe-1Zn alloys, the energy release for solidification increased in proportion to the amount of Si. To summa-

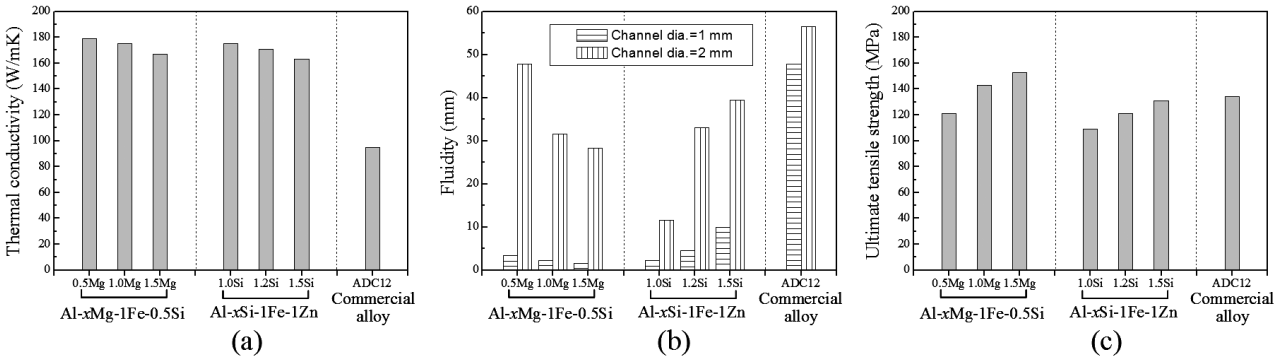

Figure 3: Measured: a) thermal conductivity, b) fluidity and c) ultimate tensile strength of Al-(0.5–1.5)Mg-1Fe-0.5Si and Al-(1.0–1.5)Si-1Fe-1Zn alloys

Slika 3: Izmerjena: a) toplotna prevodnost, b) tekočnost in c) natezna trdnost zlitin Al-(0,5–1,5)Mg-1Fe-0,5Si in Al-(1,0–1,5)Si-1Fe-1Zn

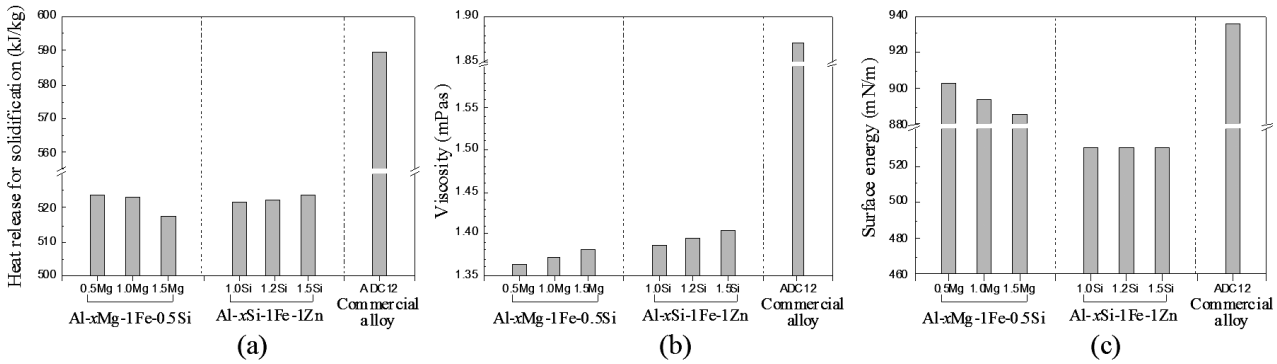

Figure 4: a) Heat release for solidification, b) viscosity and c) surface energy of Al-(0.5–1.5)Mg-1Fe-0.5Si and Al-(1.0–1.5)Si-1Fe-1Zn alloys calculated by JMatPro

Slika 4: a) Sproščanje toplote pri strjevanju, b) viskoznost in c) površinska energija zlitin Al-(0,5–1,5)Mg-1Fe-0,5Si in Al-(1,0– 1,5)Si-1Fe-1Zn, izračunana z JMatPro

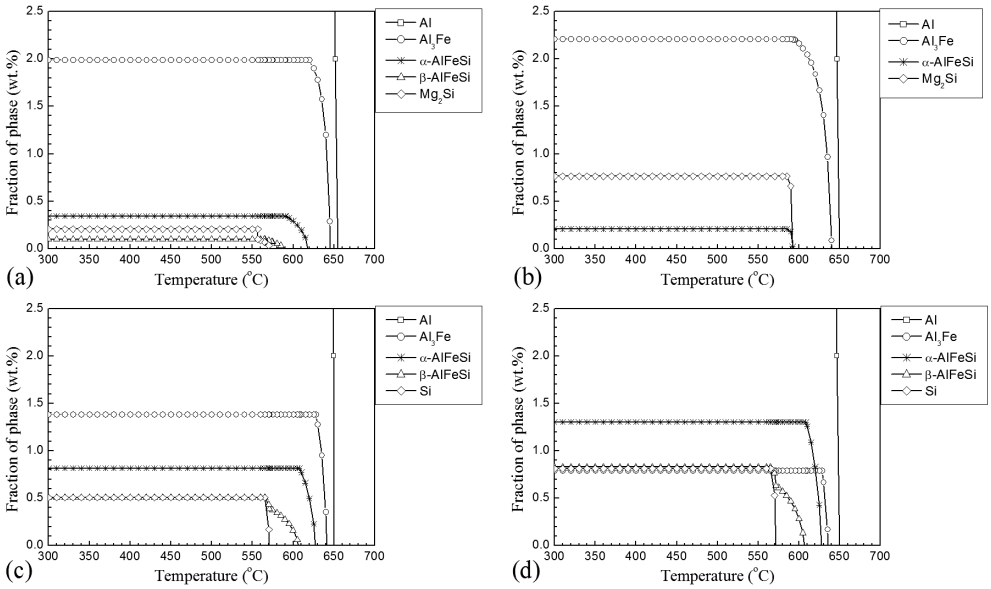

Figure 5: Phase equilibria calculated by JMatPro: a) Al-0.5Mg-1Fe-0.5Si, b) Al-1.5Mg-1Fe-0.5Si, c) Al-1.0Si-1Fe-1Zn and d) Al-1.5Si-1Fe-1Zn alloys

Slika 5: Fazna ravnotežja v zlitinah, izračunana z JMatPro: a) Al-0,5Mg-1Fe-0,5Si, b) Al-1,5Mg-1Fe-0,5Si, c) Al-1,0Si-1Fe-1Zn in d) Al-1,5Si-1Fe-1Zn

rize, the variation of energy release for the solidification coincided relatively well with the fluidity behavior, but the variation in the quantity of energy release for solidification was too small to fully explain the fluidity variation. **Figure 4b** shows the viscosity of the developed alloys calculated under the same superheat conditions. For both alloy systems, the viscosity increased in proportion to the amount of Mg and Si. It seemed that in this investigation, the viscosity did not have a significant effect on the fluidity of these experimental alloys. For reference, the reason why the viscosity decreased with increasing Mg and Si content in the work of other researchers[5,7] was that the viscosity was obtained not for a constant superheat condition but for a constant pouring-temperature condition, i.e., the variation of the liquidus temperature of the various alloy compositions was not considered. On the other hand, it is notable that the difference in the surface energy between the two alloy systems was significant, as shown in **Figure 4c**. It seemed that the superior fluidity for the small diameter channel of the Al-*x*Si-1Fe-1Zn alloys was because of the lower backpressure caused by a lower surface energy. It is apparent that the Al-*x*Si-1Fe-1Zn alloys showed a similar energy release during the solidification and even a higher viscosity, but their surface energies were nearly half those of the Al-*x*Mg-1Fe-0.5Si alloys. Actually, in this fluidity test experiment, which used a low-pressure casting machine, the backpressure in the diameter channels 1 mm calculated by the capillary effect amounted to approximately 80 % of the applied pouring pressure.

Because the solidification range and secondary phases also have an influence on the fluidity of alloy melts,[10–15] the phase-equilibria calculations were carried out prior to the microstructural examination. **Figure 5** shows the phase equilibria during solidification calculated by the Scheil equation (the nonequilibrium lever rule) using JMatPro. The Al-*x*Mg-1Fe-0.5Si alloys were typified by the fact that the amount of Al_3Fe phase, which has been reported to have a plate shape,[11] increased with increasing Mg content, whereas the solidification range decreased significantly as a result of the change of the quaternary eutectic point. In the Al-*x*Si-1Fe-1Zn alloys, the liquidus temperature decreased slightly with Si content but the quaternary eutectic point did not change, resulting in a slight decrease in the solidification range. In addition, the amount of Al_3Fe phase, which was formed by the first monovariant eutectic reaction, decreased with increasing Si content. At 1.5 % Si, the amount of the Al_3Fe phase became less than the amount of the α-AlFeSi phase, which was formed by the subsequent monovariant eutectic reaction. From these calculated solidification characteristics, it is thought that the Al_3Fe phase played a role in lessening the fluidity of the Al-*x*Mg-1Fe-0.5Si and Al-*x*Si-1Fe-1Zn alloys. The decrease in the solidification range in the Al-*x*Mg-1Fe-0.5Si alloys might also have provoked the negative effect of the Al_3Fe phase on the fluidity, which is different from the general tendency of a narrower solidification range improving the melt fluidity.[10] In other words, the decrease in the solidification range resulted in an increase in the residual liquid fraction at the stage when the Al_3Fe phase started to form. As the Mg increased from 0.5 % to 1.5 %, the residual liquid fraction increased from 50 % to 60 %, thus enlarging the Al_3Fe phase with its large aspect ratio and finally obstructing the melt flow.

To investigate the actual nonequilibrium solidification characteristics, cooling-curve analyses and microscopic tests were carried out. In **Figure 6**, the cooling-curve analyses results, which consist of cooling curves,

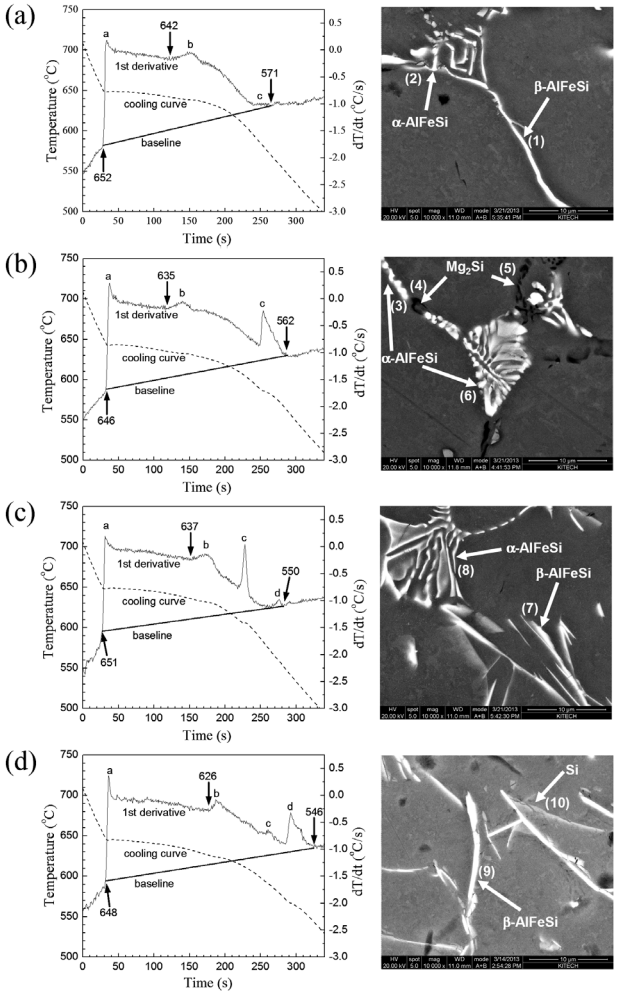

Figure 6: Cooling-curve analysis results and SEM (BSE) microstructural images in as-cast state: a) Al-0.5Mg-1Fe-0.5Si, b) Al-1.5Mg-1Fe-0.5Si, c) Al-1.0Si-1Fe-1Zn and d) Al-1.5Si-1Fe-1Zn alloys

Slika 6: Rezultati analize ohlajevalnih krivulj in SEM- (BSE)-posnetki mikrostruktur zlitin v litem stanju: a) Al-0,5Mg-1Fe-0,5Si, b) Al-1,5Mg-1Fe-0,5Si, c) Al-1,0Si-1Fe-1Zn in d) Al-1,5Si-1Fe-1Zn

their first derivatives, and baselines, and the scanning electron microscopy images with backscattered electrons [SEM(BSE)] in the as-cast state are shown. In the Al-*x*Mg-1Fe-0.5Si alloys (**Figures 6a** and **6b**), three thermal events are observed in the first-derivative curves. At the onset of solidification of any phase, the first derivative increases in value and decreases upon the completion of solidification.[8] It appears that the peaks labeled (a), (b), and (c) correspond to the crystallization of primary Al dendrites, the formation of secondary phases at the inter-dendritic regions between the secondary dendrite arms, and the final eutectic solidification reaction, respectively. From the results of the combined SEM (BSE) and EDS analyses, which are shown in **Table 3**, it was verified that in the Al-0.5Mg-1Fe-0.5Si alloy (**Figure 6a**) the plate-shaped particle (1) between the secondary dendrite arms was a β-AlFeSi phase and the irregular-shaped particle (2) at the final solidification regions was an α-AlFeSi phase. According to Rosefort et al.,[16] α- and β-AlFeSi phases in as-cast aluminum alloys can be identified with the help of SEM-EDS, i.e., the phase with the plate-like structure at high Si(*w*/%)/Fe(*w*/%) ratios above approximately 0.4 is a β-AlFeSi phase and the phase with the Chinese-script-structure at low Si(*w*/%)/Fe(*w*/%) ratios is an α-AlFeSi phase. In the high-Mg-containing Al-1.5Mg-1Fe-0.5Si alloy (**Figure 6b**), a dotted bright particle (3) and a dark particle (4) were observed at the inter-dendritic regions between the secondary dendrite arms. These dotted bright and dark particles proved to be α-AlFeSi and Mg_2Si phases, respectively. The Mg_2Si phase was also observed at the final solidification regions [particle (5)]. It is likely that the peak (c) on the first derivative curve of **Figure 6b**, which is larger than that of **Figure 6a**, was related to a larger latent-heat evolution due to Mg_2Si phase crystallization. In the Al-*x*Si-1Fe-1Zn alloys, four thermal events were observed on the first-derivative curves, as shown in **Figures 6c** and **6d**, and it was determined that the peaks (a), (b), (c), and (d) corresponded to the crystallization of primary Al dendrites, the β-AlFeSi phase at the inter-dendritic regions between secondary dendrite arms, and α-AlFeSi and Si phases at the final solidification regions, respectively. The results indicate that in the Al-1Si-1Fe-1Zn alloys (**Figure 6c**) the peak (c) tended to be relatively larger than the peak (d). The reverse findings in the Al-1.5Si-1Fe-1Zn alloys (**Figure 6d**) were attributed to the microstructural differences in the final solidification regions with Si content. That is, in a low-Si-containing Al-1Si-1Fe-1Zn alloy, an α-AlFeSi phase was mostly observed in the final solidification regions, but in a high-Si-containing Al-1.5Si-1Fe-1Zn alloy, the Si and β-AlFeSi phases prevailed.

Table 3: EDS analysis of the compositions of the particles (1)–(10) marked in **Figure 6**

Tabela 3: EDS-analiza sestave delcev (1)–(10), označenih na **sliki 6**

Point	Mg		Si		Fe		Zn		Al
	w/%	*x*/%	*w*/%	*x*/%	*w*/%	*x*/%	*w*/%	*x*/%	
(1)	0.75	0.88	5.03	5.11	10.46	5.35	–	–	bal.
(2)	0.43	0.51	1.55	1.58	10.97	5.62	–	–	bal.
(3)	1.82	2.16	1.12	1.15	12.86	6.65	–	–	bal.
(4)	6.79	7.54	6.42	6.17	1.01	0.49	–	–	bal.
(5)	8.05	8.92	4.63	4.44	1.17	0.56	–	–	bal.
(6)	1.93	2.32	1.38	1.44	14.96	7.82	–	–	bal.
(7)	–	–	7.42	7.56	10.54	5.40	0.16	0.19	bal.
(8)	–	–	4.95	5.16	12.92	6.78	1.78	0.80	bal.
(9)	–	–	9.45	9.71	9.91	5.12	1.71	0.76	bal.
(10)	–	–	17.15	17.11	3.02	1.51	2.46	1.05	bal.

Unlike the calculated phase equilibria during solidification, shown in **Figure 5**, an Al_3Fe phase (or the metastable Al_6Fe phase) was not observed in the metallographic inspection for any of the Al-*x*Mg-1Fe-0.5Si and Al-*x*Si-1Fe-1Zn alloys, as shown in **Figure 6**. Moreover, it is interesting to note that β-AlFeSi, a low-temperature-stable phase, crystallized earlier than α-AlFeSi, a high-temperature-stable phase, at the inter-dendritic

regions between the secondary dendrite arms. Except for the high-Mg-containing alloy (the Al-1.5Mg-1Fe-0.5Si alloy), the α-AlFeSi phase was observed only in the final solidification regions. These solidification characteristics could be attributed to the segregation behavior of the solute atoms, particularly Si. That is because the cooling rate was high and the solidification occurred as a fine, mushy type, the Si atoms ejected into the inter-dendritic liquid had little chance of diffusing out to a residual liquid reservoir because of the limited time and space. As a result, the β-AlFeSi phase with a high Si/Fe ratio was crystallized at interdendritic regions between the secondary dendrite arms rather than the α-AlFeSi. Thus, for the final solidification regions, which had relatively longer solidification times and lower Si concentrations than the inter-dendritic regions, an α-AlFeSi phase could crystallize. These are consistent with Darvishi's experimental results[13] regarding the presence of silicon-substituted Al_3Fe and Al_6Fe phases with α- and β-AlFeSi phases and with Dutta's simulation results,[17] which show that the increase in the cooling rate increased the Si/Fe ratio in the eutectic liquid. In the high-Mg-containing alloy (Al-1.5Mg-1Fe-0.5Si alloy) it is likely that the consumption of Si atoms due to the formation of a Mg_2Si phase enabled the α-AlFeSi phase to crystallize, even at the inter-dendritic regions between the secondary dendrite arms under the same cooling conditions. Hosseinifar et al.[18] reported a similar phase selection example in a 6xxx Al alloy: the addition of La resulted in the formation of a $La(Al,Si)_2$ phase and a decrease of the Si/Fe ratio in the eutectic liquid, favoring the crystallization of an α-AlFeSi phase rather than a β-AlFeSi phase.

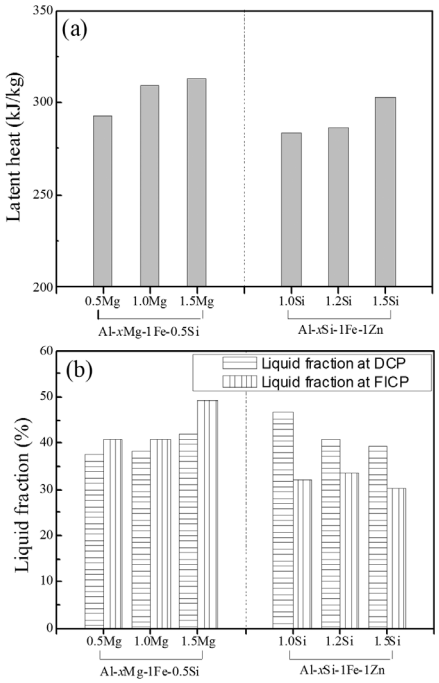

Figure 7: a) Latent heat and b) liquid fraction at DCP and FICP of Al-(0.5–1.5)Mg-1Fe-0.5Si and Al-(1.0–1.5)Si-1Fe-1Zn alloys, which were obtained from a cooling-curve analysis

Slika 7: a) Latentna toplota in b) delež taline pri DCP- in FICP-zlitin Al-(0,5–1,5)Mg-1Fe-0,5Si in Al-(1,0–1,5)Si-1Fe-1Zn, dobljeni iz analize ohlajevalnih krivulj

The characteristic solidification parameters, including the solidification range, were calculated from the cooling and first-derivative curves and the results are summarized in **Table 4**. However, it seems that the Al-*x*Mg-1Fe-0.5Si and Al-*x*Si-1Fe-1Zn alloys did not follow the general relation between the solidification range and the fluidity length of the alloy very well, in which the fluidity length is inversely proportional to the solidification range. DCP and the first intermetallic crystallization point (FICP) also did not seem to show a direct relation with the fluidity length. The onset temperatures for the (b) peaks in **Figure 6**, which were determined by the tangential line method, were used as the FICP.

Table 4: Characteristic solidification parameters for Al-*x*Mg-Fe-Si (alloy 1 series) and Al-*x*Si-Fe-Zn (alloy 2 series) alloys

Tabela 4: Značilni parametri strjevanja za Al-*x*Mg-Fe-Si (zlitina 1. serije) in Al-*x*Si-Fe-Zn (zlitina 2. serije)

Alloy		Start of solidification (°C)	End of solidification (°C)	Solidification range (°C)	FICP (°C)	DCP (°C)
1	1-1	652	571	81	642	640
	1-2	649	558	91	637	636
	1-3	646	562	84	635	632
2	2-1	651	550	101	637	641
	2-2	648	550	98	630	633
	2-3	648	546	102	626	634

From the cooling-curve analyses, the latent heat and liquid fraction at characteristic solidification points can be obtained. Knowing these values is important in order to understand the solidification characteristics of the alloy. The latent heat can be calculated by multiplying the accumulative area between the first derivative and the baseline by the specific heat.[9] The liquid fraction can be obtained by calculating the accumulative area between the first derivative and the baseline from the characteristic solidification points to the solidification end point as a fraction of the total area between these curves.[8] **Figure 7** shows the calculated latent heat and the liquid fractions at the DCP and FICP. The latent heat increased with increasing Mg and Si in the Al-*x*Mg-1Fe-0.5Si and Al-*x*Si-1Fe-1Zn alloys, as shown in **Figure 7a**. These results are different from the thermophysical modeling results of **Figure 3a**, in which the increase of Mg content decreased the latent heat of the Al-*x*Mg-1Fe-0.5Si alloys. This contrasting tendency of the latent heat with increasing Mg content is responsible for the difference in the solidification path between the phase equilibria calculation and the actual non-equilibrium solidification. In any case, it seems that the latent heat did not have a significant effect on the fluidity of these experimental alloys. In the liquid fractions at the DCP and FICP of **Figure 7b**, two interesting findings were obtained. First, in the Al-*x*Mg-1Fe-0.5Si alloys, the liquid fraction was

higher at FICP than at DCP, but this tendency is reversed in the Al-*x*Si-1Fe-1Zn alloys. Second, in the Al-*x*Mg-1Fe-0.5Si alloys, the liquid fractions at DCP and FICP increased with increasing Mg content, whereas in the Al-*x*Si-1Fe-1Zn alloys, the liquid fractions decreased with increasing Si content. The dendrite coherency seriously decreases the fluidity.[19] Therefore, it is likely that in the Al-*x*Si-1Fe-1Zn alloys, although the crystallization of the plate-like β-AlFeSi phase during solidification has a negative effect on the fluidity of Al alloys[13] and the amount of the β-AlFeSi phase increased with increasing Si content, as shown in **Figures 6c** and **6d**, its crystallization after DCP had little influence on the fluidity. It was thus concluded that in the Al-*x*Si-1Fe-1Zn alloys, the increase of the Si content effectively improved the fluidity by increasing the latent heat and lowering the DCP without disturbing the secondary phases, whereas in the Al-*x*Mg-1Fe-0.5Si alloys the secondary phases could have a negative effect on the fluidity because they crystallized before the dendrite coherency. Paes[14] and Zhang[15] reported that the presence of a Mg_2Si phase increased the viscosity of Al alloys. Considering that the liquid fraction of the Al-1.5Mg-1Fe-0.5Si alloy was approximately 50 % at FICP, the increase of the melt viscosity could be regarded as the most important factor in terms of decreasing the fluidity. Therefore, it was concluded that in the Al-*x*Mg-1Fe-0.5Si alloys, the increase of Mg content significantly deteriorated the fluidity by increasing the viscosity and increasing the DCP, in spite of the increase in the latent heat.

4 CONCLUSIONS

For the development of an aluminum alloy that combines a high thermal conductivity with a good castability and anodizability, the low-Si-containing aluminum alloys Al-(0.5–1.5)Mg-1Fe-0.5Si and Al-(1.0–1.5)Si-1Fe-1Zn were investigated. The obtained results are as follows:

1. The developed aluminum alloys exhibited a thermal conductivity of 170–190 % level (160–180 W/(m K)), a fluidity of 60–85 % level, and an equal or higher ultimate tensile strength compared to those of the ADC12 alloy.
2. In each developed alloy system, the thermal conductivity decreased and the strength increased with increasing amounts of Mg and Si, the major alloying elements. The fluidity exhibited an inverse relationship with the Mg content and a direct relationship with the Si content.
3. The contradictory fluidity variation behavior in the two alloy systems with the compositions of Mg and Si was caused by the opposing tendencies of DCP and FICP and the relatively different occurring sequences of DCP and FICP.
4. In the experimental aluminum alloys with a low Si content, the prevailing Fe-containing intermetallic compound and the solidification path were observed to be mainly dependent on the Si segregation behavior and the Mg alloying level, rather than on the initial Si/Fe alloying ratio.
5. It was found that the Al-Mg-Fe-Si-based aluminum alloys that show a higher strength and good fluidity in channels greater than 2 mm in diameter are potential materials for general cast heat-dissipating components, and that the Al-Si-Fe-Zn-based aluminum alloys that possess a lower surface energy are potential materials for thin-wall cast heat-dissipating components.

5 REFERENCES

[1] G. P. Reddy, N. Gupta, Material selection for microelectronic heat sinks, Materials and Design, 31 (**2010**), 113–117

[2] K. P. Keller, Efficiency and cost tradeoffs between aluminum and zinc die cast heatsinks, Proc. of Inter. Electronic Packaging Conf., 1997

[3] K. P. Keller, Low cost, high performance, high volume heatsinks, Proc. of 1998 IEMT-Europe Symposium, Berlin, 1998

[4] S. Ferlini, A. Morri, E. Ferri, M. Merlin, G. Giacomozzi, Effect of silicon particles and roughness on the surface treatments of cast aluminum alloys, Proc. of the 3rd Iner. Conf. on High Tech Die Casting, Vicenza, 2006

[5] J. E. Hatch, Aluminum-Properties and Physical Metallurgy, 10th ed., ASM, Ohio 2005, 210

[6] W. F. Gale, T. C. Totemeier, Smithells Metals Reference Book, 8th ed., ASM, Oxford 2004, 8-2

[7] A. T. Dinsdale, P. N. Quested, The viscosity of aluminum and its alloys-A review of data and models, Journal of Materials Science, 39 (**2004**), 7221–7228

[8] S. Farahany, H. R. B. Rada, M. H. Idris, M. R. A. Kadir, A. F. Lotfabadi, A. Ourdjini, In-situ thermal analysis and macroscopical characterization of Mg–*x*Ca and Mg–0.5Ca–*x*Zn alloy systems, Thermochimica Acta, 527 (**2012**), 180–189

[9] I. U. Haq, J. S. Shin, Z. H. Lee, Computer-Aided Cooling Curve Analysis of A356 Aluminum Alloy, Met. & Mat. Inter., 10 (**2004**), 89–96

[10] P. Bastien, J. C. Armbruster, P. Azov, Flowability and viscosity, AFS Trans., 70 (**1962**), 400–409

[11] Y. Han, C. Ban, S. Guo, X. Liu, Q. Ba, J. Cui, Alignment behavior of primary Al_3Fe phase in Al–Fe alloy under a high magnetic field, Materials Letters, 61 (**2007**), 983–986

[12] E. Taghaddos, M. M. Hejazi, R. Taghiabadi, S. G. Shabestari, Effect of iron-intermetallics on the fluidity of 413 aluminum alloy, Journal of Alloys and Compounds, 468 (**2009**), 539–545

[13] A. Darvishi, A. Maleki, M. M. Atabaki, M. Zargami, The mutual effect of iron and manganese on microstructure and mechanical properties of aluminium –silicon alloy, MJoM, 16 (**2010**), 11–24

[14] M. Paes, E. J. Zoqui, Semi-solid behavior of new Al–Si–Mg alloys for thixoforming, Mat. Sci. & Eng., A406 (**2005**), 63–73

[15] J. Zhang, Z. Fan, Y. Wang, B. Zhou, Hypereutectic aluminium alloy tubes with graded distribution of Mg Si particles prepared by centrifugal casting, Materials and Design, 21 (**2000**), 149–153

[16] M. Rosefort, C. Matthies, H. Buck, H. Koch, Light Metals 2011, TMS 2011, 711–715

[17] B. Dutta, M. Rettenmayr, Effect of cooling rate on the solidification behaviour of Al–Fe–Si alloys, Mat. Sci. & Eng., A283 (**2000**), 218–224

[18] M. Hosseinifar, D. V. Malakhov, The Sequence of intermetallics formation during the solidification of an Al-Mg-Si alloy containing La, Met. & Mat. Trans., 42A (**2011**), 825–833

[19] S. Nafisi, R. Ghomashchi, Combined grain refining and modification of conventional and rheo-cast A356 Al–Si alloy, Mat. Char., 57 (**2006**), 371–385

UDK 621.785.6
Original scientific article/Izvirni znanstveni članek

ISSN 1580-2949
MTAEC9, 48(2)203(2014)

A NEW METHOD FOR ESTIMATING THE HURST EXPONENT *H* FOR 3D OBJECTS

NOVA METODA ZA OCENJEVANJE HURSTOVEGA EKSPONENTA *H* ZA 3D-OBJEKTE

Matej Babič[1], Peter Kokol[2], Nikola Guid[2], Peter Panjan[3]

[1]Emo-Orodjarna, d .o. o., Slovenia
[2]University of Maribor, Faculty of Electrical Engineering and Computer Science, Slovenia
[3]Jožef Stefan Institute, Slovenia
babicster@gmail.com

Prejem rokopisa – received: 2012-10-23; sprejem za objavo – accepted for publication: 2013-06-10

Mathematics and computer science are very useful in many other sciences. We use a mathematical method, fractal geometry, in engineering, specifically in laser techniques. Characterization of the surface and the interfacial morphology of robot-laser-hardened material is crucial to understand its properties. The surface microstructure of robot-laser-hardened material is rough. We aimed to estimate its surface roughness using the Hurst parameter *H*, which is directly related to the fractal dimension. We researched how the parameters of the robot-laser cell impact on the surface roughness of the hardened specimen. The Hurst exponent is understood as the correlation between the random steps X_1 and X_2, which are followed by time for the time difference Δt. In our research we understood the Hurst exponent *H* to be the correlation between the random steps X_1 and X_2, which are followed by the space for the space difference Δd. We also have a space component. We made test patterns of a standard label on the point robot-laser-hardened materials of DIN standard GGG 60, GGG 60 L, GGG 70, GGG 70 L and 1.7225. We wanted to know how the temperature of point robot-laser hardening impacts on the surface roughness. We developed a new method to estimate the Hurst exponent *H* of a 3D-object. This method we use to calculate the fractal dimension of a 3D-object with the equation $D = 3 - H$.

Keywords: fractal structure, Hurst parameter *H* for 3D-objects, robot, laser, hardening

Matematika in računalništvo sta zelo uporabni veji drugih vrst znanosti. Uporabili bomo matematično metodo – fraktalno geometrijo – v inženirstvu, natančneje, v laserski tehniki. Karakterizacija površine in morfologija robotsko lasersko kaljenih materialov ima ključni pomen za razumevanje lastnosti materialov. Površina robotsko lasersko kaljenega materiala je hrapava. To hrapavost pa bi radi ocenili s Hurstovim eksponentom *H*, ki ga dobimo direktno iz fraktalne geometrije, kot meritev hrapavosti površine. Raziskali smo, kako parameter robotske celice vpliva na hrapavost kaljenih vzorcev. Hurstov eksponent *H* razumemo kot korelacijo med korakoma X_1 in X_2, ki ga dobimo med časovno razliko Δt. V naši raziskavi razumemo Hurstov eksponent *H* kot relacijo med korakoma X_1 in X_2, ki ga dobimo med prostorsko komponento. Osredinili smo se na točkovno robotsko lasersko kaljenje vzorcev standardne oznake po DIN-standardu GGG 60, GGG 60 L, GGG 70, GGG 70 L in 1.7225. Želeli smo izvedeti, kako temperatura točkovnega robotskega laserskega kaljenja vpliva na hrapavost površine. Razvili smo novo metodo za ocenjevanje Hurstovega eksponenta *H* za 3D-objekte. To metodo smo uporabili za računanje fraktalne dimenzije 3D-objektov po formuli $D = 3 - H$.

Ključne besede: fraktalna struktura, Hurstov parameter *H* za 3D-objekte, robot, laser, kaljenje

1 INTRODUCTION

The Hurst parameter[1] is understood as the correlation between the random steps X_1 and X_2, using space for the space difference Δd. It occurs in many areas of applied mathematics, including fractals and chaos theory, and is used in many fields, ranging from biophysics to network computers. The parameter was originally developed in hydrology. However, modern techniques for estimating the Hurst parameter *H* are emerging from fractal mathematics. For example, the fractal dimension was used to measure the roughness of sea coasts. The relationship between the fractal dimension *D* and the Hurst parameter *H* is given by the equation $D = 2 - H$ for 2D-objects and by $D = 3 - H$ for 3D-objects. There is also a form called statistical self-similarity, where if we have one data set of a seemingly endless string of data sets, we can assume that each data set has the same statistical properties as any other. Statistical self-similarity occurs in a surprisingly large number of areas in engineering. Fractal geometry[2,3] has offered a new perspective on maths and science and allows observation of the world around us from a new and completely different point of view. Nature is full of shapes and images that from a distance are seen to be similar. A well-known example of such a self-similar pattern is Sierpinski's pyramid. Let us assume that we have a statistically self-similar finite data series. Any part of this series would have the same statistical characteristics as the entire series or any other part of this series. Such series are often used in engineering. We used one in the analysis of robot-laser-hardened materials.[4] A robot-laser surface-hardening heat treatment is complementary to conventional flame or inductive hardening. The energy source for the laser hardening is a laser beam, which heats up very quickly. Laser hardening is a process of controlled energy intake, high performance constancy, and an accurate positioning process. A hard martensitic microstructure provides improved surface properties such as wear resistance and high strength. Point

robot-laser hardening[5–8] is a classic case of robot-laser hardening. This means that the speed of the laser beam is no longer a parameter that can be changed. In point robot-laser hardening cells we are interested in finding the optimal parameters that give the maximum hardness of the hardened material. In this work we have used a scanning electronic microscope (SEM) to search and analyse the fractal structure of the robot-laser-hardened material. First, we introduce the Hurst parameter to find how the temperature of the robot laser cell impacts on the optimal Hurst parameter H of the hardened material. We then developed a new method to estimate the Hurst parameter H of a 3D-object.

2 MATERIALS PREPARATION AND METHOD

2.1 Materials preparation

We made test patterns of a standard label on point robot-laser-hardened materials of DIN-standard GGG 60, GGG 60 L, GGG 70, GGG 70 L and 1.7225. We hardened the materials at different temperatures. So we changed the temperature parameter of the robot laser cells, $T \in [800, 2000]$ °C, with a step of 100 °C. In all the experiments we recorded the microstructure. We wanted to know how the temperature of point robot-laser hardening impacts on the surface roughness. **Figure 1** shows the transverse and longitudinal section of a hardened material. Each sample was etched and polished (IMT, Institute of Metals and Technology Ljubljana, Slovenia) and then examined under a microscope (IJS, Jožef Stefan Institute). The images were obtained using a JEOL JMS-7600F field-emission scanning electron microscopy. **Figures 2** to **6** present microstructure of robot laser hardened specimens. **Figure 7** presents boundary between hardened and non-hardened DIN 1.7225 standard material.

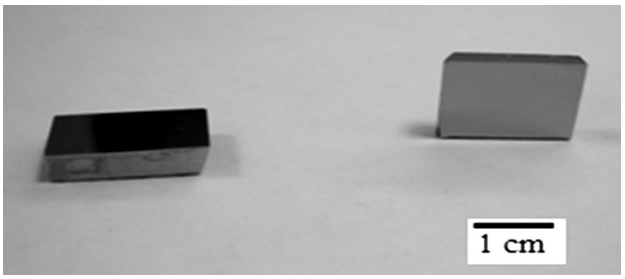

Figure 1: Transverse and longitudinal section of hardened material
Slika 1: Prečni in vzdolžni prerez kaljenega materiala

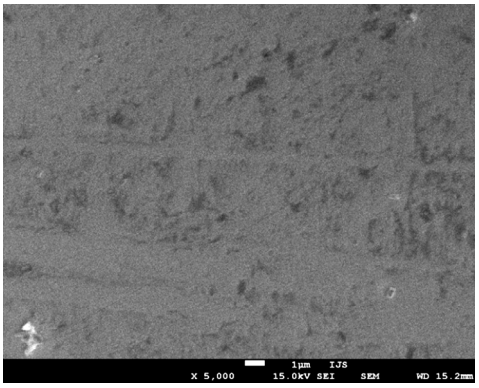

Figure 2: Microstructure of hardened DIN 1.7225 standard material (SEM)
Slika 2: Mikrostruktura kaljenega materiala po DIN-standardu 1.7225 (SEM)

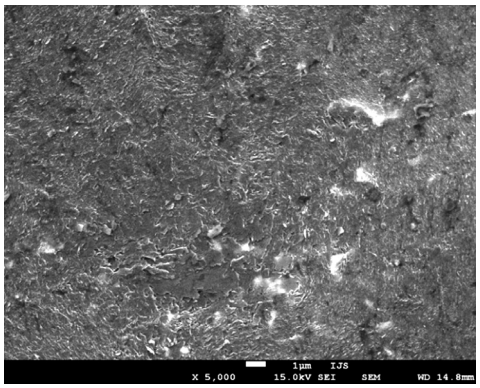

Figure 3: Microstructure of hardened DIN GGG 70 standard material (SEM)
Slika 3: Mikrostruktura kaljenega materiala po DIN-standardu GGG 70 (SEM)

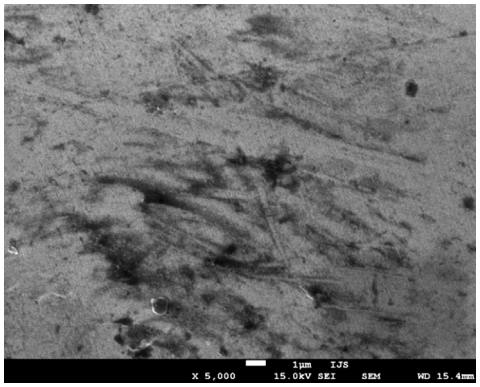

Figure 4: Microstructure of hardened DIN GGG 70 L standard material (SEM)
Slika 4: Mikrostruktura kaljenega materiala po DIN-standardu GGG 70 L (SEM)

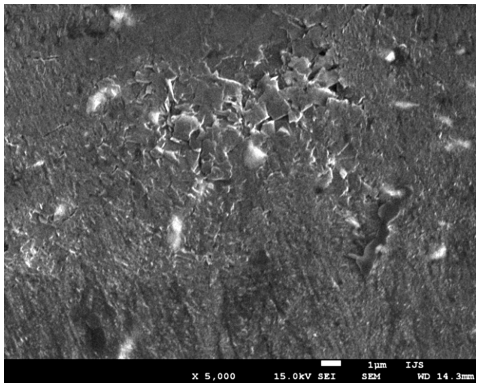

Figure 5: Microstructure of hardened DIN GGG 60L standard material (SEM)
Slika 5: Mikrostruktura kaljenega materiala po DIN-standardu GGG 60 L (SEM)

The random process is evaluated statistically using the Hurst parameter *H* or by determining the distribution function. The Hurst parameter *H* as a self-similarity criterion cannot be accurately calculated; it can only be estimated. There are several different methods[9–13] for producing estimates of the parameter *H*, which deviate from one another to some extent. In doing so, we have no criteria to determine which method gives the best result.

Different methods for estimating the Hurst exponent H have been evaluated.[14] The assessment methods in the space component domain are based on a comparison of the original process and the average process with the method of aggregation:

- The variance-time plot analysis is based on the property of the slowly decaying variance of self-similar processes undergoing aggregation.
- The R/S method. The adjusted rescaled range method or adjusted scale is also a graphical method based on the properties of the Hurst phenomenon.
- In statistics, residual variance is another name for an unexplained variation, the sum of squares of differences between the *y*-value of each ordered pair on the regression line and each corresponding predicted *y*-value; it is generally used to calculate the standard error of an estimate. In other words, residual variance helps us confirm how well the regression line that we constructed fits the actual dataset. The smaller the variance, the more accurate the predictions are.

  Methods for evaluation in the frequency or wavelet ("wavelet") space are:
- The periodogram method based on the noise 1/*f* and the Fourier transform.
- The Whittle estimator is based on minimizing the likelihood function used in the periodogram method. There is no graphical method.
- The Hurst exponent is estimated by using the wavelet transform of the series. A least-squares fit on the average of the squares of the wavelet coefficients at different scales is an estimate of the Hurst exponent. The method produces both a graphical output and a confidence interval.

Estimation of the Hurst parameter *H*[15–19] using different methods gives results that show significant differences.

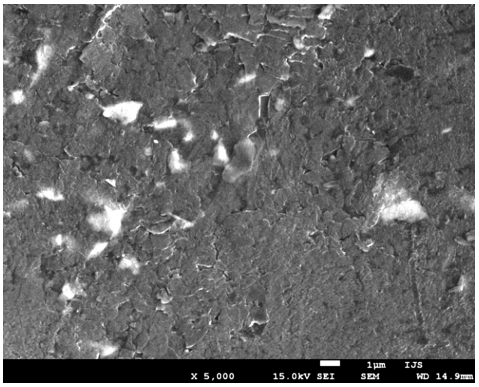

Figure 6: Microstructure of hardened DIN GGG 60 standard material (SEM)

Slika 6: Mikrostruktura kaljenega materiala po DIN-standardu GGG 60 (SEM)

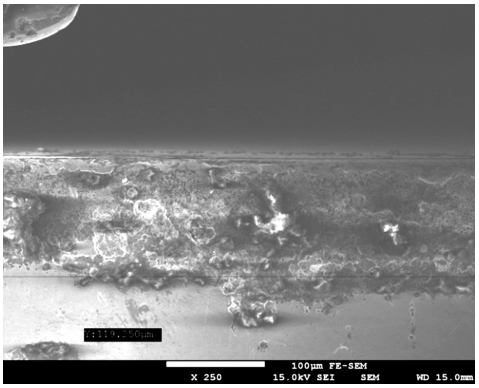

Figure 7: The boundary between hardened and non-hardened DIN 1.7225 standard material (SEM)

Slika 7: Meja med kaljenim in nekaljenim delom materiala po DIN-standardu 1.7225 (SEM)

2.2 Method

Here we present our first new method for estimating the Hurst exponent *H* for 3D-objects. First of all, we find all the coordinates (*x, y, z*) of an SEM picture. Here, we use the program ImageJ. Then we use only *z* coordinates to estimate the Hurst exponent *H*. We present all the *z* coordinates in a 2D-space component graph (**Figure 8**), which is continuous. Also, all the points (x_i, y_0, z_i) present the first space component in a 2D-graph for all the

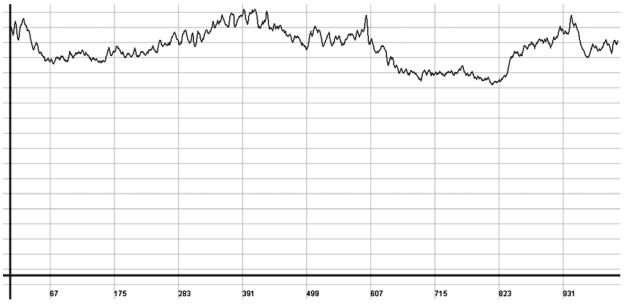

Figure 8: Space component

Slika 8: Prostorska komponenta

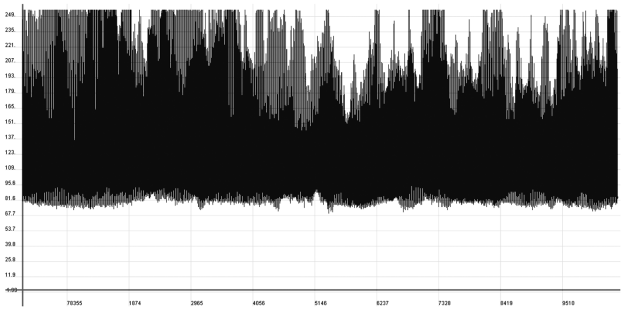

Figure 9: Long space component

Slika 9: Dolga prostorska komponenta

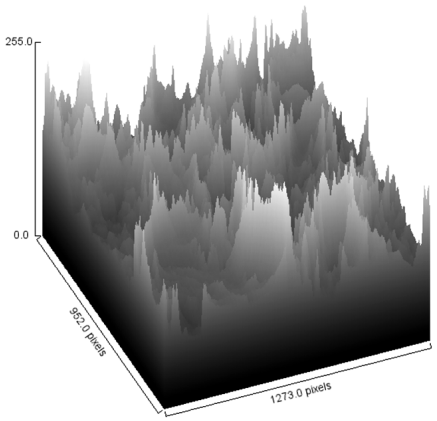

Figure 10: 3D-object of robot-laser-hardened microstructure
Slika 10: 3D-objekt lasersko kaljene mikrostrukture

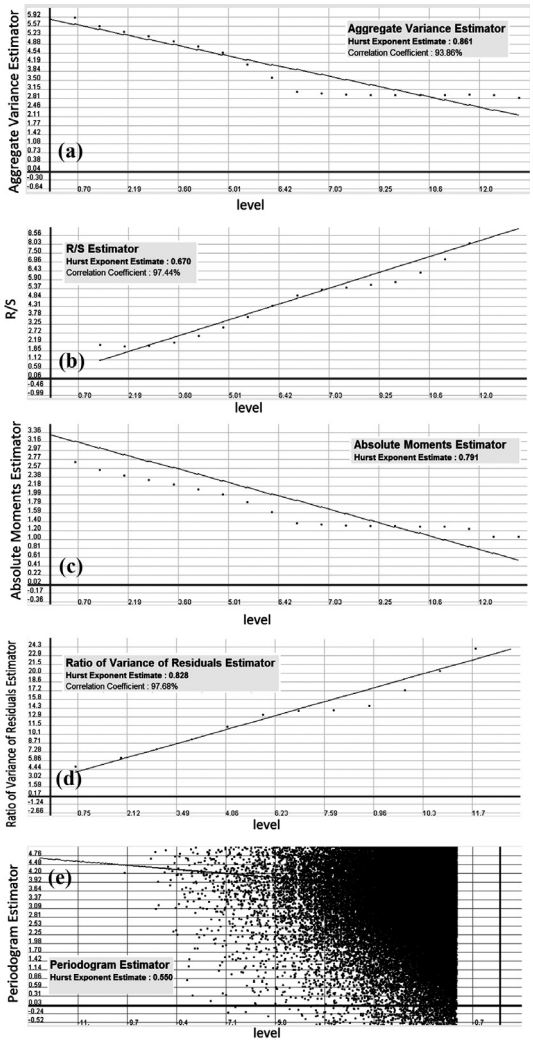

Figure 11: a) Variance method for hardened material 1.7225, b) R/S method for hardened material 1.7225, c) Absolute moments estimator for hardened material 1.7225, d) Variance of residuals method for hardened material 1.7225, e) Periodogram method for hardened material 1.7225
Slika 11: a) Variance metoda za kaljeni material 1.7225, b) R/S-metoda za kaljeni material 1.7225, c) Ocena absolutnega momenta za kaljeni material 1.7225, d) Variančna metoda ostankov za kaljeni material 1.7225, e) Metoda periodograma za kaljeni material 1.7225

points (x_i, z_i). All the points (x_i, y_1, z_i) represent the second space component in a 2D-graph for all the points (x_i, z_i). We obtained the space component for all y_i, $\forall i$ (**Figure 9**). Then we combined all of these space components into one space component. For this long space component we can estimate the Hurst exponent *H*. **Figure 10** shows the 3D-object of the point robot-laser-hardened microstructure.

3 RESULTS AND DISCUSSION

The pictures in the .jpeg format were converted into 256-grey-level numerical matrices (level 1 for black and 256 for white) with the program ImageJ. Then we entered information into the program Selfis 01B, with which we obtained the following graphs. The graphs were made only for specimen 1.7225 hardened at 800 °C.

Figures 11a to **11d** show the different methods for estimating the Hurst exponent *H*.

Figures 12 to **16** present the estimated value of the Hurst parameter *H* with five methods for five different robot-laser-hardened materials.

The collected data were entered into the program and the graphs were obtained, from which we can deduce the optimum results.

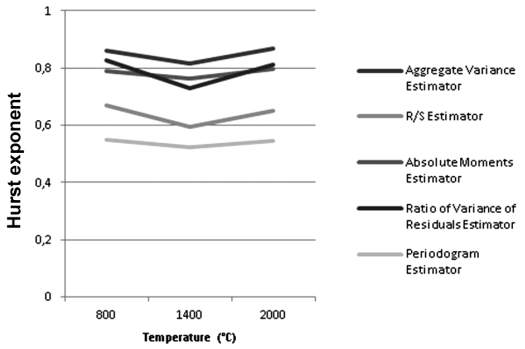

Figure 12: Relationship between estimated value of the Hurst parameter *H* and temperature of robot-laser-hardened specimens for DIN standard 1.7225
Slika 12: Odvisnost med ocenjeno vrednostjo Hurstovega parametra *H* in temperaturo robotsko lasersko kaljenih vzorcev 1.7225

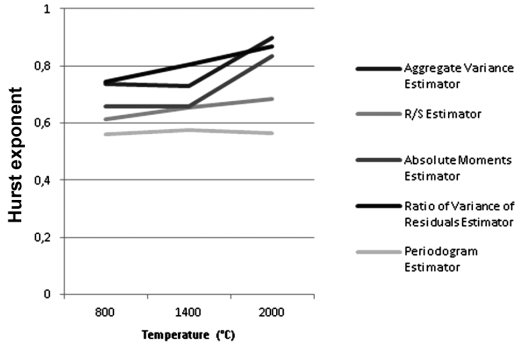

Figure 13: Relationship between estimated value of the Hurst parameter *H* and temperature of robot-laser-hardened specimens for DIN standard GGG 70
Slika 13: Odvisnost med ocenjeno vrednostjo Hurstovega parametra *H* in temperaturo robotsko lasersko kaljenih vzorcev GGG 70

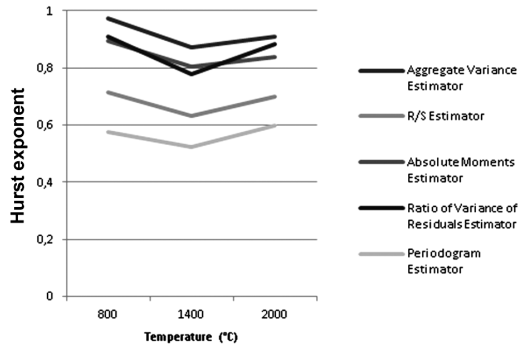

Figure 14: Relationship between estimated value of the Hurst parameter *H* and temperature of robot-laser-hardened specimens for DIN standard GGG 70 L

Slika 14: Odvisnost med ocenjeno vrednostjo Hurstovega parametra *H* in temperaturo robotsko lasersko kaljenih vzorcev GGG 70 L

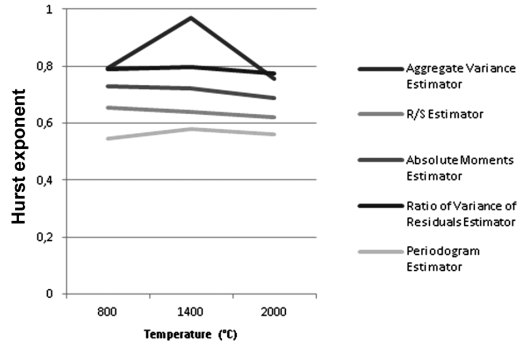

Figure 15: Relationship between estimated value of the Hurst parameter *H* and temperature of robot-laser-hardened specimens for DIN standard GGG 60 L

Slika 15: Odvisnost med ocenjeno vrednostjo Hurstovega parametra *H* in temperaturo robotsko lasersko kaljenih vzorcev GGG 60 L

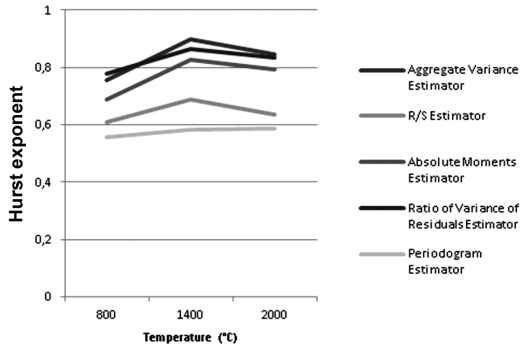

Figure 16: Relationship between estimated value of the Hurst parameter *H* and temperature of robot-laser-hardened specimens for DIN-standard GGG 60

Slika 16: Odvisnost med ocenjeno vrednostjo Hurstovega parametra *H* in temperaturo robotsko lasersko kaljenih vzorcev GGG 60

Material 1.7225: The smallest Hurst exponent *H* is obtained at a temperature of 1400 °C with all methods, which means that the roughness is higher.

Material GGG 70: The highest Hurst exponent *H* is obtained at a temperature of 2000 °C with all methods, which means that the roughness is lower.

Material GGG 70 L: The smallest Hurst exponent *H* is obtained at a temperature of 1400 °C with all methods, which means that the roughness is higher. It is similar to the material 1.7225.

Material GGG 60 L: The smallest Hurst exponent *H* is obtained at a temperature of 2000 °C with all methods, without for the periodogram method.

Material GGG 60: The smallest Hurst exponent *H* is obtained at a temperature of 800 °C with all methods, which means that the roughness is higher. The highest Hurst exponent *H* is obtained at a temperature of 1400 °C with all methods without for the periodogram method.

Smaller values are obtained with the periodogram method for all the hardened specimens at all temperatures. Higher values are obtained with the aggregate variance estimator method for hardened specimens at all the temperatures.

4 CONCLUSIONS

We conducted experiments on five different materials. We changed only the temperature parameter, $T \in [800, 2000]$ °C, in 100 °C steps. In total there were 65 samples. We were interested in which parameter of the robot laser cell achieved the roughest surface of the hardened material. We found the Hurst parameter *H* exactly. The main findings can be summarized with the following points:

- A fractal structure exists in robot-laser hardening.
- The Hurst parameter *H* was calculated using different methods. The results were compared using the program Image J and it was found that the best results were obtained by the periodogram method, which gave smaller values.
- With the help of the equation $D = 2 - H$, the fractal dimensions can be calculated for all the samples. For calculating the fractal dimensions in the 2D-plane obtained by a microscope as a two-dimensional image from which the fractal dimension can be determined.
- In the 3D-space we use equation $D = 3 - H$. In addition, we found a new process for calculating the fractal dimension of a 3D object.
- We found the optimal Hurst parameter *H* for different laser parameters of robot cells on different materials.
- The smaller the Hurst parameter *H*, the greater the surface roughness.
- We developed a new method to estimate the Hurst parameter *H* of a 3D-object.

The author of the Selfis program has written a great deal about the Hurst parameter *H*. The problem with these methods is that we estimated only the Hurst parameter *H* and that these methods are based on different bases (some of aggregation, others on wavelet transformation, etc.), which in turn lead to different estimates. Also, each method has certain advantages and limitations with regard to the captured sample (some methods are

better for large samples, some for smaller ones). Many books state that there is no precise method with which to accurately calculate the Hurst parameter and that it can only be estimated. The most common method of calculating the Hurst parameter *H* is the R/S-method.

Our findings are important from a practical point of view. The precise parameters of the robot-laser cell tempering influence the hardness of the hardened material. Materials with such properties have better wear resistance and a longer lifespan. The Hurst parameter *H* can give us information about the correlation between the roughness and the hardness of material, which is important in many industries.

Acknowledgements

The present work was supported by the European Social Fund of the European Union.

5 FUTURE WORK PLAN

In the future we plan to explore the Hurst parameter *H* as a function of several parameters in robot cells for laser hardening. The laser parameters include power, energy density, focal distance, energy density in the focus, focal position, temperature, and speed of hardening. In robot-laser hardening, many different problems are encountered. We are interested in estimating the Hurst parameter *H* in:

- two-beam laser robot hardening (where the laser beam is divided into two parts);
- areas of overlap (where the laser beam covers an already hardened area);
- robot-laser hardening at different angles (the angles change depending on the *x* and *y* axes).

6 REFERENCES

[1] S. Stoev, M. S. Taqqu, Wavelet estimation for the Hurst parameter in stable processes, In: G. Rangarang, M. Ding (eds.), Processes with Long-Range Correlations: Theory and Applications, Springer-Verlag, Berlin 2003, 61–87

[2] M. Babič, M. Milfelner, S. Stepišnik, Laser hardening metals, In: T. Perme, D. Švetak, J. Balič (eds.), IRT Industrial Forum, Portorož, 2010, Source of knowledge and experience for the profession: Proceedings of the Forum, Škofljica: Profidtp

[3] M. Babič, Optimal parameters of a robot cell for laser hardening of metals at different angles, 19. Proceedings of the International Electrotechnical and Computer Conference ERK 2010, Portoroz, Slovenia, 2010 (Codes. Electrical and Computer Conference ERK ...), Ljubljana: Slovenian section of the IEEE (in Slovene)

[4] M. Babič, T. Muhič, Fractal structure of the robot laser hardened materials, In: 18th Conference on Materials and Technology, Portorož, Slovenia, 2010, Program and abstracts book, Institute of Metals and Technology, Ljubljana, 73 (in Slovene)

[5] R. N. Bhattacharya, V. K. Gupta, E. Waymire, The Hurst effect under trend, Journal of Applied Probability, 20 (**1983**), 649–662

[6] C. C. Barton, Fractal analysis of scaling and spatial clustering of fractures, In: C. C. Barton, P. R. La Pointe (eds.), Fractals in the Earth Science, Plenum Press, New York 1995, 141–178

[7] B. B. Mandelbrot, The Fractal Geometry of Nature, W. H. Freeman, New York 1982, 93

[8] J. Grum, P. Žerovnik, R. Šturm, Measurement and analysis of residual stresses after laser hardening and laser surface melt hardening on flat specimens, Proceedings of the Conference "Quenching '96", Ohio, Cleveland, 1996

[9] M. Babič, Fractal dimension of the robot laser hardening tool steel, In: M. Robnik, (ur.), D. Korošak, (ur.), 9th Symposium of Physicists at the University of Maribor, Maribor, 2010, Book of Abstracts, London: CAMTP, [2] F. (In Slovene)

[10] J. Beran, R. Sherman, M. S. Taqqu, W. Willinger, Long-range dependence in variable bit rate video traffic, IEEE Transactions on Communications, 43 (**1995**), 1566–1579

[11] O. Rose, Estimation of the Hurst parameter of long-range dependent time series, Report No. 137, Institute of Computer Science, University of Würzburg, 1996

[12] http://phobos.informatik.uni-wuerzburg.de/TR/tr137.pdf

[13] W. Willinger, V. Paxson, R. H. Riedi, M. S. Taqqu, Long-range dependence and data network traffic, In: P. Doukhan, G. Oppenheim, M. S. Taqqu (eds.), Theory And Applications Of Long-Range Dependence, Birkhauser, 2003, 373–407

[14] H. Kettani, J. A. Gubner, A novel approach to the estimation of the Hurst parameter in self-similar traffic, Proceedings of the 27th Annual IEEE Conference on Local Computer Networks (LCN 2002), Tampa, Florida, 2002, 160–165

[15] J. M. Bardet, G. Lang, G. Oppenheim, A. Phillipe, S. Stoev, M. S. Taqqu, Semi-parametric estimation of the long-range dependence parameter: A survey, In: P. Doukhan, G. Oppenheim, M. S. Taqqu (eds.), Theory and Applications of Long-Range Dependence, Birkhauser, 2003, 557–577

[16] J. M. Bardet, G. Lang, G. Oppenheim, A. Phillipe, M. S. Taqqu, Generators of long-range dependent processes: A survey, In: P. Doukhan, G. Oppenheim, M. S. Taqqu (eds.), Theory and Applications of Long-Range Dependence, Birkhauser, 2003, 579–623

[17] C. Park, F. Godtliebsen, M. Taqqu, S. Stoev, J. S. Marron, Visualization and inference based on wavelet coeficients, SiZer, and SiNos, Computational Statistics and Data Analysis, 51 (**2007**), 5994–6012

[18] G. W. Wornell, A. V. Oppenheim, Estimation of fractal signals from noisy measurements using wavelets, IEEE Transactions on Signal Processing, 40 (**1992**), 611–623

[19] S. Stoev, V. Pipiras, M. S. Taqqu, Estimation of the self-similarity parameter in linear fractional stable motion, Signal Processing, 82 (**2002**), 1873–1901

UDK 678.7
Original scientific article/Izvirni znanstveni članek

ISSN 1580-2949
MTAEC9, 48(2)209(2014)

DESIGN OF A MICROBIAL SENSOR USING A CONDUCTING POLYMER OF POLYANILINE/POLY 4,4'-DIAMINODIPHENYL SULPHONE-SILVER NANOCOMPOSITE FILMS ON A CARBON PASTE ELECTRODE

OBLIKOVANJE MIKROBNEGA SENZORJA Z UPORABO PREVODNE POLIMERNE POLIANILINSKE/POLI 4,4'-DIAMINODIFENIL SULFONSKE SREBRNE NANOKOMPOZITNE TANKE PLASTI NA ELEKTRODI Z OGLJIKOVO PASTO

Meysam Sharifirad, Farhoush Kiani, Fardad Koohyar

Department of Chemistry, Faculty of Science, Ayatollah Amoli Branch, Islamic Azad University, Amol, Iran
f_koohyar@yahoo.com

Prejem rokopisa – received: 2012-11-03; sprejem za objavo – accepted for publication: 2013-06-07

A microbial biosensor based on Gluconobacter oxydans cells immobilized on a conducting polymer of polyaniline/Poly 4,4'-diaminodiphenyl sulphone-silver (PANI/PDDS/Ag) coated onto the surface of a carbon-paste electrode was constructed. The proposed biosensor was characterized using glucose as the substrate. Conducting polymers are electrochemically polymerized at the carbon-paste electrode substrates. The polymer films are modified by electrochemically depositing PANI/PDDS/Ag particles. The effect of changing the size of the Poly 4,4'-diaminodiphenyl sulphone-silver particles and the polymer film thickness on the voltammetric behaviour of the resulting hybrid material showed noticeable changes in the electrocatalytic current in an acid medium. The morphology of the polymer films and the distribution of the PDDS/Ag particles in the film were studied with scanning electron microscopy.

Keywords: polyaniline/Poly 4,4'-diaminodiphenyl sulphone-silver, conducting polymers, gluconobacter oxydans, voltammetric properties, nanoparticles

Konstruiran je bil mikrobni senzor na osnovi glukonobakterijskih oksidacijskih celic, pritrjenih na prevoden polimer iz polianilina/poli 4,4'-diaminodifenil sulfon–srebra (PANI/PDDS/Ag), nanesenega na površino elektrode z ogljikovo pasto. Predlagani senzor je bil karakteriziran z uporabo podlage iz glukoze. Prevodni polimeri so bili elektrokemijsko polimerizirani na elektrodo s podlago iz ogljikove paste. Polimerne tanke plasti so bile modificirane z elektrokemijskim nanosom PANI/PDDS/Ag-delcev. Spreminjanje velikosti poli 4,4'-diaminodifenil sulfonskih srebrnih delcev in debeline polimerne plasti je pokazalo občutne spremembe pri voltametričnem vedenju, rezultirajoči hibridni material pa je pokazal občutne spremembe elektrokatalitičnega toka v kislem mediju. Morfologija polimernih plasti in razporeditev PDDS/Ag-delcev v plasti sta bila pregledana na vrstičnem elektronskem mikroskopu.

Ključne besede: polianilin/poli 4,4'-diaminodifenil sulfon–srebro, prevodni polimeri, glukonobakterijski oksidant, voltametrične lastnosti, nanodelci

1 INTRODUCTION

Many types of microbial sensors have been developed as analytical tools. Such a microbial sensor consists of a transducer and a microbe as the sensing element. The characteristics of microbial sensors are in complete contrast to those of enzyme sensors or immunosensors, which are highly specific for the substrates of interest, although the specificity of the microbial sensor has been improved by genetic modifications of the microbe used as the sensing element. Microbial sensors have the advantages of a tolerance to the measuring conditions, a long lifetime, and cost performance, but they also have the disadvantage of a long response time.

Since their discovery in the mid-1970s, research on conducting polymers (CPs) has become an ever-growing research area in polymer chemistry.[1] The redox behaviour and an unusual combination of the properties of metals and plastics make conducting polymers a new class of materials.[2] The interest in conducting polymers is largely due to the wide range of possible applications due to their facile synthesis, good environmental stability and the long-term stability of the electrical conductivity. The advantage of using conducting polymers compared to more traditional sputtered metal coatings is that the polymer is soluble, enabling a non-destructive analysis of the specimens.[3] CPs were extensively studied in the past decade and used for technological applications in electrochromic devices,[4,5] gas-separation membranes,[6] enzyme immobilization[7] and have been featured in biotechnical applications since the very early days following their discovery. The biosensing approach using CPs has also been widely investigated in previous studies.[8]

There have been several attempts to produce nanoparticle polymer composites. Overall, we note four different approaches used to date. The first technique consists of the in-situ preparation of the nanoparticles in the polymer matrix. This is affected by a reduction of the metal salts dissolved in the polymer matrix.[9] The second technique involves polymerizing the matrix around the

nanoparticles.[10] The blending of pre-formed nanoparticles into pre-synthesized polymer can be considered as the third technique for the preparation of a nanoparticle polymer composite material.[11] The fourth process involves the in-situ synthesis of the composite material, with the metal nanoparticles being formed from an ionic precursor and the polymer being produced from the monomer. A major advantage of the latter method lies in the provision of a better particle-polymer interaction.[12]

Microbial cells are very promising for biosensor constructions due to them having several advantages: the enzyme does not need to be isolated, the enzymes are usually more stable in their natural environment in the cell, the co-enzymes and activators are already present in the system.[13] Cell-based biosensors are frequently used for a determination of the biological oxygen demand (BOD), the toxic agents and the assimilatable sugars as well as the selective detection of a single analyte.[14]

In this study different amounts of polymer nanocomposites aniline were examined for the detection of glucose and ethanol. The measurement was based on the respiratory activity of the cells. As well as the optimization and characterization, an application of the proposed system was carried out on real samples.

2 EXPERIMENTAL

2.1 Reagents

$LiClO_4$, $NaClO_4$, dialysis membrane, $AlCl_3$, succinyl chloride, benzene-1,4-diamine propionic acid, nitromethane, iron(III) chloride, propylene carbonate, poly(methylmethacrylate), dichloromethane, toluene, d-glucose, ethanol and gold colloidal were purchased from Sigma. Methanol and acetonitrile were purchased from Merck. All other chemicals were of analytical grade and purchased either from Merck or Sigma. The DDS were purchased from Merck, and silver nitrate from Alderich.

2.2 Apparatus

Scanning electron microscopy (SEM) images were taken using a VEGA HV (high potential) 1500 V at various magnifications. All the experiments were carried out in air atmosphere at room temperature (25 °C). A conventional three-electrode set up was employed for the CV studies. The counter electrode was a platinum sheet with a surface area of 2 cm^2. A SCE electrode was employed as the reference electrode. Electropolymerization and all other electrochemical studies were carried out using a Potentiostat/Galvanostat EG&G Model 263 A; USA well equipped with M 270 software.

2.3 Synthesis of the composite material

In a typical reaction, 0.8 g DDS was dissolved in a magnetically stirred 25 mL of methanol in a 50 mL conical flask. After complete dissolution, 100 mL dilute silver nitrate (10^{-1} mol dm^{-3}) was added drop wise. After the addition of the entire silver nitrate, the precipitated material collected at the bottom of the flask. This work accomplished for the solution of silver nitrate that the colloidal solutions were observed as milky coloured.

2.4 Cultivation of G. oxydans

The strain of *G. oxydans* was obtained from DSMZ and maintained on agar containing (g L^{-1}): d-glucose, 90; yeast extract, 15; calcium carbonate, 18; agar, 25.[15] The cell biomass was prepared by aerobic cultivation at 28 °C. Then, the cells were collected by centrifugation after reaching the late exponential phase and washed twice with 0.9 % sodium chloride solution containing $CaCl_2$ 2 mM. The biomass concentration was expressed as the weight matter determined by drying to a constant weight at 105 °C.

2.5 Microbial electrode method of making

Prior to the electropolymerization, graphite electrodes were polished on wet emery paper and washed thoroughly with distilled water, sonicated for 2–3 min, rinsed with bi-distilled water and dried at 105 °C. The electrochemical polymerization of DDS/Ag (1 mg/mL) was carried out by scanning the potential between -0.5 V and 0.8 V via cyclic voltammetry with the scan rate of 300 mV/s in $NaClO_4$ (0.2 M) and $LiClO_4$ (0.2 M)/acetonitrile medium. The concentration of the monomer was as for the polymerization of the DDS/Ag.

For the cells of bacteria to prove G. oxydans on electrode coated with polymer, first we spray it and leave the electrode surface to dry for 1 h. After the removal of unbound cells by washing with distilled water, the layer was covered with a dialysis membrane, pre-soaked in water. The membrane was fixed tightly with a silicone rubber O-ring. Daily-prepared electrodes with fresh cells were used in all the experimental steps, unless otherwise stated. Control experiments using carbon paste electrode were covered with bacterial cells and a polymer coating that was not.

2.6 Measurements

All the measurements were carried out at 30 °C under constant stirring. After each run, the electrode was washed with distilled water and kept in a phosphate buffer (pH 7) solution 50 mM at 30 °C for 7 min. The working buffer solution was renewed after each measurement. The microbial sensor was initially equilibrated in the buffer and then the substrate was added to the reaction cell. After 30 min the substrate was added to the reaction cell. The biosensor responses were registered as current densities by following the oxygen consumption at –0.7 V due to the metabolic activity of the bacterial cells in the presence of glucose.[16]

3 RESULTS AND DISCUSSION

Enzymes and cells have been used in biosensor construction for many decades. Both concepts have some advantages and challenges.[17] There have been various strategies to modify the microbial cells for applications in microbial biosensors. The principle of the bacterial biosensor is rather simple, and sensor productions only require the growth of the microorganisms. There are multiple strategies for how to use catalytic activities present in microbial cells ranging from using viable cells, non-viable cells, permeable cells, or membrane fractions. These cell-derived biocatalysts serve as an economical substitute for enzymes; an additional benefit for the biosensor performance is that the enzymes are still linked to the respiratory chain.

Since conducting polymers can act as transducers in biosensors and coating electrodes with CPs under mild conditions this opens up various possibilities for the immobilization of biomolecules and biosensing materials, the enhancement of their electrocatalytic properties, rapid electron transfer and direct communication. The co-immobilization of redox mediators or cofactors by entrapment within electropolymerized films or by covalent binding on the surface allows the simple fabrication of reagent-less biosensors.[18] The CPs have an organized molecular structure on different transducers, which allows them to function as a three-dimensional matrix for the biomolecule immobilization and preserve the activity for a long period. This property of the matrix with their functionality as a membrane has provided opportunities for sensor development. This process is reproducible with a high operational stability.[19] In this work the use of an electrochemically polymerized aniline/4,4'-diaminodiphenyl sulphone-silver as a microbial biosensing platform was examined for G. oxydans cells.

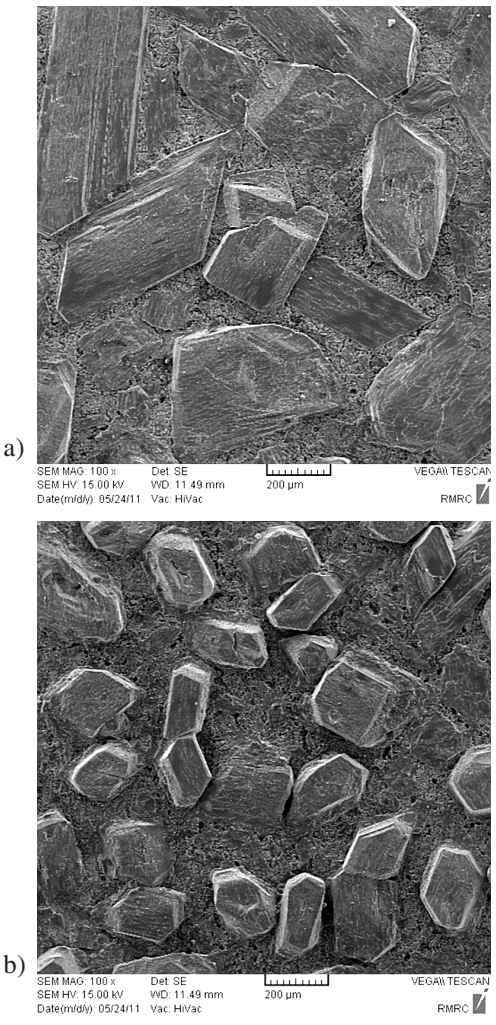

Figure 1: SEM images of bare graphite surface: a) PANI/PDDS/Ag polymer, b) bacteria-PANI/PDDS/Ag

Slika 1: SEM-posnetka gole površine grafita: a) polimer PANI/PDDS/Ag, b) bakterija PANI/PDDS/Ag

The morphologies of the bacterial sensing surfaces provide the most precise information about the cells and matrices used in the system. The scanning electron microscopy (SEM) technique is utilized to monitor the surface characteristics and shows the interaction between the biological materials and the immobilization matrices. The morphologies of bare graphite, and a polymeric matrix with and without cells were shown in **Figure 1**. Unbound cells were removed by washing the electrode surfaces several times before analysis. As seen from the micrographs, PANI/DDS/Ag provided an efficient immobilization platform with a compact structure for the cell immobilization. Hence, cells could be kept on the surface where higher sensor responses with high operational stabilities are obtained. The presence of amino groups in the structure may also contribute to attaching the micro-organisms on the matrix due to the ionic interactions between the cell surface and this functional group.

3.1 Effect of electropolymerization time

The most convenient electrochemical method employed for characterization is cyclic voltammetry. Cyclic voltammograms of bare graphite electrode carbon paste electrode (A), PDDS/Ag polymer (B), bacteria – PDDS/Ag (C), bacteria – PANI/PDDS/Ag (D) onto the graphite electrode are shown in **Figure 2**. The amount of conductive polymer on the electrode surface can be controlled by adjusting the polymerization time, which has a direct effect on the resulting current values. It has been previously reported that the microstructure of a conducting polythiophene film changes with an increase in the thickness. As the thickness depends on the deposition time, more and more defects such as voids and large molecule agglomerates could appear, causing degradation and an incompact microstructure of the films.[20] In order to observe the effect of electropolymerization time, aniline/4,4'-diaminodiphenyl sulphone-silver was polymerized onto the carbon paste surface for different periods ((5, 10 and 20) min, **Figure 3**), and then modified electrodes were used to form microbial biosen-

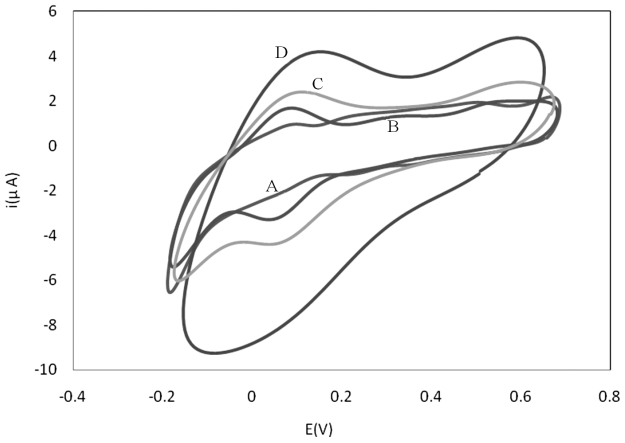

Figure 2: Cyclic voltammograms of bare carbon paste electrode (A), PDDS/Ag polymer (B), bacteria – PDDS/Ag (C), bacteria – PANI/PDDS/Ag (D) onto the graphite electrode (number of scans: 100, in potassium phosphate buffer (50 mM, pH 7))

Slika 2: Krožni voltamogrami elektrode z ogljikovo pasto (A), polimera PDDS/Ag (B), bakterije – PDDS/Ag (C), bakterije – PANI/PDDS/Ag (D) na grafitni elektrodi (število pregledovanj: 100, v kalij fosfatnem pufru (50 mM, pH 7))

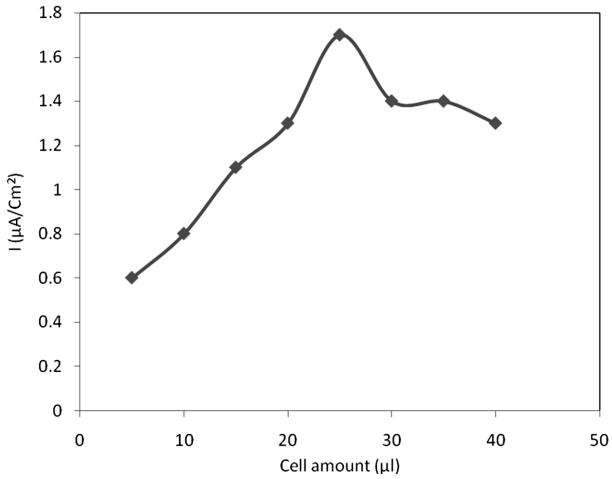

Figure 4: Effect of cell loading on the biosensor response (in potassium phosphate buffer (50 mM, pH 7), –0.7 V, 10 mM glucose)

Slika 4: Vpliv obremenitve celice na odziv biosenzorja (v kalijevem fosfatnem pufru (50 mM, pH 7), –0,7 V, glukoza 10 mM)

sors, as described in the experimental section. The best current values were obtained for 10 min of polymerization time. However, a decrease was observed when the polymerization time was higher. This could be due to the improper film structure related to the thickness after 10 min of the electropolymerization time for the cell immobilization.

3.2 Effect of cell amount

In order to determine the appropriate amount of cells, different biosensors containing (5, 10, 15, 20, 25, 30, 35 and 40) μL of bacterial cells were prepared. The highest current responses were obtained with the 25 μL of cells. When the 5 μL of cells was used the lowest current response was obtained. On the other hand, when the amount of cells was increased to 30 μL, a lower signal than that for 25 μL was obtained. This is an expected result and caused by the diffusion problem due to the high cell density. Since both amounts caused lower current values, further experiments were conducted using the 25 μL cell (**Figure 4**).

3.3 Effect of pH

The effect of pH on the microbial sensor based on PANI/PDDS/Ag was achieved by adjusting the pH between 6.0 and 8 when using phosphate buffer (50 mM). The response of the microbial sensor towards glucose (10 mM) at different pH values was shown in **Figure 5**. Since pH 7 has the maximum current response, it was chosen as the optimum pH and all the other experiments were conducted with this pH value.

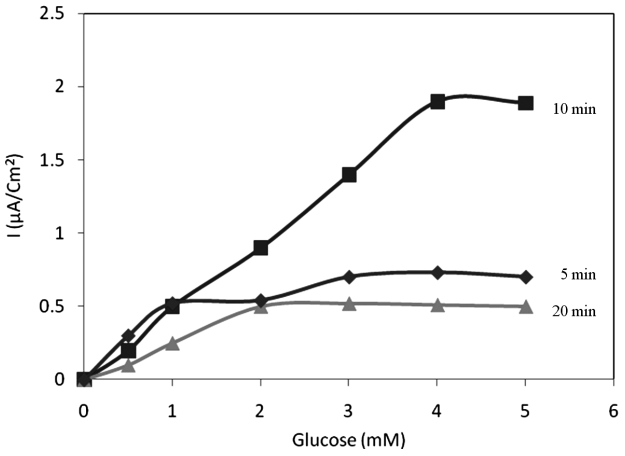

Figure 3: Effect of electropolymerization time on the biosensor response (in phosphate buffer, 50 mM, pH 7, 30 °C, –0.7 V)

Slika 3: Vpliv časa elektropolimerizacije na odzivnost biosenzorja (v fosfatnem pufru, 50 mM, pH 7, 30 °C, –0,7 V)

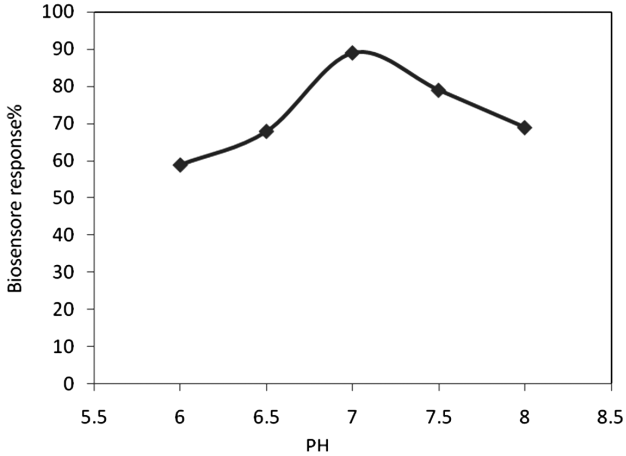

Figure 5: Effect of pH on the biosensor response (pH 6.0–8.0 phosphate buffer, 30 °C, –0.7 V)

Slika 5: Vpliv pH na odzivnost biosenzorja (pH 6,0–8,0 fosfatni pufer, 30 °C, –0,7 V)

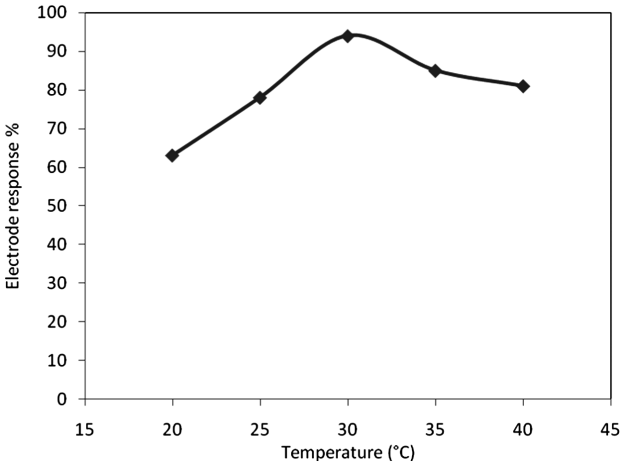

Figure 6: Effect of temperature on the electrode response for microbial biosensors (in potassium phosphate buffer, 50 mM, pH 7, –0.7 V)
Slika 6: Vpliv temperature na odzivnost elektrode pri osnovnem mikrobnem biosenzorju (v kalijevem fosfatnem pufru, 50 mM, pH 7, –0,7 V)

3.4 Effect of temperature

The amperometric response of the microbial sensors to glucose (50 mM) was followed at different temperatures, varying from 20 °C to 40 °C. From 20 °C to 25 °C an increase was observed up to 30 °C and then the signal started to decrease at 35 °C (**Figure 6**). As a result, the optimum temperature was found to be approximately 30 °C. And further experiments were conducted at this temperature.

3.5 Analytical characteristics

A microbial sensor was prepared, as described in the experimental part, to examine the analytical characteristics. The linear dynamic ranges and the equations were obtained based on optimized conditions. For the proposed system, a linear calibration graph **Figure 7** (A) was obtained for the current density versus the substrate concentration between 0.1 mM and 2.5 mM glucose. A linear relation was defined with the equation $y = 0.3116x$ ($R^2 = 0.9376$), where y is the sensor response in the current density (μA/cm^2) and x is the substrate concentration (mM).

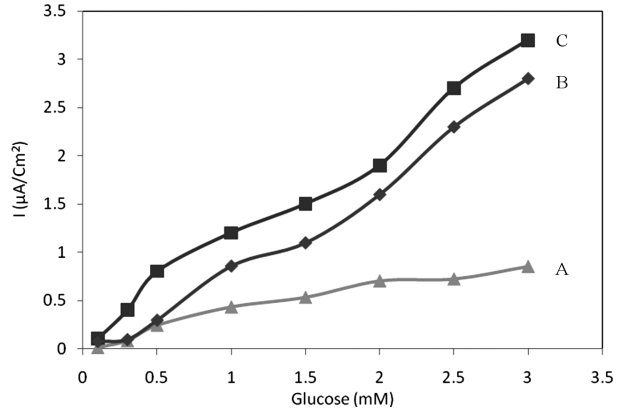

Figure 7: Calibration curves for three types of microbial biosensor including bacteria immobilized on the bare carbon paste electrode (A), PDDS/Ag polymer (B), PANI/PDDS/Ag (C) (in potassium phosphate buffer (50 mM, pH 6.5), –0.7 V)
Slika 7: Umeritvene krivulje za tri vrste mikrobnih biosenzorjev, vključno z bakterijami, pritrjenimi na elektrodi z ogljikovo pasto (A), polimer PDDS/Ag (B), PANI/PDDS/Ag (C) (v kalijevem fosfatnem pufru (50 mM, pH 6,5), –0,7 V)

Another type of electrode was covered using a polymer PDDS/silver and bacteria. It was previously reported that metal nanoparticles can display unique advantages, such as an enhancement of the mass transport, catalysis, a high effective surface area and control over the electrode microenvironment over macro-electrodes when used for electro-analysis. For instance, Pt and Au nanoparticles are very effective as matrices for enzyme sensors by taking advantage of the biocompatibility and large surface area. In our case, the calibration curve for the modified system based on silver nanoparticles was studied using the same method as described in the experimental section. However, these nanoparticles in polymer nanocomposites were a DDS. A linear relation for the glucose substrate was found between 0. 5 mM and 3 mM, as represented by the equation $y = 0.8774x$ ($R^2 = 0.9786$) and a response time of 120 s (**Figure 7** (B)). It is also possible that the high surface area due to the Ag on the polymer matrix provides the loading of the largest amount of cells, causing a larger biosensor response. The effects of different nanoparticles in terms of sensitivity and stability in microbial biosensing are now under investigation.

At the end of the calibration curve the carbon-paste electrode modified with bacteria and polymer PANI/DDS/Ag was observed (**Figure 7** (C)). The currents recorded were low in this case and irreproducible current responses were observed. A linear relation was observed in the range 0.1–3.0 mM glucose and defined by the equation $y = 1.056x$ ($R^2 = 0.9808$). This reveals that the polymer provides a good contact for the cells on the electrode surface where they can attach and survive during the operational conditions, as described in our previous study.

4 CONCLUSIONS

Conducting polymers that have an organized molecular structure can serve as proper and functional immobilizing platforms for biomolecules. These matrices provide a suitable environment for the immobilization and preserve the activity for long durations. In this paper a measurement method and environment for the bacteria and the PANI/DDS/Ag-modified electrode are described. The proposed system does not require any complicated immobilization procedure for the construction of a biosensor. The preparation is simple, cheap and is not time consuming. The biosensor showed a good linear range, a good repeatability and a high operational

stability. It can be concluded that the proposed system could also be a good alternative for BOD and toxicity estimation.

5 REFERENCES

[1] G. G. Wallace, G. M. Spinks, L. A. P. Kane-Maguire, P. R. Teasdale, Conductive Electroactive Polymers: Intelligent Materials Systems, 2th edn, CRC, London 2003, 8–10

[2] D. Kumar, R. C. Sharma, Eur. Polym. J., 34 (**1998**) 8, 1053–1060

[3] M. Angelopoulos, J. M. Shaw, M. A. Lecorre, M. Tissier, Microelectron. Eng., 13 (**1991**), 515–518

[4] E. Sahin, P. Camurlu, L. Toppare, V. M. Mercore, I. Cianga, Y. Yagci, J. Electroanal. Chem., 79 (**2005**) 2, 189–197

[5] U. H. Yildiz, E. Sahin, I. M. Akhmedov, C. Tanyeli, L. Toppare, J. Polym. Sci. Pol. Chem., 44 (**2006**) 7, 2215–2225

[6] R. Martin, W. Liang, V. Menon, R. Parthasarathy, A. Parthasarathy, Synth. Met., 55 (**1993**), 3766–3773

[7] S. Tuncagil, S. Kiralp, S. Varis, L. Toppare, Reac. Func. Poly., 68 (**2008**), 710–717

[8] T. A. Skotheim, R. Elsenbaumer, J. R. Reynolds, Handbook of Conducting Polymer, 2nd edn, Marcel Dekker, New York 1997, 963–991 (chapter 34)

[9] R. Lapuente, F. Cases, P. Garces, E. Morallon, J. L. Vazquez, J. Electroanal. Chem., 451 (**1998**), 163–171

[10] S. J. Xu, L. M. Li, Z. F. Du, L. H. Tang, Y. Wang, T. H. Wang, J. H. Li, Electrochem. Commun., 11 (**2009**), 327–330

[11] F. Patolsky, Y. Weizmann, O. Lioubashevski, I. Willner, Angew. Chem. Int. Ed., 41 (**2002**), 2323–2327

[12] M. Mertig, L. C. Ciacchi, R. Seidel, W. Pompe, Nano Lett., 2 (**2002**), 841–844

[13] Z. X. Deng, C. D. Mao, Nano Lett., 3 (**2003**), 1545–1548

[14] C. Schonenberger, B. M. I. Van der Zande, L. G. J. Fokkink, M. Henny, C. Schmid, M. Kruger, J. Phys. Chem B., 101 (**1997**), 5497–505

[15] J. Tkac, P. Gemeiner, J. S. Vitel, T. Benikovsky, E. Sturdik, V. Vala, L. Petrus, E. Hrabarova, Anal. Chim. Acta., 420 (**2000**), 1 –7

[16] D. Odaci, S. K. Kayahan, S. Timur, L. Toppare, Electrochim. Acta., 53 (**2008**), 4104–4108

[17] D. Odaci, S. Timur, A. Telefoncu, Sensors and Actuators B: Chemical., 134 (**2008**), 89–94

[18] S. Timur, U. Anik, D. Odaci, L. Gorton, Electrochem. Commun., 9 (**2007**), 1810–1815

[19] J. Tkac, J. W. Whittaker, T. Ruzgas, Biosens. Bioelectron., 22 (**2007**), 1820–1824

[20] M. Gerard, A. Chaubey, B. D. Malhotra, Biosens. Bioelectron., 17 (**2002**), 345–359

UDK 54
Original scientific article/Izvirni znanstveni članek

ISSN 1580-2949
MTAEC9, 48(2)215(2014)

A NEW GENERALIZED ALGEBRA FOR THE BALANCING OF א CHEMICAL REACTIONS

NOVA POSPLOŠENA ALGEBRA ZA URAVNOTEŽENJE KEMIJSKIH REAKCIJ א

Ice B. Risteski

2 Milepost Place # 606, Toronto, Ontario, Canada M4H 1C7
ice@scientist.com

Prejem rokopisa – received: 2012-12-01; sprejem za objavo – accepted for publication: 2013-07-15

In this article we develop a new generalized algebra for the balancing of א chemical reactions. This is a completely new approach to the balancing of these kinds of chemical reactions that is based on an understanding of reaction analysis and the elementary theory of inequalities. The generators of the reaction determined all the interactions among the stoichiometric coefficients.

Keywords: א chemical reactions, generalized algebra, balancing reactions

V tem članku smo razvili novo posplošeno algebro za uravnoteženje kemijskih reakcij. To je popolnoma nov način uravnoteženja kemijskih reakcij, ki temelji na navidezni analizi reakcij in elementarni teoriji neenakosti. Generatorji reakcij določajo vse interakcije med stehiometričnimi koeficienti.

Ključne besede: kemijske reakcije א, posplošena algebra, uravnoteženje reakcij

1 INTRODUCTION

Since the balancing of chemical reactions in chemistry is a basic and fundamental issue it deserves to be considered on a satisfactory level. This topic always draws the attention of students and teachers, but it is never a finished product. Because of its importance in chemistry and mathematics, there are several articles devoted to the subject. However, here we will not provide a historical perspective about this topic, because it has been done in so many previous publications. We can, however, still provide a full balancing of chemical reactions with the use of a generalized algebra.

In mathematics and chemistry there are several mathematical methods for balancing chemical reactions.[1–7] All of them are based on generalized matrix inverses and they have formal scientific properties that need a higher level of mathematical knowledge for their application. The so-called *chemical methods* are paradoxical and out of order.[8]

The newest approach for balancing א reactions is developed in[9]. The present article is a prolongation of the previous research.[9,10]

Generally speaking, balancing a chemical reaction that possesses atoms with fractional oxidation numbers is a tough problem in chemistry. It is really hard for reactions that have only one set of coefficients, but for א reactions that have an infinite number of sets of coefficients, this problem is extremely hard.[11,12]

In the next section we shall consider three general reactions of oxidation. They are examples of *elementary* א reactions, which possess atoms with fractional and integer oxidation numbers. Actually, we balanced three general א reactions with one, two and three arbitrary elements. The first reaction plays a very important role in metallurgy. For instance, this reaction is a basic reaction in the theory of metal corrosion, ferrous metallurgy as well as the theory of metallurgical processes, but unfortunately it was not taken into account until today. The main reason why this reaction was neglected lies in its balancing. This article will provide its full balancing, which is neither easy nor simple.

2 MAIN RESULTS

Now we shall consider the announced א reactions.

Reaction 1. Let us consider this general א reaction with one arbitrary element:

$$x_1\,\mathrm{X} + x_2\,\mathrm{O_2} \rightarrow x_3\,\mathrm{X_{0.987}O} + x_4\,\mathrm{X_2O_3} + x_5\,\mathrm{X_3O_4} \quad (1)$$

The above chemical reaction (1) reduces to the following system of linear equations:

$$\begin{aligned} x_1 &= 0.987x_3 + 2x_4 + 3x_5, \\ 2x_2 &= x_3 + 3x_4 + 4x_5 \end{aligned} \quad (2)$$

Since the system (2) has two linear equations and five unknowns, we can solve it in 5!/[2!(5 – 2)!] = 10 ways. Actually, we shall determine all the possible general solutions of the system (2). They are the following pairs: (x_1, x_2), (x_1, x_3), (x_1, x_4), (x_1, x_5), (x_2, x_3), (x_2, x_4), (x_2, x_5), (x_3, x_4), (x_3, x_5) and (x_4, x_5).

1° Let x_3, x_4 and x_5 be arbitrary real numbers, then the general solution of the system (2) is:

$$x_1 = 0.987x_3 + 2x_4 + 3x_5,$$
$$x_2 = x_3/2 + 3x_4/2 + 2x_5 \quad (3)$$

After the substitution of (3) into (1), the balanced reaction takes on this general form:

$$(0.987x_3 + 2x_4 + 3x_5)\ \mathbf{X} + (x_3/2 + 3x_4/2 + 2x_5)\ \mathbf{O}_2 \rightarrow x_3\ \mathbf{X}_{0.987}\mathbf{O} + x_4\ \mathbf{X}_2\mathbf{O}_3 + x_5\ \mathbf{X}_3\mathbf{O}_4, \quad \forall\ x_3, x_4, x_5 \in \Re. \quad (4)$$

This means that by finding the coefficients of the products we find the coefficients of the reactants.

2° Assume x_2, x_4 and x_5 are arbitrary real numbers, then the general solution of the system (2) is:

$$x_1 = 1.977x_2 - 0.961x_4 - 0.948x_5,$$
$$x_3 = 2x_2 - 3x_4 - 4x_5 \quad (5)$$

The balanced reaction (1) obtains this general form:

$$(1.977x_2 - 0.961x_4 - 0.948x_5)\ \mathbf{X} + x_2\ \mathbf{O}_2 \rightarrow (2x_2 - 3x_4 - 4x_5)\ \mathbf{X}_{0.987}\mathbf{O} + x_4\ \mathbf{X}_2\mathbf{O}_3 + x_5\ \mathbf{X}_3\mathbf{O}_4 \quad (6)$$

Since the generators (5) are positive, it should immediately follow these inequalities:

$$1.977x_2 - 0.961x_4 - 0.948x_5 > 0,$$
$$2x_2 - 3x_4 - 4x_5 > 0 \quad (7)$$

From (7) we obtain the inequality:

$$x_2 > 1.5x_4 + 2x_5 \quad (8)$$

The expression (8) is a necessary and sufficient condition for a general reaction (6) to hold. In other words, the reaction is possible if and only if the condition (8) is satisfied.

3° Suppose x_2, x_3 and x_5 are arbitrary real numbers. The general solution of the system (2) is:

$$x_1 = 4x_2/3 + 0.961x_3/3 + x_5/3,$$
$$x_4 = 2x_2/3 - x_3/3 - 4x_5/3 \quad (9)$$

If we substitute (9) into (1), the general form of the balanced reaction is:

$$(4x_2/3 + 0.961x_3/3 + x_5/3)\ \mathbf{X} + x_2\ \mathbf{O}_2 \rightarrow x_3\ \mathbf{X}_{0.987}\mathbf{O} + (2x_2/3 - x_3/3 - 4x_5/3)\ \mathbf{X}_2\mathbf{O}_3 + x_5\ \mathbf{X}_3\mathbf{O}_4 \quad (10)$$

Since the generator $x_4 > 0$, it should immediately follow that:

$$x_2 > 0.5x_3 + 2x_5 \quad (11)$$

The reaction (10) is possible if and only if the condition (11) is satisfied. The inequality (11) is a necessary and sufficient condition to hold (10).

4° Let x_2, x_3 and x_4 be arbitrary real numbers. The general solution of the system (2) is:

$$x_1 = 3x_2/2 + 0.948x_3/4 - x_4/4,$$
$$x_5 = x_2/2 - x_3/4 - 3x_4/4 \quad (12)$$

After the substitution of (12) into (1), the general chemical reaction takes on this form:

$$(3x_2/2 + 0.948x_3/4 - x_4/4)\ \mathbf{X} + x_2\ \mathbf{O}_2 \rightarrow x_3\ \mathbf{X}_{0.987}\mathbf{O} + x_4\ \mathbf{X}_2\mathbf{O}_3 + (x_2/2 - x_3/4 - 3x_4/4)\ \mathbf{X}_3\mathbf{O}_4 \quad (13)$$

Since the generators x_1, $x_5 > 0$, then it must be:

$$3x_2/2 + 0.948x_3/4 - x_4/4 > 0,$$
$$x_2/2 - x_3/4 - 3x_4/4 > 0 \quad (14)$$

After (14) it immediately follows that:

$$x_2 > x_3/2 + 3x_4/2 \quad (15)$$

The inequality (15) is a necessary and sufficient condition to hold the general reaction (13), *i.e.*, the reaction (13) holds if and only if (15) is satisfied.

5° Suppose x_1, x_4 and x_5 are arbitrary real numbers. The general solution of the system (2) is:

$$x_2 = x_1/1.974 + 0.961x_4/1.974 + 0.948x_5/1.974,$$
$$x_3 = x_1/0.987 - 2x_4/0.987 - 3x_5/0.987 \quad (16)$$

The balanced chemical reaction (1) obtains this general form:

$$x_1\ \mathbf{X} + (x_1/1.974 + 0.961x_4/1.974 + 0.948x_5/1.974)\ \mathbf{O}_2 \rightarrow (x_1/0.987 - 2x_4/0.987 - 3x_5/0.987)\ \mathbf{X}_{0.987}\mathbf{O} + x_4\ \mathbf{X}_2\mathbf{O}_3 + x_5\ \mathbf{X}_3\mathbf{O}_4 \quad (17)$$

Since the generator $x_3 > 0$, then it must be:

$$x_1 > 2x_4 + 3x_5 \quad (18)$$

The above inequality (18) is a necessary and sufficient condition to hold (17), *i.e.*, the reaction (17) holds if and only if (18) is satisfied.

6° Assume x_1, x_3 and x_5 are arbitrary real numbers. The general solution of the system (2) is:

$$x_2 = 3x_1/4 - 0.961x_3/4 - x_5/4,$$
$$x_4 = x_1/2 - 0.987x_3/2 - 3x_5/2 \quad (19)$$

The balanced chemical reaction (1) has this general form:

$$x_1\ \mathbf{X} + (3x_1/4 - 0.961x_3/4 - x_5/4)\ \mathbf{O}_2 \rightarrow x_3\ \mathbf{X}_{0.987}\mathbf{O} + (x_1/2 - 0.987x_3/2 - 3x_5/2)\ \mathbf{X}_2\mathbf{O}_3 + x_5\ \mathbf{X}_3\mathbf{O}_4 \quad (20)$$

Since the generators x_2, $x_4 > 0$, then it must be that:

$$3x_1 - 0.961x_3 - x_5 > 0,$$
$$x_1 - 0.987x_3 - 3x_5 > 0 \quad (21)$$

From (21) we obtain:

$$x_1 > 0.987x_3 + 3x_5 \quad (22)$$

The above expression (22) is a necessary and sufficient condition to hold the general reaction (20), *i.e.*, the reaction (20) holds if and only if (22) is satisfied.

7° Assume x_1, x_3 and x_4 are arbitrary real numbers. The general solution of the system (2) is:

$$x_2 = 2x_1/3 - 0.474x_3/3 + x_4/6,$$
$$x_5 = x_1/3 - 0.987x_3/3 - 2x_4/3 \quad (23)$$

The balanced chemical reaction (1) has this general form:

$$x_1\ \mathbf{X} + (2x_1/3 - 0.474x_3/3 + x_4/6)\ \mathbf{O}_2 \rightarrow x_3\ \mathbf{X}_{0.987}\mathbf{O} + x_4\ \mathbf{X}_2\mathbf{O}_3 + (x_1/3 - 0.987x_3/3 - 2x_4/3)\ \mathbf{X}_3\mathbf{O}_4 \quad (24)$$

Since the generators x_2, $x_5 > 0$, then these inequalities should follow:

$$4x_1 - 0.948x_3 + x_4 > 0,$$
$$x_1 - 0.987x_3 - 2x_4 > 0 \quad (25)$$

From (25) we obtain:

$$x_1 > 0.987x_3 + 2x_4 \quad (26)$$

The inequality (26) is a necessary and sufficient condition to hold the general reaction (24), *i.e.*, the reaction (24) holds if and only if (26) is satisfied.

8° Let us assume x_1, x_2 and x_5 are arbitrary real numbers. The general solution of the system (2) is:

$$x_3 = 3x_1/0.961 - 4x_2/0.961 - x_5/0.961,$$
$$x_4 = -x_1/0.961 + 1.974x_2/0.961 - 0.948x_5/0.961 \quad (27)$$

After the substitution of (27) into (1), the general chemical reaction obtains this form:

$$x_1\,\mathbf{X} + x_2\,\mathbf{O}_2 \rightarrow (3x_1/0.961 - 4x_2/0.961 - x_5/0.961)\,\mathbf{X}_{0.987}\mathbf{O} + (-x_1/0.961 + 1.974x_2/0.961 - 0.948x_5/0.961)\,\mathbf{X}_2\mathbf{O}_3 + x_5\,\mathbf{X}_3\mathbf{O}_4 \quad (28)$$

Since the generators x_3, $x_4 > 0$, then these inequalities should follow:

$$3x_1 - 4x_2 - x_5 > 0,$$
$$-x_1 + 1.974x_2 - 0.948x_5 > 0 \quad (29)$$

From (29) we obtain:

$$4x_2/3 + x_5/3 < x_1 < 1.974x_2 - 0.948x_5,$$
$$x_2 > 2x_5 \quad (30)$$

The inequalities (30) are necessary and sufficient conditions to hold the general reaction (28). In other words, the reaction (28) holds if and only if (30) are satisfied.

9° Suppose x_1, x_2 and x_4 are arbitrary real numbers. The general solution of the system (2) is:

$$x_3 = 4x_1/0.948 - 6x_2/0.948 + x_4/0.948,$$
$$x_5 = -x_1/0.948 + 1.974x_2/0.948 - 0.961x_4/0.948 \quad (31)$$

The balanced chemical reaction (1) has this general form:

$$x_1\,\mathbf{X} + x_2\,\mathbf{O}_2 \rightarrow (4x_1/0.948 - 6x_2/0.948 - x_4/0.948)\,\mathbf{X}_{0.987}\mathbf{O} + x_4\,\mathrm{X}_2\mathbf{O}_3 + (-x_1/0.948 + 1.974x_2/0.948 - 0.961x_4/0.948)\,\mathbf{X}_3\mathbf{O}_4 \quad (32)$$

Since the generators x_3, $x_5 > 0$, then these inequalities should follow:

$$4x_1 - 6x_2 - x_4 > 0,$$
$$-x_1 + 1.974x_2 - 0.961x_4 > 0 \quad (33)$$

From (33) we obtain:

$$3x_2/2 - x_4/4 < x_1 < 1.974x_2 - 0.961x_4,$$
$$x_2 > 3x_4/2 \quad (34)$$

The inequalities (34) are necessary and sufficient conditions to hold the general reaction (32), *i.e.*, the reaction (32) holds if and only if (34) are satisfied.

10° Let us assume x_1, x_2 and x_3 are arbitrary real numbers. The general solution of the system (2) is:

$$x_4 = -4x_1 + 6x_2 + 0.948x_3,$$
$$x_5 = 3x_1 - 4x_2 - 0.961x_3 \quad (35)$$

The balanced chemical reaction (1) has this general form:

$$x_1\,\mathbf{X} + x_2\,\mathbf{O}_2 \rightarrow x_3\,\mathbf{X}_{0.987}\mathbf{O} + (-4x_1 + 6x_2 + 0.948x_3)\,\mathbf{X}_2\mathbf{O}_3 + (3x_1 - 4x_2 - 0.961x_3)\,\mathbf{X}_3\mathbf{O}_4 \quad (36)$$

Since the generators x_4, $x_5 > 0$, then follow these inequalities:

$$-4x_1 + 6x_2 + 0.948x_3 > 0,$$
$$3x_1 - 4x_2 - 0.961x_3 > 0 \quad (37)$$

From (37) we obtain:

$$4x_2/3 + 0.961x_3/3 < x_1 < 3x_2/2 + 0.474x_3/2,$$
$$x_2 > x_3/2 \quad (38)$$

The inequalities (38) are necessary and sufficient conditions to hold the general reaction (36), *i.e.*, the reaction (36) holds if and only if (38) are satisfied.

Example 1. For instance, if we substitute **X** = Fe, Mn, Pb in (1), we immediately obtain three sub-particular ℵ balanced reactions.

Next, we shall consider the following two ℵ reactions.

Reaction 2. Let us balance this general ℵ reaction with two arbitrary elements:

$$x_1\,\mathbf{X}_2 + x_2\,\mathbf{Y}_2 + x_3\,\mathbf{O}_2 \rightarrow x_4\,\mathbf{XYO} + x_5\,\mathbf{XYO}_2 + x_6\,\mathbf{XYO}_3 \quad (39)$$

The above chemical reaction (39) reduces to the following system of linear equations:

$$2x_1 = x_4 + x_5 + x_6,$$
$$2x_2 = x_4 + x_5 + x_6,$$
$$2x_3 = x_4 + 2x_5 + 3x_6 \quad (40)$$

Since the system (40) has three linear equations and six unknowns, we can solve it in 6!/[3!(6 – 3)!] = 20 ways. Actually, we must determine all the possible general solutions of the system (40). They are the following triads: (x_1, x_2, x_3), (x_1, x_2, x_4), (x_1, x_2, x_5), (x_1, x_2, x_6), (x_1, x_3, x_4), (x_1, x_3, x_5), (x_1, x_3, x_6), (x_1, x_4, x_5), (x_1, x_4, x_6), (x_1, x_5, x_6), (x_2, x_3, x_4), (x_2, x_3, x_5), (x_2, x_3, x_6), (x_2, x_4, x_5), (x_2, x_4, x_6), (x_2, x_5, x_6), (x_3, x_4, x_5), (x_3, x_4, x_6), (x_3, x_5, x_6) and (x_4, x_5, x_6).

Since the size of our article is limited, we shall determine only one general solution of the system (40). It is the solution (x_1, x_2, x_3).

1° Let x_4, x_5 and x_6 be arbitrary real numbers, then the general solution of the system (40) is:

$$x_1 = x_2 = (x_4 + x_5 + x_6)/2,$$
$$x_3 = (x_4 + 2x_5 + 3x_6)/2 \quad (41)$$

After the substitution of (41) into (39), the balanced reaction obtains this general form:

$$[(x_4 + x_5 + x_6)/2]\,\mathbf{X}_2 + [(x_4 + x_5 + x_6)/2]\,\mathbf{Y}_2 + [(x_4 + 2x_5 + 3x_6)/2]\,\mathbf{O}_2 \rightarrow x_4\,\mathbf{XYO} + x_5\,\mathbf{XYO}_2 + x_6\,\mathbf{XYO}_3 \quad (42)$$

$$\forall\, x_4, x_5, x_6 \in \Re\ .$$

For reaction (39) to be fully balanced, the remaining 19 triads must be determined.

Example 2. For **X** = H and **Y** = Cl, we obtain a sub-particular reaction.

Reaction 3. Now we shall balance this general א reaction with three arbitrary elements:

$$x_1\ \mathbf{XY}_2 + x_2\ \mathbf{Z} \rightarrow x_3\ \mathbf{XY} + x_4\ \mathbf{X}_2\mathbf{Y}_3 + x_5\ \mathbf{X}_3\mathbf{Y}_4 + x_6\ \mathbf{X}_3\mathbf{Z} + x_7\ \mathbf{ZY} + x_8\ \mathbf{ZY}_2 \qquad (43)$$

The above chemical reaction (43) reduces to the following system of linear equations:

$$\begin{gathered} x_1 = x_3 + 2x_4 + 3x_5 + 3x_6, \\ 2x_1 = x_3 + 3x_4 + 4x_5 + x_7 + 2x_8, \\ x_2 = x_6 + x_7 + x_8 \end{gathered} \qquad (44)$$

Since the system (44) has three linear equations and eight unknowns, we can solve it in $8!/[3!(8-3)!] = 56$ ways. Actually, we must determine all the possible general solutions of the system (44). They are the following triads: (x_1, x_2, x_3), (x_1, x_2, x_4), (x_1, x_2, x_5), (x_1, x_2, x_6), (x_1, x_2, x_7), (x_1, x_2, x_8), (x_1, x_3, x_4), (x_1, x_3, x_5), (x_1, x_3, x_6), (x_1, x_3, x_7), (x_1, x_3, x_8), (x_1, x_4, x_5), (x_1, x_4, x_6), (x_1, x_4, x_7), (x_1, x_4, x_8), (x_1, x_5, x_6), (x_1, x_5, x_7), (x_1, x_5, x_8), (x_1, x_6, x_7), (x_1, x_6, x_8), (x_1, x_7, x_8), (x_2, x_3, x_4), (x_2, x_3, x_5), (x_2, x_3, x_6), (x_2, x_3, x_7), (x_2, x_3, x_8), (x_2, x_4, x_5), (x_2, x_4, x_6), (x_2, x_4, x_7), (x_2, x_4, x_8), (x_2, x_5, x_6), (x_2, x_5, x_7), (x_2, x_5, x_8), (x_2, x_6, x_7), (x_2, x_6, x_8), (x_2, x_7, x_8), (x_3, x_4, x_5), (x_3, x_4, x_6), (x_3, x_4, x_7), (x_3, x_4, x_8), (x_3, x_5, x_6), (x_3, x_5, x_7), (x_3, x_5, x_8), (x_3, x_6, x_7), (x_3, x_6, x_8), (x_3, x_7, x_8), (x_4, x_5, x_6), (x_4, x_5, x_7), (x_4, x_5, x_8), (x_4, x_6, x_7), (x_4, x_6, x_8), (x_4, x_7, x_8), (x_5, x_6, x_7), (x_5, x_6, x_8), (x_5, x_7, x_8) and (x_6, x_7, x_8).

As we mentioned previously, the size of the article is limited, and so we shall determine only one general solution for the system (44). It is the solution (x_1, x_2, x_3).

1° Let us assume x_4, x_5, x_6, x_7 and x_8 are arbitrary real numbers, then the general solution of the system (44) is:

$$\begin{gathered} x_1 = x_4 + x_5 - 3x_6 + x_7 + 2x_8, \\ x_2 = x_6 + x_7 + x_8, \\ x_3 = -x_4 - 2x_5 - 6x_6 + x_7 + 2x_8 \end{gathered} \qquad (45)$$

After the substitution of (45) into (43), the balanced reaction obtains this general form:

$$(x_4 + x_5 - 3x_6 + x_7 + 2x_8)\ \mathbf{XY}_2 + (x_6 + x_7 + x_8)\ \mathbf{Z} \rightarrow (-x_4 - 2x_5 - 6x_6 + x_7 + 2x_8)\ \mathbf{XY} + x_4\ \mathbf{X}_2\mathbf{Y}_3 + x_5\ \mathbf{X}_3\mathbf{Y}_4 + x_6\ \mathbf{X}_3\mathbf{Z} + x_7\ \mathbf{ZY} + x_8\ \mathbf{ZY}_2 \qquad (46)$$

Since the generators x_1, $x_3 > 0$, these inequalities should immediately follow:

$$\begin{gathered} x_4 + x_5 - 3x_6 + x_7 + 2x_8 > 0, \\ -x_4 - 2x_5 - 6x_6 + x_7 + 2x_8 > 0 \end{gathered} \qquad (47)$$

From (47) we obtain:

$$x_7 + 2x_8 > x_4 + 2x_5 + 6x_6 \qquad (48)$$

The above inequality (48) is a necessary and sufficient condition to hold the general reaction (46), *i.e.*, the reaction (46) holds if and only if (48) is satisfied.

For reaction (43) to be fully balanced the remaining 55 triads must be determined.

Example 3. For X = Mn ∨ Fe, Y = O, and Z = C we obtain a sub-particular reaction.

3 DISCUSSION

The א chemical reactions are a special kind of reactions that have non-unique coefficients. In chemistry, until now, they were balanced like a reaction with an infinite number of coefficients, which is incorrect. Every א reaction has $n!/[k!(n-k)!]$ general reactions, where n is the number of reaction molecules and k is the number of reaction elements. Each of these general reactions has an infinite number of sets of coefficients. In other words, every א reaction reduces to $n!/[k!(n-k)!]$ general reactions with an infinite number of particular sub-reactions for each of them.

In this article we determined all the general reactions of the reaction (1), which are given by the expressions (4), (6), (10), (13), (17), (20), (24), (28), (32) and (36). Also, for all of them we determined the necessary and sufficient conditions for which they hold. In three examples we showed that this approach to the balancing of א reactions works successfully. We would also like to mention that the examples 1, 2 and 3 are derived sub-particular reactions, which are not fully balanced. The readers can derive the other general solutions very easily, because they are similar to those of reaction (1), which we derived using the technique of generalized algebra.

4 CONCLUSION

In this article three א general chemical reactions are balanced. All the chemical reactions looked similar to *elementary* molecular reactions, but they were very hard to balance. Using this method of generalized algebra, the author proved again that balancing chemical reactions does not have anything to do with chemistry – it is a purely mathematical issue.

The strengths of the method of generalized algebra are:

1. This method provides an alternative approach for balancing א chemical reactions. This method showed that matrix methods can be substituted by the method of generalized algebra.
2. Since this method of generalized algebra is well formalized, it belongs to the class of consistent methods for balancing chemical reactions.
3. This method of generalized algebra showed that for any א chemical reaction a topology of its solutions can be introduced.
4. In fact, the offered method of generalized algebra simplifies the mathematical operations provided by the previous well-known matrix methods and is very suitable for daily practice. The method of generalized algebra has this advantage, because it fits for all א

chemical reactions, which previously were only balanced by the methods of generalized matrix inverses.

5. For a determination of general reactions any method for the solution of a system of linear equations can be used.
6. Using this method the general forms of the balanced chemical reactions are determined much faster than by other matrix methods.
7. From the general balanced reactions the other particular and sub-particular reactions can be determined.
8. Using the method of generalized algebra the dimension of the solution space can be determined.
9. Using this method the basis of the solution space can be determined.
10. Necessary and sufficient conditions for which some reaction holds can be determined by this method as well. These conditions determine the possibility of the reaction interval.
11. This method gives an opportunity to be extended with other numerical calculations necessary for ℵ reactions.
12. The method of generalized algebra represents a good basis for building a software package.

The weak sides of the method are:

1. Using this method the minimal reaction coefficients cannot be determined.
2. This method cannot recognize when a chemical reaction reduces to one generator reaction.
3. It cannot predict quantitative relations among the reaction coefficients.
4. This method cannot arrange the molecules' disposition.
5. The method of generalized algebra cannot predict reaction stability.

This method opens doors in chemistry and mathematics for new research on ℵ chemical reactions, which unfortunately today cannot be balanced using a computer, because there is not such a method. The method of generalized algebra creates a large challenge for researchers to extend and adapt its usage for computer application. This is not an easy and simple job, but it deserves to be realized as soon as possible.

5 REFERENCES

[1] I. B. Risteski, The new algebraic criterions to even out the chemical reactions, In: 22nd October Meeting of Miners & Metallurgists: Collection of Papers, Institute of Copper Bor & Technical Faculty Bor, Bor, 1990, 313–318

[2] I. B. Risteski, A new approach to balancing chemical equations, SIAM Problems & Solutions, 2007, 1–10

[3] I. B. Risteski, A new nonsingular matrix method for balancing chemical equations and their stability, Internat. J. Math. Manuscripts, 1 (**2007**), 180–205

[4] I. B. Risteski, A new pseudoinverse matrix method for balancing chemical equations and thier stability, J. Korean Chem. Soc., 52 (**2008**), 223–238

[5] I. B. Risteski, A new generalized matrix inverse method for balancing chemical equations and their stability, Bol. Soc. Quím. México, 2 (**2008**), 104–115

[6] I. B. Risteski, A new singular matrix method for balancing chemical equations and their stability, J. Chinese Chem. Soc., 56 (**2009**), 65–79

[7] I. B. Risteski, A new complex vector method for balancing chemical equations, Mater. Tehnol., 44 (**2010**) 4, 193–203

[8] I. B. Risteski, New discovered paradoxes in theory of balancing chemical reactions, Mater. Tehnol., 45 (**2011**) 6, 503–522

[9] I. B. Risteski, A new algebra for balancing special chemical reactions, Chemistry: Bulg. J. Sci. Educ., 21 (**2012**), 223–234

[10] I. B. Risteski, A new formal geometrical method for balancing continuum class of chemical reactions, Chemistry: Bulg. J. Sci. Educ., 21 (**2012**), 708–725

[11] I. B. Risteski, New very hard problems of balancing chemical reactions, Chemistry: Bulg. J. Sci. Educ., 21 (**2012**), 574–580

[12] I. B. Risteski, A new topology of solutions of chemical equations, J. Korean Chem. Soc., 57 (**2013**), 176–203

UDK 621.793
Original scientific article/Izvirni znanstveni članek

ISSN 1580-2949
MTAEC9, 48(2)221(2014)

ELECTRODEPOSITION AND CHARACTERIZATION OF Cu-Zn ALLOY FILMS OBTAINED FROM A SULFATE BATH

ELEKTRONANOS IN KARAKTERIZACIJA PLASTI ZLITIN Cu-Zn, NASTALIH IZ SULFATNE KOPELI

Abdelouahab Redjechta[1], Kzmel Loucif[1], Loubna Mentar[2], Mohamed Redha Khelladi[2], Abdelkrim Beniaiche[3]

[1]Laboratoire des Matériaux Non Métalliques, Institut d'Optique et Mécanique de Précision, Université Ferhat Abbas-Sétif 1, 19000 Sétif, Algeria
[2]Laboratoire de Chimie, Ingénierie Moléculaire et Nanostructures, Ferhat Abbas-Sétif 1, 19000 Sétif, Algeria
[3]Laboratoire des Systèmes Photoniques et Optiques Non Linéaires, Institut d'Optique et Mécanique de Précision, Université Ferhat Abbas-Sétif 1, 19000 Sétif, Algeria
redjechtaabdelouahab@yahoo.fr

Prejem rokopisa – received: 2013-02-26; sprejem za objavo – accepted for publication: 2013-04-16

In this work, we report the influence of the deposition potential on the electrodeposition process, current efficiency, surface morphology and microstructure of Cu-Zn alloys deposited on a Ru substrate from a sulfate solution with an addition of EDTA. The study was carried out by means of cyclic voltammetry (CV), chronoamperometry, atomic force microscopy (AFM) and X-ray diffraction (XRD) techniques analyzing the electrochemical behavior, surface morphology and structural characterization, respectively. The experimental results show that the electrochemical behavior of Cu-Zn electrodeposits varied with the deposition potential. The AFM measurement showed that the Cu-Zn thin films obtained at all the potentials are homogenous in appearance being of a small crystallite size, and a variation in the film roughness with deposition potentials is established. An analysis of X-ray diffraction patterns indicates that the electrodeposited Cu-Zn alloys exhibit β- and γ-phases.

Keywords: copper-zinc, electrodeposition, cyclic voltammetry, morphology, X-ray diffraction

V tem delu poročamo o vplivu potenciala nanosa pri postopku elektronanašanja na učinkovitost toka, morfologijo površine in mikrostrukturo zlitine Cu-Zn, nanesene na podlago iz Ru iz sulfatne raztopine z dodatkom EDTA. Za analizo elektrokemijskega vedenja, morfologije površine in značilnosti strukture so bile uporabljene ciklična voltametrija (CV), kronoamperometrija, mikroskopija na atomsko silo (AFM) in rentgenska difrakcija (XRD). Rezultati raziskav kažejo, da se elektrokemijsko vedenje elektronanosov Cu-Zn spreminja s spreminjanjem potenciala pri nanašanju. AFM-meritve so pokazale, da so tanke plasti Cu-Zn, dobljene pri vseh potencialih, na videz homogene z majhnimi kristalnimi zrni, spreminjanje potenciala pa vpliva na hrapavost površine. XRD-analize pokažejo, da zlitina Cu-Zn po elektronanosu vsebuje β- in γ-faze.

Ključne besede: baker-cink, elektronanos, ciklična voltametrija, morfologija, rentgenska difrakcija

1 INTRODUCTION

The production of the coatings made of zinc and its alloys has recently been of interest since alloy coatings provide a better corrosion protection than pure-zinc coatings. In addition, alloy coatings are very interesting due to their high strength, good plasticity and excellent mechanical properties. There are several methods for obtaining these alloys: physical vapor deposition (PVD), chemical vapor deposition (CVD), sputtering and molecular beam epitaxy (MBE) techniques are just a few of them. These methods have several advantages and are used for specific applications. However, due to certain limitations, such as high capital and high-energy costs, an alternative method is required. Recently, the electrochemical deposition (electrodeposition) has been used as an alternative technique for producing these structures on different surfaces. Electrochemical processes offer many advantages, including a room-temperature operation, low-energy requirements, fast deposition rates, a fairly uniform deposition over complex three-dimensional objects, low costs and a simple scale-up with an easily maintainable equipment.[1] The control of the solution composition and deposition parameters determines the properties of a deposit. In electrodeposition, the mechanism growth, the morphology and the micro-structural properties of a film depend on electrodeposition conditions such as the electrolyte composition, the electrolyte pH and the deposition potential.[2]

Numerous studies of the electrodeposition of Cu-Zn alloys from aqueous baths have been carried out.[3,4] It has been reported that different electrochemical deposition parameters such as deposition potential or current density, temperature, pH, substrate-surface preparation and bath composition affect considerably the properties of deposits.[5–9] It is known that high-quality micrometer-thick films (smooth and bright deposits) can be prepared at a reasonably high deposition rate using baths with a high metallic-ion concentration and small amounts of additives.[10,11] In the same way, due to a large difference between the standard electrode potentials of Cu and Zn (≅1.1 V), these ions should be complex in electrodeposition solutions to facilitate their codeposition. Therefore, in

this work, an organic additive of $C_{10}H_{14}Na_2O_8$, $2H_2O$, called EDTA, was added to the sulfate bath.

The objective of the present work was to study the electrodeposition process and properties of the Cu-Zn alloys from a sulfate electrolyte with EDTA. The morphology and structure of the deposits were examined.

2 EXPERIMENTAL WORK

A deposition of Cu-Zn alloys was carried out in a bath of 0.14 M $CuSO_4$ for Cu, 0.06 M $ZnSO_4$ for Zn (Aldrich) with the Na_2SO_4 support electrolyte, 0.5 M H_3BO_3 (in order to control the pH of the solution and improve the quality of the deposit) and 0.35 M $C_{10}H_{14}Na_2O_8$, $2H_2O$ (EDTA) at pH ≈ 4.2 (**Table 1**). All the measurements were made at room temperature. Ethylenediaminetetra acetic acid, widely abbreviated as EDTA, was chosen as the complexing agent for a deposition of theses alloys. Plating baths were prepared from the chemicals of analytical grade and bidistilled water, and the pH was adjusted with dilute sulfuric acid when needed. Before the electrodeposition, each solution was stirred with a nitrogen gas flow. The conventional electrochemical measurements were taken using a glass cell consisting of a three-electrode assembly that was connected to a VoltaLab 40 (PGZ301 and Volta Master 4) controlled by a personal computer. A platinum sheet was used as the counter electrode (anode) and the cathode (the Ru substrate) potentials were referred with respect to the saturated calomel electrode (SCE). The working electrode was an thick Ru layer approximately 200 nm deposited by sputtering onto each silicon wafer at a low temperature (150 °C) to get a better adherence. Before the electrodeposition, the substrates were first cleaned ultrasonically in acetone and ethanol and then also with distilled and deionized water. The Cu-Zn thin-film deposition onto the Ru surface (an area of 0.5 cm^2) was studied by means of cyclic voltammetry (CV) and chronoamperometry (CA) techniques. The CV for all the solutions was initially carried out between –1.2 V and 0.2 V (SCE) at a scan rate of 20 mV s^{-1}. The surface morphologies of the deposits were examined with atomic force microscopy (AFM). The roughness (the root-mean-square height deviation) of the samples was obtained directly from the AFM software (PicoScan 5.3 from Molecular Imaging). The crystalline structures of the deposits were identified with X-ray diffraction using a Philips diffractometer with a 2θ range 10–100° and Cu K_α radiation (λ = 0.15406 nm).

Table 1: Bath composition and conditions for the Cu-Zn electrodeposition

Tabela 1: Sestava kopeli in razmere pri elektronanašanju Cu-Zn

Bath	$ZnSO_4$, $7H_2O$/M	$CuSO_4$, $5H_2O$/M	Na_2SO_4 /M	H_3BO_3 /M	EDTA /M
Zn	0.06		1	0.5	0.35
Cu		0.14	1	0.5	
Cu-Zn	0.06	0.14	1	0.5	0.35

3 RESULTS AND DISCUSSIONS

3.1 Electrochemical study

Cyclic voltammetry was performed to understand the electrochemical behavior of the Cu(II) and Zn(II) species on the Ru electrode. **Figure 1** shows the cyclic voltammograms of the Ru electrode recorded in different ion solutions of Cu, Zn and Cu-Zn. In effect, **Figure 1a** shows a cyclic voltammogram of a solution containing 0.14 M $CuSO_4$ with a cathodic scan limit of –0.8 V vs. SCE. Two sharp peaks are observed at –0.141 V and 0.072 V, corresponding to a reduction and a dissolution of Cu, respectively. In the Cu electrodeposition, the charge transfer step is fast and the growth rate is controlled with the rate of the Cu-ion mass transfer to the

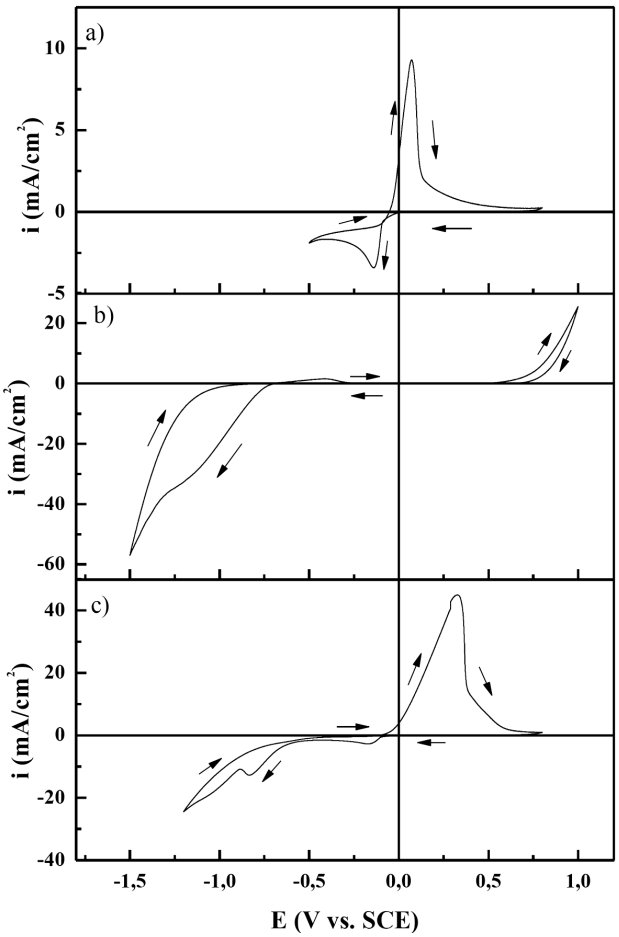

Figure 1: Cyclic voltammograms obtained for: a) 0.14 M $CuSO_4$, b) 0.06 M $ZnSO_4$ + 0.35 M EDTA and c) 0.14 M $CuSO_4$ + 0.06 M $ZnSO_4$ + 0.35 M EDTA with the cathodic scan limit of –1.20 V vs. SCE, at the scan rate of 20 mV s^{-1}; supporting electrolyte is 1 M Na_2SO_4 + 0.5 M H_3BO_3 (pH 4.2)

Slika 1: Ciklični voltamogrami, dobljeni z: a) 0,14 M $CuSO_4$, b) 0,06 M $ZnSO_4$ + 0,35 M EDTA in c) 0,14 M $CuSO_4$ + 0,06 M $ZnSO_4$ + 0,35 M EDTA s katodno omejitvijo –1,20 V proti SCE, pri hitrosti skeniranja 20 mV s^{-1}; osnovni elektrolit je 1 M Na_2SO_4 + 0,5 M H_3BO_3 (pH 4,2)

growing centers. The consistency of the cyclic-voltammetry behavior upon the potential cycling indicates that the anodic stripping process completely removes Cu from the electrode surface. The data in this figure indicates the absence of an underpotential deposition peak, with the Cu reduction occurring at the significant overpotential to the Nernstian value. This is due to a weak deposit/substrate interaction, as the early stages of an electrodeposition of Cu on Ru surfaces correspond to the Volmer-Weber growth mechanism.[12]

Figure 1b shows a cyclic voltammogram obtained in 0.06 M $ZnSO_4$. During a direct scan, it is possible to note that the increase in the current begins at –0.7 V; this is due to the electrodeposition of Zn and hydrogen evolution. In the reverse potential scan, the absence of the peak corresponding to the dissolution of the previously deposited Zn is observed. For the Cu and Zn solution (**Figure 1c**), the voltammogram obtained shows the presence of cathodic and anodic peaks related to the deposition and dissolution of the metals. In the cathodic scan, it can be observed that the increases in the current were detected at –0.152 V and –0.75 V, being characteristic of the potential deposition processes of Cu and Zn onto Ru surfaces, respectively. After this limit, the hydrogen evolution is predominant. During the inverse of the potential scan, it is possible to observe, in all the curves, the presence of crossovers which are typical of the formation of a new phase involving a nucleation process.[13]

To elucidate the role of an applied potential, the current efficiency (CE) during the codeposition process was determined. The deposition CE was calculated from the ratio of the cathodic electric charge, which passed during the electrodeposition of the Cu-Zn alloy, to that of the anodic one required for the total alloy dissolution. The Cu-Zn alloy thin films were obtained in the potentiostatic mode at different deposition potentials. The dependence of CE on different deposition potentials is shown in **Figure 2**. The efficiencies of the deposits decrease considerably with the potential and then reach their minima at more negative potentials. This decrease in CE is due to the process of hydrogen evolution. It is clear from these results that there is an appreciable decrease in the value of CE as the deposition potentials become more negative than ≈ –1.0 V. This is due to the hydrogen evolution reaction (HER) that becomes more significant than the Zn and Cu electrodeposition. This, in turn, increases the pH level at the cathode, causing the metal hydroxide to be included in the deposit.[11] These observations indicate that the control of the deposition potential is very important for realizing a high CE in the Cu-Zn deposition process. Similar results for Cu-Zn deposits are observed by de Almeida et al.[14]

The current was recorded as a function of time to study the deposition mechanisms of Cu-Zn alloys during their growth. The electrochemical deposition was performed using the standard chronoamperometry technique to study the nucleation and growth mechanism of Cu-Zn on ruthenium. Deposition potentials were chosen according to the reduction peaks appearing on the cyclic voltammograms. Deposition is conducted at the constant potentials in the potentiostatic mode, during which current transients are recorded. **Figure 3** shows the current transients obtained at four different potentials: –1.0 V, –1.1 V, –1.2 V and –1.3 V vs. SCE. In this figure, at the beginning of the applied potentials, a high cathodic current is seen for a short time. After that, the current rapidly decreases due to a depletion of the metal-ion concentrations close to the electrode surface, subsequently reaching a stable value. The current-time transients have a normal dependence on the overpotentials, whereas the current density increases with an increase in the overpotential. This is specific to the nucleation and growth process and for longer times, merging into a common curve caused by the diffusion-controlled pro-

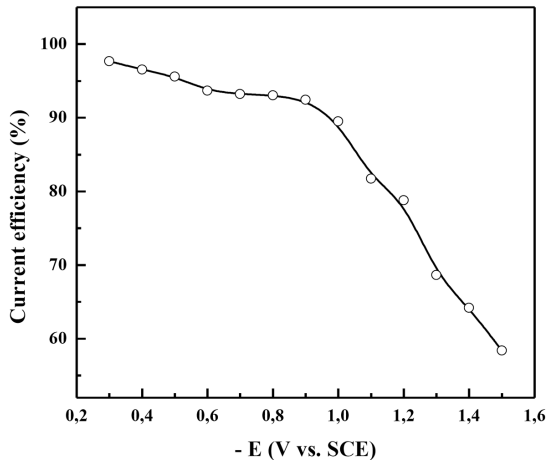

Figure 2: Effect of the deposition potential on the current efficiency of the Cu-Zn electrodeposition process

Slika 2: Vpliv potenciala nanosa na učinkovitost elektronanašanja Cu-Zn

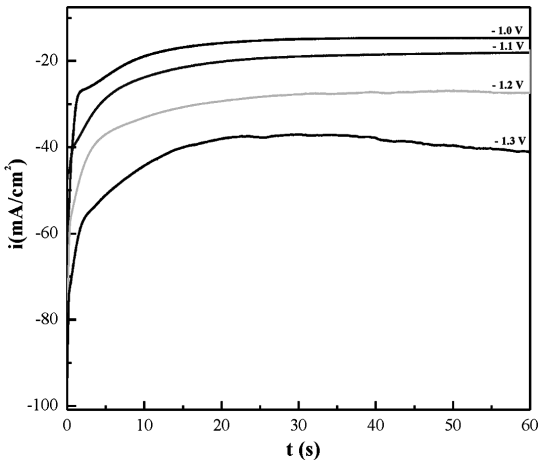

Figure 3: Evolution of current densities versus deposition time during the deposition of Cu-Zn on the Ru surface at different deposition potentials

Slika 3: Razvoj gostote toka v primerjavi s časom nanosa Cu-Zn na površino Ru pri različnih potencialih nanašanja

cess and described with the Cottrell equation.[15] According to the *i–t* curves, each transient has one well-defined, recognizable current maximum seen as a clear first peak followed by a sharp fall and subsequent growth. The *i–t* transients have a normal dependence on the overpotentials, whereas the current density increases with an increase in the overpotential. The peak corresponds to the nucleation of the metallic sites on the surface and it is followed by a reduction in the current exhibiting a three-dimensional (3D) growth. An increase in the peak current at higher overpotentials means that the number of sites (nucleation rate) increases due to a higher nucleation rate.[15]

3.2 Morphological and Structural Analysis

The morphology of the electrodeposited surface was imaged *ex situ* after the Cu-Zn electrodeposition using AFM measurements. **Figure 4** shows 2 μm × 2 μm AFM images of the deposited Cu-Zn alloy films obtained at different deposition potentials. The figures reveal that, with all the applied potentials, the images have a granular surface. However, the dimensions of the visible features in the images are different. It is known that a film electrodeposited on a polycrystalline substrate is also polycrystalline. During electrolysis, Cu-Zn crystallites randomly grow on the polycrystalline substrate and may form conglomerates. The composition and crystallite sizes strongly depend on the applied potential. If the current density is very small, there will be insufficient crystalline growth centers and the deposited layer will be rough-grained. If the current density is high, the deposited layer will be porous and soft.

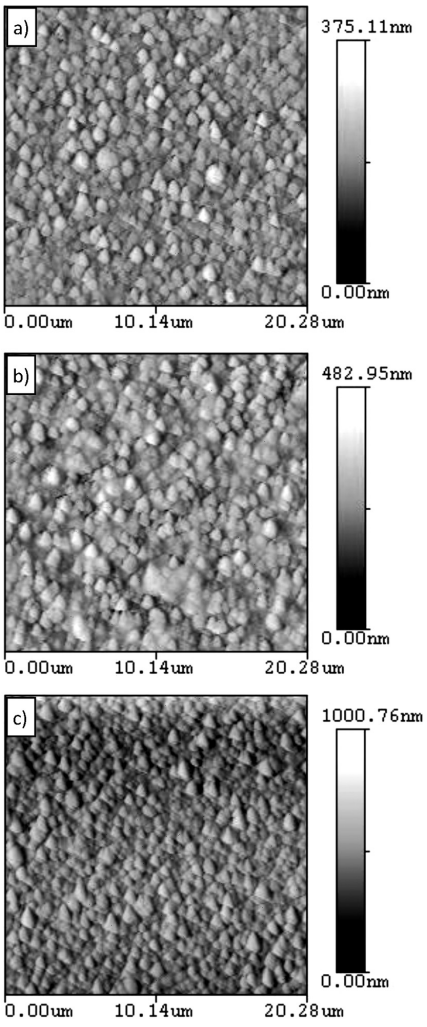

Figure 4: AFM images of the Cu-Zn thin films prepared at different cathodic potentials: a) –1.1 V, b) –1.2 V and c) –1.3 V vs. SCE
Slika 4: AFM-posnetki tankih plasti Cu-Zn, pripravljenih pri različnih katodnih potencialih: a) –1,1 V, b) –1,2 V in c) –1,3 V v odvisnosti od SCE

The surface topography is traditionally analyzed with surface-roughness measurements such as the root-mean-square (RMS) roughness, the average roughness and the peak-to-valley roughness.[16] In brief, the surface roughness R_q (denoted also as RMS) and the mean roughness R_a were calculated using the standard software (**Table 2**). The surface roughness increases with the film thickness for the films deposited using both potentials, and the variation in the surface morphology with the applied potential is consistent with the general theory.[17]

Table 2: Dependence of the surface roughness and crystallite size of the electrodeposited Cu-Zn thin films on deposition potentials
Tabela 2: Odvisnost hrapavosti površine in velikosti kristalnih zrn Cu-Zn tanke plasti po elektrononašanju od potenciala pri nanosu

E/(V vs. SCE)	R_q/nm	R_a/nm	*D*/nm
–1.10	42.72	33.12	48.20
–1.20	53.04	65.60	46.50
–1.30	108.62	82.08	46.10

The effect of the current density on this surface morphology can be explained since a high current density results in higher rates of the crystal nucleation (a higher mobility of atoms), giving rise to finer crystal structures and, hence, a smoother surface.[17] However, a new theory[18,19] has emerged, proposing that the concentration of metallic ions does change the bath homogeneously, but rather preferentially increases near the substrate (cathode). This relative concentration in the discharging zone is of a little significance at a low current density, at which the surface of a deposited film is rough. At a high current density, the convexity of the film increases, being associated with a relative concentration of ions in the discharging zone. The surface of a film deposited under these conditions is very smooth. The convex part of the film attracts more ions by acting as a focus of discharge, further increasing the convexity of the film. This may explain the mechanism of deposition.[20]

Figure 5 shows the XRD patterns of the Cu-Zn films deposited on the Ru substrates in the sulfate/EDTA bath under different deposition potentials of –1.1 V, –1.2 V and –1.3 V vs. SCE in the 2θ scan range of 25–60°. All the XRD patterns show many peaks corresponding to two distinct phases, β and γ, respectively. It is clear that

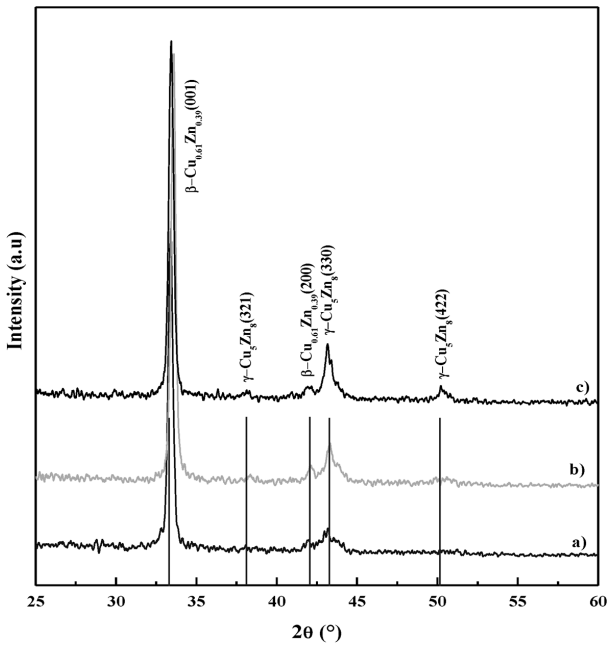

Figure 5: X-ray diffraction patterns of the electrodeposited Cu-Zn alloy films obtained at different deposition potentials: a) –1.1 V, b) –1.2 V and c) –1.3 V vs. SCE

Slika 5: XRD-posnetki tankih plasti Cu-Zn, dobljeni pri različnih potencialih nanašanja: a) –1,1 V, b) –1,2 V in c) –1,3 V v primerjavi s SCE

the XRD patterns from the Cu-Zn electrodeposits are different from those of pure Zn and Cu, indicating that crystalline alloys are indeed formed in these Cu-Zn electrodeposits. Furthermore, the γ phase diffraction lines increase in intensity as the deposition potential becomes more negative; in other words, the γ phase increases as the Cu content in the electrodeposited Cu-Zn alloy decreases. At a higher deposition potential, a decrease in the Cu concentration is explained with the fact that, at these potentials, a reduction in Cu is mass-transport limited. A further increase in the deposition overpotential would only increase the amount of Zn being deposited.[21–23] From these results, the γ phase was more dominant than the β phase in the Cu-Zn alloy thin films.

The average crystallite size of the particles is calculated from the full width at half maximum (FWHM) of the respective peaks using the Scherrer relation:[24]

$$D = \frac{0.9\lambda}{\beta \cos\theta} \quad (1)$$

where D is the crystallite size, λ is the wavelength of X-ray radiation (λ = 0.15406 nm), β is the FWHM of the peak and θ is the diffraction angle.

Also, **Table 2** shows the average crystallite size obtained from XRD for [001] planes, for the β phase of the alloys electrodeposited at three different applied potentials. The average crystallite size decreases with the increasing Zn concentration in the films and with the increasing applied potentials. This observation shows that, at a more negative potential, the deposition rate is high and, hence, the atoms are incorporated in the film with little surface migration, thus limiting the grain size.

4 CONCLUSIONS

Smooth, compact and bright binary Cu-Zn alloys were deposited on a Ru substrate from a sulfate electrolyte with an EDTA additive. The electrodeposition behavior of the sulfate electrolyte was studied using cyclic voltammetry. A possibility of depositing pure copper and zinc with a trace of copper was revealed during a cathodic scan of the substrate potential. The effects of deposition potentials on the microstructures of Cu-Zn were investigated by means of AFM and XRD techniques. The AFM images showed Cu-Zn clusters of an equivalent size randomly distributed in the surface defects acting as active sites. An X-ray diffraction measurement reveals that the Cu-Zn alloy exhibits two phases, the β and γ phases. According to these results, the γ phase was more dominant than the β phase in the Cu-Zn alloy thin films.

5 REFERENCES

[1] D. Y. Park, N. V. Myung, M. Schwartz, K. Nobe, Electrochim. Acta, 47 (**2002**), 2893

[2] Southampton Electrochemistry Group, In: T. J. Kemp (Ed.), Instrumental Methods in Electrochemistry, Ellis Horwood Ltd., Chichester, UK 1985

[3] D. Pletcher, Industrial Electrochemistry, Chapman and Hall, London 1984, 187

[4] R. W. Mackey, In: F. A. Lowenheim (Ed.), Modern Electroplating, John Wiley & Sons, Inc., New York 1974, 418

[5] K. Raeissi, A. Saatchi, M. A. Golozar, J. A. Szpunar, J. Appl. Electrochem., 34 (**2004**), 1249

[6] L. H. Mendoza-Huizar, C. H. Rios-Reyes, M. G. Gómez-Villegas, J. Mex. Chem. Soc., 53 (**2009**), 243

[7] N. M. Younan, J. Appl. Electrochem., 30 (**2000**), 55

[8] J. P. Millet, M. Gravria, H. Mazille, D. Marchandise, J. M. Cuntz, Surf. Coat. Technol., 123 (**2000**), 164

[9] C. S. Lin, H. B. Lee, S. H. Hsieh, Metall. Trans. A, 31A (**2000**), 475

[10] P. F. J. de Leon, E. Albano, V. R. C. Salvarezza, Phys Rev E, 66 (**2002**), 1

[11] M. Paunovic, M. Schlesinger, Fundamental of Electrochemical Deposition, John Wiley & Sons, Inc., New Jersey, USA 2006, 210–218

[12] L. Huang, F. Z. Yang, S. K. Xu, S. M. Zhou, Trans. Inst. Met. Finish, 84 (**2004**), 47

[13] R. Greef, R. Peat, L. M. Peter, D. Pletcher, J. Robinson, Instrumental Methods in Electrochemistry, Ellis Horwood, Chichester 1985, Ch. 9

[14] M. R. H. de Almeida, E. P. Barbano, M. F. de Carvalho, I. A. Carlos, J. L. P. Siqueira, L. L. Barbosa, Surface & Coatings Technology, 206 (**2011**), 95

[15] A. J. Bard, L. R. Faulkner, Electrochemical Methods, Fundamentals and Applications, 2nd Ed., Wiley, New York 2001

[16] J. M. Bennett, L. Mattsson, Introduction to Surface Roughness and Scattering, Optical Society of America, Washington, D.C. 1989

[17] I. Ohno, J. Surf. Finishing Soc. Jpn., 39 (**1988**), 149

[18] T. Watanabe, The Surface Science Society of Japan, 2nd Thin Film Fundamental Seminar, 1999, 115

[19] K. Inoue, T. Nakata, T. Watanabe, Mater. Transact., 43 (**2002**), 1318

[20] A. Sahari, A. Azizi, N. Fenineche, G. Schmerber, A. Dinia, Surf. Rev. Lett., 12 (**2005**), 391
[21] M. R. Khelladi, L. Mentar, A. Azizi, L. Makhloufi, G. Schmerber, A. Dinia, J Mater Sci: Mater Electron, 23 (**2012**), 2245
[22] L. Mentar, M. R. Khelladi, A. Beniaiche, A. Azizi, Int. J. Nanoscience, 12 (**2013**), 1250038
[23] P. Y. Chen, M. C. Lin, I. W. Sun, J. Electrochem. Soc., 147 (**2000**), 3350
[24] B. D. Cullity, Elements of X-ray Diffraction, Addison-Wesley, USA 1978

UDK 621.941:004.032.26
Original scientific article/Izvirni znanstveni članek

ISSN 1580-2949
MTAEC9, 48(2)227(2014)

EXPERIMENTAL DESIGN AND ARTIFICIAL NEURAL NETWORK MODEL FOR TURNING THE 50CrV4 (SAE 6150) ALLOY USING COATED CARBIDE/CERMET CUTTING TOOLS

EKSPERIMENTALNA ZASNOVA IN MODEL UMETNE NEVRONSKE MREŽE ZA STRUŽENJE JEKLA 50CrV4 (SAE 6150) Z UPORABO ORODIJ S KARBIDNO ALI KERMETNO PREVLEKO

Murat Tolga Ozkan[1], Hasan Basri Ulas[2], Musa Bilgin[3]

[1]Gazi University, Faculty of Technology, Department of Industrial Design Engineering, 06500 Ankara, Turkey
[2]Gazi University, Faculty of Technical Education, Mechanical Education Department, 06500 Ankara, Turkey
[3]Erzincan University, Vocational Technical School, Mechanical Program, 24000 Erzincan, Turkey
mtozkan06@yahoo.com

Prejem rokopisa – received: 2013-03-08; sprejem za objavo – accepted for publication: 2013-06-18

In this experimental study, the 50CrV4 (SAE 6150) steel was subjected to the machining tests with coated carbide and cermet cutting tools in a turning operation. The tests were carried out at various cutting speeds, feed rates and cutting depths. In the light of these parameters, cutting forces and surface-roughness values were determined. Three components (F_a, F_r and F_c) of the cutting forces were measured during the tests using a dynamometer, while the machined surface-roughness values were determined using a surface roughness measuring unit. A multiple regression analysis and experimental design were performed statistically. The measured surface-roughness values were used for the modeling with an artificial neural network system (ANNS). The relations between the cutting forces and the surface-roughness values were also defined.

Keywords: turning operations, coated carbide/cermet cutting tools, cutting force, surface roughness, artificial neural network

V tej študiji je bilo jeklo 50CrV4 (SAE 6150) strojno obdelano s struženjem z orodji za rezanje s karbidno ali kermetno prevleko. Preizkusi so bili opravljeni pri različnih hitrostih rezanja, podajanja in globine rezanja. Iz teh parametrov so bile ugotovljene sile pri rezanju in vrednosti hrapavosti površine. Tri komponente sil rezanja (F_a, F_r in F_c) so bile merjene med poskusom z dinamometrom, medtem ko so bile vrednosti hrapavosti površine izmerjene z merilnikom za hrapavost površine. Izvršena je bila večkratna regresijska analiza in statistična obdelava izvedbe poskusov. Izmerjene vrednosti hrapavosti so bile uporabljene za modeliranje s sistemom umetne nevronske mreže (ANNS). Določena je bila tudi odvisnost med silami rezanja in hrapavostjo površine.

Ključne besede: postopek struženja, rezilna orodja s karbidno ali kermetno prevleko, sila rezanja, hrapavost površine, umetna nevronska mreža

1 INTRODUCTION

Machining experiments are usually costly and time consuming. In order to eliminate the cost and to reduce the time, some advanced techniques were developed. These are generally called modeling. There are several modeling methods. Empirical modeling, analytical modeling, mechanistic modeling, finite-element modeling and artificial neural network modeling are some of these modeling methods. With these techniques, predictions are made using the experimentally obtained results.

Boubekri et al.[1] investigated different cutting conditions on three grades of steel, namely, 1018 (low-carbon, cold-rolled steel), 304 (austenitic stainless steel) and 4140 (low-alloy steel) using uncoated carbide inserts as the tool material. Mathematical models were developed for predicting the forces acting on the tool for different cutting conditions and materials.

Kumar et al.[2] studied the performance of an alumina-based ceramic cutting tool as an attractive alternative for carbide tools in the machining of steels in its hardened condition. Two types of ceramic cutting tools, namely, the Ti[C, N] mixed alumina-ceramic cutting tool and zirconia-toughened alumina-ceramic cutting tool were used for the investigation. The performance of these ceramic cutting tools related to the surface finish was also discussed.

Tekiner and Yeşilyurt[3] carried out machining tests to determine the best cutting conditions and cutting parameters in the turning of AISI 304 stainless steels by taking into consideration the process sound. The ideal cutting parameters and cutting-process sounds were determined.

The tests involving the AISI 4340 steel were performed using two hardness values, 42 HRC and 48 HRC; for the former, a coated carbide insert was used as the cutting tool, whereas for the latter a polycrystalline cubic boron nitride insert was employed. The machining tests on the AISI D2 steel hardened to 58 HRC were conducted using a mixed-alumina cutting tool. The cutting forces, surface roughness, tool life and wear mechanisms were assessed. The results indicated that when turning

the AISI 4340 steel, using low feed rates and depths of cut, the forces were higher when machining the softer steel and that the surface roughness of the machined part was improved as the cutting speed was elevated and it deteriorated with the increasing feed rate.[4]

The wear mechanisms of the cutting tools made of tungsten-carbide (WC), PCBN and PCD were investigated using the tool life and the temperature results available in the literature. For the tool/work combinations of WC/steel and PCBN/hardened-steel, under practical conditions, the tool wear was found to be greatly influenced by the temperature.[5]

The AISI 4340 low-alloy steel was assumed for the workpiece. Cubic boron-nitride (CBN) or polycrystalline (PCBN) inserts are widely used as the cutting-tool material in high-speed machining of hardened tool steels due to high hardness, high abrasive-wear resistance and chemical stability at high temperature. Cutting forces and feed forces were determined with numerical simulations. The cutting force and feed force increased with the increasing feed, tool-edge radius, negative rake angle, and workpiece hardness. The results from the simulations were compared to the experimental results reported in the literature.[6]

The effects of the cutting speed, cutting force and feed rate on the flank wear land and tool life of the TiN coated carbide inserts in boring operations were studied when machining the 38MnVS5 alloy. The results showed that the machinability of microalloyed steel is better than that of heat-treated alloy steels under identical conditions.[7]

The tribological influences of PVD-applied TiAlN coatings on the wear of cemented carbide inserts and the microstructure influence on the wear behaviors of the coated tools were investigated under dry and wet machining. The turning test was conducted with variable high cutting speeds ranging from 210 m/min to 410 m/min.[8]

The tested work materials were plain carbon steel JIS S45C and BN free-machining steels. The JIS S45C was used as the standard. The tool wear in turning the BN free-machining steel was smaller than that in turning the standard steel. In the case of turning BN1 with P30 at 200 m/min, 300 m/min, the wear-progress rate of the flank wear and crater depth were about half as much as that in turning the standard steel. The BN free-machining steel showed a slightly lower cutting temperature and a smaller cutting force in comparison with the standard steel at the tested cutting speeds.[9]

The cutting-force data used in the analyses was gathered with a tool-breakage detection system detecting the variations of the cutting forces measured with a three-dimensional force dynamometer. The workpiece materials used in the experiments were: cold-work tool steel, AISI O2 (90 MnCrV8); hot-work tool steel, AISI H10 (X32CrMo33); and mould steel, AISI improved 420 (X42Cr13). The cutting tools used were HSS tools, uncoated WC and coated TiAlN and TiC + TiCN + TiN inserts (ISO P25). No cutting fluid was used during the turning operations. During the experiments, the cutting forces, flank wear and surface-roughness values were measured throughout the tool life and the machining performances of the tool steels were compared.[10]

Orthogonal cutting experiments were performed on a high-speed machining center with the surface speeds of up to 500 m/min and the uncut chip thicknesses ranging from 0.1 mm to 0.3 mm. The results indicate that in certain critical regions of the thermal field, the improved machinability correlates with significant reductions in the temperature exceeding the measurement uncertainties. Such micro-scale temperature measurements will help to design the materials with further improved machinability.[11]

Three different carbide cutting tools were used, namely, TiCN + TiC + TiCN + Al_2O_3 + TiN-coated carbide tools with multilayer coatings of 7.5 μm and 10.5 μm and an uncoated WC/Co tool. The turning experiments were carried out at four different cutting speeds, which were (125, 150, 175 and 200) m/min. The feed rate (f) and depth of cut (a_p) were kept fixed at 0.25 mm/r and 1.5 mm/r, respectively, throughout the experiments. The tool performance was evaluated with respect to the tool wear, the surface finish produced and the cutting forces generated during turning.[12]

Cakir and Isik[13] performed a study about the tool-life testing with single-point turning tools. The cutting-force data used in the analysis was gathered with a tool-breakage detection system detecting the variations of the cutting forces measured with a three-dimensional force dynamometer. Six pairs of ductile iron specimens, austempered at (300, 350 and 400) °C for 1 h and 2 h were tested. The cutting tools used in the tests were coated carbide inserts, ISO SNMG 120408 (K10), clamped on the tool holders, CSBNR 2525 M12. No cutting fluid was used during the turning operations. During the experiments, the cutting forces, flank wear and surface-roughness values were measured throughout the tool life and the machining performances of ADI having different structures were compared.

Lalwani et al.[14] carried out a machining study focusing on the effect of the cutting parameters (cutting speed, feed rate and depth of cut) on the cutting forces (feed force, thrust force and cutting force) and the surface roughness in the finish hard turning of the MDN250 steel (equivalent to the 18Ni(250) maraging steel) using a coated ceramic tool. A non-linear quadratic model best describes the variation in the surface roughness with the major contribution of the feed rate and the secondary contributions of the interaction effect between the feed rate and the depth of cut, the second-order (quadratic) effect of the feed rate and the interaction effect between the speed and depth of cut. The suggested models of the cutting forces and surface roughness are adequately map-

ped within the limits of the cutting parameters considered.

In another study, coated tungsten-carbide ISO P-30 turning-tool inserts were subjected to a deep cryogenic treatment (–176 °C). The machining studies were conducted on a C45 workpiece using both untreated and deep cryogenic treated tungsten-carbide cutting-tool inserts. The cutting force during the machining of the C45 steel is lower in the case of the deep cryogenic treated carbide tools when compared with the untreated carbide tools. The surface finish produced when machining the C45 steel workpiece is better with the deep cryogenic treated carbide tools than with the untreated carbide tools.[15]

The objective of the work is to determine the influence of cutting fluids on the tool wear and surface roughness during turning AISI 304 with a carbide tool. A further attempt was made to identify the influence of coconut oil on reducing the tool wear and surface roughness during the turning process. The performance of coconut oil was also compared with two other cutting fluids, namely, an emulsion and a neat cutting oil (immiscible with water).[16]

Ebrahimi and M. M. Moshksar[17] machined microalloyed steel (30MnVS6) and quenched-tempered (QT) steels (AISI 1045 and AISI 5140) under different cutting conditions. An experimental investigation was conducted to determine the effects of the cutting speed, feed rate, hardness, and workpiece material on the flank wear and tool life of the coated cemented carbide inserts in the hard-turning process. A statistical analysis was used for evaluating different factors of the cutting forces. Chip characteristics and the chip/tool contact length were also investigated.

In another study, the machining of the uncoated AISI 1030 steel (i.e., the orthogonal cutting), PVD- and CVD-coated cemented carbide inserts with different feed rates of (0.25, 0.30, 0.35, 0.40 and 0.45) mm/r, with the cutting speeds of (100, 200 and 300) m/min and a constant depth of cut (i.e., 2 mm), without using a cooling liquid was accomplished. The effects of the surface roughness, the coating method, the coating material, the cutting speed and the feed rate on the workpiece were investigated. Afterwards, these experimental studies were carried out on artificial neural networks (ANNs). The training and test data of the ANNs were prepared using experimental patterns for the surface roughness. Therefore, the surface-roughness value was determined with an ANN with an acceptable accuracy.[18]

Gaitonde et al.[19] made a study analyzing the effects of the depth of cut and the machining time on the machinability aspects such as machining force, power, specific cutting force, surface roughness and tool wear using second-order mathematical models during turning high-chromium AISI D2 cold-work tool steel with the CC650, CC650WG and GC6050WH ceramic inserts.

The effects of the machining parameters on the cutting force, specific cutting pressure, cutting temperature, tool wear and surface-finish criteria were investigated during the experimentation. The present approach and the results will help manufacturing engineers to understand the machinability of Inconel 718 during high-speed turning.[20]

Two AISI 4140 steels with different machinability ratings and three types of tools were compared. The control-volume approach was used to estimate the energy partition from the thermal images and the energy outflows were compared for the measurement of the cutting power. This provides a new physical tool for examining machinability, tool wear and subsurface damage.[21]

The work is an experimental study of hard turning the AISI 52100 bearing steel with a CBN tool. The relationships between the cutting parameters (cutting speed, feed rate and depth of cut) and machining output variables (surface roughness, cutting forces) are analyzed and modeled with the response-surface methodology (RSM). Finally, the depth of cut exhibits the maximum influence on the cutting forces as compared to the feed rate and cutting speed.[22]

There are many studies in the literature about the artificial neural network modeling of the surface roughness. The main purpose of this study is to carry out the turning tests on the 50CrV4 (SAE 6150) steel using coated carbide/cermet cutting tools and to carry out the modeling with an artificial neural network. There are many studies in the literature about the SAE 6150 material. These studies are especially related to physical and mechanical properties. However, there is no sufficient study on the machinability of the SAE 6150 material.

2 MATERIALS AND METHOD

The turning tests were carried out on the commercially available 50CrV4 (equivalent to SAE 6150) steel workpiece specimens. These steel specimens were produces by CEMTAS, TR and their chemical composition is shown in **Table 1**.

The 50CrV4 (SAE 6150) workpiece specimens were prepared in accordance with the requirements of the ISO

Table 1: Workpiece material 50CrV4 (SAE 6150) and its chemical composition (*w*/%)
Tabela 1: Material obdelovancev 50CrV4 (SAE 6150) in njegova kemijska sestava (*w*/%)

Material	Hardness (HB)	Material content						
		C	Si	Mn	P	S	Cr	V
50CrV4 - SAE(AISI)6150	311	0.50	0.31	0.78	0.009	0.008	1.06	0.15

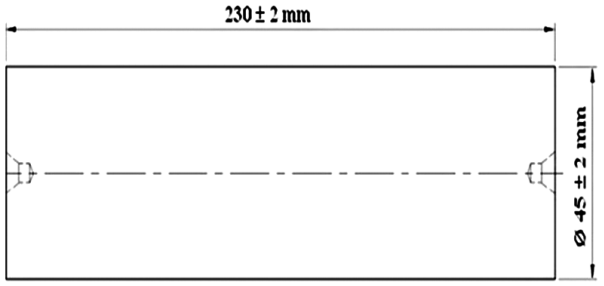

Figure 1: Experimental-workpiece-specimen geometry
Slika 1: Geometrija poskusnega vzorca

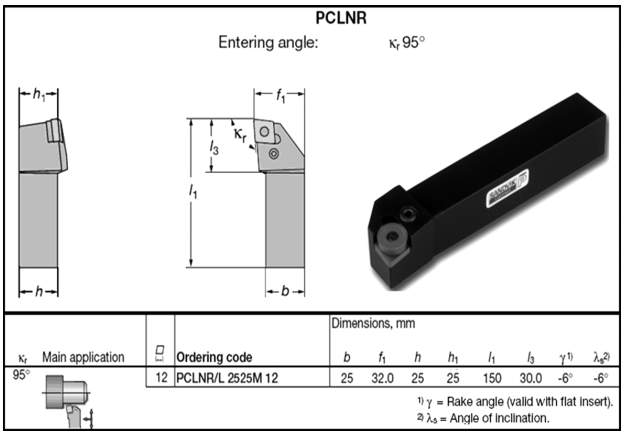

Figure 2: Tool-holder specifications
Slika 2: Specifikacija nosilca orodja

3685 standard. The size of the specimens was determined in accordance with the diameter/length ratio that should not exceed 1/10. Prior to the machining tests through a surface turning operation, both faces of the specimens were machined and center drilled on a universal lather. The dimensions of the workpiece specimens are shown in **Figure 1**.

Tool holder was also chosen according to the requirements specified in ISO 3685 for the machinability tests. The specifications of the tool holder, produced by SANDVIK, were PCLNR 2525 12. The tool-holder features are shown in **Figure 2**.

The cutting inserts with six different features were used for the machining tests. These cutting inserts were coated carbide and cermet cutting tools. In addition, the cutting-insert tip radii were (0.4, 0.8 and 1.2) mm. The cutting-insert grades and technical specifications are shown in **Table 2**.

The machining tests were carried out at the cutting speeds of (150, 200, 250, 250 and 300) m/min, the feed rates of (0.12, 0.16, 0.20) mm/r and the depths of cut of (0.5, 1, 1.5) mm without a coolant, using the cutting tools whose specifications are given in **Table 2**. The cutting speed, depth of cut and feed rate were chosen according to the manufacturer's recommendations, the

Table 2: Cutting-tool technical specifications
Tabela 2: Tehnične značilnosti poskusnega orodja za rezanje

Cutting-tool number	Cutting-tool material	Cutting tool	Coating method	Coating material	Code	Tip radius	ISO grade
1	Carbide		CVD	Al_2O_3+TiCN	GC4215	0.4	CNMG 12 04 04-PF-P15
2	Carbide		CVD	Al_2O_3+TiCN	GC4215	0.8	CNMG 12 08 04-PF-P15
3	Carbide		CVD	Al_2O_3+TiCN	GC4215	0.12	CNMG 12 12 04-PF-P15
4	Cermet		PVD	TiN+TiCN	GC1525	0.4	CNMG 12 04 04-PF-P15
5	Cermet		PVD	TiN+TiCN	GC1525	0.8	CNMG 12 08 04-PF-P15
6	Cermet		PVD	TiN+TiCN	GC1525	0.12	CNMG 12 12 04-PF-P15

Table 3: Cutting parameters used in the experimental study
Tabela 3: Parametri rezanja, uporabljeni pri eksperimentih

Cutting tool	Tip radius R_ε/mm	Depth of cut d/mm	Feed rate f/(mm/r)	Cutting speed v/(mm/min)
Coated carbide	0.4–0.8–1.2	0.5–1–1.5	0.12–0.16–0.20	150–200–250–250–300
Coated cermet	0.4–0.8–1.2	0.5–1–1.5	0.12–0.16–0.20	150–200–250–250–300

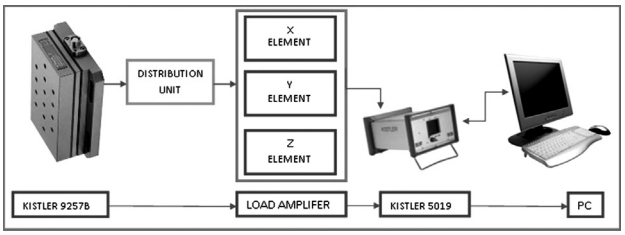

Figure 3: Schematic presentation of the experimental assembly
Slika 3: Shematski prikaz eksperimentalnega sestava

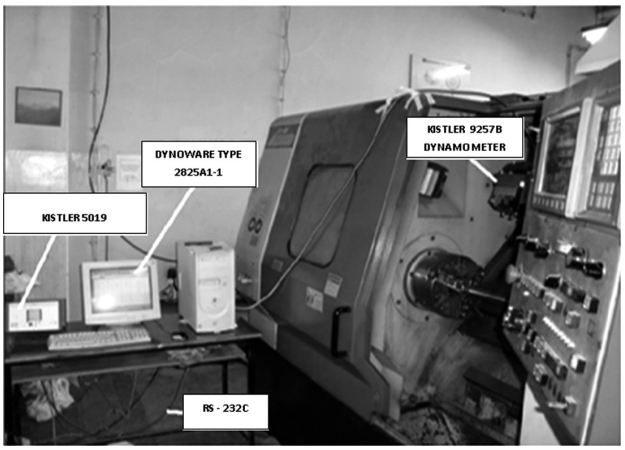

Figure 4: Experimental setup
Slika 4: Eksperimentalni sestav

related literature and the ISO 3685 standard. **Table 3** shows the types of cutting tool, tip radius, depth of cut, feed rate and cutting speed.

An industrial-type Johnford TC-35 CNC lathe was used as the machine tool. To measure the axial (*Fx*), radial (*Fy*) and main (*Fz*) cutting-force components, a KISTLER 9257B dynamometer was used. This dynamometer was connected with a KISTLER TYPE 5019 multichannel charge amplifier and the cutting-force signals were sent to a computer with an RS-232C cable connection. The graphs were obtained with the DynoWare Type 2825A1-2 software. F_x (F_a), F_y (F_r) and F_z (F_c) force values were determined during the machining processes. These values were calculated as the average scalar values in newtons (N) by the DynoWare software.

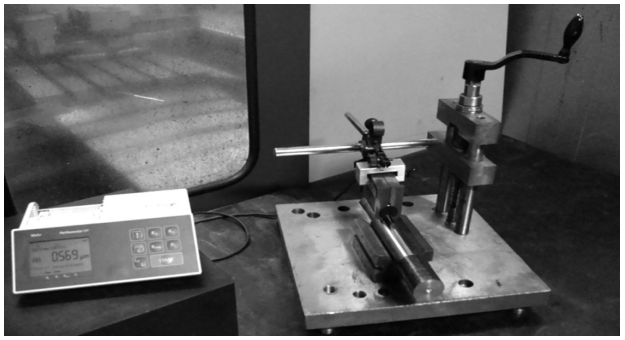

Figure 5: Surface-roughness measurement device
Slika 5: Naprava za merjenje hrapavosti površine

A schematic presentation of the experimental setup is shown in **Figure 3,** while the experimental setup is shown in **Figure 4**.

For the measurement of the surface-roughness values, a MAHR-Perthometer M1 model device was used (**Figure 5**). The cut-off length and the sampling length were chosen to be 0.8 mm and 5.6 mm, respectively. Three measurements were made parallel to the longitudinal axis of the workpiece at the intervals of 120°. The average surface roughness, R_a, was taken into account in all the measurements.

3 ARTIFICIAL NEURAL NETWORK MODEL

The concept of an artificial neural network has emerged with the idea that it simulates the operating principles of a human brain. The first studies were made with mathematical modeling of biological neurons that make up the brain cells. An artificial neural network consists of a large number of interconnected processing elements. Artificial neural network processing elements are called simple nerves.

An artificial neural network contains a large number of interconnected nodes. A nerve is the basic unit of an artificial neural network. An artificial nerve is, thus, simpler than a biological nerve. **Figure 6** shows an artificial neural network algorithm. All the artificial neural networks are derived from this basic structure. The differences in the structure of artificial neural networks result in different classification types.

The learning procedure can be affected by establishing correct correlations between the input and the output in artificial neural networks. This process falls below a certain value of the error between the foreseen output and the desired output. Artificial neural networks learn like a human. The more samples are used for learning, the more accurate is the obtained result. When a certain input is entered, the network can make changes to the data in order to give similarly accurate answers. The Levenberg-Marquardt (Levenberg, 1944; Marquardt, 1963) method uses a search direction that is a solution of the linear set of equations:

$$(J(x_k)^T J(x_k)+x_k I)d_k = -J(x_k)^T F(x_k) \quad (1)$$

or, optionally, of the equations:

$$(J(x_k)^T J(x_k)+l_k \operatorname{diag}(J(x_k)^T J(x_k)))d_k = \\ = -J(x_k)^T F(x_k) \quad (2)$$

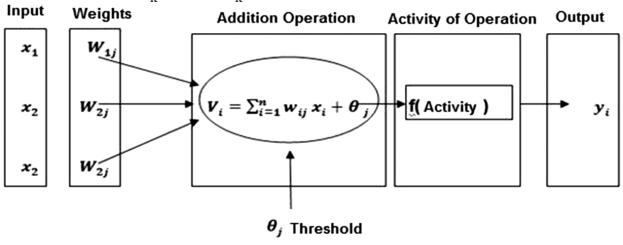

Figure 6: Artificial neural network
Slika 6: Umetna nevronska mreža

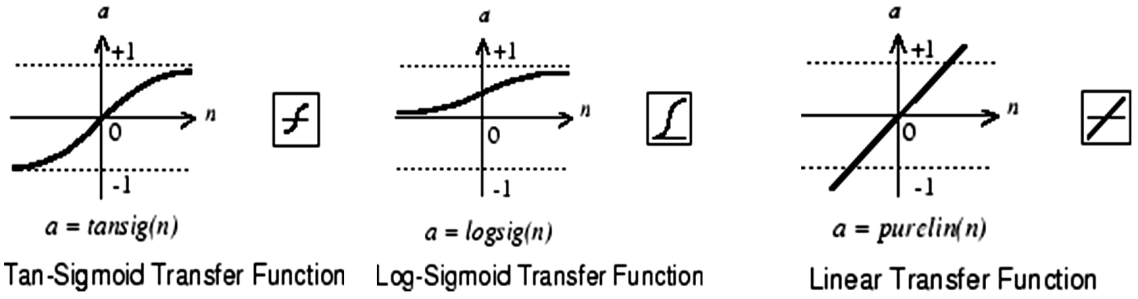

Figure 7: Used ANN functions
Slika 7: Uporabljene funkcije ANN

where scalar λ_k controls both the magnitude and direction of d_k. It is necessary to set the Scale Problem option to 'none' to choose Equation 1 and to 'Jacobian' to choose Equation 2.

Multilayer networks often use the log-sigmoid transfer function (logsig). The function generates the outputs between 0 and 1 as a neuron's net input goes from the negative to the positive infinity. Alternatively, multilayer networks can use the tan-sigmoid transfer function (tansig). Sigmoid output neurons are often used for pattern-recognition problems, while linear output neurons are used for function-fitting problems. The linear transfer function is shown below (**Figure 7**).

4 RESULTS AND DISCUSSIONS

4.1 Experimental study results

In this study, the influence of the machining parameters (cutting speed, feed rate and depth of cut) on the cutting forces (F_a, F_r and F_c) and surface-roughness values were investigated when machining the 50CrV4 (SAE 6150) steel. The surface-roughness values were analyzed on the basis of the process variables such as cutting speed, feed rate, depth of cut, and cutting-tool type. In addition, the influences of these variables on the cutting force were also examined. The relations between the cutting forces and the surface roughness were defined. A total of 270 experiments were performed to examine the effects of these variables. The minimum surface-roughness value was obtained with the coated cermet cutting tool, while the maximum surface-roughness value was obtained with the coated carbide cutting tool. The cutting-force components were measured (F_a, F_r, F_c). Maximum F_a, F_r and F_c were obtained with the coated carbide cutting tool. However, minimum F_a and F_r were obtained with the coated cermet cutting tool. Maximum R_a was obtained with the coated cermet cutting tool, while minimum Ra was obtained with the coated carbide cutting tool. A direct relation can be seen between the cutting forces and surface-roughness values. The lower are F_a and F_r, the lower are the surface-roughness values (**Table 4**).

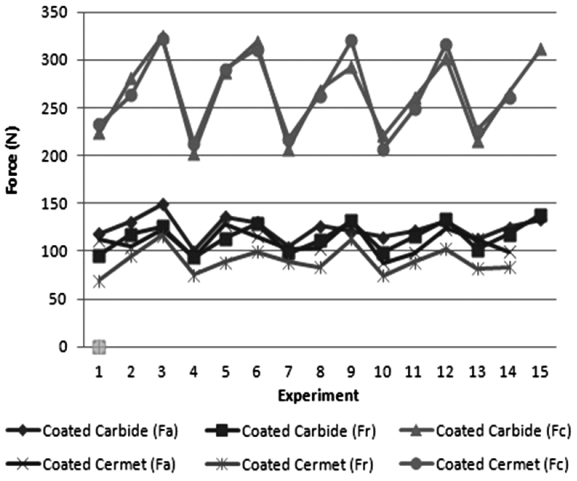

Figure 8: Comparison of the cutting forces: machining with coated carbide/cermet cutting tools
Slika 8: Primerjava sil pri rezanju: rezanje z orodjem s karbidno ali kermetno prevleko

Table 4: Maximum/minimum values of the cutting force and surface roughness
Tabela 4: Maksimalne/minimalne vrednosti sil pri rezanju in hrapavost površine

Cutting tool (coated carbide/cermet)	Cutting tool (z)	Depth of cut *d*/mm	Cutting speed *v*/(mm/min)	Feed rate *f*/(mm/r)	F_x (F_a)/N	F_y (F_r)/N	F_z (F_c)/N	Surface roughness R_a/μm	Min/max
Cermet	6	0.5	250	0.12	74.37	118.83	218.68	0.345	$F_{a\,min}$
Carbide	2	1.5	150	0.2	454.17	203.88	836.12	1.619	$F_{a\,max}$
Cermet	4	1.5	200	0.12	321.63	51.72	516.02	0.702	$F_{r\,min}$
Carbide	3	1.5	250	0.2	399.06	319.58	804.36	1.336	$F_{r\,max}$
Carbide	1	0.5	175	0.12	100.11	94.04	202.54	0.634	$F_{c\,min}$
Carbide	3	1.5	200	0.2	409.48	305.07	859.52	1.315	$F_{c\,max}$
Cermet	6	0.5	250	0.12	74.37	118.83	218.68	0.345	$R_{a\,min}$
Carbide	1	1.5	150	0.2	437.23	110.79	814.09	1.893	$R_{a\,max}$

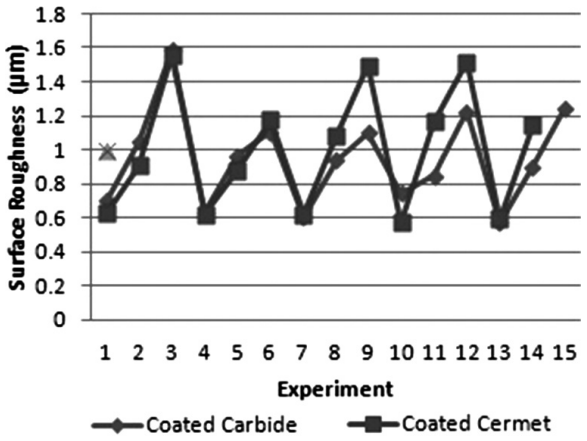

Figure 9: Comparison of the surface-roughness values: machining with coated carbide/cermet cutting tools
Slika 9: Primerjava vrednosti hrapavosti površine: rezanje z orodjem s karbidno ali kermetno prevleko

The cutting-force values were found to influence the resulting surface-roughness values. When F_a, F_r and F_c increase, the surface roughness also increases. There is a direct correlation between the F_a, F_r, F_c values and R_a. When the resulting surface-roughness values are examined, it is seen that the surface-roughness values obtained with the coated cermet cutting tools are lower than those obtained with coated carbide tools. The resultant force components of F_a, F_r and F_c have a direct correlation with R_a. Maximum F_a, F_r and F_c appeared with the coated carbide cutting tools (**Figure 8**). However, the minimum surface-roughness values were obtained with the coated cermet cutting tools (**Figure 9**). The lower surface-roughness values obtained with the coated cermet cutting tools can be explained with a lower built-up-edge (BUE) formation tendency of the cermet cutting tools. The presence of BUE on the cutting tool significantly increases the surface-roughness values.

4.2 Performance of the ANN model

An experimental design was accomplished. A 2^7 fully factorial experimental design was planned. Totally, 8 column × 270 line data was obtained from the experiments. This data was divided into groups. 70 % of the data was used for the training, 15 % of the data was used for the validation of the results and 15 % of the data was used to test the results. A multiple regression analysis was accomplished (R^2 = 0.81810949, adjusted

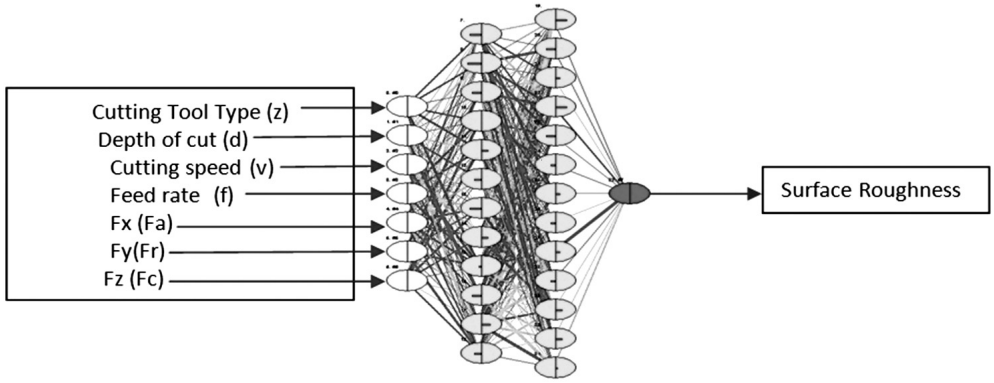

Figure 10: ANN model
Slika 10: ANN-model

Table 5: Iterations to find the best ANN model
Tabela 5: Približki pri iskanju najboljšega ANN-modela

Net name	Training performance	Test performance	Training error	Test error	Training algorithm
MLP 7-26-1	0.942287	0.910443	0.002352	0.003235	BFGS 52
MLP 7-14-1	0.957514	0.913514	0.001748	0.003132	BFGS 54
MLP 7-29-1	0.957661	0.911581	0.001738	0.003189	BFGS 90
MLP 7-26-1	0.940432	0.904966	0.002425	0.003485	BFGS 59
MLP 7-20-1	0.947744	0.907168	0.002135	0.003365	BFGS 73
MLP 7-54-1	0.960559	0.916491	0.001624	0.003013	BFGS 109
MLP 7-26-1	0.943531	0.910626	0.002302	0.003236	BFGS 50
MLP 7-37-1	0.987255	0.952368	0.000532	0.001757	BFGS 132
RBF 7-53-1	0.929539	0.905647	0.002851	0.003411	RBFT
MLP 7-50-1	0.955443	0.904887	0.001829	0.003456	BFGS 67
MLP 7-43-1	0.962073	0.909532	0.001561	0.003283	BFGS 52
MLP 7-74-1	0.944994	0.907058	0.002245	0.003363	BFGS 66
MLP 7-45-1	0.943063	0.908330	0.002321	0.003342	BFGS 52

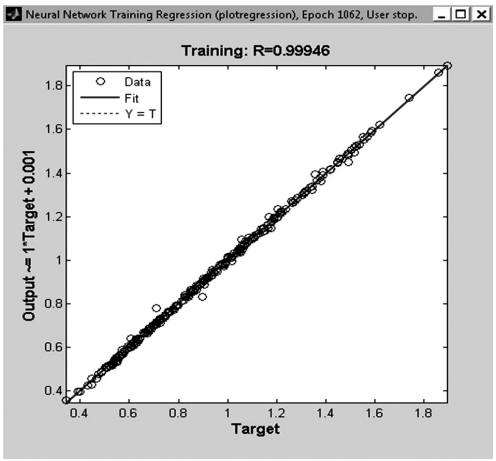

Figure 11: ANN training result
Slika 11: Rezultati ANN-usposabljanja

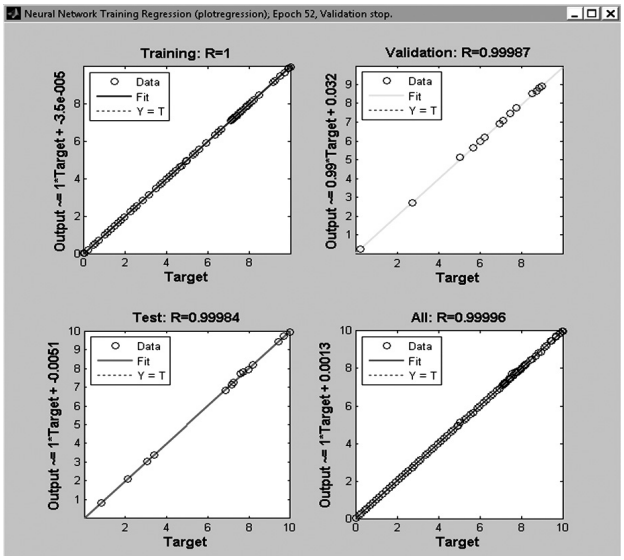

Figure 12: ANN results: training, validation and the test
Slika 12: Rezultati ANN: usposabljanje, ocena in preizkus

R^2 = 0.81324982). The results obtained with the multiple regression analyses were not enough to interpret the experiment results. For this reason, an Annova analysis was also performed. But Annova did not make any contribution towards interpreting the experimental results either. The Statistica software was used for the statistical analysis. The artificial neural network (ANN) model could not be improved. A code was developed for modeling the ANN using Matlab. Different ANN models were tried (**Table 5**) and the best ANN model with the highest learning level was chosen. The code used in the model resulted in very sound results (*RMS* = 0.0055829150, R^2 = 0.9997334826 and *MEP*/% = –0.0000134181). These are the average values of all the ANN-model results.

There are many commercial ANN software products. In this study, the Matlab neural network toolbox was used to obtain a neural network model. There are seven inputs (type of cutting tool, coated carbide/cermet cutting tools, depth of cut, cutting speed, feed rate, F_a, F_r, F_c forces and one output (surface roughness). A multi-layer feed-forward perceptron (MLP 12-13-1) was used in the ANN model. The tansig, logsig and purelin functions were used on the Matlab code and the Levenberg-Marquardt training method was used in the ANN model. **Figure 10** shows the ANN model.

Figure 11 shows the training performance of the model. According to the graphs, the training percentage is a maximum. This shows that the training value can be acceptable. The resulting value is very close to 1. **Figure 12** shows the ANN results: the training, validation and the test regression-analysis results. The performance of the ANN model relates to the deviation between the actual output values and predicted output values. **Table 6** shows a comparison of the experimental values and the Matlab neural-network predictions. The error amounts were used for the analysis of three statistical values.

Table 6: ANN test data
Tabela 6: Podatki ANN-preizkusa

Cutting tool (z)	Depth of cut *d*/mm	Cutting speed *v*/(mm/min)	Feed rate *f*/(mm/r)	F_x (F_a)/N	F_y(F_r)/N	F_z (F_c)/N	Experimental surface roughness (R_a/μm)	ANN model test (*MATLAB*)	*RMS*	R^2	*MEP*
1	0.5	150	0.12	118.5	95.61	224.01	0.708	0.703709	0.004291	0.999963	0.006097
1	0.5	150	0.16	130.96	118.18	280.97	1.046	1.041602	0.004398	0.999982	0.004223
2	1	175	0.12	235.44	163.89	403.76	0.603	0.604894	0.001894	0.99999	–0.00313
2	1	175	0.16	221.03	164.91	474.29	0.866	0.868187	0.002187	0.999994	–0.00252
2	1	175	0.2	237.59	177.01	567.95	1.106	1.103077	0.002923	0.999993	0.00265
3	0.5	200	0.16	83.21	155.97	249.81	0.711	0.713359	0.002359	0.999989	–0.00331
3	0.5	200	0.2	97.96	173.58	310.1	1.018	1.014781	0.003219	0.99999	0.003172
3	0.5	225	0.12	86.49	148.89	226.71	0.465	0.470102	0.005102	0.999882	–0.01085
4	0.5	225	0.2	123.95	102.78	316.82	1.515	1.502162	0.012838	0.999927	0.008546
4	0.5	250	0.12	113.08	82.18	226.48	0.596	0.582287	0.013713	0.999445	0.02355
4	0.5	250	0.2	121.36	121.4	301.84	1.568	1.565077	0.002923	0.999997	0.001868
5	0.5	250	0.2	92.58	126.44	292.2	1.387	1.385913	0.001087	0.999999	0.000784
5	1	150	0.12	204.73	134.97	394.89	0.637	0.636777	0.000223	0.999999	0.000351

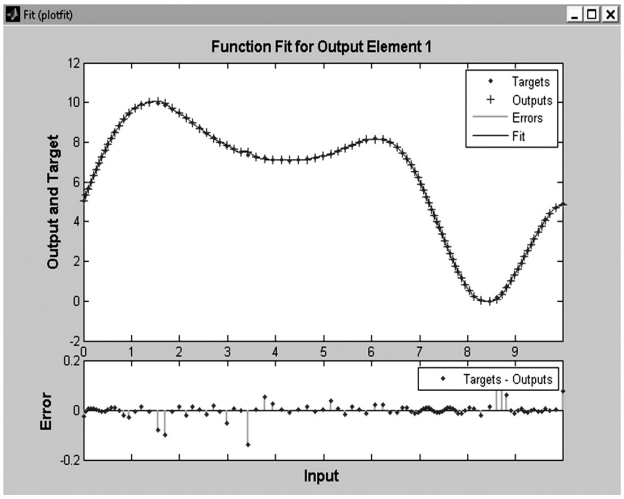

Figure 13: ANN function fit for the output
Slika 13: ANN-funkcja, primerna za izhod

Figure 13 shows ANN function fit for output. **Figure 14** shows ANN error histogram (30 Bins and 20 Bins). These are the statistical errors of the *RMSE* (the root mean square error), R^2 (the absolute fraction of variance) and the *MEP* (the mean error percentage). If these error amounts are calculated according to the value of the output surface roughness, the *RMSE* is found to be smaller than 0.004291, R^2 is 0.999963 and the MEP is around 0.006097 for the training and test data.

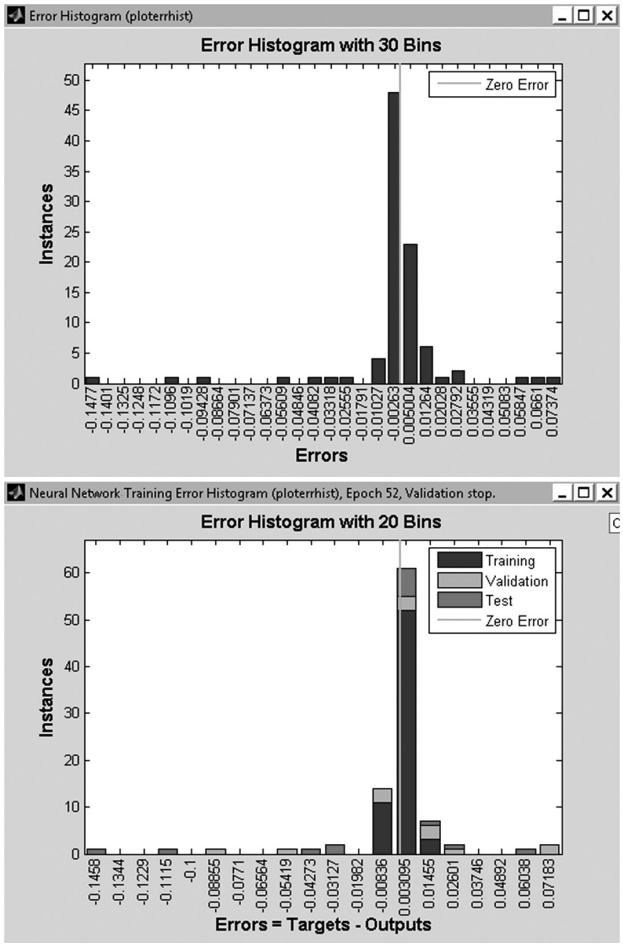

Figure 14: ANN error histograms, 30 Bins and 20 Bins
Slika 14: Histogram ANN-napak, 30 Bins in 20 Bins

The *RMSE*, R^2 and *MEP* values are obtainable with the following equations:

$$RMSE = \sqrt{\frac{1}{p}\sum j\left(t_j - o_j\right)^2} \tag{3}$$

$$RMSE = \sqrt{\left|0.708 - 0.703709\right|^2} = 0.004291$$

The statistical error amount:

$$R^2 = 1 - \frac{\sum j(t_j - o_j)^2}{\sum j(o_j)^2} \tag{4}$$

$$R^2 = 1 - \frac{(0.708 - 0.703709)^2}{(0.703709)^2} = 0.999963$$

and the average percent error:

$$MEP/\% = \frac{\sum j\left(\frac{t_j - o_j}{t_j}\cdot 100\right)}{p} \tag{5}$$

$$MEP/\% = \frac{0.708 - 0.703709}{0.703709}\cdot 100 = 0.006097$$

values are obtained, where t is the target value, o is the output and p is the number of the samples.

5 CONCLUSIONS

An ANN was developed for predicting the surface-roughness values in turning the 50CrV4 (SAE 6150) steel using the cutting forces (F_a, F_r and F_c) and machining parameters. The influences of the machining parameters (cutting speed, feed rate, depth of cut and cutting-tool material) on the cutting forces and surface roughness were investigated. The optimum configuration of the ANN consisted of three layers with the LM neural network approach. The statistical-analysis results are: *RMSE* = 0.004291, R^2 = 0.999963, *MEP*/% =0.006097. The predicted surface-roughness values using the ANN model are in good agreement with the experimentally obtained surface-roughness values. The ANN based on the calculation can be used to predict the surface roughness depending on the machining parameters. These results can be used to predict the cutting forces and surface roughness in machining the 50CrV4 (SAE 6150) steel using the coated carbide and cermet cutting tools. In conclusion, a surface-roughness prediction not requiring an experimental study with ANN models can provide both simplicity and fast calculation. It is shown that an ANN model can be used as an effective and alternative method of experimental studies improving both the time and economical optimization of the machining.

6 REFERENCES

[1] N. Boubekri, J. Rodriguez, S. Asfour, Development of an aggregate indicator to assess the machinability of steels, Journal of Materials Processing Technology, 134 (**2003**), 159–165

[2] A. S. Kumar, A. R. Durai, T. Sornakumar, Machinability of hardened steel using alumina based ceramic cutting tools, International Journal of Refractory Metals & Hard Materials, 21 (**2003**), 109–117

[3] Z. Tekiner, S. Yeşilyurt, Investigation of the cutting parameters depending on process sound during turning of AISI 304 austenitic stainless steel, Materials and Design, 25 (**2004**), 507–513

[4] J. G. Lima, R. F. Ávila, A. M. Abrão, M. Faustino, J. Paulo Davim, Hard turning: AISI 4340 high strength low alloy steel and AISI D2 cold work tool steel, Journal of Materials Processing Technology, 169 (**2005**), 388–395

[5] J. A. Arsecularatne, L. C. Zhang, C. Montross, Wear and tool life of tungsten carbide, PCBN and PCD cutting tools, International Journal of Machine Tools & Manufacture, 46 (**2006**), 482–491

[6] L. L. Qian, M. R. Hossan, Effect on cutting force in turning hardened tool steels with cubic boron nitride inserts, Journal of Materials Processing Technology, 191 (**2007**), 274–278

[7] A. Ebrahimi, M. M. Moshksar, Study of machinability in boring operation of microalloyed and heat-treated alloy steels, Materials Science and Engineering A, 460–461 (**2007**), 314–323

[8] S. K. Khrais, Y. J. Lin, Wear mechanisms and tool performance of TiAlN PVD coated inserts during machining of AISI 4140 steel, Wear, 262 (**2007**), 64–69

[9] R. Tanaka, Y. Yamane, K. Sekiya, N. Narutaki, T. Shiraga, Machinability of BN free-machining steel in turning, International Journal of Machine Tools & Manufacture, 47 (**2007**), 1971–1977

[10] Y. Işık, Investigating the machinability of tool steels in turning operations, Materials and Design, 28 (**2007**), 1417–1424

[11] P. J. Arrazola, I. Arriola, M. A. Davies, A. L. Cooke, B. S. Dutterer, The effect of machinability on thermal fields in orthogonal cutting of AISI 4140 steel, CIRP Annals – Manufacturing Technology, 57 (**2008**), 65–68

[12] R. Yiğit, E. Celik, K. F. Findik, S. Köksal, Effect of cutting speed on the performance of coated and uncoated cutting tools in turning nodular cast iron, Journal of Materials Processing Technology, 204 (**2008**), 80–88

[13] M. C. Cakir, Y. Isik, Investigating the machinability of austempered ductile irons having different austempering temperatures and times, Materials and Design, 29 (**2008**), 937–942

[14] D. I. Lalwani, N. K. Mehta, P. K. Jain, Experimental investigations of cutting parameters influence on cutting forces and surface roughness in finish hard turning of MDN250 steel, Journal of Materials Processing Technology, 206 (**2008**), 167–179

[15] T. V. SreeramaReddy, T. Sornakumar, M. VenkataramaReddy, R. Venkatram, Machinability of C45 steel with deep cryogenic treated tungsten carbide cutting tool inserts, Int. Journal of Refractory Metals & Hard Materials, 27 (**2009**), 181–185

[16] M. A. Xavior, M. Adithan, Determining the influence of cutting fluids on tool wear and surface roughness during turning of AISI 304 austenitic stainless steel, Journal of Materials Processing Technology, 209 (**2009**), 900–909

[17] A. Ebrahimi, M. M. Moshksar, Evaluation of machinability in turning of microalloyed and quenched-tempered steels: Tool wear, statistical analysis, chip morphology, Journal of Materials Processing Technology, 209 (**2009**), 910–921

[18] M. Nalbant, H. Gokkaya, I. Toktas, G. Sur, The experimental investigation of the effects of uncoated, PVD- and CVD-coated cemented carbide inserts and cutting parameters on surface roughness in CNC turning and its prediction using artificial neural networks, Robotics and Computer-Integrated Manufacturing, 25 (**2009**), 211–223

[19] V. N. Gaitonde, S. R. Karnik, L. Figueria, J. P. Davim, Machinability investigations in hard turning of AISI D2 cold work tool steel with conventional and wiper ceramic inserts, Int. Journal of Refractory Metals & Hard Materials, 27 (**2009**), 754–763

[20] D. G. Thakur, B. Ramamorthy, L. Vijarayaghavan, Study on the machinability characteristics of superalloy Inconel 718 during high speed turning, Materials and Design, 30 (**2009**), 1718–1725

[21] P. J. Arrazola, I. Arriola, M. A. Davies, Analysis of the influence of tool type, coatings, and machinability on the thermal fields in orthogonal machining of AISI 4140 steels, CIRP Annals – Manufacturing Technology, 58 (**2009**), 85–88

[22] K. Boucha, M. Y. Athmane, T. Mabrouki, F. J. Rigal, Statistical analysis of surface roughness and cutting forces using response surface methodology in hard turning of AISI 52100 bearing steel with CBN tool, Int. Journal of Refractory Metals & Hard Materials, 28 (**2010**), 349–361

UDK 621.793:669.14
Original scientific article/Izvirni znanstveni članek

ISSN 1580-2949
MTAEC9, 48(2)237(2014)

ESTIMATION OF THE BORON DIFFUSION COEFFICIENTS IN FeB AND Fe_2B LAYERS DURING THE PACK-BORIDING OF A HIGH-ALLOY STEEL

DOLOČANJE KOEFICIENTA DIFUZIJE BORA V PLASTEH FeB IN Fe_2B MED BORIRANJEM VISOKO LEGIRANEGA JEKLA V SKRINJI

Zahra Nait Abdellah[1,2], Mourad Keddam[1]

[1]Laboratoire de Technologie des Matériaux, Département de Sciences des Matériaux, Faculté de Génie Mécanique et Génie des Procédés, USTHB, B.P N°32, 16111 El-Alia, Bab-Ezzouar, Alger, Algérie
[2]Département de Chimie, Faculté des sciences, Université Mouloud Mammeri, 15000 Tizi-Ouzou, Algérie
keddam@yahoo.fr

Prejem rokopisa – received: 2013-03-31; sprejem za objavo – accepted for publication: 2013-06-07

In this work we propose a diffusion model to estimate the boron diffusion coefficients in FeB and Fe_2B layers during the pack-boriding of AISI M2 steel in the temperature range 1173–1323 K for a treatment time of 4–8 h.
The proposed model is based on the mass-balance equations at the two growth fronts – FeB/Fe_2B and Fe_2B/substrate – under certain assumptions. The estimated values of the boron activation energies in the FeB and Fe_2B layers were compared with the literature data. The present model was extended to predict the thickness of each boride layer for the borided samples at different temperatures for 10 h. Iso-thickness diagrams were established to be used as a tool for predicting the thickness of each boride layer as a function of the two parameters: temperature and time. Finally, a simple equation was proposed to estimate the required time to obtain a single Fe_2B layer by diffusion annealing.

Keywords: boriding, incubation times, Fick's laws, simulation, growth kinetics, annealing

Predstavljeno delo predlaga model difuzije za določanje koeficienta difuzije bora v plasteh FeB in Fe_2B med boriranjem v skrinji jekla AISI M2 v temperaturnem območju 1173–1323 K pri spreminjanju trajanja postopka od 4 h do 8 h.
Predlagani model temelji na enačbi masne balance na dveh rastočih mejnih ploskvah (FeB/Fe_2B) in (Fe_2B/osnova) pri določenih predpostavkah. Določena vrednost aktivacijske energije bora v FeB- in Fe_2B-plasti je bila primerjana s podatki iz literature. Predstavljeni model je bil razširjen, da bi lahko napovedal debelino vsake od obeh boridnih plasti za borirane vzorce pri različnih temperaturah in trajanju do 10 h. Postavljeni so bili diagrami enake debeline, ki so uporabni kot orodje za napovedovanje debeline vsakega od boriranih slojev v odvisnosti od dveh parametrov (temperature in časa). Predlagana je preprosta enačba za določanje potrebnega časa za nastanek plasti Fe_2B z difuzijskim žarjenjem.

Ključne besede: boriranje, inkubacijski čas, Fickovi zakoni, simulacija, kinetika rasti, žarjenje

1 INTRODUCTION

One of the surface-modification methods for improving the surface properties of ferrous and non-ferrous alloys is boriding. According to the Fe-B binary system, two kinds of iron borides, i.e., FeB and Fe_2B, with a narrow range of composition can be identified.[1] The boriding process applies in the temperature range 1073–1323 K between 1 h to 10 h and it can be carried out in solid, liquid or gaseous media. The possible formation of the FeB and Fe_2B iron borides depends upon various factors, such as the boron activity of the boriding medium, the chemical composition of the substrate, the process temperature and the treatment time. The morphology of the boride layers is influenced by the presence of alloying elements in the matrix. Saw-tooth-shaped layers are obtained in low-alloy steels, whereas in high-alloy steels, the interfaces tend to be flat. The modelling of the boriding kinetics is considered as a suitable tool to match the case depth with the intended industrial applications for this borided steel. So, the modelling of the growth kinetics for boride layers has gained much attention to simulate the boriding kinetics during recent decades.[2–26]

In the present work an original diffusion model is proposed to estimate the boron diffusion coefficients in the FeB and Fe_2B layers grown on AISI M2 steel by considering the boride incubation times. A non-linear boron-concentration profile is assumed through the boride layers. The mass-balance equations were applied to the two diffusion fronts: the FeB/Fe_2B and Fe_2B/substrate interfaces in the temperature range 1173–1323 K. In addition, a simple equation was proposed to estimate the required time to obtain a single Fe_2B layer by diffusion annealing.

2 THE DIFFUSION MODEL

The model takes into account the FeB/Fe_2B bilayer growth on the saturated substrate with boron atoms, as shown in **Figure 1**.

C_{up}^{FeB} and C_{low}^{FeB} (= 16.23 % B) are the upper and lower boron mass concentrations in the FeB, while C_{up}^{FeB} (= 9 % B) and C_{low}^{FeB} (= 8.83 % B) are, respectively, the upper

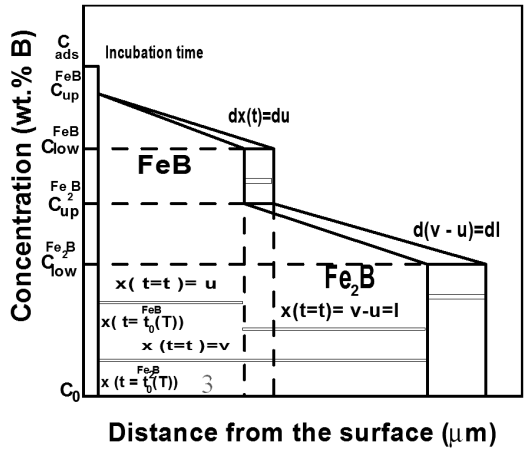

Figure 1: Boron concentration profile through the FeB/Fe_2B bilayer
Slika 1: Profil koncentracije bora skozi plasti (FeB/Fe_2B)

and lower boron concentrations in the Fe_2B. C_{ads} denotes the adsorbed concentration of boron,[15] while u is the position of the FeB/Fe_2B interface, and v is the position of the Fe_2B/substrate interface. C_0 is the boron solubility in the matrix and is equal to $35 \cdot 10^{-4}$ % B.[2] The upper boron content in the FeB phase (C_{up}^{FeB}), imposed by the boriding medium, gives rise to the two iron borides: FeB and Fe_2B. From a thermodynamic point of view, the FeB phase exhibits a narrow composition range (of about the mole fraction x = 1 % B or the mass fraction w = 0.2 % B), as identified by Massalski.[27] The upper boron content in the FeB phase was taken in the composition range of mass fractions 16.25–16.43 % B to obtain a bilayer configuration consisting of the two iron borides, FeB and Fe_2B.

The following assumptions are considered during the formulation of the diffusion model:

- The kinetics is dominated by the diffusion-controlled mechanism
- The growth of the boride layers is a consequence of the boron diffusion perpendicular to the sample surface
- The range of homogeneity of the iron borides is about x = 1 % B
- The iron borides nucleate after a certain incubation time
- The boride layer is thin in comparison to the sample thickness
- A local equilibrium occurs at the phase interfaces
- A planar morphology is assumed for the phase interfaces
- The volume change during the phase transformation is ignored
- The diffusion coefficient of boron in each iron boride does not vary with the boron concentration and follows an Arrhenius relationship
- A uniform temperature is assumed throughout the sample
- The alloying elements have no effect on the boron diffusion
- The presence of porosity is neglected during the boron diffusion.

The initial conditions of the diffusion problem are set up as follows:

$$C_{FeB}\{x(t \succ 0)=0\}=0$$
$$C_{Fe_2B}\{x(t \succ 0)=0\}=0 \quad (1)$$
$$C_{Fe}\{x(t \succ 0)=0\}=0$$

The boundary conditions are given by the following equations:

$$C_{FeB}\left\{x[t=t_0^{FeB}(T)]=0\right\}=C_{up}^{FeB} \text{ for } C_{ads} \succ 16.23wt.\%B \quad (2)$$

$$C_{FeB}\left\{x[t=t_0^{FeB}(T)]=0\right\}=C_{low}^{FeB} \text{ for } C_{ads} \prec 16.23wt.\%B$$

and with the FeB phase: (3)

$$C_{Fe_2B}\left\{x[t=t_0^{Fe_2B}(T)]=0\right\}=C_{up}^{Fe_2B} \text{ for}$$

$8.83wt.\%B \prec C_{ads} \prec 16.23wt.\%B$ and without the FeB phase: (4)

$$C_{Fe_2B}\left\{x[t=t_0^{Fe_2B}(T)]=0\right\}=C_{low}^{Fe_2B} \text{ for } C_{ads} \prec 8.83wt.\%B$$

and without the FeB phase: (5)

$$C_{FeB}(x(t=t)=u)=C_{low}^{FeB} \quad (6)$$
$$C_{Fe_2B}(x(t=t)=u)=C_{up}^{Fe_2B} \quad (7)$$
$$C_{Fe_2B}(x(t=t)=v)=C_{low}^{Fe_2B} \quad (8)$$
$$C_{Fe}(x(t=t)=v)=C_0 \quad (9)$$

The mass-balance equations[28] are given by the equations (10) and (11):

$$w_{FeB}\left(\frac{du}{dt}\right)=\left[J_B^{FeB}-J_B^{Fe_2B}\right]_{x=u} \quad (10)$$

$$w_{Fe_2B}\left(\frac{dv}{dt}\right)+w'\left(\frac{du}{dt}\right)=\left[J_B^{Fe_2B}\right]_{x=v} \quad (11)$$

with

$$w_{FeB}=\left[0.5\times(C_{up}^{FeB}-C_{low}^{FeB})+(C_{low}^{FeB}-C_{up}^{Fe_2B})\right]$$
$$w_{Fe_2B}=\left[0.5\times(C_{up}^{Fe_2B}-C_{low}^{Fe_2B})+(C_{low}^{Fe_2B}-C_0)\right]$$
$$w'=0.5\times(C_{up}^{Fe_2B}-C_{low}^{Fe_2B})$$

The boron flux through a given boride layer is obtained from Fick's first law as follows:

$$J_B^i=-D_B^i\frac{\partial C_i(x,t)}{\partial x} \text{ with } i = (\text{FeB or } Fe_2B) \quad (12)$$

D_B^{FeB} and $D_B^{Fe_2B}$ are, respectively, the diffusion coefficients of boron in the FeB and Fe_2B phases. The boron concentration profile in the FeB layer is given by:

$$C_{FeB}(x,t)=C_{up}^{FeB}+\frac{(C_{low}^{FeB}-C_{up}^{FeB})}{erf\left(\frac{u}{2\sqrt{D_B^{FeB}t}}\right)}\cdot erf\left(\frac{x}{2\sqrt{D_B^{FeB}t}}\right)$$

For $0 \le x \le u$ (13)

In the same way, the boron concentration profile in the Fe_2B layer can be obtained as follows:

$$C_{Fe_2B}(x,t) = C_{up}^{Fe_2B} + \frac{(C_{low}^{Fe_2B} - C_{up}^{Fe_2B})}{\left[erf\left(\frac{u}{2\sqrt{D_B^{Fe_2B} t}}\right) - erf\left(\frac{v}{2\sqrt{D_B^{Fe_2B} t}}\right)\right]} \cdot \left[erf\left(\frac{u}{2\sqrt{D_B^{Fe_2B} t}}\right) - erf\left(\frac{x}{2\sqrt{D_B^{Fe_2B} t}}\right)\right]$$

For $u \le x \le v$ (14)

The FeB layer thickness u grows parabolically according to equation (15), where k_{FeB} represents the parabolic growth constant at the FeB/Fe_2B interface:

$$u = k_{FeB}\left[t - t_0^{FeB}(T)\right]^{1/2} \quad (15)$$

The distance v is the location of the Fe_2B/substrate interface and k its parabolic growth constant (equation (16)) and the difference ($l = v - u$) denotes the layer thickness of the Fe_2B (equation 17):

$$v = k\left[t - t_0(T)\right]^{1/2} \quad (16)$$

$$l = v - u = k\left[t - t_0(T)\right]^{1/2} - k_{FeB}\left[t - t_0^{FeB}(T)\right]^{1/2} \quad (17)$$

with $t_0^{FeB}(T) \succ t_0(T)$ and $k \succ k_{FeB}$

where $t_0(T)$ is the boride incubation time of the total boride layer and $t_0^{FeB}(T)$ is the boride incubation time of the FeB layer. To take into account the effect of the boride incubation times when solving the mass-balance equations, it is necessary to define the two parameters $\beta_{FeB}(T)$ and $\beta(T)$:

$$\beta_{FeB}(T) = \left[1 - \frac{t_0^{FeB}(T)}{t}\right]^{0.5} \quad (18)$$

and

$$\beta(T) = \left[1 - \frac{t_0(T)}{t}\right]^{0.5} \quad (19)$$

The layer thickness of the FeB (u) is related to the $\beta_{FeB}(T)$ parameter by equation (20):

$$u = k_{FeB}\beta_{FeB}(T)\sqrt{t} \quad (20)$$

In the same way, the layer thickness of the Fe_2B (l) is expressed using equation (21):

$$l = \left[k\beta(T) - k_{FeB}\beta_{FeB}(T)\right]\sqrt{t} \quad (21)$$

3 ESTIMATION OF THE BORON DIFFUSION COEFFICIENTS IN THE FeB AND Fe_2B LAYERS

To estimate the boron diffusion coefficients in the FeB and Fe_2B layers, the experimental results published by Campos-Silva et al.[29] on borided AISI M2 steel were used. In this reference work, the powder-pack boriding was carried out at four temperatures, (1173, 1223, 1273 and 1323) K, for three exposure times, (4, 6 and 8) h, using the B_4C Durborid as a boriding medium. Eighty measurements were performed on different cross-sections of the borided samples from the AISI M2 steel to determine the thickness of each boride layer.

Tables 1 and **2** list the experimental parabolic growth constants for each phase interface with the corresponding incubation times. The experimental values of the parabolic growth constants at each phase interface were obtained from the slopes of the curves relating the squared boride layer thickness to the boriding time. The boride incubation times were deduced for a null boride layer thickness.

Table 1: Experimental values of the parabolic growth constants at the FeB/Fe_2B interface in the temperature range 1173–1323 K with the corresponding boride incubation times

Tabela 1: Eksperimentalne vrednosti konstant parabolične rasti na stiku (FeB/Fe_2B) v temperaturnem območju 1173–1323 K, z ustreznim inkubacijskim časom borida

T/K	Experimental growth Constants: k_{FeB}/(μm $s^{-1/2}$)	$t_0^{FeB}(T)$/s
1173	0.065	10131
1223	0.121	6085.7
1273	0.179	4347.8
1323	0.238	3815.5

Table 2: Experimental values of the parabolic growth constants at the Fe_2B/substrate interface in the temperature range 1173–1323 K with the corresponding boride incubation times

Tabela 2: Eksperimentalne vrednosti konstant parabolične rasti na stiku (Fe_2B/podlaga) v temperaturnem območju 1173–1323 K, z ustreznim inkubacijskim časom borida

T/K	Experimental growth Constants: k/(μm $s^{-1/2}$)	$t_0(T)$/s
1173	0.168	8806.2
1223	0.305	4729
1273	0.448	4323
1323	0.589	3742.7

It was demonstrated that the higher boriding temperatures involve the shorter incubation times,[24] as shown in **Tables 1** and **2**. The two respective parameters $\beta_{FeB}(T)$ and $\beta(T)$ are linearly dependent on the boriding temperature and can be approximated by equations (22) and (23) from a linear fitting of the experimental data displayed in **Figure 2**:

$$\beta_{FeB}(T) = (1{\cdot}39\times10^{-3}\,T - 0.8579) \quad (22)$$

and

$$\beta(T) = (1{\cdot}40\times10^{-3}\,T - 0.8470) \quad (23)$$

For this purpose, a computer code written in Matlab (version 6.5) was used to estimate the boron diffusivity in each boride layer. This program requires the following input data: the time, the temperature, the lower and upper boron concentrations at each phase interface as well as the two parameters $\beta_{FeB}(T)$ and $\beta(T)$. By solving the mass-balance equations (equations (10) and (11)) via the Newton-Raphson method,[30] it is possible to determine the boron diffusion coefficients in the FeB and Fe_2B layers. **Table 3** summarizes the estimated values of the boron diffusion coefficients in the FeB and Fe_2B layers for an upper boron content equal to w = 16.40 % in the FeB phase.

Figure 3 depicts the temperature dependence of the boron diffusion coefficients in the FeB and Fe_2B layers according to the Arrhenius equation. The value of the

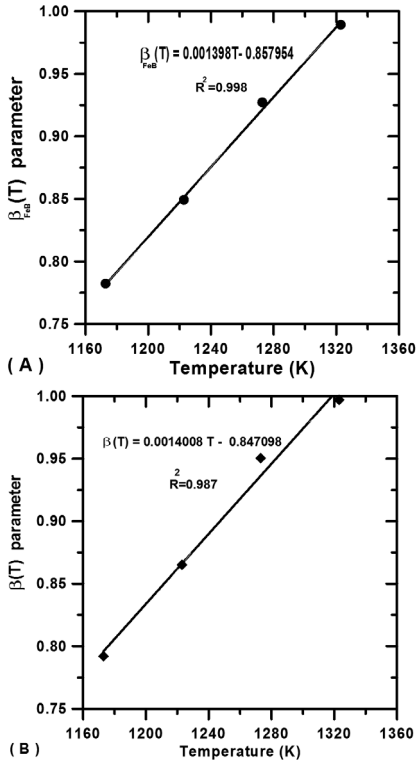

Figure 2: Evolution of the two parameters as a function of the boriding temperature: a) $\beta_{FeB}(T)$ and b) $\beta(T)$

Slika 2: Razvoj dveh parametrov v odvisnosti od temperature boriranja: a) $\beta_{FeB}(T)$ in b) $\beta(T)$

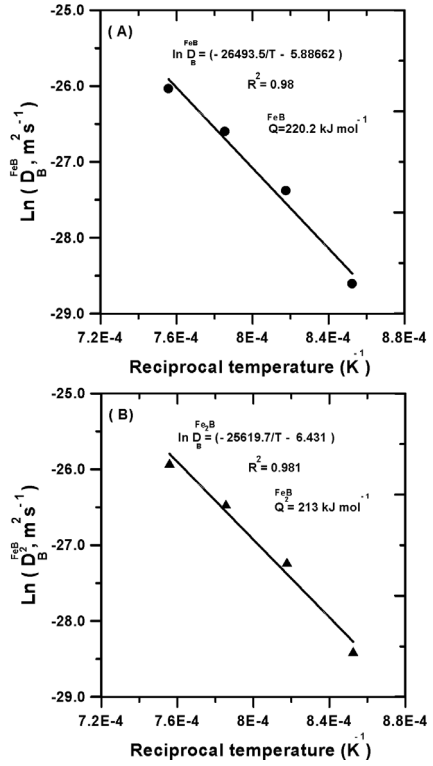

Figure 3: An Arrhenius relationship between the boron diffusion coefficient and the temperature: a) FeB layer, b) Fe_2B layer

Slika 3: Arrheniusova odvisnost med koeficientom difuzije bora in temperaturo: a) FeB-plast, b) Fe_2B-plast

Table 3: Determination of the boron diffusion coefficient in each boride layer for an upper boron mass fraction content of w =16.40 % in the FeB layer

Tabela 3: Določanje koeficienta difuzije bora v vsaki boridni plasti za zgornji masni delež vsebnosti bora 16,40 % v plasti FeB

T/K	$D_B^{FeB}(m^2s^{-1})\times10^{-12}$	$D_B^{Fe_2B}(m^2s^{-1})\times10^{-12}$
1173	0.376	0.462
1223	1.282	1.502
1273	2.797	3.227
1323	4.915	5.539

boron activation energy in each boride layer can be easily obtained from the slopes of the corresponding curves. So, the boron diffusion coefficients in the FeB and Fe_2B layers are, respectively, given by equations (24) and (25):

$$D_B^{FeB} = 2.8\times10^{-3}\ \exp\frac{-220.2\ \text{kJ/mol}}{RT}\ (\text{m}^2\,\text{s}^{-1}) \qquad (24)$$

$$D_B^{Fe_2B} = 1.6\times10^{-3}\ \exp\frac{-213\ \text{kJ/mol}}{RT}\ (\text{m}^2\,\text{s}^{-1}) \qquad (25)$$

where R is the universal gas constant (= 8.314 J/(mol K)), and T represents the absolute temperature in Kelvin.

The reported values of the activation energies[24,29,31–33] of the borided steels are listed in **Table 4** together with the values from this work. The obtained values of the activation energies are found to be dependent on the boriding method and on the chemical composition of the substrates.

In **Table 5**, a comparison was achieved between the experimental boride layer thicknesses and the simulated ones at different temperatures for 10 h of treatment. The simulated results were obtained from equations (20) and (21). The present model was able to predict the boride layer thickness (FeB or Fe_2B) for the given boriding conditions.

Table 4: Values of the boron activation energies obtained for different borided steels

Tabela 4: Vrednosti aktivacijske energije bora, dobljene iz različnih boriranih jekel

Material	Boriding method	Activation energy of FeB E/(kJ mol^{-1})	Activation energy of Fe_2B E/(kJ mol^{-1})	Reference
AISI M2	Paste	283	239.4	32
AISI4140	Paste	–	168.5	33
AISI H13	Powder-pack	–	186.2	31
AISI 316L	Powder-pack	204	198	24
AISI M2	Powder-pack	223	207	29
AISI M2	Powder-pack	220.2	213	Present study

Table 5: Experimental (exp.) and simulated (sim.) values of the boride layer thickness in the temperature range 1173–1323 K for 10 h of treatment, with an upper boron mass fraction of content of w = 16.40 % in the FeB phase

Tabela 5: Eksperimentalne (exp.) in simulirane (sim.) vrednosti za debelino plasti borida v temperaturnem območju 1173–1323 K, za 10 h obdelave pri gornjem masnem deležu vsebnosti bora 16,40 %, v FeB plasti

T/K	FeB (μm) exp.	FeB (μm) sim.	Fe_2B (μm) exp.	Fe_2B (μm) sim.
1173	10.17	10.30	19.66	16.70
1223	20.98	17.89	32.81	28.23
1273	28.30	29.75	51.83	45.81
1323	40.24	47.60	72.28	71.67

In **Table 6**, the predicted values of the boride layer thicknesses are compared with the experimentally determined values in the temperature range 1173–1323 K for a treatment time varying from 4 h to 8 h. Good agreement was observed between the experimental data and the simulation results for an upper boron content equal to w = 16.40 % in the FeB phase.

Table 6: Experimental (exp.) and simulated values (sim.) of the boride layer thickness in the temperature range 1173–1323 K for different treatment times with an upper boron content w = 16.40 % in the FeB phase

Tabela 6: Eksperimentalne (exp.) in simulirane (sim.) vrednosti debeline plasti borida pri temperaturah 1173–1323 K za različne čase obdelave in zgornjo vsebnostjo bora w = 16,40 % v FeB-fazi

T/K	Time (h)	FeB (μm) exp.	FeB (μm) sim.	Fe_2B (μm) exp.	Fe_2B (μm) sim.
1173	4	4.24	6.47	8.31	10.53
	6	6.96	7.92	12.04	12.89
	8	8.88	9.15	14.87	14.89
1223	4	11.03	11.32	18.96	17.85
	6	15.07	13.86	24.54	21.86
	8	18.23	16.00	29.08	25.24
1273	4	17.94	18.81	27.02	28.97
	6	23.51	23.04	35.37	35.48
	8	28.00	26.60	42.09	40.97
1323	4	24.48	24.89	36.31	35.90
	6	31.73	32.27	46.97	46.43
	8	37.61	38.25	55.61	54.98

Figure 4 displays the iso-thickness diagrams describing the evolution of the boride layer thickness as a function of the time and the boriding temperature. The results derived from **Figure 4** can be used as a tool to predict the boride layer thickness in relation with its practical use in an industrial area.

4 OBTAINING OF A SINGLE LAYER OF Fe_2B BY DIFFUSION ANNEALING

In industrial practice it is possible to reduce the brittleness of boride layers by controlling their microstructure. It is known that a single Fe_2B boride layer is more desirable than a dual FeB-Fe_2B layer.[34] This makes it possible to reduce the FeB layer thickness by applying a diffusion annealing in a hydrogen atmosphere. During this stage, the supply of boron is stopped since the concentration gradient of boron in the FeB is null (i.e., $C_{up}^{FeB} = C_{low}^{FeB}$ = 16.23 %), the FeB layer will be converted into an Fe_2B layer. The time required to eliminate the FeB layer during the diffusion annealing can be obtained from equation (26):

$$t_{u_{FeB}=0} = \frac{u \times l \times (C_{low}^{FeB} - C_{up}^{Fe_2B})}{D_B^{Fe_2B}(C_{up}^{Fe_2B} - C_{low}^{Fe_2B})} \quad (26)$$

where u is the FeB layer thickness (μm), l the Fe_2B layer thickness (μm) and $D_B^{Fe_2B}$ represents the boron diffusion coefficient in Fe_2B. It is clear that the annealing time depends on the boron diffusion coefficient in Fe_2B, and also on the thickness of each boride layer. During the diffusion annealing, an infinitesimal reduction of the FeB layer is related to the infinitesimal growth of the Fe_2B layer by equation (27):

$$\Delta u = -\left(\frac{w_{Fe_2B}}{w_{FeB} + w_{Fe_2B} + w'}\right)\Delta l = -0.5493\Delta l \quad (27)$$

The value of the Fe_2B layer thickness l' (μm) after diffusion annealing becomes:

$$l' = l + \frac{\Delta u}{0.5493} \quad (28)$$

Table 7 presents the simulation results obtained from equations (26) and (28) to estimate the Fe_2B layer thickness after diffusion annealing and the time required

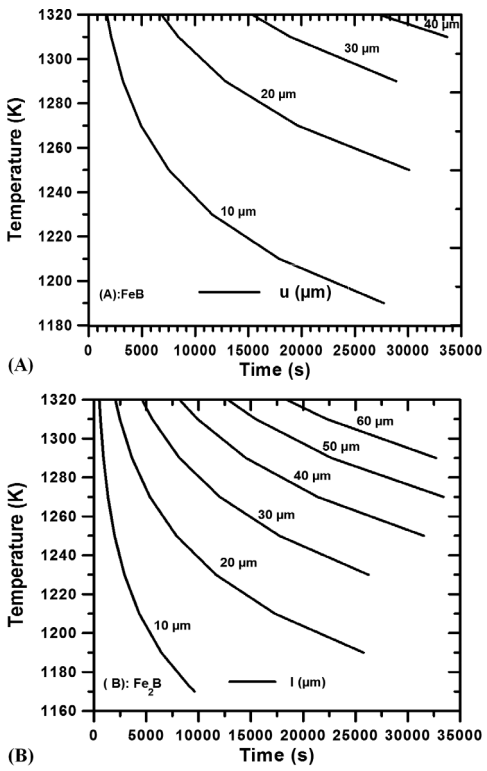

Figure 4: Iso-thickness diagrams describing the evolution of the boride layers: a) FeB, b) Fe_2B

Slika 4: Diagram enakih debelin opisuje razvoj boridnih plasti: a) FeB, b) Fe_2B

to eliminate the FeB layer in the case of the borided samples treated at different temperatures for 10 h. The obtained annealing times are increased with an increase of the boriding temperature since the boride layer becomes thicker. In this context, Kulka et al.[26] have experimentally determined the annealing time using a hydrogen atmosphere to obtain a single Fe_2B layer on gas borided Armco Fe at 1173 K for 2 h in a gas mixture (H_2–BCl_3). They found that the total elimination of the FeB layer took about 1 h.

Furthermore, it was shown by Dybkov et al.[35] that annealing of a borided Fe–Cr sample for 6 h resulted in the disappearance of the FeB layer.

Table 7: Estimation of the Fe_2B layer thickness and the time required to eliminate the FeB layer for the borided samples at different temperatures for 10 h

Tabela 7: Določanje debeline plasti Fe_2B in čas, potreben za odpravo FeB plasti, za vzorce, borirane 10 h pri različnih temperaturah

T/K	FeB (μm) sim.	Fe_2B (μm) sim.	Fe_2B (μm) After diffusion annealing Equation (28)	Annealing time $t_{u_{FeB}=0}$/h Equation (26)
1173	10.30	16.70	35.45	4.15
1223	17.89	28.23	60.79	4.99
1273	29.75	45.81	99.96	5.92
1323	47.60	71.67	158.32	6.93

5 CONCLUSIONS

In this work an original diffusion model was proposed to estimate the boron diffusion coefficients in the FeB and Fe_2B layers grown on AISI M2 steel. To determine the boron activation energy in each boride layer, the mass-balance equations were formulated, including the effect of the boride incubation times. The estimated boron activation energies were compared with the literature data. The present model was extended to predict the thickness of each boride layer for the borided samples at different temperatures for 10 h. Iso-thickness diagrams were established to be used as a tool to predict the thickness of each boride layer as a function of the two parameters (temperature and time). The required time to obtain a single Fe_2B layer by diffusion annealing was estimated on the basis of a simple equation. The formation of a single Fe_2B layer on AISI M2 steel depended on the boriding parameters.

Acknowledgements

This work was carried out in the framework of the CNEPRU project under code number J0300220100093 of the Algerian Ministry of Higher Education and Scientific Research.

6 REFERENCES

[1] S. A. Sinha, Boriding, J. Heat Treat., 4 (**1991**), 437–447
[2] M. Keddam, Appl. Surf. Sci., 253 (**2006**), 757–761
[3] M. Keddam, Int. J. Mater. Res., 100 (**2009**), 901–905
[4] M. Keddam, S. M. Chentouf, Appl. Surf. Sci., 252 (**2005**), 393–399
[5] R. D. Ramdan, T. Takaki, Y. Tomita, Mater. Trans., 49 (**2008**), 2625–2631
[6] M. Keddam, Defect Diffus. Forum, 273–276 (**2008**), 318–322
[7] I. Campos, M. Islas, G. Ramírez, L. Zuniga, C. Villa Velázquez, C. Mota, Appl. Surf. Sci., 253 (**2007**), 6226–6231
[8] M. Keddam, Appl. Surf. Sci., 236 (**2004**), 451–455
[9] I. Campos, G. Ramírez, U. Figueroa, C. V. Velázquez, Surf. Eng., 23 (**2007**), 216–222
[10] I. Campos, G. Ramírez, U. Figueroa, J. Martinez, O. Morales, Appl. Surf. Sci., 253 (**2007**), 3469–3475
[11] D. S. Kukharev, S. P. Fizenko, S. I. Shabunya, J. Eng. Phys. Therm., 69 (**1996**), 187–193
[12] C. M. Brakman, A. J. W. Gommers, E. J. Mittemeijer, J. Mater. Res., 4 (**1989**), 1354–1370
[13] I. Campos-Silva, M. Ortíz-Domínguez, Int. J. Microstructure and Materials Properties, 5 (**2010**), 26–38
[14] M. Ortiz-Domínguez, E. Hernandez-Sanchez, J. Martinez-Trinídad, M. Keddam, I. Campos-Silva, Kovove Materialy, 48 (**2010**), 1–6
[15] L. G. Yu, X. J. Chen, K. A. Khor, G. Sundararajan, Acta Mater., 53 (**2005**), 2361–2368
[16] M. Keddam, R. Chegroune, Appl. Surf. Sci., 256 (**2010**), 5025–5030
[17] M. Keddam, M. Ortiz-Domínguez, I. Campos-Silva, J. Martinez-Trinídad, J. Appl. Surf. Sci., 256 (**2010**), 3128–3132
[18] M. Keddam, Defect Diffus. Forum, 297–301 (**2010**), 269–274
[19] M. Ortiz-Domínguez, I. Campos-Silva, J. Martínez-Trinidad, M. Elías-Espinosa, E. Hernández-Sánchez, D. Bravo-Bárcenas, Defect Diffus. Forum, 297–301 (**2010**), 294–299
[20] I. Campos-Silva, M. Ortiz-Domínguez, M. Keddam, N. López-Perrusquia, A. Carmona-Vargas, M. Elias-Espinosa, Appl. Surf. Sci., 255 (**2009**), 9290–9295
[21] I. Campos-Silva, N. López-Perrusquia, M. Ortiz-Domínguez, U. Figueroa-López, O. A. Gómes-Vargas, A. Meneses-Amador, G. Rodríguez-Castro, Kovove Mater., 47 (**2009**), 1–7
[22] I. Campos-Silva, M. Ortiz-Domínguez, C. Villa Velazquez, R. Escobar, N. López, Defect Diffus. Forum, 272 (**2007**), 79–86
[23] I. Campos-Silva, M. Ortiz-Domínguez, N. López-Perrusquia, R. Escobar-Galindo, O. A. Gómez-Vargas, E. Hernández-Sánchez, Defect Diffus. Forum, 283–286 (**2008**), 681–686
[24] I. Campos-Silva, M. Ortiz-Domínguez, O. Bravo-Bárcenas, M. A. Doñu-Ruiz, D. Bravo-Bárcenas, C. Tapia-Quintero, M. Y. Jiménez-Reyes, Surface and Coatings Technology, 205 (**2010**), 403–412
[25] M. Keddam, Appl. Surf. Sci., 257 (**2011**), 2004–2010
[26] M. Kulka, N. Makuch, A. Pertek, L. Maldzinski, Journal of Solid State Chemistry, 199 (**2013**), 196–203
[27] T. B. Massalski, Binary Alloys Phase diagrams, 2nd ed., ASM International, Metals Park, OH 1990
[28] M. Keddam, M. E. Djeghlal, L. Barrallier, Mater. Sci. Eng., A 378 (**2004**), 475–478
[29] I. Campos-Silva, M. Ortiz-Domínguez, C. Tapia-Quintero, G. Rodriguez-Castro, M. Y. Jiménez-Reyes, E. Chavez-Gutiérrez, Journal of Materials Engineering and Performance, 21 (**2012**) 8, 1714–1723
[30] W. H. Press, B. P. Flannery, S. A. Teukolsky, Numerical recipes in Pascal: the art of scientific computing, Cambridge University, 1989
[31] K. Genel, Vacuum, 80 (**2006**), 451–457
[32] I. Campos, R. Torres, O. Bautista, G. Ramirez, L. Zuniga, Appl. Surf. Sci., 252 (**2006**), 2396–2403
[33] Z. Nait Abdellah, M. Keddam, A. Elias, International Journal of Materials Research, 104 (**2013**), 260–265
[34] G. Celebi, M. Ipek, C. Bindal, A. H. Ucisik, Materials Forum, 29 (**2005**), 456–460
[35] V. I. Dybkov, W. Lengauer, K. Barmak, Journal of Alloys and Compounds, 398 (**2005**), 113–122

UDK 621.791.75
Original scientific article/Izvirni znanstveni članek

ISSN 1580-2949
MTAEC9, 48(2)243(2014)

FINITE ELEMENT MODELLING OF SUBMERGED ARC WELDING PROCESS FOR A SYMMETRIC T-BEAM

MODELIRANJE POSTOPKA OBLOČNEGA VARJENJA POD PRAŠKOM SIMETRIČNEGA T-NOSILCA Z METODO KONČNIH ELEMENTOV

Osman Culha

Celal Bayar University, Engineering Faculty, Department of Materials Engineering, Muradiye Campus, Manisa, Turkey
osman.culha@cbu.edu.tr

Prejem rokopisa – received: 2013-04-11; sprejem za objavo – accepted for publication: 2013-06-10

Metallurgical welding joints are extensively used in the fabrication industry, including ships, offshore structures, steel bridges and pressure vessels. The merits of such welded structures include a high joint efficiency, water and air tightness, and low fabrication costs. However, residual stresses and distortions can occur near the weld bead due to localized heating by the welding process and subsequent rapid cooling. This paper is focused on deriving a simulation solution to predict the design parameters, such as the temperature-stress distribution, the approximate gradient and the nodal displacement on the plates during the process of submerged arc welding (SAW). During the construction of an AH 36 quality T-beam profile using the SAW process, thermal residual stress and distortion occurs due to heat fusion from the source to the joint part of the symmetric T-beam. The value of the design parameter is achieved by performing a thermal elasto-plastic analysis using finite-element techniques. Furthermore, this investigation provides an available process analysis to enhance the fabrication process of welded structures.

Keywords: submerged arc welding (SAW), finite element modelling (FEM), stress-temperature distribution

Metalurško varjeni spoji se splošno uporabljajo v industriji, vključno z ladjedelništvom, za naftne ploščadi, jeklene mostove in tlačne posode. Prednosti takih varjenih konstrukcij so velika zmogljivost spoja, tesnost za vodo in zrak, nizki proizvodni stroški. Vendar pa se v okolici kopeli zvara zaradi lokalnega segrevanja in hitrega ohlajanja lahko pojavijo zaostale napetosti in izkrivljanje. Članek je osredinjen na izpeljavo rešitve simulacije za predvidenje parametrov kot so: razporeditev temperature – napetosti, približek gradienta in izkrivljanja vozlov na ploščah med postopkom obločnega varjenja pod praškom (SAW). Med sestavljanjem AH 36 kvalitete T-nosilca s postopkom SAW se pojavijo termične zaostale napetosti in izkrivljanja zaradi toplote zlivanja od vira do spojnega mesta simetričnega T-nosilca. Vrednosti parametrov so dobljene z izvajanjem termične elasto-plastične analize s tehniko končnih elementov. Poleg tega ta preiskava omogoča analizo procesa za pospešitev izdelave varjenih konstrukcij.

Ključne besede: obločno varjenje pod praškom (SAW), modeliranje z metodo končnih elementov (FEM), razporeditev napetosti – temperature

1 INTRODUCTION

Metallurgical welding joints are extensively used in the fabrication industry, which includes ships, offshore structures, steel bridges and pressure vessels. Among the merits of such welded structures are a high joint efficiency, water and air tightness, and low fabrication costs. However, residual stresses and distortions can occur near the weld bead due to localized heating by the welding process and subsequent rapid cooling. Additionally, phase transformations that occur in the weld metal and adjacent heat-affected zone (HAZ), e.g., in structural steels, contribute to the evolution of residual stress. Stress regions near the weld may promote brittle fractures, fatigue, or stress-corrosion cracking. Meanwhile, residual stresses in the base plate may reduce the buckling strength of the structure members.[1] The inherent characteristics of weldments, such as metallurgical or geometrical defects, the presence of stress raisers and heterogeneous material properties, make them particularly vulnerable to failure. In material selection it is general practice to specify weld metals with strengths higher than those of the parent plate. This overmatching policy is thought to be able to offset potential problems, such as a reduced toughness and the presence of defects in the weld metals.[2] Therefore, the residual stresses of welding must be minimized to control them according to the respective requirements. Previous investigators developed several methods, including heat treatment, hammering, preheating, vibration stress relieving, and weld sequencing, to reduce the residual stresses attributed to welding.[3–5] As known, many welded structures that cannot be subjected to post-weld manufacturing measures after the welding contain residual stresses of varying degree that can result in unintended deformations of the welded component, increase the susceptibility to hydrogen-induced cold cracking, and also combine with tensile stresses experienced during service to promote brittle fracture, fatigue failure, and stress-corrosion cracking. Thus, developing an available welding sequence and accurately predicting the welding residual stresses for a welds system are necessary in order to achieve the safest design.[1–9]

On the other hand, traditional methods for welding-induced residual stress and strain characterization are mainly experimental, and include hole drilling, X-ray, neutron diffraction, ultrasonic and demountable mechanical gauge measurement. However, the application of these methods in practice is usually limited by either their cost or accuracy. Numerical simulations based on finite-element modelling are used to study the influence of welding sequences on the distribution of the residual stress and distortion generated when welding a flat-bar stiffener to a steel plate. The simulation consists of sequentially coupled thermal and structural analyses using an element birth-and-death technique to model the addition of weld metal to the workpiece. The temperature field during welding and the welding-induced residual stress and distortion fields are predicted and the results are compared with experimental measurements and analytical predictions.[10,11]

The intense heat input from the welding process and the molten steel, which is deposited into the joint, contribute to the thermal expansion and contraction of the heated parts. Also, residual stresses released in the rolled and raw-cut material will have some influence on the final shape of the beam. If the welding is carried out on only one side of the web the plate will bend upwards and sideways (sweep and camber). If two welds are made simultaneously, one on each side of the web, the beam tends only to exhibit beam camber due to the shrinkage produced after welding. Distortion can be minimized in symmetrical designs by applying the heat into the material in a symmetrical manner. The remaining distortion on the final part can rarely be tolerated in subsequent assemblies and must be eliminated with either thermal or mechanical methods. Both mechanical and thermal straightening techniques are used to straighten the beams subjected to plate shrinkage. Mechanical straightening requires large, expensive machines, which produce process "wrinkles". As with thermal straightening, this technique adds another step to the production line for beams. Thermal straightening requires that the opposite (upper) side of the beam is heated – which later induces a compensating shrinkage. This is supposed to compensate for the initial shrinkage induced during the welding process mentioned above and can be carried out with a propane burner or induction line heating. In accordance with these explanations, the aims of the study were to obtain the temperature, stress and displacement region of a submerged arc welding (SAW) process for welded T-beam dimensions of 180 mm × 28 mm and 630 mm × 14 mm, AH 36 quality steel bars using the finite-element method.

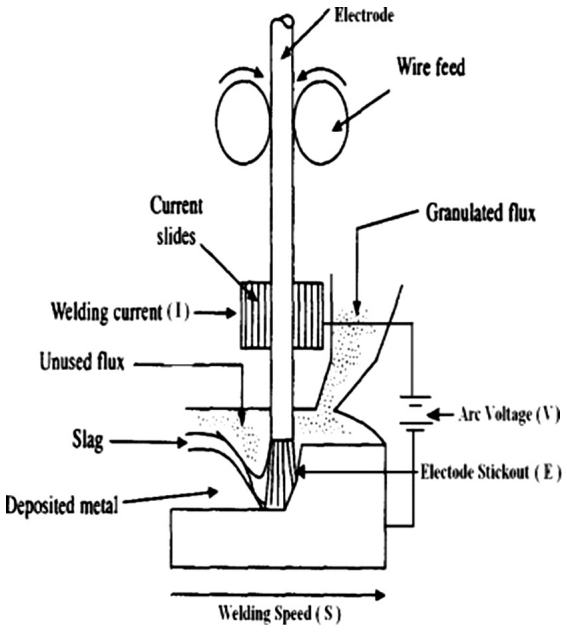

Figure 1: Schematics of submerged arc welding process
Slika 1: Shematski prikaz obločnega varjenja pod praškom

2 SUBMERGED ARC WELDING (SAW) PROCEDURES FOR FLAT BARS

Submerged arc welding is a method in which the heat required to fuse the metal is generated by an electric current passing between the welding wire and the workpiece. The tip of the welding wire, the arc and the weld area are covered by a layer of granular flux. A hopper and a feeding mechanism are used to provide a flow of flux over the joint being welded. A conveyor tube is

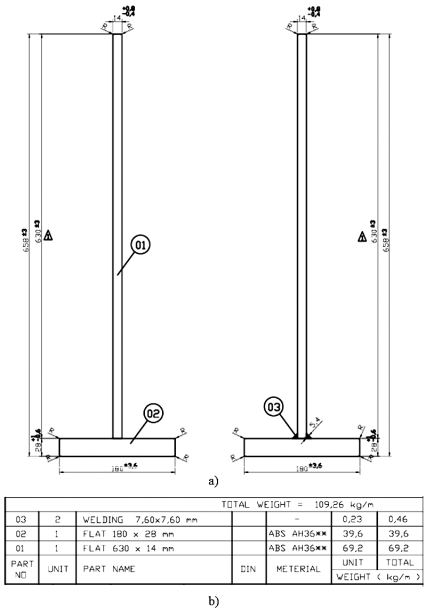

Figure 2: Dimensional representation of steel bars for finite-element model analysis
Slika 2: Predstavitev dimenzij jeklenih palic, uporabljenih za analizo z metodo končnih elementov

Table 1: Process parameters of submerged arc welding (SAW)
Tabela 1: Procesni parametri pri obločnem varjenju pod praškom (SAW)

Wire diameter (mm)	Amperage (A)	Voltage (V)	Welding speed (mm/min)
2.4	780	28	740

provided to control the flow of the flux and is always kept ahead of the weld zone to ensure an adequate supply of flux ahead of the arc. The intense heat evolved by the passage of the electric current through the welding zone melts the end of the wire and the adjacent edges of the workpieces, creating a puddle of molten metal. The puddle is in a liquid state and is turbulent. For this reason any slag or gas bubble is quickly swept to the surface. The flux completely shields the welding zone from any contact with the atmosphere. Additionally, SAW can use a much higher heat input and has slower solidification and cooling characteristics. Also, the silicon content will be much higher in submerged arc welding if care is not exercised in selecting the proper flux material. SAW can be used for the welding of materials in higher gauges and has the advantage of a high weld-metal quality and a smooth and uniform weld finish. The deposit rate, deposition efficiency and the weld speed are high. This means that smoke and arc flash are absent in this procedure (**Figure 1**).

According to these advantages of the SAW process, it was applied to two different steel plates (as shown in **Figure 2**; 180 mm × 28 mm and 630 mm × 14 mm) at Özkan Iron Steel Industry Co., Ltd. for the production of a symmetrical T-beam process. The SAW production-line parameters such as wire diameter, amperage, voltage and welding speed are listed **Table 1**. In particular, since the heat input amount per millimetre was affected by these parameters, they were controlled and modified depending on the dimensions of the steel plate.

3 FINITE-ELEMENT MODELLING OF WELDING FLAT BARS

The simulation technologies were developed in accordance with the development of computers. In many applications, the numerical simulation is applied to save costs. In the field of the welding, the numerical simulations were proposed and applied to the practical field in order to determine the welding conditions. The accuracy of the dimensions after the welding of the steel structure becomes an important factor for the product costs. The dimensions become inaccurate due to the welding distortion. Therefore, the control of the welding distortion is demanded in the steel structure welding so as to improve the productivity. For this purpose, an estimation of the amount of deformation is needed and its behaviour is investigated in this study.

The finite-element modelling (FEM) procedure for SAW was used to determine: a) the thermal stress formation and distribution, b) the temperature gradient, c) the deformation characteristics and d) the thermal straightening regions of the produced T-beam by welding. The SAW process under consideration was applied for the manufacture of a T-beam 180 mm × 28 mm and 630 mm × 14 mm steel plates, as shown in **Figure 3**. A two-dimensional (2D) FE model was used to investigate the detailed residual stress and strain distributions around the welded region of the T-beam. Therefore, the FE model 2D coupled temperature-displacement transient model was structured for the dimensions of the real steel plates. Additionally, the same thermal properties of the base and weld metals, such as the thermal conductivity, convection, expansion and the specific heat capacity, were taken for this analysis.

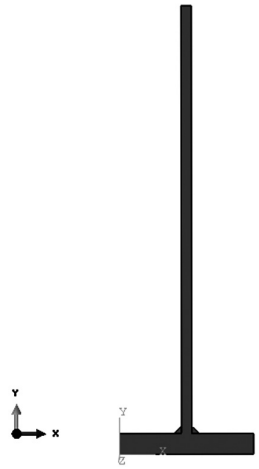

Figure 3: 2D model assembly of FE analysis
Slika 3: 2D modelni sestav za FE-analizo

On the other hand, the yield strengths of the base and weld metals were taken at room temperature. The

Table 2: Composition of the steel used in the experiments
Tabela 2: Sestava jekla, uporabljenega pri poskusu

Material	C	Si	Mn	Cu	Al	V	P	S
AH 36	0.14	0.20	0.90	0.25	0.027	0.07	0.028	0.030

Table 3: Thermal and mechanical properties of AH 36 quality steel[12]
Tabela 3: Toplotne in mehanske lastnosti jekla AH 36[12]

Temperature, °C	Elastic Modulus, GPa	Poisson ratio, υ	Thermal Conductivity, K/W/(m °C)	Specific heat, J/(kg °C)	Thermal expansion coefficient, α/(10^{-6}/°C)	Thermal convection coefficient, h/W/(m^2 °C)
20	207	0.30	52	485	11.8	3.2
100	202	0.31	50	486	11.8	5.5
200	200	0.33	48	495	12.1	6.3
300	198	0.34	45	513	12.7	6.8
400	181	0.36	42	532	13.2	7.4
500	112	0.38	38	555	13.7	7.7
600	65	0.40	34	586	14.2	7.8
700	42	0.42	30	636	14.7	8.1
800	33	0.44	27	683	14.8	8.3
900	24	0.46	26	698	14.7	8.5
1000	13	0.48	28	698	14.7	8.6
1100	7	0.48	30	698	14.7	8.7
1200	7	0.48	31	698	14.7	8.8
1300	7	0.47	32	698	14.7	8.9
1400	7	0.47	34	698	14.7	9.0
1450	7	0.47	35	698	14.7	9.1
1500	7	0.47	95	698	14.7	9.2

Young's modulus and Poisson's ratio variations were assumed to be the same in the base and weld metals between 40 °C and 1450 °C.[10,12] The Von Mises yield criterion and the associated flow rule were used together with kinematic hardening and a bilinear representation of the stress – strain curve. Kinematic hardening is believed to be the best model that can simulate the reverse plasticity and Bauschinger effect that is expected to occur during multipass welding. The density of both materials was assumed to be constant at a value of 7800 kg/m^3. The composition of the AH 36 quality steel plates and weld metal used in the T-beam production is shown in **Table 2** and the properties used for the modelling of the temperature distributions and distortions are listed in **Table 3**.

Furthermore, creating the mesh design of the entire model was very important, especially when the problem had different thermal regions. So, the elements were finest in the welded area and became coarser away from the steel plates. In **Figure 4**, the welded regions of the steel plates were partitioned and meshed as the structured elements type and numbered as CPE4T: A4-node plane strain thermally coupled quadrilateral, bilinear displacement and temperature with 2000. In the region away from the location of the weld, the temperature gradient is significantly lower and the mesh was then made less dense in this region to reduce the number of degrees of freedom and thus the time required for the solution.

4 RESULTS AND DISCUSSION

4.1 Thermal history

A temperature-displacement analysis of the symmetrical T-beam welding with the given welding condition was performed using the 2D finite-element method. During this step, the temperature histories for each node were computed during the multipass welding process. Ogawa et al.[13] states that the weld pass can be divided into a number of small parts (mesh blocks) with the same length to simulate the deposition of the weld metal. In each weld pass, the volume of the moving heat source is equal to that of these elements composing the corresponding weld bead in one mesh block. The elements involved in each block are successively activated and then heated to model the moving heat source. However, since the main aim of study was to obtain the temperature gradient, distributions and thermal stress formation for whole body of the welded T-beam, a cooling procedure was applied to the welding zone from 1450 °C to 40 °C as soon as the welding process for the steel plates was finished. In this way the temperature gradient-distribution and the thermal stress-deformation amount, owing to cooling to room temperature, and the thermal expansion can be achieved using the finite-element model with the transient temperature-displacement analysis. According to this cooling procedure, the temperature contours of the weldments are shown in **Figures 5a** and **5b**. It indicated that the grey region was the welding place and its temperature was 1450 °C. When the cooling step of the symmetrical T-beam started and the temperature reduced from 1450 °C to 40 °C in 377 increments, the temperature distributions and thermal gradient took place from the cross-section of the welding region to flat bars, as shown in **Figures 6a** and **6b**. According to the nodal temperature variation versus time results, as graphically represented in **Figure 6a**, for example, at the node 348 (near the bottom plate), the reduction of the temperature from 1450 °C to 40 °C is faster than for the other nodes because of the cold bottom plate. So as the location of the temperature measurement changed from near the bottom plate to the centre of the welding region, the reduction of the temperature rate decreased and the cooling effect on the thermal gradient was small. On the other hand, the temperature distribution of the bottom steel plate is shown in **Figure 6b**. In accordance with the results, the temperature is increased from 40 °C to 88 °C at the node 145 (near the welding region) due to the heat diffusion from the welding region to the bottom steel plate over time. In addition, the temperature increase of

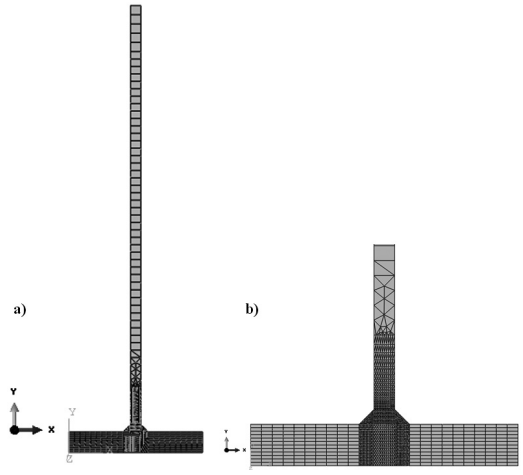

Figure 4: Mesh designs of 2D symmetrical welded T-beam: a) normal view and b) magnified view of welded region

Slika 4: Postavitev mreže 2D simetrično varjenega T-nosilca: a) normalen pogled, b) povečano področje zvara

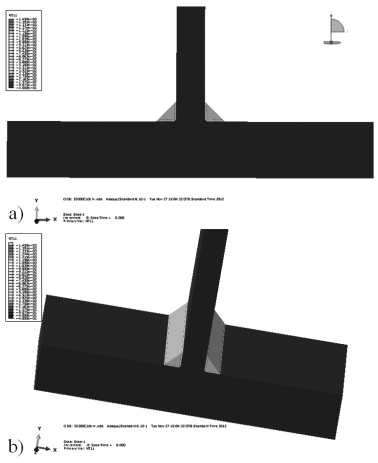

Figure 5: Temperature contour of welded region for: a) 2D model and b) representation of extruded 2D model

Slika 5: Kontura temperaturnega področja varjenja za: a) 2D model in b) ekstrudiran 2D model

the surface of the bottom steel plate is slowed down as it moves away from the source region (from node 145 to node 137).

4.2 Mechanical analysis

The same finite-element mesh as used in the thermal analysis was employed in the mechanical analysis. The analysis was conducted using temperature histories computed with the thermal analysis as the input information. Similar to the thermal analysis, in the mechanical analysis, the temperature-dependent mechanical properties,[10,12,13] such as Young's modulus, yield strength and thermal expansion coefficient, are employed. The elastic strain-stress relationship is modelled using the isotropic Hooke's law, and the plastic behaviour is considered through the Von Misses criterion. According to the counter analysis of the welding region as represented in **Figure 7a**, the nodal stress distribution shows that the thermal residual stress exceeded the yield stress of the welding material and the region is plastically deformed (stress exceeded 350 MPa). In detail, it can be seen that the nodal stress distribution is decreased from node 145 to node 142, as approximately 280 MPa to 70 MPa with time. When the temperature gradient effect started to disappear at the surface of the bottom steel plate (move away from the welding region), the thermal stress formation began to reduce, as shown in **Figure 7b**.

In this study an elastic-perfectly-plastic material model is used with Von Mises failure criteria and the

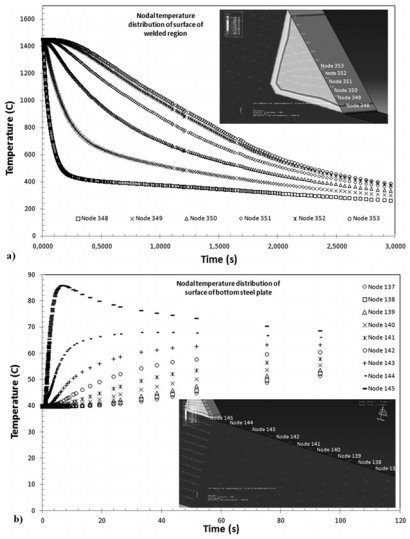

Figure 6: Nodal temperature distributions of: a) welding zone and b) surface of bottom steel plate for coupled temperature-displacement analysis

Slika 6: Razporeditev temperaturnih vozlov: a) področje zvara in b) površina spodnje plošče za skupno analizo temperatura – izkrivljanje

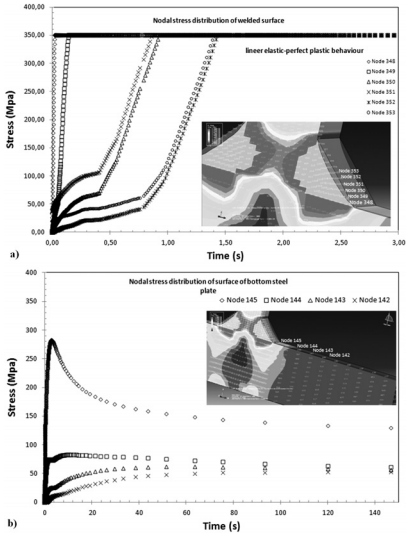

Figure 7: Von Mises stress formation and distribution stress distribution of: a) welding surface and b) bottom steel plate

Slika 7: Nastanek in razporeditev Misesovih napetosti: a) varjena površina, b) spodnja jeklena plošča

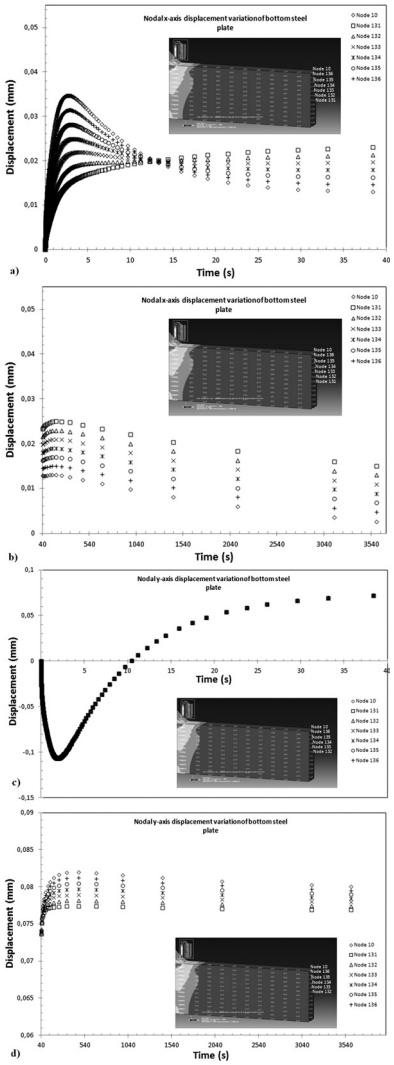

Figure 8: Nodal *x*-axis displacement variation of bottom steel plate between: a) 0–40 s, b) 40–3600 s after welding, c) nodal *y*-axis displacement variation of bottom steel plate between 0–40 s, d) 40–3600 s after welding

Slika 8: Variiranje izkrivljanj vozlov po *x*-osi na spodnji plošči: a) med 0–40 s, b) 40–3600 s po varjenju, c) variiranje izkrivljanj vozlov po *y*-osi na spodnji plošči med 0–40 s, d) 40–3600 s po varjenju

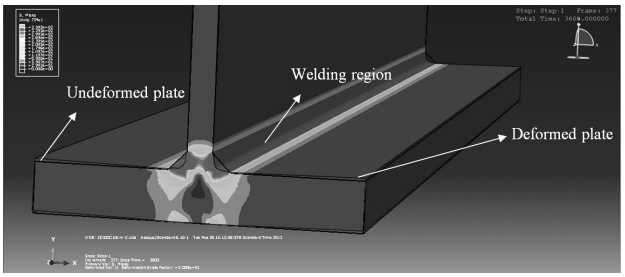

Figure 9: Deformed and undeformed model representation of welding using superimposed plot option of finite-element simulation
Slika 9: Predstavitev modela, deformiranega in nedeformiranega, pri varjenju s predpostavko možnosti simulacije z metodo končnih elementov

associated flow rule, which states that the plastic flow is orthogonal to the yield surface. Nonlinearities due to the large strain and displacement are considered. Strain hardening is not included and was also neglected in several previous studies.[14,15] Experiments by Karlsson and Josefson[16] showed a nearly ideal plastic behaviour for the material at temperatures above 800 °C. Since most plastic strains during welding occur at high temperature, this indicates that a perfectly plastic behaviour is suitable.[10] So, the bottom plate of the welded material model has a displacement due to the thermal gradient, the stress and the strain distribution with time. According to the results of the finite-element simulation of the model, the *x*-axis nodal displacement (node number system: 10, 131, 132, 133, 134, 135 and 136) of the bottom steel plate is illustrate in **Figure 8a**: 40 s after welding and **Figure 8b**: 40–3600 s after welding. **Figures 8a** and **8b** explain that when the cooling procedure began at the welding region, the nodal displacement of the bottom-edge steel plate was firstly increased (positive direction) from starting point to 0.034 mm until 13 s, then decreased to 0.015 mm at the end of the cooling step. On the other hand, the y-axis net nodal displacement of the bottom region after 2 s, between 2–10 s and 10–3600 s was decreased to the –0.11 mm (negative direction), increased to the 0.0 point and increased form 0.0 point to the +0.081 mm, respectively. So a detailed analysis showed that the thermal expansion and the stress caused a deformation at the welding region and joint steel plate as shown in **Figure 8**. The deformed and undeformed bottom steel plate are represented in contours in **Figure 9**. It is clear that the bottom steel plate had a deformation depending on the thermal expansion of the welding region and the heat fusion from the source to the steel joints using a superimposed plot option of the analysis.

5 CONCLUSION

A finite-element analysis of the Submerged Arc Welding (SAW) process was applied to the T-beam joint of AH 36 quality steel plates to obtain the temperature history, thermal gradient, stress distribution and nodal displacement of the 2D model. According to the analysis, the following time-dependent results were obtained:

The temperature gradient and the thermal history of model were decreased from the welding region to the bottom steel plate, as represented graphically and with contours. The temperature decreased from 1450 °C to 40 °C at the welding zone and increased from 40 °C to 86 °C at the surface of the bottom steel plate.

In this research a 2D model was constructed as 2D and extruded to 3D. According to the analysis results the formation of the thermal stress at the welding zone exceeded the yield strength of material, and at 350 MPa plastic deformation occurred. When the cooling procedure of the welding finished, the graphical and contour representation showed that the bottom steel plate of the joints had a shrinkage effect due to the thermal stress. In addition, the thermal stress decreased from 350 MPa to approximately 80 MPa away from the welding zone.

The nodal displacement of the model revealed that the *x* and *y* axes net displacements of the bottom steel plate were 0.015 mm and 0.081 mm, respectively.

Acknowledgement

The author wishes to thank The Scientific and Technological Research Council of Turkey (TUBITAK-1501) for the financial support of the project titled and numbered as: Design and developed of thermal straightening machine using induction heating for welding application of steel joints and 3110745, respectively. The author would also like to thank the project team of Ozkan Iron and Steel Industry Co. Ltd.; Hakan Erçay and Serhat Turgut for their technical facilities.

6 REFERENCES

[1] T. L. Teng, P. H. Chang, W. C. Tseng, Computers and Structures, 81 (**2003**), 273
[2] B. Petrovski, M. Koçak, Mis-Matching of Welds, ESIS 17 (Edited by K. H. Schwalbe, M. Koçak), Mechanical Engineering Publications, London 1994, 511
[3] F. Jonassen, J. L. Meriam, E. P. Degarmo, Weld J, 25 (**1946**) 9, 492
[4] E. F. Rybicki, P. A. Mcguire, Trans ASME J. Eng Mater Technol., 104 (**1982**), 267
[5] R. L. Koch, E. F. Rybicki, R. D. Strttan, J. Eng Mater Technol., 107 (**1985**), 148–53
[6] B. L. Josefson, Trans ASME J. Press Vessel Technol., 104 (**1982**), 245
[7] C. Heinze, C. Schwenk, M. Rethmeier, Journal of Constructional Steel Research, 19 (**2011**), 1847
[8] P. J. Withers, H. K. D. H. Bhadeshia, Mater. Sci. Technol., 17 (**2001**), 366
[9] T. Kannengießer, T. Böllinghaus, M. Neuhaus, Weld World, 50 (**2006**), 11
[10] L. Gannon, Y. Liu, N. Pegg, M. Smith, Marine Structures, 23 (**2010**), 385
[11] S. W. Wen, P. Hilton, D. C. J. Farrugia, Journal of Material Processing Technology, 119 (**2001**), 203
[12] P. Michaleries, A. Debiccari, Welding Journal, 76 (**1997**), 172
[13] K. Ogawa, D. Deng, S. Kiyoshima, N. Yanagida, K. Saito, Computational Materials Science, 45 (**2009**), 1031
[14] L. Tall, Welding Journal, 43 (**1964**), 10
[15] Y. Ueda, T. Yamakawa, Proceedings of international conference on mechanical behaviour of materials, 1971, 10
[16] R. Karlsson, B. Josefson, ASME Journal of Pressure Vessel Technology, 112 (**1990**), 84

UDK 669.24:621.941:519.233.4
Original scientific article/Izvirni znanstveni članek

ISSN 1580-2949
MTAEC9, 48(2)249(2014)

OPTIMIZATION OF THE TURNING PARAMETERS FOR THE CUTTING FORCES IN THE HASTELLOY X SUPERALLOY BASED ON THE TAGUCHI METHOD

OPTIMIRANJE SIL ODREZAVANJA S TAGUCHIJEVO METODO PRI STRUŽENJU SUPERZLITINE HASTELLOY X

Abdullah Altin

Van Vocational School of Higher Education, Yuzuncu Yıl University, 65080 Van, Turkey
aaltin@yyu.edu.tr

Prejem rokopisa – received: 2013-04-23; sprejem za objavo – accepted for publication: 2013-06-11

In this study the effects of the cutting-tool coating material and cutting speed on the cutting forces and surface roughness were determined using the Taguchi experimental design. For this purpose, the nickel-based superalloy Hastelloy X was machined under dry cutting conditions with three different cemented-carbide tools. The main cutting force, F_z, is considered to be the cutting force as a criterion. The mechanical loading and the abrasiveness of the carbide particles have an increasing effect on the cutting forces. According to the results of the analysis of variance (ANOVA), the effect of the cutting speeds was not important. Depending on the tool-coating material, the lowest main cutting force was found to be 538 N and the lowest average surface roughness, 0.755 μm, both at 100 m/min with a multicoated cemented-carbide insert KC9240, whose top layer is coated by TiN. Moreover, the experimental results indicated that the CVD cutting tools performed better than the PVD and the uncoated cutting tools when turning the Hastelloy X in terms of the surface quality and the cutting forces with the current parameters.

Keywords: machinability, Hastelloy X, superalloy, cutting force, surface quality

V tej študiji so s Taguchijevim eksperimentalnim sestavom določeni vplivi materiala oplaščenega rezilnega orodja, hitrosti rezanja na silo odrezavanja in hrapavost površine. V ta namen je bila superzlitina na osnovi niklja Hastelloy X obdelana pri suhih razmerah s tremi različnimi orodji iz karbidne trdine. Kot merilo je bila vzeta glavna sila rezanja F_z. Mehansko obremenjevanje in abrazivnost karbidnih delcev vplivata na povečevanje sile pri odrezavanju. Skladno z rezultati analize variance (ANOVA) vpliv hitrosti odrezavanja ni bil pomemben. Odvisno od prevleke na rezalnem orodju je bila ugotovljena najmanjša strižna sila 538 N in najmanjša povprečna hrapavost (0,755 μm), oboje pri 100 m/min z večplastnim nanosom na vložku iz karbidne trdine KC9240 z vrhnjim prekritjem iz TiN. Rezultati poskusov so pokazali, da je pri struženju Hastelloy X s stališča kvalitete površine, sil pri rezanju pri danih parametrih CVD rezilno orodje boljše od PVD in od orodja brez prevlek.

Ključne besede: obdelovalnost, Hastelloy X, superzlitina, sile rezanja, kvaliteta površine

1 INTRODUCTION

Nickel-based alloys constitute an important class of materials that are used under demanding conditions of high corrosion resistance and high-temperature strength. These characteristics together with their good ductility and ease of cold working make them generally very attractive for a wide variety of applications; nearly all of which exploit their corrosion resistance in atmospheric, salt water and various acidic and alkaline media.[1] Hastelloy X is a nickel-chromium-iron-molybdenum alloy that has been developed for high-temperature applications and is derived from the strengthening particles, Ni_2(Mo, Cr), which are formed after a two-step age-hardening heat-treatment process. With their face-centred cubic (FCC) structure, the Ni-Cr-Mo-W alloys, known as Hastelloys, are used for marine engineering, chemical and hydrocarbon processing equipment, valves, pumps, sensors and heat exchangers.[2] Hastelloy X is chosen by many for use in furnace applications because it has an unusual resistance to oxidizing, reducing, and neutral atmospheres. The resistance to localized corrosion makes the alloy an attractive material as a general-purpose filler metal, or weld overlay.[3] Hastelloy X is widely used in the clamshell of a rocket, engine tailpipes, afterburner components, cabin heaters, and other aircraft parts.[4] It has also been found to be resistant in petrochemical applications. Hastelloy X is widely used in a number of industries.[5] Wang,[6] Richards and Aspinwall,[7] Ezugwu and Wang,[8] with Khamsehzadeh[9] studied the effect of applied stress and temperatures generated at the cutting edge and they were found to influence the wear rate and, hence, the tool life. Notching at the tool nose and the depth of cutting region was a prominent failure mode when machining nickel-based alloys. This is due to a combination of high temperature, high workpiece strength, work hardening and abrasive chips. Kramer and Hartung,[10,11] observed that cemented-carbide tools used for machining nickel-based alloys at a cutting speed of 30 m/min failed due to the thermal softening of the cobalt binder phase and the subsequent plastic deformation of the cutting edge. Focke et al.[12] examined worn tools, which revealed a layer of "disturbed material" beneath the crater and the cutting edge. Hastelloy is a registered trademark name of Haynes International Inc. The Hastelloy trademark is applied as a prefix for a range of corrosion-resistant nickel-based alloys

promoted under the name "superalloys" or "high-performance alloys". Within corrosion applications, Hastelloy alloys may be chosen as a trade-off between performance, cost and other technical issues, e.g., suitability for welding. Hastelloy alloys are generally less attractive for use in acids compared to Tantaline (Tantaline is recognized as the leading performance/price option).

Nomenclature	
v	cutting speed (m/min)
f	feed (mm/r)
d_a	axial depth (mm)
y	tool life (min)
F_m	feed (mm/min)
TL	total length

2 MATERIALS AND METHOD

2.1 Experiment Specimens

Specimens of Hastelloy X, which has an industrial usage, were prepared with dimensions of diameter Ø2 × 40 inches and then used for the experiments. The chemical composition and mechanical properties of the specimens are given in **Tables 1** and **2,** respectively. As the contents of the workpiece, chromium (21 %) and molybdenum (17 %), are high, the material is hard to machine. The material consists of approximately 50 % nickel, making the alloy suitable for high-temperature applications. The specimen was annealed and has a hardness of Rockwell B 90.

2.2 Machine Tool and Measuring Instrument of Cutting Forces

The machining tests were carried out on a JOHN-FORD T35 industrial-type CNC lathe with a maximum power of 10 kW and a rotating speed between 50 r/min and 3500 r/min. During the dry cutting process, a Kistler brand 9257 B-type three-component piezoelectric dynamometer under a tool holder with an appropriate load amplifier was used for measuring three orthogonal cutting forces (F_x, F_y, F_z). This allows direct and continuous recording and a simultaneous graphical visualization of the three cutting forces. The technical properties of the dynamometer and a schematic figure of the experimental setup are given in **Table 3** and **Figure 1**, respectively.

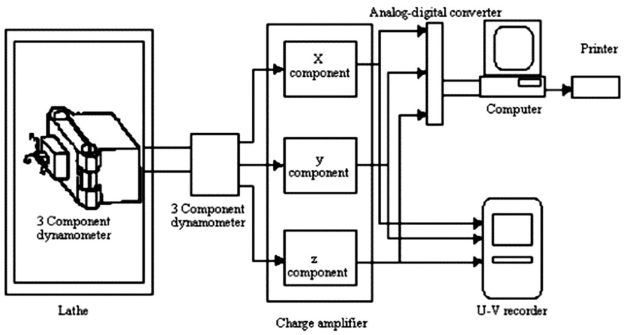

Figure 1: Measurement of the cutting forces and a schematic figure of the dynamometer unit
Slika 1: Merjenje sil pri rezanju in shematski prikaz dinamometrske enote

Table 1: Chemical composition of the workpiece material (Hastelloy X), *w*/%
Tabela 1: Kemijska sestava obdelovanca (Hastelloy X), *w*/%

Ni	Cr	Mo	Fe	Co	W	Mn	Al	Si	C	B
50	21	17	2	1	1	0.80	0.50	0.08	0.01	0.01

Table 2: Mechanical properties of Hastelloy X
Tabela 2: Mehanske lastnosti Hastelloy X

Hardness conductivity(HB)	Tensile strength (MPa)	Yield strength (MPa)	Breaking extension % (5 do)	Thermal (W/m K)
388	1370	1170	23.3	11.4

Table 3: Technical properties of dynamometer
Tabela 3: Tehnične lastnosti dinamometra

Force interval (F_x, F_y, F_z)	-5…10 kN
Reaction	< 0.01 N
Accuracy F_x, F_y	≈ 7.5 pC/N
Accuracy F_z	≈ 3.5 pC/N
Natural frequency $f_0(x, y, z)$	3.5 kHz
Working temperature	0…70 °C
Capacitance	220 pF
Insulation resistance at 20 °C	> 1013 Ω
Grounding insulation	> 108 Ω
Mass	7.3 kg

2.3 Cutting Parameters, Cutting Tool and Tool Holder

The cutting speeds (50, 65, 80, and 100) m/min were chosen by taking into consideration the ISO 3685 standard, as recommended by the manufacturers. The depth of the cut (1.5 mm) and the constant feed rate (0.10–0.15 mm/r) were chosen to be constant. During the cutting process, the machining tests were conducted with three different cemented-carbide tools, i.e., Physical Vapour Deposition (PVD) coated with TiN/TiCN/TiN; Chemical Vapour Deposition (CVD) coated with TiN+AL_2O_3-TiCN+TiN; and WC/CO. The dimensions of the test specimens were 2 × 40 inches in terms of diameter and length. The properties of the cutting tools and the level of the independent variables are given in **Tables 4** and **5**. Surtrasonic 3-P measuring equipment was used for the measurement of the surface roughness. The measurement processes were carried out with three replications. For measuring the surface roughness on the workpiece during machining, the cut-off and sampling length were considered as 0.8 mm and 2.5 mm, respectively. The ambient temperature was (20 ± 1) °C. The resultant cutting force was calculated to evaluate the machining performance. The following are the details of the tool geometry CNMG inserts when mounted on the tool holder: (a) CNMG shape; (b) axial rake angle, 6°;

Table 4: Properties of the cutting tools
Tabela 4: Lastnosti rezilnih orodij

Coating material (top layer)	Coating method and layers	ISO grade of material (grade)	Geometric form	Manufacturer and code
TiN	CVD (TiN, Al2O3, TiCN, TiN, WC)	P25-40, M20-30	CNMG120404RP	Kennametal KC9240
TiN	PVD (TiN, TiCN, TiN, WC)	P25-40, M20-30	CNMG120404FN	Kennametal KT315
WC-CO	Uncoated	P25-40, M20-30	CNMG120404MS	Kennametal K313

(c) end relief angle, 5°; and (d) sharp cutting edge. The cutting tool was mounted in the tool holder (PCLNR 2525M12) and used for such cutting tools (CNMG 120404) with an approach angle of 75°. Analysis of variance (ANOVA) was applied to the experimental study.

Table 5: Level of independent variables
Tabela 5: Nivoji neodvisnih spremenljivk

Variables	Level of variables			
	Lower	Low	Medium	High
Cutting speed, v/(m/min)	50	65	80	100
Feed, f/(mm/r)	0.1–0.15	0.1–0.15	0.1–0.15	0.1–0.15
Axial depth, d_a/mm	1.5	1.5	1.5	1.5

3 RESULTS AND DISCUSSION

3.1 Cutting forces and surface roughness

After the test specimens were prepared for experimental purposes, they were measured with a three-component piezoelectric dynamometer to obtain the main cutting force. According to **Figure 2**, increasing the cutting speed decreases the main cutting force, excluding the area between 80 m/min and 100 m/min for K313. The lowest obtained values for the main cutting force at the cutting speeds of 50 m/min, 662 N, 65 m/min, 622 N, 80 m/min, 601 N, and 100 m/min, 538 N at a 0.1 mm/r constant feed rate, respectively. The lowest main cutting force was observed at 100 m/min cutting speed as 538 N. In **Figure 2** the main cutting force depending on the cutting speed and the uncoating material of the cutting tool were changed in all the experiments. The cutting forces and surface roughness according to the experimental cutting parameters are given in **Table 6**. According to W. Konig, the cutting speed must be increased in order to reduce the main cutting forces.[13] However, in this study, a decrease was observed in the main cutting force between 50 m/min and 100 m/min. It is thought that this case is caused by the good performance of the cutting tool. The effect of the TiN-coated carbide inserts was found to be important for the main cutting force, but the effect of the cutting speeds was not important in the analysis of variance. The main cutting force decreases in spite of increasing the cutting speed from 50 m/min to 100 m/min. As a result of the experimental data, an increase of 100 % in the cutting speed (from 50 m/min to 100 m/min), a decrease in the main cutting force with K313 (6.5 %), KT315 (10 %) and KC9240 (19 %) was found with the 0.1 mm/r constant feed rate, and the decreasing contact surface area caused the main cutting force to decrease in comparison to the increased cutting speed. The decrement of the cutting force depends on the material type, the working conditions and the cutting speed range.[14] The high temperature for the flow region and the decreasing contact area and chip thickness cause the cutting force to decrease, depending on the cutting speed.[15]

As is widely known, the cutting speed must be decreased to improve the average surface roughness.[16] The scatter plot between the surface roughness and the cutting speed as shown in **Figure 3** indicated that there was a linear relationship between the surface roughness and the cutting speed. The results of **Figure 3** show that the average surface roughness decreases by 66 % with an increasing cutting speed from 50 m/min to 100 m/min

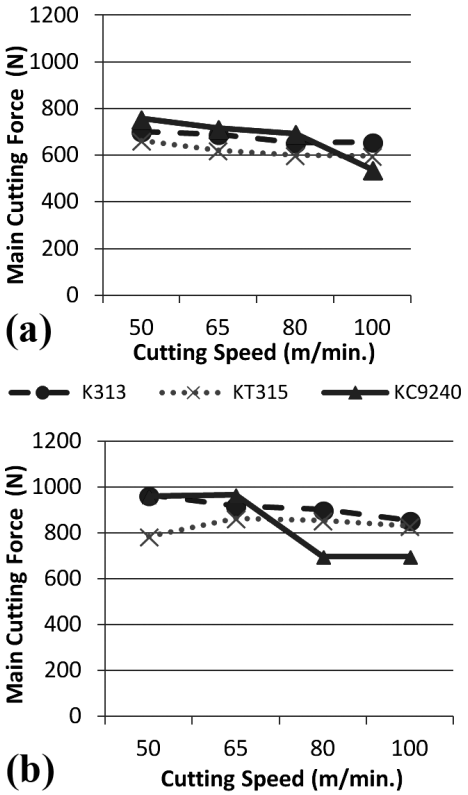

Figure 2: Change of main cutting force in Hastelloy X, according to the cutting speed: a) at f = 0.1 mm/r, b) at f = 0.15 mm/r
Slika 2: Spreminjanje glavne sile rezanja materiala Hastelloy X pri hitrostih rezanja: a) f = 0,1 mm/r in b) f = 0,15 mm/r

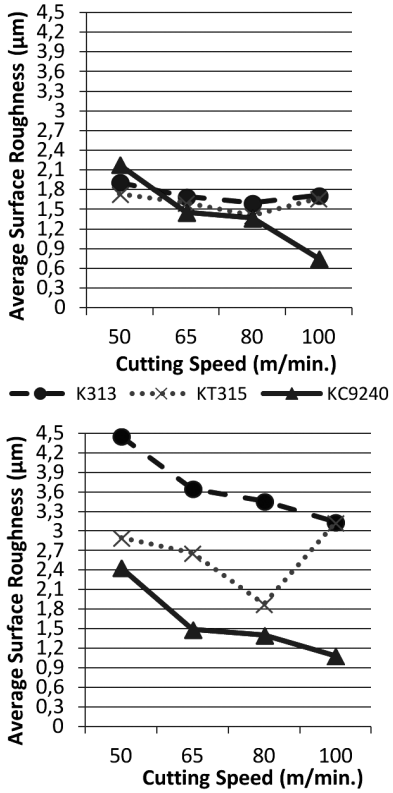

Figure 3: According to cutting speed the change of the average surface roughness in Hastelloy X: a) at f = 0.1 mm/r, b) at f = 0.15 mm/r

Slika 3: Spreminjanje povprečne hrapavosti Hastelloya X od hitrosti rezanja: a) pri f = 0,1 mm/r in b) pri f = 0,15 mm/r

Table 6: Cutting forces and surface roughness according to the experimental cutting parameters when turning Hastelloy X

Tabela 6: Sile rezanja in hrapavost površine pri ustreznih parametrih poskusa rezanja pri struženju Hastelloy X

Experiment number	Cutting tool	Cutting speed (m/min)	Feed rate (mm/r)	Depth of cut (mm)	F_x/N	F_y/N	F_z/N	R_a/µm
1	K313	65	0.1	1.5	366	75	691	1.7
2	K313	80	0.1	1.5	323	67	655	1.599
3	K313	100	0.1	1.5	316	72	658	1.717
4	KT315	65	0.1	1.5	295	132	622	1.605
5	KT315	80	0.1	1.5	281	130	601	1.41
6	KT315	100	0.1	1.5	277	130	598	1.667
7	KC9240	65	0.1	1.5	446	203	715	1.455
8	KC9240	80	0.1	1.5	441	184	694	1.368
9	KC9240	100	0.1	1.5	393	158	538	0.755
10	K313	65	0.15	1.5	398	96	919	3.649
11	K313	80	0.15	1.5	371	90	901	3.462
12	K313	100	0.15	1.5	325	78	854	3.137
13	KT315	65	0.15	1.5	358	177	863	2.669
14	KT315	80	0.15	1.5	356	179	855	1.88
15	KT315	100	0.15	1.5	335	177	830	3.132
16	KC9240	65	0.15	1.5	527	272	966	1.492
17	KC9240	80	0.15	1.5	446	187	696	1.405
18	KC9240	100	0.15	1.5	436	195	697	1.085

with the KC9240 cutting tool (0.1 mm/r constant feed rate).

3.2 Optimization with the Taguchi Method

In this part the optimization of the turning parameters was carried out in terms of the cutting forces with the Taguchi analysis. The importance order of the effects of each control factor on the turning forces was identified. For this purpose, the factors selected in the Taguchi experimental design and the levels of these factors are shown in **Table 7**. Taguchi's L18 2*1 3*2 mixed design was used. In the Taguchi method there are three categories, i.e., "the smallest is better", "the biggest is better" and "the nominal is better" for the calculation of the signal/noise (*S/N*) ratio. In this research "smallest is better" was used since the minimum of the cutting force and surface roughness was intended. In the *i*th experiment, the *S/N* ratio can be calculated using the following equation.[17–19]

$$\eta_i = -10 \log_{10} \frac{1}{n} \sum_{1}^{n} Y_i^2 \qquad (1)$$

n is the number of replications and Y_i is the measured characteristic.

Table 7: Cutting parameters and levels

Tabela 7: Parametri rezanja in nivoji

Control parameters		Units	Levels		
			1	2	3
Feed rate	(A)	m/min	65	80	100
Cutting speed	(B)	(mm/r)	0.1	0.15	
Cutting tool	(C)		KC313	KT315	KC9240

3.3 Confirmation Experiments

The final step of the Taguchi experimental design process includes confirmation experiments.[18,19] To achieve this, the results of the experiments were compared with the predicted values using the Taguchi method and the error rates were obtained. The *S/N* ratios were predicted using the following model:[18–20]

$$\eta_{\text{pred}} = \eta_m + \sum_{i=1}^{k} (\eta_i - \eta_m) \qquad (2)$$

Moreover, the optimum turning parameters were obtained for the performance characteristics using the Taguchi analysis, where m is the total mean of the *S/N* ratios, i is the mean *S/N* ratio at the optimum level and k is the number of the main design parameters that significantly affect the performance characteristics. After predicting the *S/N* ratios other than 18 experiments (with Eq.2), the main cutting force or F_z was calculated using the following equation:[20]

$$Y_{\text{pred}} = 10^{\frac{-S/N}{20}} \qquad (3)$$

where Y_{pred} is the main cutting force or F_z with regard to the *S/N* ratio.

3.4 Taguchi Analysis for F_z

Figure 4 shows the main effect plot for the *S/N* ratios, giving the effect of cutting parameters on the cutting force F_z. The smallest main cutting force is obtained with the cutting insert KT315. In this way, to achieve the minimum cutting forces it is understood that the KC9240 cutting tool should be used at a 0.10 mm/r feed rate and 100 m/min cutting speed.

After analysing the effect of the cutting parameters on the cutting force, in order to find out which F_z cutting force it effected, a variance analysis was made. According to the results of the ANOVA in **Table 8**, it is understood that the most effective cutting parameters that effected the cutting force was 65.99 % and the cutting speed was 11.14 %.

Table 8: ANOVA results for F_z
Tabela 8: ANOVA-rezultati za F_z

Source	DF	Sum of squares	Mean square	*F*	Prob > *F*	Distribution %
A	1	181805	181805	57.75	0.002	65.99
B	2	30700	15350	4.88	0.085	11.14
C	2	13213	6607	2.1	0.238	4.80
A*B	2	4024	2012	0.64	0.574	1.46
B*C	2	9391	4696	1.49	0.328	3.41
A*C	4	23792	5948	1.89	0.276	8.64
Error	4	12592	3148			4.57
Total	17	275517				100.00

3.5 Taguchi Analysis for R_a

Figure 5 shows the effect of feed rate, cutting speed and cutting-tool material on the average surface roughness. According to this figure, in order to obtain the smallest surface roughness, it is necessary to use the KC9240 cutting tool at a low feed rate (0.10 mm/r) and a high cutting speed (100 m/min). Besides this, in order to find out which important parameter affects the surface the roughness, the variance analysis was made with this aim. According to the results of the ANOVA in **Table 9**, the cutting parameters which effect the surface roughness, the cutting tool (40.38 %), feed rate, (33.15%) and 15.57 % feed speed and cutting tool's interaction were found.

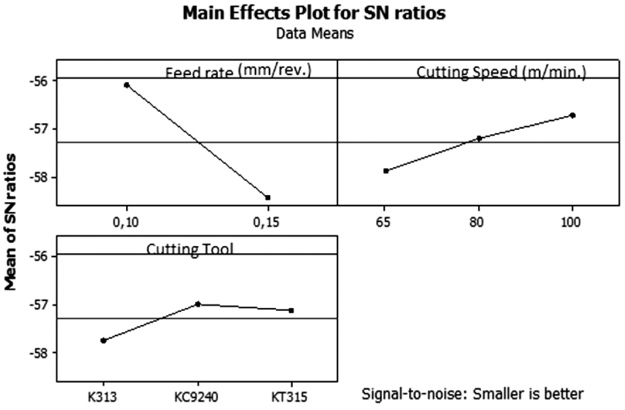

Figure 4: Mean response graphs of the cutting forces according to the feed rate, cutting speed and cutting tool
Slika 4: Prikaz odziva sil rezanja glede na hitrost podajanja, hitrost rezanja in rezilnega orodja

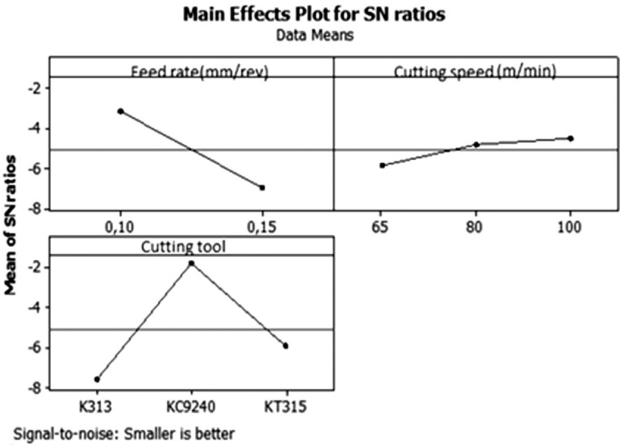

Figure 5: Mean response graphs of the surface roughness according to feed rate, cutting speed and cutting tool
Slika 5: Prikaz odziva hrapavosti površine glede na hitrost podajanja, hitrost rezanja in rezilnega orodja

Table 9: ANOVA results for R_a
Tabela 9: ANOVA rezultati za R_a

Source	DF	Sum of squares	Mean square	*F*	Prob > *F*	Distribution %
A	1	4.1424	4.1424	56.56	0.002	33.15
B	2	0.18817	0.09408	1.28	0.371	1.51
C	2	5.04646	2.52323	34.45	0.003	40.38
A*	2	0.06687	0.03343	0.46	0.663	0.54
B*C	2	0.81483	0.20371	2.78	0.173	6.52
A*C	4	1.94611	0.97305	13.29	0.017	15.57
Error	4	0.29294	0.07323			2.34
Total	17	12.49777				100.00

4 CONCLUSIONS

The goal of this study was to identify the effect of turning parameters such as feed rate, cutting speed and cutting tools on the main cutting force and surface roughness using an analysis of Taguchi. The experimental design described here was used to develop the main cutting force and the surface-roughness prediction model for the Hastelloy X turning operation. The results of this experimental study can be summarized as follows:

- The main cutting force decreased with increasing cutting speed and the cutting force increased at higher feed rates.
- According to the analysis of Taguchi, in order to obtain the smallest cutting force and surface roughness, it was necessary to use the KC9240 cutting tool

at a low feed rate (0.10 mm/r) and a high cutting speed (100 m/min).

- The minimum main cutting force is obtained with CNMG 120404-type multicoated TiN+AL_2O_3-TiCN+TiN carbide tools, while the maximum main cutting force is obtained as 965 N with the CNMG 120404-type uncoated carbide tools. However, cemented carbide tools have no significant effect on the main cutting force when machining Hastelloy X.
- An increasing relation between the cutting speed and the arithmetic average surface roughness as well as between the coating number and the average surface roughness is observed.
- In the case of coated tools, the effect of cutting speed on the surface roughness is no more pronounced than the effect of uncoated cemented-carbide inserts.
- The minimum average surface roughness is determined with CNMG 120404-type multicoated TiN+AL_2O_3-TiCN+TiN carbide tools, while the maximum average surface roughness is observed with CNMG 120404-type uncoated tools. Moreover, uncoated and multiple-layer coated tools have a significantly different effect on the average surface roughness.
- It was found that there is a positive correlation between the main cutting force and the average surface roughness.

Acknowledgments

The authors would like to express their gratitude to the University of Yuzuncu Yıl for the financial support Under Project No. BAP 2012-BYO-013.

5 REFERENCES

[1] Q. Zhang, R. Tang, K. Yin, X. Luo, L. Zhang, Corrosion behavior of Hastelloy C-276 in supercritical water, CSci., 51 (**2009**), 2092–2097

[2] V. B. Singh, A. Gupta, The electrochemical corrosion and passivation behavior of Monel 400 in concentrated acids and their mixtures, Transaction of JWRI., 34 (**2000**), 19–23

[3] Haynes Hastelloy C-22HS Standard Product Catalogue, Haynes International, Indiana, 2007, 2–16

[4] P. C. Jindal, A. T. Santhanam, U. Schleinkofer, A. F. Shuster, Performance of PVD TiN, TiCN, and TiAlN coated cemented carbide tools in turning, Int. J. Recfrac. Met. Hard Mater., 17 (**1999**), 163–170

[5] Website of trademark owner of Hastelloy C-276. www.hynesintl.com

[6] M. Wang, Ph. D. Thesis, South Bank University, London, 1997

[7] N. Richards, D. D. Aspinwall, Use of ceramic tools for machining nickel-based alloys, Int. J. Mach. Tools Manuf., 29 (**1989**) 4, 575–588

[8] E. O. Ezugwu, Z. M. Wang, Performance of PVD and CVD coated tools when machining nickel-based, Inconel 718 alloy, In: N. Narutaki, et al. (Eds.), Third International Conference on Progress of Cutting and Grinding, 111 (**1996**), 102–107

[9] H. Khamsehzadeh, Behaviour of ceramic cutting tools when machining superalloys, Ph.D. Thesis, Universtiy of Warwick, 1991

[10] J. Barry, G. Byrne, Cutting tool wear in the machining of hardened steels. Part I. Cubic boron nitride cutting tool wear, Wear, 247 (**2001**), 139–151

[11] B. M. Kramer, P. D. Hartung, Proc. Int. Conf. of Cutting Tool Mat., Fort Mitchell, KY, (**1980**), 57–74

[12] A. E. Focke, F. E. Westermann, A. Ermi, J. Yavelak, M. Hoch, Failure mechanisms of superhard materials when cutting superalloys, in: Proc. 4th Int.-Am. Conf. of Mat. and Tech, Caracus, Venezuela, 1975, 488–497

[13] W. Konig, A. Berktold, J. Liermann, N. Winands, Top quality components not only by grinding, Ind. Diamond Rev., 3 (**1994**), 127–132

[14] C. Çakır, Modern metal cutting principles, Vipaş, Bursa 2000

[15] Sandvik, Modern metal cutting practical Handbook, Sandvik 1994

[16] R. I. King (Ed.), Handbook of high speed mach., techn. Chapman and Hall, London 1985

[17] A. Taskesen, K. Kütükde, Optimization of the drilling parameters for the cutting forces in B4C-reinforced Al-7XXX-series alloys based on the Taguchi method, Mater. Tehnol., 47 (**2013**) 2, 169–176

[18] G. Tosun, Statistical analysis of process parameters in drilling of AL/SIC P metal matrix composite, International Journal of Advanced Manufacturing Technology, 55 (**2011**) 5–8, 477–485

[19] R. K. Roy, A primer on the Taguchi method / Ranjit K. Roy, Van Nostrand Reinhold, New York, 1990

[20] K. Palanikumar, Experimental investigation and optimization in drilling of GFRP composites, Measurement, Journal of the International Measurement Confederation, 44 (**2011**) 10, 2138–2148

UDK 539.42:669.018
Original scientific article/Izvirni znanstveni članek

ISSN 1580-2949
MTAEC9, 48(2)255(2014)

THERMOCYCLIC- AND STATIC-FAILURE CRITERIA FOR SINGLE-CRYSTAL SUPERALLOYS OF GAS-TURBINE BLADES

TERMOCIKLIČNA IN STATIČNA MERILA ZA PORUŠITVE LOPATIC PLINSKIH TURBIN IZ MONOKRISTALNIH SUPERZLITIN

Leonid B. Getsov[1], Artem S. Semenov[2], Elena A. Tikhomirova[3], Alexander I. Rybnikov[1]

[1]NPO ZKTI, Russia
[2]St. Petersburg State Polytechnical University, Russia
[3]Klimov Company, Russia
guetsov@yahoo.com, semenov.artem@googlemail.com

Prejem rokopisa – received: 2013-05-17; sprejem za objavo – accepted for publication: 2013-06-28

The problem of the thermo-mechanical fatigue (TMF) of single-crystal turbine blades has not been fully investigated theoretically or experimentally. In the present work TMF tests were performed for two single-crystal nickel-based alloys (ZhS36 and ZhS32) with various crystallographic orientations (⟨001⟩, ⟨011⟩, ⟨111⟩) under different temperatures and cycle durations. The dependence of the failure modes (crystallographic or non-crystallographic) on the loading regimes was analyzed. The non-linear viscoelastic, elastoplastic and viscoelastoplastic material models with non-linear kinematic hardening were used to predict the cyclic stress-strain state, ratcheting and creep of the samples. The deformation criterion of damage accumulation was introduced to the lifetime prediction. A stress analysis of the single-crystal samples, with concentrators (in the form of circular holes) and without them, was carried out using physical models of the plasticity and creep. These material models take into account that an inelastic deformation occurs due to a slip mechanism and it is determined with the crystallographic orientation. The proposed failure model using the deformation criterion allows qualitative and quantitative predictions of the TMF fracture process in single crystals.

Keywords: gas-turbine blade, single crystal, thermo-mechanical fatigue, damage, crystallographic and non-crystallographic failure modes

Problem termo-mehanske utrujenosti (TMF) monokristalnih turbinskih lopatic še ni v celoti raziskan niti teoretično niti eksperimentalno. V tem delu so bili izvršeni TMF-preizkusi na dveh monokristalnih zlitinah na osnovi niklja (ZhS36 in ZhS32) z različno kristalografsko orientacijo (⟨001⟩, ⟨011⟩, ⟨111⟩) pri različnih temperaturah in trajanju ciklov. Analizirana je bila odvisnost načina porušitve (kristalografska ali nekristalografska) od vrste obremenjevanja. Modeli nelinearne viskoelastičnosti, elastoplastičnosti in viskoelastoplastičnosti z nelinearnim kinematičnim utrjevanjem so bili uporabljeni za napovedovanje cikličnega stanja napetost – raztezek, nazobčanja in lezenja vzorcev. V napovedovanje dobe trajanja je bilo vpeljano deformacijsko merilo akumuliranja poškodb. Izvršena je bila analiza napetosti v monokristalnem vzorcu s koncentratorji (v obliki okroglih lukenj) in brez njih, z uporabo fizikalnega modela plastičnosti in lezenja. Ti materialni modeli upoštevajo, da se pojavi neelastična deformacija z mehanizmom lezenja in je določena s kristalografsko orientacijo. Predlagani model porušitve z uporabo deformacijskih meril omogoča kvalitativno in kvantitativno napovedovanje TMF- procesa preloma monokristala.

Ključne besede: lopatica plinske turbine, monokristal, termo-mehanska utrujenost, poškodba, kristalografski in nekristalografski način porušitve

1 INTRODUCTION

The use of single-crystal alloys for the manufacturing of the blades of a gas-turbine engine allows a significant increase in the gas temperature before a turbine and sets a number of tasks that should help increase the reliability of a stress and strength analysis. In the present investigation, the results of the experimental studies of single-crystal nickel-based alloys, as well as the approaches to the computation of the stress-strain state and strength of the structural parts are considered and discussed.

2 MATERIALS AND METHODS OF RESEARCH

Numerous experimental studies were performed on two single-crystal alloys, ZhS32 and ZhS36 (**Table 1**) with different alloying and, most importantly, different carbon amounts and were designed to expand the information given in[1,2]. The tests of the mechanical properties, creep and thermal-fatigue resistance at different temperatures were carried out.

The creep tests were conducted on an installation of ATS (Applied Test Systems, Inc.) determining the kinetics of the accumulated inelastic deformation during the first stage and in the steady state of the creep. The test methods for TMF are described in detail in[3,4]. For the tests, rigidly clamped samples with polished surfaces were used, as shown in **Figure 1**. The tests were conducted in a vacuum that allowed us, during the testing, to observe the formation of slip bands and crack initiation, and to determine the rate of the crack propagation on a polished surface using the magnification of 250-times.

The tests were conducted with various values for the maximum (T_{max} = 900–1100 °C) and minimum (T_{min} =

Table 1: Chemical compositions of the ZhS32 and ZhS36 single-crystal alloys, *w*/%
Tabela 1: Kemijska sestava monokristalnih zlitin ZhS32 in ZhS36, *w*/%

Alloy	C	Cr	Co	Mo	W	Ta	Re	Nb	Al	Ti	Ni
ZhS32	0.12–0.18	4.3–5.6	8.0–10.0	0.8–1.4	7.7–9.5	3.5–4.5	3.5–4.5	1.4–1.8	5.6–6.3	–	Base
ZhS36	0.03	4.03	8.48	1.41	11.50	-	1.94	1.07	5.70	0.91	Base

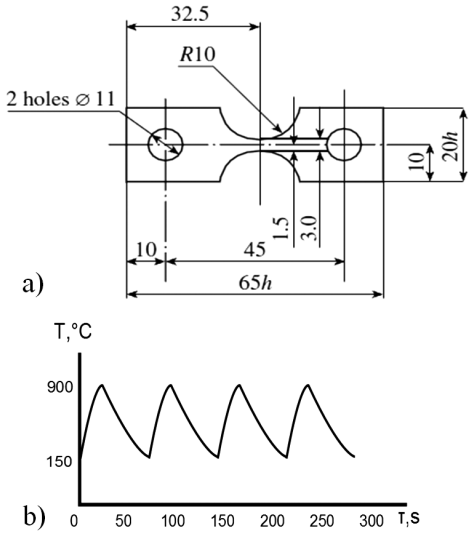

Figure 1: a) Specimen for the thermal-fatigue test, b) with typical cyclic-temperature changes over time in the central point
Slika 1: a) Vzorec za preizkus toplotnega utrujanja, b) z značilnim nihanjem temperature v srednjem delu

150–700 °C) cycle temperatures. The tests with the retardation times of 2 min and 5 min at T_{max} were carried out for some parts of the samples. Some samples had the stress concentrator in the form of a central hole with the diameter of 0.5 mm. The test specimens had different crystallographic orientations: ⟨001⟩, ⟨011⟩ or ⟨111⟩. To determine the crystallographic orientation for each sample Laue's diffraction patterns were obtained and three Euler angles and Schmid factors were computed.

On the basis of the results of a crystallographic analysis, possible directions (angles) of the slip bands on the specimen surfaces were calculated with the aim to compare them with the angles, at which the samples were destroyed. The location of the fracture nucleus was determined with the results of fractographic studies using a TESCAN microscope. The comparison of the experimental data on the orientation of the fracture surfaces with the results of the crystallographic analysis and with the results of the finite-element analysis of the specimens allowed us to define the dependence of the failure mechanism (crystallographic or non-crystallographic) on the parameters of the thermal cycle.

3 RESULTS OF EXPERIMENTAL STUDIES

The tests of mechanical properties show that single-crystal alloys do not have a high plasticity at all the temperatures (see, for example, **Table 2**). Low values of plasticity δ are observed for the carbon-free ZhS36 alloy (as opposed to the carbon ZhS32 alloy) at 500 °C (as opposed to the cases of high temperatures where $T > 900$ °C).

Table 2: Mechanical properties of single-crystal alloys with orientation ⟨001⟩ at 500 °C
Tabela 2: Mehanske lastnosti monokristalne zlitine z orientacijo ⟨001⟩ pri 500 °C

Alloy		$R_{p0.2}$ MPa	R_m MPa	A %	Z %
ZhS36		964 967	982 1000	1.3 2.3	5.0 6.9
ZhS32	Schedule t/t 1	850	880	19.5	35.5
	Schedule t/t 2	810	1110	13.0	11.7

Figure 2 shows the short-term creep curves of alloy ZhS32. The curves obtained under the stress of 550 MPa at 850 °C significantly differ for various samples. The results of the creep tests for alloy ZhS36 are given in[5].

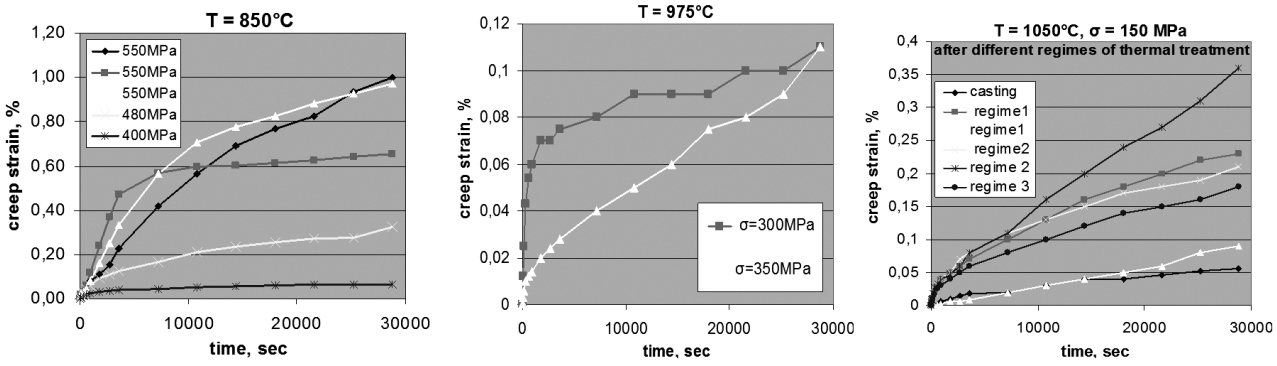

Figure 2: Creep curves of alloy ZhS32 at (850, 975 and 1050) °C
Slika 2: Krivulje lezenja zlitine ZhS32 pri (850, 975 in 1050) °C

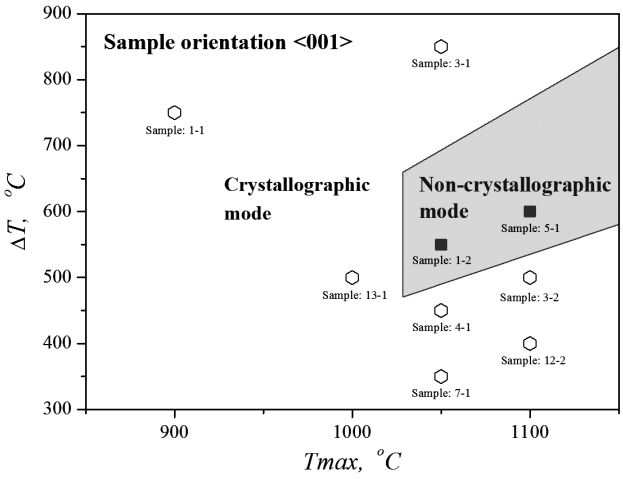

Figure 3: Map of the fracture mechanisms for alloy ZhS32 under thermal cyclic loading

Slika 3: Prikaz področij mehanizmov porušitve za zlitino ZhS32 pri toplotnem cikličnem obremenjevanju

The tests of the ZhS36 alloy show that the conditions for failure under the thermal cyclic loading depend on the crystallographic orientation of the single-crystal alloy and also on the temperatures of the cycle. Unfortunately, the experiments conducted on the ZhS36 alloy with orientations ⟨001⟩, ⟨011⟩ and ⟨111⟩ were not numerous and the obtained results reflect only a trend. However, a formulation of the failure criterion depends on the failure mode (crystallographic or non-crystallographic).[6] In this research, we obtained the conditions (a range of thermal-cycle parameters) (**Figure 3**) for the fracture modes of the ZhS32 alloy with the orientations close to ⟨001⟩. An accumulation of unilateral irreversible deformation (ratcheting) was observed in all the tests (**Figure 4**) for both alloys.

4 CRITERIA OF FAILURE UNDER STATIC LOADING

Single-crystal superalloys, as a rule, are plastic materials and the possibility of a brittle fracture under static loading of gas-turbine blades is remote. However, this issue requires a special investigation. We considered such a possibility on the basis of two (stress and deformation) failure criteria.

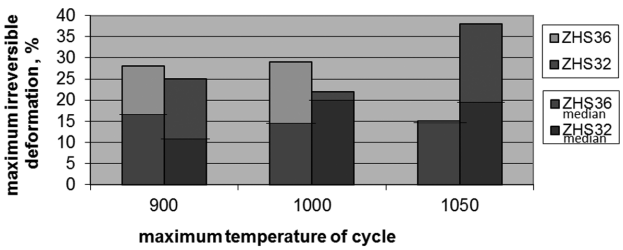

Figure 4: Ratcheting of alloys ZhS32 and ZhS36 under thermal cyclic loading

Slika 4: Zobčenje pri zlitinah ZhS32 in ZhS36 pri toplotnem cikličnem obremenjevanju

The effect of stress on deformation capacity ε^* is determined with the formulas of Mahutov N. A. or Hancock J. W. and Mackenzie A. C.[7]:

$$\varepsilon^* = \varepsilon_{\text{pr}} \cdot 1.7 \exp^{-1.5\frac{\sigma_{\text{mean}}}{\sigma_i}} \tag{1}$$

$$\varepsilon^* = \frac{\varepsilon_{\text{pr}} K_{\text{e}} \sigma_i^2}{3\sigma_1 \sigma_{\text{mean}}} \tag{2}$$

where ε_{pr} is the maximum deformation, determined from the experiments under short-term tension, and K_{e} is the characteristic of the material state (in a brittle state $K_{\text{e}} = 1$, in a viscous state $K_{\text{e}} = 1.2$).

We need to consider the effect of stress on the fracture conditions in terms of the power criterion. Let us consider the general case of stress: $\sigma_2 = A_1\sigma_1$, $\sigma_3 = A_2\sigma_1$, where A_1 and A_2 can vary from $-\infty$ to 1. Depending on the relations between σ_1, σ_2, σ_3 and on the ratio of $\sigma_{\text{pr}}/\sigma_{0.2}$, there is an area of brittle damage, in which the ultimate tensile stress is used as the limiting strength characteristic σ_{pr} for the local stresses.

The above relation can also be written in a different form. Let us consider the case where $\sigma_1/\sigma_i > 1$. Using an approximation of the stress-strain curve in the form of $\sigma_i = \sigma_{0.2} + A\varepsilon_i^{p^m}$ and the fracture condition according to the first theory of strength, $\sigma_1 = \sigma_{\text{pr}}$. $q = \sigma_1/\sigma_i$, we obtain $q(\sigma_{0.2} + A\varepsilon_i^{p^m}) = \sigma_{\text{pr}}$, where the plastic deformation is defined with the equation:

$$\varepsilon_i^p = \left\lceil \frac{\sigma_{\text{pr}}/q - \sigma_{0.2}}{\text{A}} \right\rceil^{\frac{1}{\text{m}}} \tag{3}$$

For $k = \sigma_{\text{pr}}/\sigma_{0.2}$, using:

$$\varepsilon_i^p = \left\lceil \frac{\sigma_{\text{pr}} k/q - \sigma_{0.2}}{\text{A}} \right\rceil^{\frac{1}{\text{m}}} = \left\lceil \frac{\sigma_{\text{pr}}(k/q - 1)}{\text{A}} \right\rceil^{\frac{1}{\text{m}}}$$

with $k/q > 1$, a brittle fracture takes place as $k/q = 1$.

An analysis of crack initiation in the blades under static loading (centrifugal force and bending) on the basis of the *stress-failure criterion* should include:

1. A thermal finite-element analysis of the steady-state temperature field in a blade;
2. An elastic finite-element analysis of the stress fields with the subsequent definitions of $q = \sigma_1/\sigma_2$ and $k = \sigma_{\text{pr}}/\sigma_{0.2}$ at the corresponding temperatures for all the elements of cooled blades;
3. According to the first strength theory we assume that $\sigma_{\text{pr}} = \sigma_{\text{separation}} \approx \sigma_{\text{F}} / (1 - \psi)$ and verify the absence of equality for $q = k$ at all the points. For the remaining cases, we calculate the values of the plastic strain using equation (3);
4. An estimation of the strength by comparing ε_i^p (3) with the limiting plasticity ε^* (1) or (2).

An analysis of the crack initiation in the blades under static loading (centrifugal force and bending) on the basis of the *strain-failure criterion* should include:

1. A thermal finite-element analysis of the steady-state temperature field in a blade;
2. An elastoplastic finite-element analysis with a definition of the zones of plastic deformation and maximum values $\varepsilon^{p}_{i\max}$ for all the elements of cooled blades;
3. A comparison of the obtained value for $\varepsilon^{p}_{i\max}$ with the limiting characteristic ε^* (1) or (2) at the corresponding temperatures, also taking into account a decrease under the effect of aging at the operating temperatures and during long exposures;
4. A viscoelastic finite-element analysis of the stress-relaxation processes with the initial conditions obtained with the elastoplastic analysis (see 2);
5. A calculation of the equivalent stress. If the value of $(\sigma_0 - \sigma_{res})/E$ is lower than, or approximately equal to, the maximum ductility under creep conditions at a suitable temperature, determined with the formulas:

$$p^* = \varepsilon_c \cdot 1.7 \exp^{-1.5\frac{\sigma_{mean}}{\sigma_i}} \tag{4}$$

$$p^* = \frac{\varepsilon_c K_e \sigma_i^2}{3\sigma_1 \sigma_{mean}} \tag{5}$$

then a brittle fracture under the conditions of stress relaxation is possible.

An acceptance of the assumption that fine microcracks are formed in the zone of inelastic deformation. Determination of the size of the zone of inelastic deformation (plastic and creep) and a comparison with the limit values corresponding to the beginning of the accelerated crack growth in non-linear fracture mechanics.

5 CRITERIA OF FAILURE UNDER THERMAL CYCLIC LOADING

For a prediction of a TMF failure of single-crystal materials, it is reasonable to use the deformation criterion proposed in[6]. The crack-initiation criterion is the condition for achieving the critical value of the total damage initiated by different mechanisms:

$$D_1(\Delta\varepsilon^{p}_{eq}) + D_2(\Delta\varepsilon^{c}_{eq}) + D_3(\varepsilon^{p}_{eq}) + D_4(\varepsilon^{c}_{eq}) = 1 \tag{6}$$

The criterion (6) is based on the linear summation of the damages caused by the cyclic plastic strain:

$$D_1 = \frac{1}{C_1}\sum_{i=1}^{n}(\Delta\varepsilon^{p}_{eqi})^{k} \tag{7}$$

the cyclic creep strain:

$$D_2 = \frac{1}{C_2}\sum_{i=1}^{n}(\Delta\varepsilon^{c}_{eqi})^{m} \tag{8}$$

the unilaterally accumulated plastic strain:

$$D_3 = \frac{1}{\varepsilon^{p}_{r}}\max\varepsilon^{p}_{eq} \tag{9}$$

and the unilaterally accumulated creep strain:

$$D_4 = \frac{1}{\varepsilon^{c}_{r}}\max\varepsilon^{c}_{eq} \tag{10}$$

C_1, C_2, k, m, ε^{p}_{r}, ε^{c}_{r} are the material parameters depending on the temperature and on the crystallographic orientation. Usually the relations $k = 2$, $m = 5/4$, $C_1 = (\varepsilon^{p}_{r})^{k}$, $C_2 = (\frac{3}{4}\varepsilon^{c}_{r})^{m}$ are used.

Different norms of the strain tensor are considered as an equivalent strain for (6); among them there are: *the maximum shear strain in the slip system* with normal $\mathbf{n}_{\{111\}}$ to the slip plane and slip direction $\mathbf{l}_{\langle 011\rangle}$:

$$\varepsilon_{eq} = \mathbf{n}_{\{111\}} \cdot \boldsymbol{\varepsilon} \cdot \mathbf{l}_{\langle 011\rangle} \tag{11}$$

the maximum tensile strain (the maximum eigenvalue of the strain tensor):

$$\varepsilon_{eq} = \varepsilon_1 = \max\arg\{\det(\boldsymbol{\varepsilon} - \lambda\mathbf{l}) = 0\} \tag{12}$$

the von Mises *strain intensity*:

$$\varepsilon_{eq} = \sqrt{\tfrac{2}{3}\mathrm{dev}\boldsymbol{\varepsilon}\cdot\cdot\mathrm{dev}\boldsymbol{\varepsilon}} = \sqrt{\tfrac{2}{9}\left[(\varepsilon_x-\varepsilon_y)^2+(\varepsilon_y-\varepsilon_z)^2+(\varepsilon_z-\varepsilon_x)^2+\tfrac{3}{2}(\gamma_{xy}^2+\gamma_{yz}^2+\gamma_{zx}^2)\right]} \tag{13}$$

and *the maximum shear strain*:

$$\varepsilon_{eq} = \tfrac{1}{2}\left[\varepsilon_1 - \varepsilon_3\right] = \tfrac{1}{2}\left[\max\arg\{\det(\boldsymbol{\varepsilon}-\lambda\mathbf{l}) = 0\} - \max\arg\{\det(\boldsymbol{\varepsilon}-\lambda\mathbf{l}) = 0\}\right] \tag{14}$$

Equivalent strain (11) corresponds to the crystallographic failure mode, while equivalent strains (12)–(14) correspond to the non-crystallographic failure mode.

6 RESULTS OF THE FINITE-ELEMENT SIMULATION

The stress-strain analysis of single-crystal samples (**Figure 1**), with a concentrator (in the form of a central circular hole) or without a concentrator, was carried out on the basis of the finite-element program PANTOCRATOR[8] with an application of physical models of plasticity. These material models take into account that an inelastic deformation occurs in accordance with the crystal-slip systems due to a slip mechanism and, therefore, the deformation is strongly sensitive to the crystallographic orientation. The elastoplastic and viscoelastoplastic material models[9,10] with non-linear kinematic and isotropic hardening, also accounting for the self-hardening of each system and the latent hardening[11] between the slip systems, are used in the finite-element simulations. The application of viscoelastic models leads to unrealistically overestimated levels of the stress.

The obtained results for the inhomogeneous stress, strain and damage fields allow us to find the location of the specimen critical point. The damage field is obtained with criterion (6) on the basis of the analysis of the

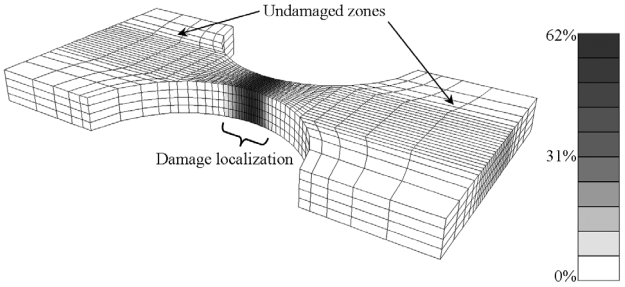

Figure 5: Damage-field distribution after the first cycle for sample 5-1 with the ⟨001⟩ orientation

Slika 5: Širjenje področja poškodbe po prvem ciklu pri vzorcu 5-1 z orientacijo ⟨001⟩

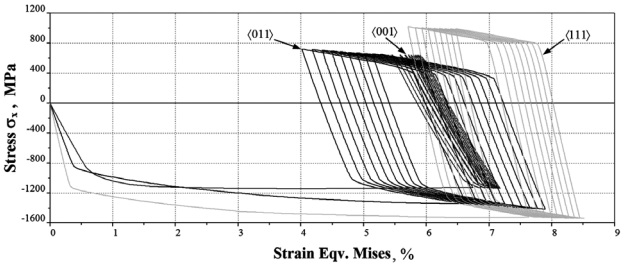

Figure 6: Influence of the crystal orientation on the cyclic stress-strain curve. Results of the finite-element simulations of the thermal cycles with T_{max} = 900 °C and T_{min} = 150 °C (the central point of the specimen).

Slika 6: Vpliv orientacije kristala na ciklično krivuljo napetost – raztezek. Rezultati simulacije s končnimi elementi za toplotne cikle s T_{max} = 900 °C in T_{min} = 150 °C (sredinski del vzorca).

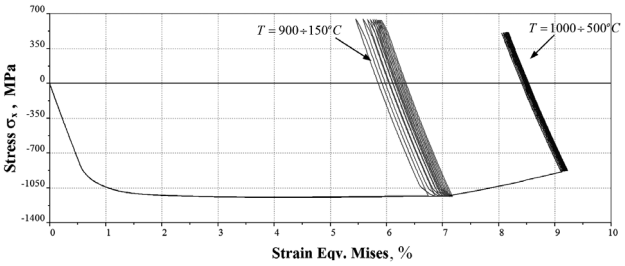

Figure 7: Influence of the temperature program on the cyclic stress-strain curve. Results of the finite-element simulations of the specimens with the ⟨001⟩ orientation (the central point of a specimen).

Slika 7: Vpliv temperaturnega programa na krivuljo napetost – raztezek. Rezultati simulacije s končnimi elementi za vzorce z orientacijo ⟨001⟩ (sredinski del vzorca).

strain-field evolution using the experimental data on the creep and elastoplastic deformation-resistance curves. The typical damage-field distribution after the first thermal cycle (20 °C → T_{max} = 900 °C → T_{min} = 150 °C) is presented in **Figure 5** for sample 5-1 of ZhS36 with orientation ⟨001⟩.

The results of the finite-element simulations show that the crystallographic orientation has a significant influence on the stress-strain state of the samples (**Figure 6**), as confirmed also by the experiments.[12] The width of the hysteresis loops and the unilaterally accumulated strain are also very sensitive to the thermal cyclic regime (**Figure 7**).

The numbers of the cycles to crack initiation, calculated on the basis of criterion (6) using different equivalent strains, (11)–(14), are given in **Table 3**. A satisfactory correlation is observed between the criterion predictions and the results of the experiments (without a sufficient statistical representation).

7 CONCLUSIONS

1. In the investigations of I. L. Svetlov, E. R. Golubovsky and other researchers a series of tests were conducted regarding the definition of the thermal fatigue resistance and short-term creep of the single-crystal ZhS32 alloy, determining the temperature range causing the changes in the failure modes.
2. The failure criteria for the single-crystal alloys under static and thermal cyclic loadings are proposed and discussed. A satisfactory correlation is observed between deformation criterion (6) and the obtained experimental results. All the considered variants of equivalent strains (11)–(14) give practically the same results. The criterion using von Mises strain intensity (13) offers the most conservative estimation.
3. The finite-element simulations of single-crystal specimens under thermal cyclic loading were performed using different material models. The obtained results indicate an applicability of the proposed deformation criteria of failure for the single-crystal ZhS32 and ZhS36 alloys for the temperatures up to 1100 °C.

Table 3: Deformation-criterion (6) predictions vs. experimental results for the crack initiation life

Tabela 3: Napovedi merila deformacij (6) v odvisnosti od eksperimentalnih rezultatov za začetek nastanka razpoke

	Orientation	T_{max}/°C	T_{min}/°C	Number of cycles to crack initiation				
				$\varepsilon_{eq} = \varepsilon_{nl}$ (11)	$\varepsilon_{eq} = \varepsilon_1$ (12)	$\varepsilon_{eq} = \varepsilon_i$ (13)	$\varepsilon_{eq} = \gamma_{max}$ (14)	Experiment
Sample 5-1		900	150	338	275	195	280	435
Sample 5-3		1000	500	218	196	150	172	305
Sample 1-2		900	150	85	73	59	75	190
Sample 2-1		900	150	15	9	10	15	17
Sample 1-1*		900	150	5	4	3	4	10
Sample 2-6*		1000	500	61	44	56	57	10–130
Sample 4-1*		900	150	6	4	4	5	10

*Specimen with a concentrator (the radius of the central hole is 0.25 mm)

Acknowledgements

The study was supported by the Russian Fundamental Research Program, Project No.12-08-00943. The authors are also grateful to S. M. Odabai-Fard for helping prepare the paper.

8 REFERENCES

[1] E. N. Kablov, E. R. Golubovsky, Heat-resistant nickel alloys, Mechanical Engineering, Moscow 1998

[2] R. E. Shalin, I. L. Svetlov, E. B. Kachanov, V. N. Toloraiya, O. S. Gavrilin, Single crystals of nickel-base superalloys, Mechanical Engineering, Moscow 1997

[3] L. B. Getsov, N. I. Dobina, A. I. Rybnikov, A. S. Semenov, A. A. Staroselsky, N. V. Tumanov, Thermal fatigue resistance of single crystal alloy, Strength of Materials, (**2008**) 5, 54–71

[4] L. B. Getsov, A. I. Rybnikov, A. S. Semenov, Thermal fatigue strength of heat-resistant alloys, Thermal Engineering, 56 (**2009**), 412–420

[5] L. B. Getsov, Materials and strength components of gas turbines, Rybinsk, Publ. House, Gas Turbine Technology, 1–2 (2011)

[6] L. B. Getsov, A. S. Semenov, Failure criteria for polycrystalline and single crystal materials under thermal cyclic loading, Proc. NPO CKTI, N296, Strength of materials and resource elements of power, St. Petersburg, 2009, 83–91

[7] L. B. Getsov, B. Z. Margolin, D. G. Fedorchenko, The determination of elements of engineering safety margins in the calculation of structures by finite element method, Proc. NPO CKTI, N296, Strength of materials and resource elements of power, St. Petersburg, 2009, 51–66

[8] A. S. Semenov, PANTOCRATOR-finite-element software package, focused on the solution of nonlinear problems in mechanics, Proc. of V Int. Conf. Scientific and technical problems of forecasting the reliability and durability of the structures and methods for their solution, Publishing House of Polytechnic University, St. Petersburg 2003, 466–480

[9] G. Cailletaud, A Micromechanical Approach to Inelastic Behaviour of Metals, Int. J. Plast., 8 (**1991**), 55–73

[10] J. Besson, G. Cailletaud, J. L. Chaboche, S. Forest, Non-linear mechanics of materials, Springer, 2010

[11] U. F. Kocks, T. J. Brown, Latent hardening in aluminium, Acta Metall., 14 (**1966**), 87–98

[12] L. Getsov, A. Semenov, A. Staroselsky, A failure criterion for single crystal superalloys during thermocyclic loading, Mater. Tehnol., 42 (**2008**) 1, 3–12

UDK 621.396.44:621.396/.398:655.1
Original scientific article/Izvirni znanstveni članek

ISSN 1580-2949
MTAEC9, 48(2)261(2014)

UHF RFID TAGS WITH PRINTED ANTENNAS ON RECYCLED PAPERS AND CARDBOARDS

UHF RFID-ZNAČKE Z NATISNJENIMI ANTENAMI NA RECIKLIRANEM PAPIRJU IN KARTONU

Urška Kavčič[1], Matej Pivar[2], Miloje Đokić[2], Diana Gregor Svetec[2], Leon Pavlovič[3], Tadeja Muck[2]

[1]Valkarton Rakek, d. o. o., Rakek, Slovenia
[2]University of Ljubljana, Faculty of Natural Sciences and Engineering, Ljubljana, Slovenia
[3]University of Ljubljana, Faculty of Electrical Engineering, Ljubljana, Slovenia
urskavcic@gmail.com

Prejem rokopisa – received: 2013-05-30; sprejem za objavo – accepted for publication: 2013-07-03

The integration of passive RFID tags in different applications is important in order to increase product functionality. The present research was focused on the optimization of the printing process conditions for the screen printing of passive UHF RFID antennas for the box tracking in logistics and for newspaper tracking in the retail trade. The antennas were printed on uncoated and coated recycled papers and coated cardboards. Two different conductive inks were applied with a semi-automatic screen printer. Drying conditions were varied in order to obtain a good print quality and the appropriate electrical properties of the conductive printed layer on all the printing substrates. The integration of flip chips was applied to the printed antennas. At the end of our research, an analysis of the printed antennas and the final UHF RFID tags was carried out. The quality of the printed antennas was first evaluated by image analysis, after which the electrical properties, such as the impedance and radiation patterns, were measured. To analyse the quality of UHF RFID tags, the maximum reading length was also determined.
We demonstrated that working UHF RFID tags with screen printed antennas can be realized on substrates with lower quality, such as uncoated recycled papers. The main influence on the final working tag is the quality of the conductive ink itself.

Keywords: printed RFID antenna, tag integration, recycled paper, cardboard

Vključitev pasivnih RFID-značk v različne aplikacije je pomembna, da dosežemo dobro funkcionalnost izdelka. Predstavljena raziskava je bila osredinjena na optimizacijo razmer sitotiskarskega procesa, s katerim so bile natisnjene UHF RFID-antene za sledenje embalaže in časopisov v trgovinskih verigah. Antene so bile natisnjene na nepremazane in premazane reciklirane papirje in na premazane embalažne kartone. Uporabljeni sta bili dve prevodni tiskarski barvi, ki sta bili na tiskovni material naneseni s polavtomatskim sitotiskarskim strojem. Razmere pri sušenju so bile optimizirane, tako da so bile dosežene dobra kakovost in primerne električne lastnosti odtisov na vseh tiskovnih materialih. Na tiskanih antenah je bilo izvedeno kontaktiranje čipov. Na koncu raziskav je bila izvedena analiza natisnjenih anten in končno izdelanih značk. Kakovost tiskanih anten je bila ovrednotena s slikovno analizo ter z merjenjem impedance in sevalnega diagrama anten. Za določanje kakovosti končne značke je bila določena še maksimalna razdalja odčitavanja.
Dokazali smo, da je UHF RFID-značke mogoče tiskati s sitotiskom tudi na nizkocenovne tiskovne materiale, kot je nepremazan recikliran papir. Glavni vpliv na delovanje končne značke ima kakovost prevodne tiskarske barve.

Ključne besede: tiskane RFID-antene, izdelava RFID-značke, recikliran papir, embalažni karton

1 INTRODUCTION

The future of automatic identification and data capturing in the field of packaging is increasingly dedicated to radio-frequency identification (RFID), which enables wireless identification and saves a lot of time (and money) in comparison to barcode technology. RFID is an automated identification technology that consists of a reader, a reader antenna and a tag (which consists of an antenna and a chip). It uses radio waves to transfer the information between the reader and the tag at long distances. The RFID tag can work at different frequencies: low (LF: 125 kHz or 134 kHz), high (HF: 13.56 MHz) or ultrahigh (UHF: 860–960 MHz) radio-frequency ranges. Due to the fact that the higher the frequency, the larger the distance at which the information can be read, in packaging identification UHF RFID tags are mostly used.

The RFID tag can be produced conventionally by an etching process or can be printed. While the conventional production of RFID tags is still very expensive and environmentally unfriendly, many researchers are trying to produce printed RFID tags, where the electronic components are printed in-line, roll-to-roll, in the same process as the packaging layout itself. The printing, unlike conventional etching, is an additive process, and is far more ecological and economical than the subtractive etching process. This could reduce the amount of material used for production, i.e. the waste that is a side product of production, and consequently the total cost per tag. RFID antennas can be printed with different printing technologies:[1] offset lithography, flexography, gravure, ink jet, electrophotography and screen printing. Different printing technologies enable different accuracy, resolution and ink thickness. Most research has been carried out using inkjet[2–5] and screen[6–9] printing technologies. There have also been some using gravure printing,[10,11] but less with offset and flexography. Many research programmes have also been undertaken to test the performance of RFID printed antennas[12–19] and chip

bonding.[20,21] Printed antennas are usually applied to different foils[22,23] or photo papers. There are also some researches made on the field of printed paper-based RFID or sensors,[17,24–29] but none of them analysed the printing RFID antennas on recycled paper and cardboard. The research in that field analysed the printing substrates from the electrical point of view and not from the graphical point of view. For this reason, in this paper the application of silver conductive ink to recycled papers and packaging cardboards is presented.

The goal of our research was to optimize the printing process and drying conditions for the screen printing of passive UHF antennas directly on packaging and paper substrates. The antennas were printed with silver conductive printing inks using a semi-automatic screen printer. After that the silicon chip was applied to the antenna. At the end of our research, the analysis of the printed antennas and final UHF RFID tags was carried out. The quality of the printed antennas was evaluated by image analysis and the resistance to abrasion, which is important if the antennas printed on packaging or on newspaper are not additionally protected with another protective layer. At the end the impedance and radiation patterns were measured. To analyse the quality of the UHF RFID, the tag reading length was determined by measuring the received power in watts.

2 EXPERIMENTS

The current investigation involved the selection of the UHF RFID antenna for the central frequency of 868 MHz (**Figure 1**), antenna printing, drying optimization, analysis of antenna printability, mounting the chip onto antenna and an analysis of RFID tag reading.

2.1 Printing

The UHF RFID antennas were printed with two conductive printing inks: SunChemical[30] (CRSN2442, SunTronic Silver 280, Thermal Drying Silver Conductive Ink) and DuPont[31] (DuPont 5064H silver conductor). As printing substrates, two coated cardboards and two recycled papers (one coated and one uncoated) were used. A RokuPrint semi-automatic screen printer and monofilament polyester plain weave mesh with 120 L/cm were used (theoretical ink volume 16.3 cm^3/m^2).

Figure 1: Antenna printing form
Slika 1: Tiskana oblika antene

The properties of the printing inks and printing substrates are presented in **Tables 1** and **2**.

Table 1: Printing inks properties[30,31]
Tabela 1: Lastnosti tiskarskih barv[30,31]

Property		SunChemical	DuPont
Solids		69–71	63–66
Viscosity		2–3	10–20
Sheet resistance: $R_\square$/mΩ for 25 μm)		10–32	≤6 on 125 μm PET film
Drying conditions	Static box oven	150 °C/ 30 min	130 °C/ (10–20 min)
	Reel-to-reel	100–130 °C/ (30–90 s)	140 °C/ (2 min)

2.2 Print penetration

The print penetration was determined in accordance with the IGT–W24 and ICP–T17 methods. At the moment of printing a quantity of ink or varnish is absorbed by the surface of the paper. This amount is determined by the absorption of the liquid in the surface recesses (roughness) and the absorption into the paper pores at the surface. With the IGT test method the sum of the two phenomena is determined: the oil absorption or varnishability. The reciprocal value of this is called print penetration. A large stain indicates a low roughness/absorption of the paper.

The final values for the print penetration were calculated according to Equation 1, where *PP* is the print penetration and *l* is stain length of the print in mm:

$$PP = 10^3/l \quad (1)$$

2.3 Optimization of drying conditions

After printing, the optimization of the drying conditions was determined to achieve the lowest sheet resistance of the prints. Based on experiments, a two-stage drying process was determined as optimal (**Figure 2**). The samples were dried according to the printing substrate and the printing ink. The optimal drying was

Table 2: Properties of printing substrates
Tabela 2: Lastnosti podlag za tiskanje

Standard	Type	Grammage (g/m^2)	Thickness (μm)	Roughness (μm) (Stylus TR200)	Porosity (mL/min) (Bendtsen)	Water absorptiveness (g/m^2) ($Cobb_{60}$)
		ISO 536	ISO 534	ISO 4287	ISO 5636-3	ISO 535
paper 1	coated recycled paper	60	60	2.226	16.00	not determinable
paper 2	uncoated recycled paper	60	113	5.706	381.00	not determinable
cardboard 1	coated cardboard	245	400	0.463	27.33	5.609
cardboard 2	coated cardboard	350	525	0.482	12.00	4.427

Figure 2: Schematic representation of two-stage (combined) drying process
Slika 2: Shematski prikaz dvostopenjskega sušenja

determined as the point where the sheet resistance of the printed samples became constant and did not get any lower with longer drying times or higher temperatures.

2.4 Analysis of printed conductive ink layer

After printing and the two-stage drying process, the analysis of the printed conductive ink layer was carried out. The print mottle, abrasion and sheet resistance of the printed ink layer were determined.

2.4.1 Print mottle

The print uniformity (print mottle) was determined using image analysis (ImageJ software). The print mottle was determined with a traditional STFI method, by calculation of the coefficient of variation (*CV*), where σ is the standard deviation of the grey values and R is the mean grey value:[32]

$$CV/\% = \sigma/R \times 100 \quad (2)$$

2.4.2 Abrasion

The abrasion was determined on the samples (5.1 cm × 23 cm) using a Param RT-01 Rub tester instrument (according to the standard ASTM D 5264). The printed samples were positioned on the table, and the unprinted specimen of the same printing substrate was mounted on the weight, which rubs the printed sample. The test duration is determined by the number of strokes (a stroke is one back-and-forth cycle) the sample is rubbed. The speed of the rub was 106 cycles per minute using a mass 0.9 kg. The abrasion was determined on the receptor surface of 4.8 cm × 10 cm size using image analysis after 100 (paper) or 500 (cardboard) strokes. The uncoated (and coated) recycled paper has a rougher surface than the coated cardboard and consequently the abrasion of the printing ink on the paper was much higher than on the cardboard. If 500 strokes were applied to paper, the abrasion would not be determinable using image analysis. On the other hand, after 100 strokes on cardboard there is no evident abrasion. That is why only 100 strokes were applied to paper and 500 to cardboards. The results present the proportion of the area coated with the rubbed ink on the receptor surface.

2.4.3 Resistance

The resistance was measured on the test element presented in **Figure 3** between points 1 and 2 using a DT-890G multimeter. The nominal length was L = 22 mm and width W = 3 mm. The nominal number of squares was $N_{sq} = L/W = 10.3$. The final results are given as the value of the conductive printed layer sheet resistance $R_{\square}$ (mΩ).

2.5 RFID tag analysis

2.5.1 Antenna evaluation

The numerical simulation of the antenna impedance was carried out using a commercial 3-D solver (Ansoft HFSS). In addition, the radiation patterns in the *E* (electric field) and *H* (magnetic field) planes for the paper and cardboard printed antennas were measured at an outdoor antenna-measuring polygon.

2.5.2 RFID tag reading

After the antennas had been printed and analysed, the strap chip (NXP) with impedance $Z = 22 - j195\ \Omega$ [33] was assembled onto the printed antennas. Then the analysis of the RFID tag was performed using an IDS-R902 reader (IDS Microchip, Ljubljana, Slovenia). The IDS-R902 reader consists of an IDS reader and a Patch A0025 antenna (Poynting GmbH, Dortmund, Germany). The reader is based on the IDS-R902 circuit, supports the ISO18000-6 C or EPC Gen 2 Protocol and measures the strength of the modulated signal backscattered from the tag. The reader antenna (gain 4.5 = 6.5 dBi) emits circularly polarized UHF radiation with a frequency f = 867 MHz. Its output power is 400 mW (+26 dBm). The reader uses an amplitude shift keying and has a maximum input sensitivity of 25 pW (–76 dBm). The quality of the final UHF RFID tag was evaluated by measuring the power in W (dBm) for every 5 cm by moving the tag straight from the reader.

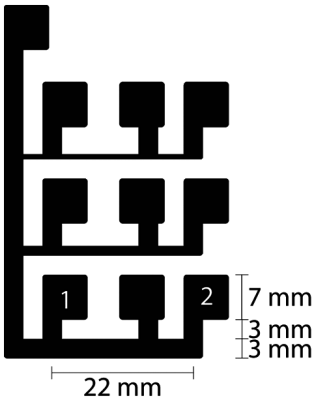

Figure 3: Test element for resistance measurement
Slika 3: Preizkusni element za merjenje upornosti

3 RESULTS AND DISCUSSION

3.1 Print penetration

Print penetration is a measure of the penetration velocity of the printing ink into the printing substrate. It represents the properties (roughness, porosity and absorptiveness) of the printing substrate. **Figure 4** shows that recycled papers have a higher print penetration than cardboards. Again, the higher penetration can be detected with uncoated recycled paper, which can be directly connected to the roughness and print mottle.

3.2 Drying optimization

The drying optimization was determined as the point where the resistance became constant with a higher temperature or longer drying. The optimal drying conditions were determined as presented in **Table 3**. Samples were first dried in the hot zone and then they were exposed to the Heat&Press process (**Figure 2**).

During the drying process, the printing substrate exposed to high temperatures changes its surface colour, which is significant when the final product is graphically designed, such as with packaging, where the colours and final product's appearance are very important. The colour difference (ΔE) of the printing substrate was determined for both printing inks (**Figure 5**). It is clear that the printing substrates printed with DuPont printing ink change their colour more than the samples printed with SunChemical printing ink, due to the higher heating temperature. Even so, all the values are very low and the colour change is hard to detect with the eye. The printing with SunChemical printing ink is also more appropriate from an ecological point of view, because of the lower drying temperature.

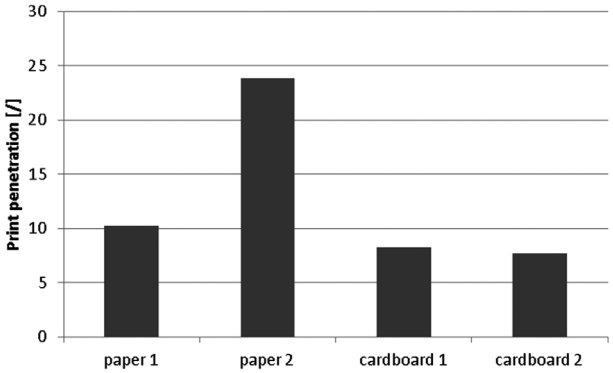

Figure 4: Print penetration of the printing substrates
Slika 4: Tiskarska penetracija na podlagah za tiskanje

3.3 Analysis of printed conductive ink layer

3.3.1 Print mottle

In **Figure 6** the print mottle for all the printing substrates is presented. The print mottle is dependent on the surface properties of the printing substrate. Usually, it is the result of an uneven ink layer or non-uniform ink absorption across the printing substrate.[34] The higher roughness (**Table 2**), print penetration (**Figure 4**) and water absorptiveness (**Table 2**) of the two recycled papers affect the higher print mottle, as presented in **Figure 6**. The difference between the two conductive inks is also obvious, with the DuPont printing ink having a slightly higher non-uniformity. The final antenna performance is also dependent on the print quality of the printed conductive lines. If the antenna is printed onto rough substrates the conductive Ag particle in ink could not be connected and the final conductivity could be questionable. In that case the final antenna performance would not be as good as expected based on the antenna design and simulation.

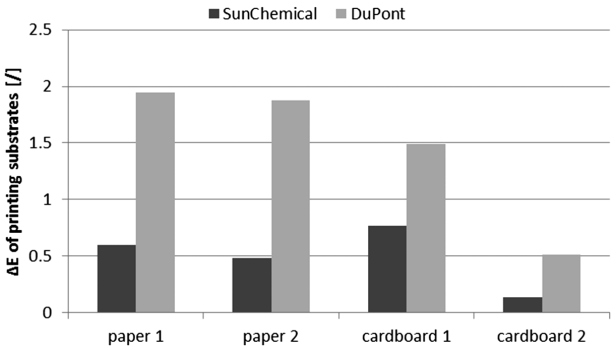

Figure 5: ΔE of printing substrates after two stages drying process
Slika 5: ΔE podlag za tiskanje po dvostopenjskem sušenju

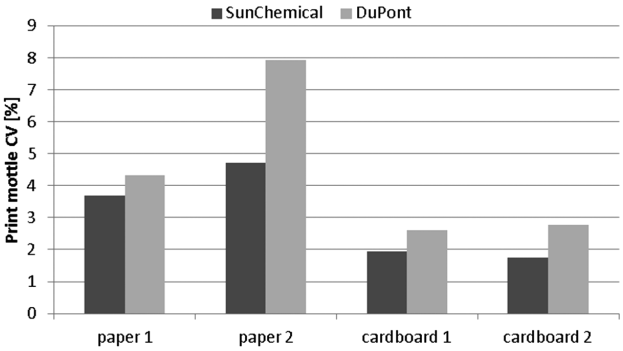

Figure 6: Print mottle
Slika 6: Tiskovna neenakomernost

Table 3: Drying conditions
Tabela 3: Razmere pri sušenju

	Hot zone				Heat&Press	
Printing substrate	Time (s)	Temperature (°C)		Printing ink	Time (s)	Temperature (°C)
Cardboard	135	115		SunChemical	10	150
Paper	90	115		DuPont	10	190

3.3.2 Abrasion

The abrasion of the printed antennas is important, while prints have to have good conductivity, which is degraded if the prints' abrasion is too high. In that case it is possible to get a inhomogeneous printed conductive layer and small holes can appear on the surface of the antenna, because of the printing substrate roughness.

In **Figure 7** it is clear that the prints printed on papers have much higher abrasion (at lower rub) than those printed on cardboard. It is also evident that the DuPont printing ink has higher abrasion than the SunChemical ink. On paper (especially on uncoated recycled paper), the binder penetrates more quickly and deeply into the substrate than on coated cardboard, and consequently the conductive silver particles remain unbounded at the surface. Moreover, the surface of the paper is rougher (**Table 2**) and when rubbed more the particles remain on the receptor (unprinted specimen), and the abrasion is higher.

3.3.3 Sheet resistance

The sheet resistance was calculated and is presented in **Figure 8**. All the samples achieved a good sheet resistance, i.e., lower than $R_{\square}$ = 100 mΩ, with the antennas printed with DuPont printing ink being even lower than those printed with SunChemical ink. In the inks' specification (**Table 1**), the specified resistances are much lower than those presented in **Figure 8**. This is because the resistances in **Table 1** correspond to a thick dry film 25 µm, while the measured thicknesses of the dry film in our experiment were much lower (the thickness was determined on a cross-section of the printed samples), between 6 µm and 10 µm, and consequently the sheet resistance is higher.

3.4 RFID tag analysis

3.4.1 Antenna evaluation

The radiation patterns in the E- and H-planes were evaluated by measurements of antennas on two printing substrates. The uncoated recycled paper (paper 2) and coated cardboard (cardboard 1) were selected as they had

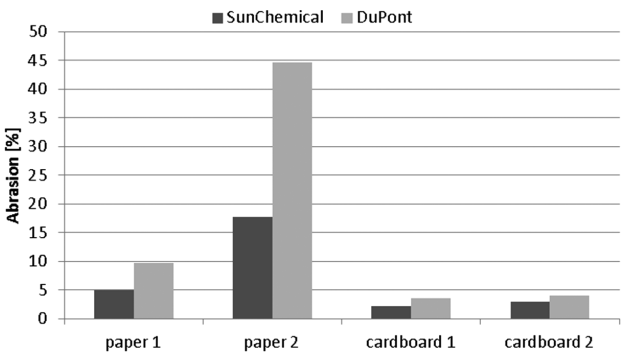

Figure 7: Abrasion
Slika 7: Abrazija

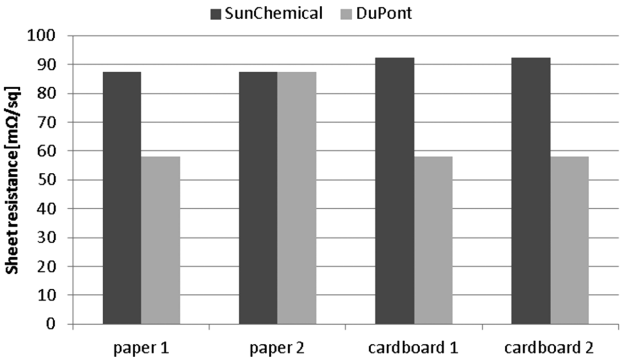

Figure 8: Sheet resistance of the prints
Slika 8: Plastna upornost odtisov

the highest and the lowest print mottles (**Figure 6**) and abrasions (**Figure 7**) of the four samples. The samples printed with the SunChemical printing ink were selected on the basis of lower heating temperatures, lower abrasion and smaller print mottle in comparison with the DuPont printing ink. The results revealed that the patterns are nearly the same for both measured antennas, regardless of which printing substrate was used (**Figure 9**).

The measured radiation patterns have slight irregularities in the measurement, especially at the nulls. This is

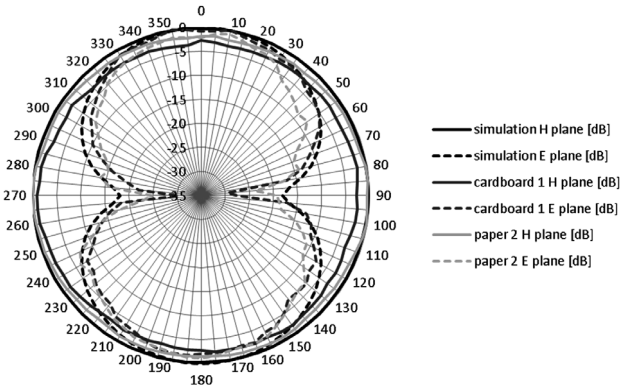

Figure 9: Radiation pattern for antennas printed on both cardboard and on recycled paper and its simulation
Slika 9: Sevalni diagram antene, natisnjene na embalažnem kartonu in recikliranem papirju ter njena simulacija

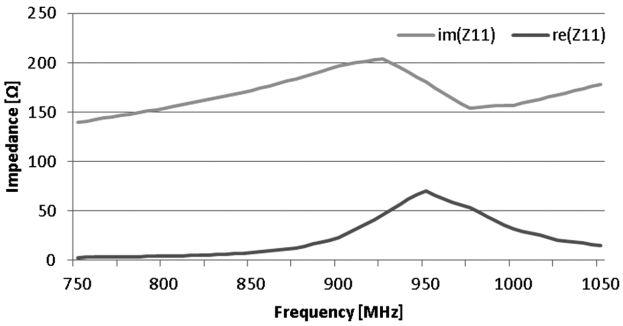

Figure 10: Simulated antenna impedance
Slika 10: Simulirana impedanca antene

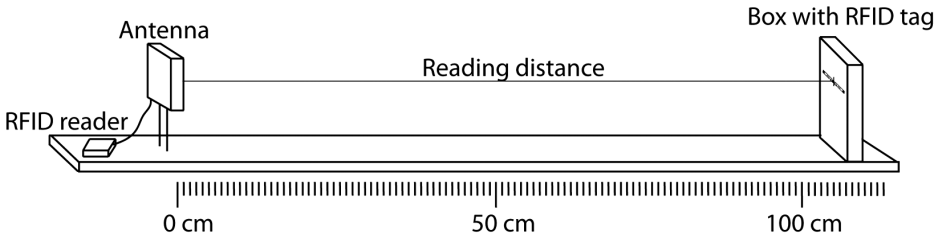

Figure 11: Measurements of tag readability
Slika 11: Merjenje berljivosti natisnjenih značk

due to the disturbance to the antenna and the obstruction of the attached balun that was used for the balanced antenna to the coaxial cable interface. Without the balun interference, the radiation patterns should be approximately the same as the simulated ones shown in **Figure 9**.

Besides the radiation pattern, the impedance of the antenna was simulated (**Figure 10**). The simulated antenna impedance of about 15 + j180 Ω at 868 MHz ensures a good match to the RFID chip impedance (22 - j195 Ω).

3.4.2 RFID tag reading

The NXP chips on strap were attached to the printed antennas and the largest reading distances with the corresponding power values were measured in a real environment on five samples, as presented in **Figure 11**. The printed antenna was oriented horizontally to the transmitting antenna. **Figure 12** shows that the power (an average of 5 measurements) diminishes with the distance of reading from around 10 nW to almost 100 pW (-50 dBm to almost -70 dBm) at one metre distance. The largest measured distance where the tags still worked was 105 cm. It was observed that the power of the tags printed on paper was a little lower than that of the tags printed on cardboard.

4 CONCLUSIONS

The analysed influences of drying conditions on the quality of the printed conductive layers were proven to be significant, not only in terms of the quality of the printing but also on the relevant electrical parameters measured on the printed antennas. A higher drying temperature increases the final conductivity. The paper and cardboard enable drying to 150 °C or a maximum of 200 °C. A higher drying temperature causes the substrate to become yellow.

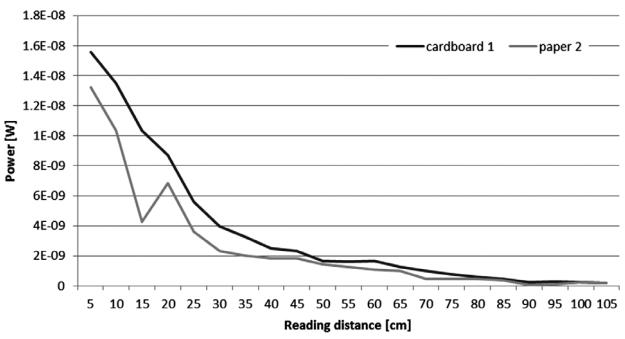

Figure 12: Reading distances and corresponding power values
Slika 12: Razdalje odčitavanja in pripadajoče vrednosti moči

The two-stage drying process with Heat&Press makes it possible to use a lower drying temperature and a shorter drying time. Comparing the printing inks, the DuPont ink has a slightly lower resistance, which is its only advantage over the SunChemical ink. On the other hand, the weakness of the DuPont ink is that it requires a higher drying temperature. SunChemical ink shows lower print mottle and has lower abrasion. It means that antennas printed with SunChemical ink are more uniform on their surface and more mechanically stable.

The printing substrate, especially the coating, has significant influences on better ink formation, higher uniformity and also on better abrasion resistance. This effect is visible especially on coated recycled paper and cardboards compared with uncoated recycled paper.

The design of the UHF antenna is appropriate for both printing substrates – no differences in radiation pattern were observed between antennas printed on coated cardboard and those on uncoated recycled paper.

By the end of our research we had shown that working UHF RFID tags with screen-printed antennas can be realized on substrates of extremely low quality, such as uncoated recycled papers. The main influence on the final working tag is the quality of the conductive ink itself.

Acknowledgements

The authors express their gratitude to Ralf Zichner (Fraunhofer), and to the companies Ams R&D and RLS. Thanks are also due to Avery Dennison for permission to use their antenna design. Urška Kavčič acknowledges assistance from the European Social Fund ("Operation part-financed by the European Union, European Social Fund").

5 REFERENCES

[1] A. Blayo, B. Pineaux, Printing processes and their potential for RFID printing, Joint Conference on Smart Objects and Ambient Intelligence: Innovative context-Aware Services: Usage and Technologies, Grenoble, 2005, 27–30

[2] S. Pranonsatit, D. Worasawate, P. Sritanavut, Affordable ink-jet printed antennas for RFID applications, IEEE Transactions on Components Packaging and Manufacturing Technology, 5 (**2012**) 2, 878–883

[3] M. L. Allen, K. Jaakkola, K. Nummila, H. Seppa, Applicability of Metallic Nanoparticle Inks in RFID Applications, IEEE Transactions on Components and Packaging Technologies, 32 (**2009**) 2, 325–332

[4] V. Subramanian, P. C. Chang, J. B. Lee, S. E. Molesa, S. K. Volkman, Printed organic transistors for ultra-low-cost RFID applications, IEEE Transactions on Components and Packaging Technologies, 28 (**2005**) 4, 742–747

[5] K. Futera, M. Jakubowska, G. Kozioł, Printed electronic on flexible and glass substrates, Photonics Letters of Poland, 2 (**2010**) 2, 85–87

[6] M. Sloma, M. Jakubowska, A. Kolek, K. Mleczko, P. Ptak, A. W. Stadler, Z. Zawislak, A. Mlozniak, Investigations on printed elastic resistors containing carbon nanotubes, Journal of Materials Science-Materials in Electronics, 22 (**2011**) 9, 1321–1329

[7] K. Janeczek, A. Młożniak, G. Kozioła, A. Araźna, M. Jakubowska, P. Bajurko, Screen printed UHF antennas on flexible substrates, SPIE Proceedings, 7745 (**2010**)

[8] M. Jakubowska, M. Sloma, A. Mlozniak, Printed transparent electrodes containing carbon nanotubes for elastic circuits applications with enhanced electrical durability under severe conditions, Materials Science and Engineering B-Advanced Functional Solid-State Materials, 176 (**2011**) 4, 358–362

[9] U. Kavčič, L. Pavlovič, M. Pivar, M. Đokić, B. Batagelj, T. Muck, Printed electronics on recycled paper and cardboards = Tiskana elektronika na recikliranem papirju in kartonu, Informacije MIDEM, 43 (**2013**) 1, 50–57

[10] M. Pudas, N. Halonen, P. Granat, J. Vahakangas, Gravure printing of conductive particulate polymer inks on flexible substrates, Progress in Organic Coatings, 54 (**2005**) 4, 310–316

[11] D. Sung, A. D. Vornbrock, V. Subramanian, Scaling and Optimization of Gravure-Printed Silver Nanoparticle Lines for Printed Electronics, IEEE Transactions on Components and Packaging Technologies, 33 (**2010**) 1, 105–114

[12] S. L. Merilampi, T. Bjorninen, A. Vuorimaki, L. Ukkonen, P. Ruuskanen, L. Sydanheimo, The effect of conductive ink layer thickness on the functioning of printed UHF RFID antennas, Proceedings of the IEEE, 98 (**2010**) 9, 1610–1619

[13] D. Y. Shin, Y. Lee, C. H. Kim, Performance characterization of screen printed radio frequency identification antennas with silver nanopaste, Thin Solid Films, 517 (**2009**) 21, 6112–6118

[14] A. Syed, K. Demarest, D. D. Deavours, Effects of antenna material on the performance of UHF RFID tags, International Conference on RFID, Grapevine, 2007, 57–62

[15] P. V. Nikitin, S. Lam, K. V. S. Rao, Low cost silver ink RFID tag antennas, IEEE Antennas and Propagation Society International Symposium, 2B (**2005**), 353–356

[16] A. Rida, L. Yang, R. Vyas, S. Bhattacharya, M. M. Tentzeris, Design and integration of inkjet-printed paper-based UHF components for RFID and ubiquitous sensing applications, 37th European Microwave Conference, Munich, Germany, 2007, 724–727

[17] Y. Li, M. M. Tentzeris, Design and Characterization of Novel Paper-based Inkjet-Printed RFID and Microwave Structures for Telecommunication and Sensing Applications, Microwave Symposium, 2007. IEEE/MTT-S International, (**2007**), 1633–1636

[18] U. Bogataj, M. Maček, T. Muck, M. Klanjšek Gunde, Readability and modulated signal strength of two different ultra-high frequency radio frequency identification tags on different packaging, Packaging Technology and Science, 25 (**2012**) 7, 373–384

[19] U. Bogataj, M. Macek, T. Muck, Impact study of disturbance on readability of two similar UHF RFID tags, Informacije Midem-Journal of Microelectronics Electronic Components and Materials, 41 (**2011**) 3, 197–201

[20] J. Lee, J. Kim, M. Kim, N. Kang, J. Lee, Reliability of flip-chip bonded RFID die using anisotropic conductive paste hybrid material, Transactions of Nonferrous Metals Society of China, 21 (**2011**), S175–S181

[21] J. S. Rasul, Chip on paper technology utilizing anisotropically conductive adhesive for smart label applications, Microelectronics Reliability, 44 (**2004**) 1, 135–140

[22] K. C. Chin, C. H. Tsai, L. C. Chang, C. L. Wei, W. T. Chen, C. S. Chen, S. J. Lai, Design of Flexible RFID Tag and Rectifier Circuit using Low Cost Screen Printing Process. [online].[cited 2012]. Available from World Wide Web: http://www.pcb007.com/pdf/RFID-design.pdf

[23] K. Janeczek, Performance of RFID tag antennas printed on flexible substrates, XII International PhD Workshop [OWD-2010], Wisla, Poland, 2010

[24] A. Dziedzic, P. Slobodzian, Electromagnetic properties of materials used for paper printed RFID tag antennas, International Conference on Electromagnetics in Advanced Applications, Torino, 2009, 760–763

[25] V. Lakafosis, A. Rida, R. Vyas, Y. Li, S. Nikolaou, M. M. Tentzeris, Progress towards the first wireless sensor networks consisting of inkjet-printed, paper-based RFID-enabled sensor tags, Proceedings of the IEEE, 98 (**2010**) 9, 1601–1609

[26] X. Jingtian, Z. Hailong, T. T. Ye, Exploration of printing-friendly RFID antenna designs on paper substrates, RFID (RFID), 2011 IEEE International Conference on RFID, (**2011**), 38–44

[27] A. Rida, Y. Li, R. Vyas, M. M. Tentzeris, Conductive Inkjet-Printed Antennas on Flexible Low-Cost Paper-Based Substrates for RFID and WSN Applications, Antennas and Propagation Magazine, IEEE, 51 (**2009**) 3, 13–23

[28] R. Zichner, R. R. Baumann, Communication Quality of Printed UHF RFID Transponder Antennas, LOPE-C, Messe Frankfurt, Germany, 2011, 361–363

[29] S. Merilampi, L. Ukkonen, L. Sydanheimo, P. Ruuskanen, M. Kivikoski, Analysis of Silver Ink Bow-Tie RFID Tag Antennas Printed on Paper Substrates, International Journal of Antennas and Propagation, 2007 (**2007**), 9 pages

[30] SunChemical Technical information leaflet: CRSN2442 SunTronic Silver 280 Thermal Drying Silver Conductive Ink, September 2009

[31] DuPont Technical data sheet: DuPont 5064H, Silver conductor, August 2011

[32] C. M. Fahlcrantz, P. A. Johansson, P. Aslund, The influence of Mean Reflectance on Percieved Print Mottle, Journal of Imaging Science and Technology, 47 (**2003**) 1, 54–59

[33] NXP product data sheet SL3ICS1002/1202 UCODE G2XM and G2XL

[34] Print mottle, Sappi, Tech tips

UDK 669.1:004.032.26
Original scientific article/Izvirni znanstveni članek

ISSN 1580-2949
MTAEC9, 48(2)269(2014)

TOPMOST STEEL PRODUCTION DESIGN BASED ON THROUGH PROCESS MODELLING WITH ARTIFICIAL NEURAL NETWORKS

PROJEKTIRANJE PROIZVODNJE VRHUNSKIH JEKEL NA PODLAGI MODELIRANJA SKOZI PROCES Z UMETNIMI NEVRONSKIMI MREŽAMI

Tadej Kodelja[1], Igor Grešovnik[1,2], Robert Vertnik[2,3], Božidar Šarler[1,2,4]

[1]Center of Excellence BIK, Solkan, Slovenia
[2]University of Nova Gorica, Nova Gorica, Slovenia
[3]Štore Steel d.o.o., Research, Štore, Slovenia
[4]IMT, Ljubljana, Slovenia
bozidar.sarler@imt.si

Prejem rokopisa – received: 2013-06-14; sprejem za objavo – accepted for publication: 2013-07-03

Application of artificial neural networks for modeling of a complete process path in a steel production – from the scrap steel to the material properties of semi products – is presented. The described approach is introduced as an alternative to physics based through process modeling, with the advantage of lower complexity of the software and much lower computing times for calculating the influence of a specific settings of the process parameters. This new approach can be beneficially used in designing the production process. This is clearly demonstrated by estimating the influence of 34 alloying elements and process parameters of 6 process steps on 5 final mechanical properties of spring steel (elongation, tensile strength, yield stress, hardness after rolling and necking), based on 1879 recorded data sets from the production line in Štore Steel company. The ANN used is of a multilayer feedforward type with sigmoid activation function and supervised learning. An important feature of this approach is its dependence on accurate and sufficient data, acquired from the modeled process. Therefore, special care must be devoted to validation of the obtained model and error estimation. The reliability and other characteristics of the available data can vary to a great extent in real industrial practice, therefore analysis of the models is a highly customized task that has to be performed on a case to case basis. A flexible and easily extensible software base has been developed in the scope of the described work in order to adequately support research, development and practical application of this kind of models.

Keywords: steel production, mechanical properties of steel, artificial neural networks, response approximation, feed forward networks with back propagation

Predstavimo uporabo umetnih nevronskih mrež za modeliranje celotne procesne poti izdelave jeklenih polizdelkov – od rene do snovnih lastnosti polizdelkov. Opisani pristop je vpeljan kot alternativa fizikalnemu modeliranju skozi proces s prednostjo manjše kompleksnosti programske opreme ter bistveno manjšimi računskimi časi za izračun vpliva specifične nastavitve procesnih parametrov. Takšen pristop se lahko s pridom uporablja pri načrtovanju proizvodnega procesa. To je nazorno prikazano pri oceni vpliva 34 legirnih elementov in procesnih parametrov 6 procesnih korakov na 5 končnih snovnih lastnosti vzmetnega jekla (raztezek, natezna trdnost, meja tečenja, trdota po valjanju in skrček), na podlagi 1879 zabeleženih podatkovnih setov iz proizvodne linije podjetja Štore Steel. Uporabljena je usmerjena nevronska mreža s sigmasto aktivacijsko funkcijo in nadzorovanim učenjem. Pomembna značilnost tega pristopa je njegova odvisnost od pravilnih in zadostnih podatkov, pridobljenih iz procesa. Zato se je potrebno posebej posvetiti validaciji pridobljenega modela in oceni napak. Zanesljivost in ostale značilnosti razpoložljivih podatkov, pridobljenih iz realnih industrijskih procesov, se običajno zelo razlikujejo, zato je analiza takšnih modelov zelo specifična in mora biti narejena od primera do primera. V ta namen je bila izdelana fleksibilna in enostavno razširljiva programska oprema, ki omogoča primerno podporo raziskavam, razvoju in praktični uporabi tovrstnih modelov.

Ključne besede: izdelava jekla, mehanske lastnosti jekla, umetne nevronske mreže, aproksimacija odziva, nevronske mreže s povratnim razširjanjem napak

1 INTRODUCTION

Controlling the final mechanical properties of products or semi products is very important for steel production companies. This is a difficult task because there are a number of sequentially connected processes where the output of one process is an input to the next one. Different physics based numerical models can be used to predict the outcomes, but their development can be very complicated and time consuming.[1,2] Artificial neural networks (ANN) based models[3,4] can be used as an alternative to these physics based numerical models. Over the last years, ANNs have been successfully used across an extraordinary range of problem domains. Examples can be found in almost all fields of industry as well as in research areas that show promise for the future.[5] ANNs are already being used in steel production industries in modeling of blast furnace,[6] continuous casting, steel rolling,[7] etc. The first use of ANN in modeling of the entire production path (also referred to as "through process modeling") has been demonstrated for production of aluminum foil in[8]. Furthermore, a preliminary study[9] was made for complete steel production path, while in this study, additional parametric studies and sensitivity tests were added. The main drawback of

ANN models over physics based models is the fact that they can be used based on the specific training data only, and do not allow generalization to different production plants. Only the developed methodology is transferable.

In the present paper, we study the possibility of using ANN-based models as a comprehensive decision support tool in steel production. We explore the prediction of important mechanical properties of steel (elongation, tensile strength, flow limit, hardness and shrinkage) based on values of influential process parameters that determine the complete steel production path. The steel manufacturing process in the Štore Steel company and the respective available data were considered[10] as a basis for the present study. The manufacturing process path consists of six individual processes:[11,12] steel making, continuous casting of steel, hydrogen removal, reheating, multiple stage rolling, and cooling on the cooling bed. Each of these processes can be independently modeled by a physics based numerical model.[13–21] The state of the steel (shape, microstructure) of an individual process influences the downstream processing (subsequent processes in the process chain) and thus act as a part of input data (e.g. defining initial or boundary conditions) in the model of that process. This is schematically represented in **Figure 1**. In the current work we use another approach where an ANN is used to build a complete model of the whole production chain. We model the outcomes after the last process step and relate them to process parameters defining all processes involved in the production path. After the model is built, we can explore the effect of variation of process parameters to the final material properties, e,g. by changing process parameters independently in parametric and sensitivity tests and observing model outputs.

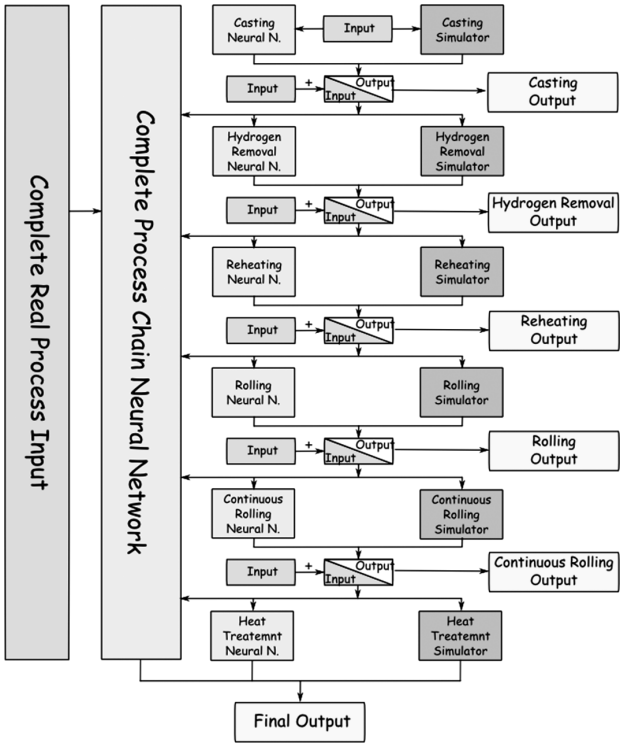

Figure 1: Steel manufacturing process modeling strategy
Slika 1: Strategija modeliranja procesa izdelave

2 MODELING SOFTWARE

A software for construction and use of ANN-based models has been developed in the scope of this work. The software was designed to match the challenges and requirements met when solving this kind of problems. In particular, it has to provide good flexibility in designing training strategies, filtering training data, verification of results, testing different network layouts, integration with other software, etc. This is crucial when approximating behavior of steel processing systems with large number of processing parameters. Data obtained from such systems is often inaccurate or even corrupted due to practical limitations in acquisition procedures. Response sampling can not be planned in advance but is accommodated to production schedules in the factory, therefore information available may be deficient in some regions of parameter space in order to obtain good response approximation and therefore verification of results plays an important role. The software platform has been elaborated in[22,23].

The Aforge.Net library is used as ANN framework.[24] A convenient characteristics of neural networks is that approximation can be performed in two separate stages (**Figure 2**). In the training stage, the network is trained by using the sampled response (either measured or calculated by a numerical model). In the approximation stage, trained network is used for all subsequent calculations of approximated response at arbitrary values of input parameters. This gives the neural networks an important advantage over other modeling techniques, since the second stage if very fast as compared to the first stage. The software takes full advantage of this feature by separating these stages. This is especially

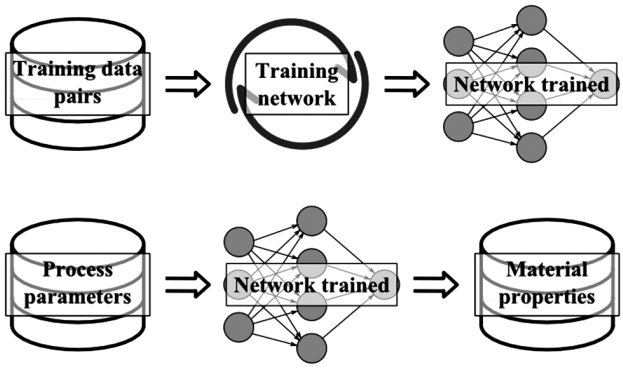

Figure 2: Approximation with neural networks: training a network with presented data pairs (top) and calculation of approximated response with trained network (bottom)
Slika 2: Aproksimacija z nevronskimi mrežami: učenje mreže na podlagi podatkovnih parov (zgoraj) in izračun aproksismiranega odziva z naučeno mrežo (spodaj)

important when performing extensive analyses of the considered process on the basis of the developed ANN models, or when incorporating the models in automatic optimization procedures.[25,26]

3 CONSTRUCTION OF THE ANN-BASED PROCESS MODEL

In the considered production setup from the Štore Steel company, the complete process is defined by 123 influential parameters (**Table 1**). There are 24 parameters defining the steel grade, 12 process parameters defining the continuous casting, 2 parameters the hydrogen removal, 4 parameters the reheating furnace, 31 parameters the rolling mill, 43 parameters the continuous rolling mill, and 7 parameters the cooling bed. On the output side, five mechanical properties of the final product are observed and represent the output values of the model (**Table 2**).

Table 1: Process parameters (input)
Tabela 1: Procesni parametri (vhod)

Processes / properties	Number of parameters
Composition	24
Continuous casting of steel	12
Hydrogen removal	2
Billet reheating furnace	4
Rolling mill	31
Continuous rolling mill	43
Cooling bed	7
Total	123

Table 2: Material properties (output)
Tabela 2: Snovne lastnosti (izhod)

Final mechanical properties	Elongation (A)
	Tensile strength (R_m)
	Yield stress ($R_{p0.2}$)
	Hardness after rolling (HB)
	Necking (Z)

For construction of the models, data was manually collected from different databases representing production of the steelwork in year 2011. Data was first separated for two billet dimensions (140 mm and 180 mm) which undergo considerably different process parameters. In addition, the data had to be filtered by applying a number of specially designed criteria in order to exclude corrupted data and overshoots. After these procedures, a total of 1879 data sets for dimension 140 mm have been prepared and used in the training procedure.

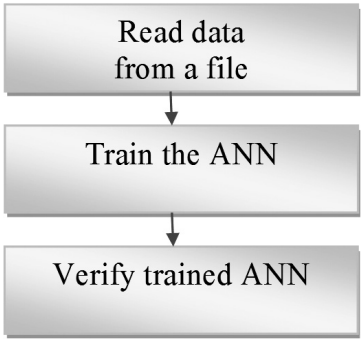

Figure 3: Training and verification procedure for model construction
Slika 3: Proces učenja in verifikacije pri izdelavi modela

This data was randomly divided into disjoint training and verification sets. Training data was then used in training a feed forward neural network with sigmoid activation function, in which we iteratively minimize error of the model on this data by the back propagation algorithm. After the convergence was achieved, the model was validated on the verification set that was not involved in the training, in order to estimate its accuracy (**Figure 3**).

A number of training procedures with different ANN architectures and training parameters have been performed in order to find the best settings. **Figure 4** shows convergence of maximum relative training errors for 15 different ANN settings.

Optimal settings (listed in **Table 3**) were identified by the convergence curve that reaches the lowest error at the end of the training procedure.

Table 3: ANN training and architecture settings
Tabela 3: Nastavitve učenja in arhitekture umetne nevronske mreže

Training parameters	
Learning rate	0.4
Momentum	0.6
Alpha value	1.0
Architecture	
Neurons in input layer	34
Neurons in 1st hidden layer	25
Neurons in output layer	5

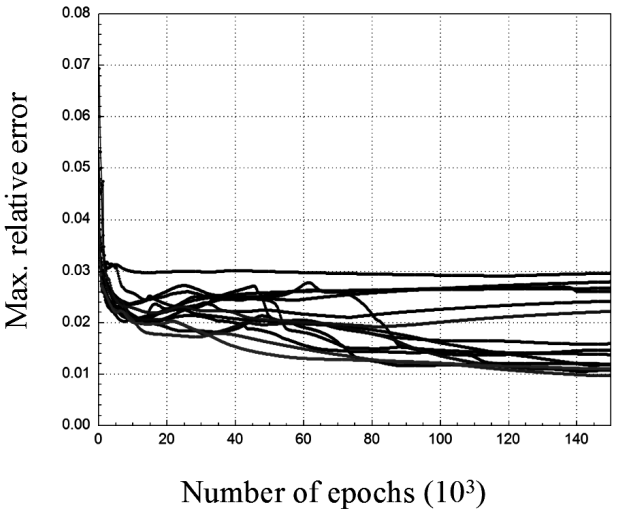

Figure 4: Maximal relative training error convergence for the best 15 trained ANNs
Slika 4: Največja relativna napaka konvergence napake učenja za 15 najboljših umetnih nevronskih mrež

In order to build the final model, we trained the ANN with optimal architecture and training parameters from **Table 3**. The maximum number of epochs was set to 10^5. Training procedures were performed on the HP ProLiant DL 380 G7 workstation with 2 six core 3.47 GHz Intel Xenon X5690 processors (6*256 kB L2 and 12 MB L3 cache), with 24GB installed RAM. Trained neural network which gave us the best results was trained in approximately 13 hours. A remark should be given here, that training of ANN is indeed a cumbersome and CPU time consuming task, typically on the same order of a computational cost of a physics based model. However, when the ANN is trained, the use of it is typically several orders of magnitude faster than executing the physical model.

4 RESULTS

The training procedure results in the artificial intelligence model that relates the modeled output values **v** to the input parameters **p**:

$$\mathbf{v} = \mathbf{v}(\mathbf{p}) \tag{1}$$

In the present context, **v** contains mechanical properties from **Table 2** and **p** contains process parameters from **Table 1**.

The obtained model can be used for a detailed study of response of final mechanical properties on variation of process parameters, which gives operators a better insight into the process and can be used as a valuable decision support tool. This is endorsed by low computational times necessary to evaluate a single response once the model is built, which are around 10^{-3} s in our case.

For illustration, we show dependence of hardness on carbon fraction around different points in the space of model input parameters (**Figure 5**). We have randomly selected 5 sets of parameters (points in the parameter space) from the training data. Then we varied the parameter of interest (in our case the carbon mass fraction), while the other parameters remained fixed. The parameter was varied from the minimum to the maximum value attained by that parameter within the training data.

It can be seen from **Figure 5** that hardness generally increases with increasing carbon mass fraction, which is in line with the well-established metallurgical knowledge. This is observed for different fixed combinations of other parameters, while the precise form of the relation varies significantly with the values of other parameters of the model. Since influences of individual parameters are highly correlated, it is important for some purposes to study behavior over larger range of process settings. This facilitates to obtain a deeper insight in the process. The described approach employing ANN-based models is ideal for such purpose due to the short calculation times and exhaustiveness of information that is provided by such models.

In another illustrative example, we take a different point of view. Instead of focusing on influence of individual parameters, we try to obtain a broader picture of the comparative influence of different parameters on the observed outcomes. We first chose a set from the training data sets close to the center of the interval containing the measured data. We denote the vector of input parameters of this set by $p_c = p_i$. We then varied one by one each component of the vector (i.e. the particular composition or process parameter) while the others were held fixed, and observed how the modeled quantities change as result of this variation. More precisely, we considered the following function of one variable:

$$u_{ij}(t) = v_i(p_{c1}, p_{c2}, \ldots, p_{cj-1}, t, p_{cj+1}, \ldots, p_c)$$
$$i = 1, \ldots N_v, \; j = 1, \ldots, N_p \tag{2}$$

where N_p is the number of model parameters and N_v is the number of output quantities of the model. Each element of the parameter vector p_c was varied over the whole interval that the given parameter attained in the provided industrial data. The variations were then calculated for each output value (denoted by index i in equation (2) and for each parameter (index j in equation (2) and used as a measure of influence of the specific

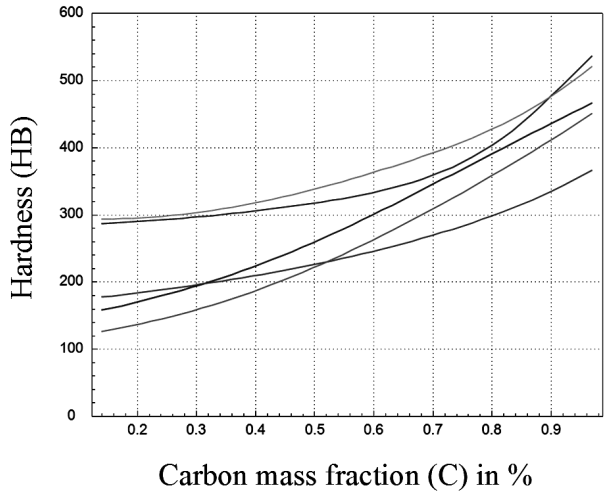

Figure 5: Steel hardness after rolling as a function of the carbon mass fraction, calculated by the ANN model on five training sets

Slika 5: Trdota jekla po valjanju kot funkcija masnega deleža ogljika, izračunana z umetno nevronsko mrežo na petih učnih množicah

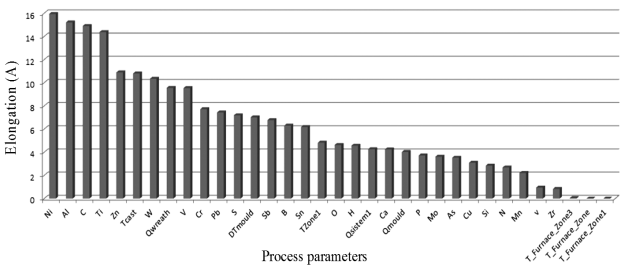

Figure 6: Influence of process parameters on changes in elongation (*A*), ordered from the most influential one on the left, to the least influential one on the right

Slika 6: Vplivi procesnih parametrov na spremembe v elongaciji (*A*), urejeni od najbolj vplivnih na levi do najmanj vplivnih na desni

parameter. The results are shown in **Figures 6** to **10** and are for each parameter calculated by:

$$\Delta u_{ij}(t) = \left(\max u_{ij}(t) - \min u_{ij}(t)\right) \quad (3)$$

where $\max u_{ij}(t)$ and $\min u_{ij}(t)$ represents maximum and minimum influence of j-th parameter on i-th output value.

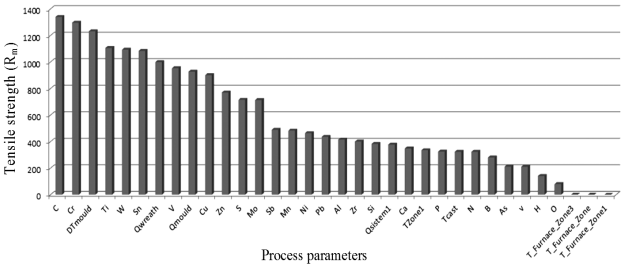

Figure 7: Influence of process parameters on changes in tensile strength (R_m)
Slika 7: Vplivi procesnih parametrov na natezno trdnost (R_m)

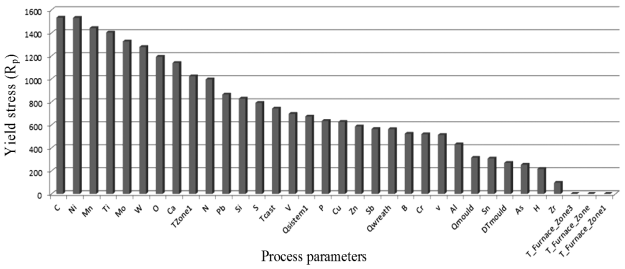

Figure 8: Influence of process parameters on changes in yield stress (R_p)
Slika 8: Vplivi procesnih parametrov na mejo tečenja (R_p)

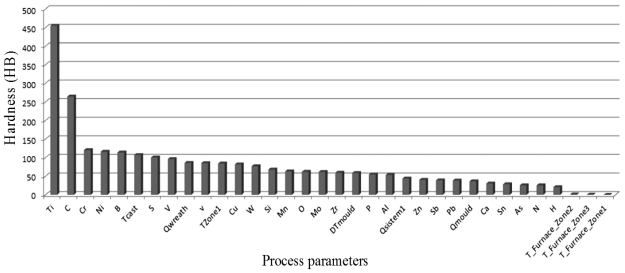

Figure 9: Influence of process parameters on changes in hardness after rolling (HB)
Slika 9: Vplivi procesnih parametrov na spremembe trdote po valjanju (HB)

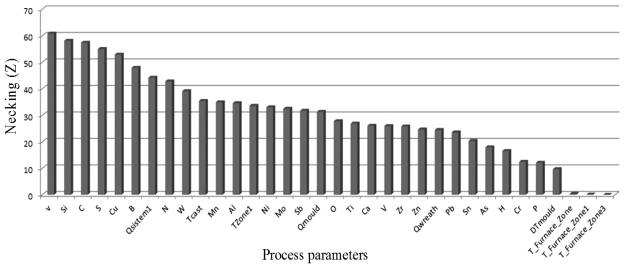

Figure 10: Influence of process parameters on changes in necking (Z)
Slika 10: Vplivi procesnih parametrov na spremembe vratu tečenja (Z)

Table 4 shows 3 most influential parameters for each material property. From the available parameters that we use for training the ANN (**Figures 6** to **10**), different elements of the composition of the material are the most influential for all five properties. Process parameters do not have major influence. The most important parameters obtained from the present ANN response are temperature of the liquid steel (Tcast) for elongation and hardness after rolling, temperature difference in the mould (Dtmould) for tensile strength, cooling water temperature in zone 1 (TZone1) for yield stress and cooling water flow rate in first spray system (Qsistem1) for necking. Obviously, the response of the model is not entirely expected. This indicates that the represented methodology should be used with care and finally judged by engineering expert knowledge. It is however true, that in the present model, several important process parameters are missing due to the lack of data acquisition in the plant (particularly for rolling), since a new rolling mill has been installed recently.

Table 4: The 3 most influential parameters for each mechanical property
Tabela 4: Trije najbolj vplivni parametri za posamično mehansko lastnost

	Elongation (A)	Tensile strength (R_m)	Yield stress (R_p)	Hardness after rolling (HB)	Necking (Z)
1	Ni	C	C	Ti	V
2	Al	Cr	Ni	C	Si
3	Ti	Delta temperature in the mould	Mn	Ni	C

5 CONCLUSIONS

ANN have been used to model a complete production path in a steelwork. The developed methodology is essentially a black box modeling approach. Outcomes of the process can be predicted for arbitrary combination of process parameters without directly considering the physical background of the modeled process, but are instead relying on information about previous realizations of the process. As an example, a model of production line in the Štore Steel company was studied, reduced to 34 influential process parameters and with 5 observed properties of the final product. Several combinations of models that will include even less influential parameters will be studied in the future.

A significant advantage of the approach, as compared to the physics based numerical models, is much lower complexity of the model. There is no need to calibrate the model in order to compensate for physical simplifications and inaccurate knowledge of model constants, since the model is based on the realistic data gained from the actual process. Once the model is built, evaluation times are extremely short, in the order of a millisecond,

compared to several hours or even days that would be necessary for state-of-the-art physics based models of the same process. This represents a great advantage in tasks where large number of evaluations are required, such as automatic optimization of process parameters or detailed parametric studies.[22,23] This kind of modeling has therefore a great potential to enable better insight and understanding of industrial processing, as well as to serve as a powerful decision support tool. This potential was indicated in the present paper by clearly presenting influence on individual process parameters on the outcomes.

The drawback of the approach is its dependence on reliable and abundant data that is sometimes hard to obtain. Great attention must be paid to estimation of accuracy of the model in imperfect conditions with regard to the available data.[9] This will remain the main focus of future research, where influence of various factors on model accuracy will be studied which will eventually lead to procedures for reliable prediction of error bounds, which is crucial for industrial use. This will incorporate arrangements where controlled acquisition of training data is possible, e.g. by using physics based models. In this context, a large portion of work is devoted to building a flexible, modular and scalable software base to support such work. Finally, it should be noted, that the presented methodology stimulated more careful and complete data acquisition of the process parameters in Štore Steel company, needed for continuation of the present work and for better process repeatability as such.

Acknowledgment

The Centre of Excellence for Biosensors, Instrumentation and Process Control (COBIK) is an operation financed by the European Union, European Regional Development Fund and Republic of Slovenia, Ministry of Education, Science Culture and Sport. The financial support of COBIK, Slovenian Research Agency and Štore Steel company in the framework of the research program P2-0379 and the project L2-3651 is kindly acknowledged.

6 REFERENCES

[1] B. Šarler, R. Vertnik, S. Saletić, G. Manojlović, J. Cesar, BHM Berg- und Hüttenmännische Monatshefte, 150 (**2005**), 300–306

[2] B. Šarler, R. Vertnik, A. Z. Lorbiecka, I. Vušanović, B. Senčič, BHM Berg-und Hüttenmännische Monatshefte, (**2013**), 1–9, doi: 10.1007/s00501-013-0147-7

[3] R. Rojas, Neural Networks – A Systematic Introduction, Springer-Verlag, Berlin 1996

[4] J. Kocijan, Modelling of dynamic systems with artificial neural networks and related methods, Založba Univerze v Novi Gorici, Nova Gorica 2007

[5] F. Fogelman-Soulie, P. Gallinari, Industrial Applications of Neural Networks, World Scientific Publishing Co, Great Britain 1998

[6] J. Jimenez, J. Mochon, D. S. De Alaya, F. Obeso, ISIJ International, 52 (**2004**), 1935–1944

[7] Y. Bissessur, Control Theory and Applications, 147 (**2000**), 633–640

[8] Š. Trčko, B. Šarler, Use of artificial neural networks in predicting properties of household foil in Impol aluminum industry, M. Valant, U. Pirnat, Slovenska konferenca o materialih in tehnologijah za trajnostni razvoj, Ajdovščina, 2009, Knjiga povzetkov, Zbornik, Založba Univerze v Novi Gorici, Nova Gorica 2009, 126–130

[9] I. Grešovnik, T. Kodelja, R. Vertnik, B. Senčič, M. Kovačič, B. Šarler, Computers, Materials & Continua, 30 (**2012**), 19–38

[10] Štore Steel d.o.o., 2012, Available from World Wide Web: www.store-steel.si/DefaultE.asp

[11] W. R. Irwing, Continuous Casting of Steel, The Institute of Materials, London 1993

[12] J. G. Lenard, Primer on Flat Rolling, Elsevier, Amsterdam 2007

[13] R. Vertnik, B. Šarler, International Journal of Cast Metals Research, 22 (**2009**), 311–313

[14] R. Vertnik, M. Založnik, B. Šarler, Eng. Anal. Bound. Elem., 30 (**2006**), 847–855

[15] G. Kosec, M. Založnik, B. Šarler, H. Combeau, Computers, Materials & Continua, 22 (**2011**), 169–195

[16] A. Z. Lorbiecka, B. Šarler, Computers, Materials & Continua, 18 (**2010**), 69–103

[17] A. Z. Lorbiecka, R. Vertnik, H. Gjerkeš, G. Manojlovič, B. Senčič, J. Cesar, B. Šarler, Computers, Materials & Continua, 8 (**2009**), 195–208

[18] I. Kovačević, B. Šarler, Material Science Forum, 508 (**2006**), 579–584

[19] U. Hanoglu, S. Islam, B. Šarler, Materials Technology, 445 (**2011**), 545–547

[20] M. Kovačič, B. Šarler, Materials and Manufacturing Processes, 26 (**2011**), 464–474

[21] M. Kovačič, B. Šarler, Materials and Manufacturing Processes, 24 (**2009**), 369–374

[22] I. Grešovnik, T. Kodelja, R. Vertnik, B. Šarler, Applied Mechanics and Materials, 101–102 (**2012**), 838–841

[23] I. Grešovnik, T. Kodelja, R. Vertnik, B. Šarler, Application of artificial neural networks to improve steel production process, Proc. of the 15th Inter. Conf. on Artificial Intelligence and Soft Computing, Napoli, Italy, 2012, 249–255

[24] Aforge.Net., 2012, Artificial Intelligence Library. Available from World Wide Web: http://www.aforgenet.com/.

[25] I. Gresovnik, A General Purpose Computational Shell for Solving Inverse and Optimisation Problems – Applications to Metal Forming Processes, Ph. D. thesis, University of Wales Swansea, U.K., 2000

[26] I. Grešovnik, Journal of Mechanical Engineering, 9 (**2007**), 582–598

UDK 621.318.1:66.017
Original scientific article/Izvirni znanstveni članek

ISSN 1580-2949
MTAEC9, 48(2)275(2014)

THE PREPARATION OF MAGNETIC NANOPARTICLES BASED ON COBALT FERRITE OR MAGNETITE

PRIPRAVA MAGNETNIH NANODELCEV NA OSNOVI KOBALTOVEGA FERITA ALI MAGNETITA

Aleš Stambolić[1], Marjan Marinšek[2]

[1]Institute of Metals and Technology, Lepi pot 11, 1000 Ljubljana, Slovenia
[2]Faculty of chemistry and chemical technology, Aškerčeva cesta 5, 1000 Ljubljana, Slovenia
ales.stambolic@imt.si

Prejem rokopisa – received: 2013-12-19; sprejem za objavo – accepted for publication: 2014-01-02

Cobalt ferrite and magnetite nanoparticles are superparamagnetic materials. Stable suspensions of superparamagnetic nanoparticles are magnetic fluids. Stable magnetic fluids are prepared by the addition of surfactants to supporting polar or nonpolar media. We have studied the preparation of magnetic nanoparticles based on cobalt ferrite or magnetite, and stabilized the obtained product in an aqueous suspension. We found the optimal co-precipitation time for cobalt ferrite at 90 °C to be 2 h. Under such conditions the product exhibited the lowest amount of amorphous phase (46.2 %), average particle diameter 10.2 nm and a relatively high proportion of agglomerated particles (≈30 %). The product is therefore destabilized in an aqueous solution of polyvinylpyrrolidone K. The optimal co-precipitation time for magnetite at 90 °C is 30 min. After 30 min the product has no amorphous phase, average particle diameter is 6.8 nm and the proportion of agglomerated particles is low (≈3 %). The product is poorly stabilized because the proportion of agglomerated particles increases when the magnetite is re-dispersed in an aqueous solution of polyvinylpyrrolidone K. Magnetite prepared with the Massart method has a small amount of amorphous phase (≈4 %), average particle diameter is ≈6 nm and a low proportion of agglomerated particles (4.5 %) and is therefore well stabilized in an aqueous solution of polyvinylpyrrolidone K.

Keywords: cobalt ferrite, magnetite, superparamagnetic nanoparticles, co-precipitation, stabilization of magnetic fluids

Nanodelci kobaltovega ferita in magnetita imajo superparamagnetne lastnosti. Stabilne suspenzije superparamagnetnih nanodelcev imenujemo magnetne tekočine. Stabilne magnetne tekočine pripravimo z dodatkom surfaktantov v nosilni polarni ali nepolarni medij. Sintetizirali smo magnetne nanodelce kobaltovega ferita in magnetita ter dobljeni produkt stabilizirali v vodnem mediju. Določen je bil optimalen čas soobarjanja kobaltovega ferita pri 90 °C, in sicer 2 h. V tem času ima produkt najnižjo vsebnost amorfne faze (46,2 %), povprečno velikost delca 10,2 nm in delež neželenih aglomeratov pa je ≈30 %. Ko se delce kobaltovega ferita redispergira v vodi z dodanim surfaktantom, nastane destabilizirana suspenzija, katere vzrok je visok delež aglomeratov. Optimalen čas koprecipitacije magnetita pri 90 °C je 30 min. Takrat produkt ne vsebuje amorfne faze, povprečna velikost delca je 6,8 nm, delež aglomeriranih delcev je ≈3 %. Produkt se nato redispergira v vodnem mediju z dodanim surfaktantom, kjer je magnetit slabo stabiliziran zaradi povečanja deleža aglomeratov med redisperzijo. Magnetit, pridobljen z metodo po Massartu, vsebuje ≈4 % amorfne faze, ima povprečno velikost delca ≈6 nm, delež aglomeratov 4,5 % in je zato odlično stabiliziran v vodni raztopini polivinilpirolidona K.

Ključne besede: kobaltov ferit, magnetit, superparamagnetni nanodelci, koprecipitacija, stabilizacija magnetnih tekočin

1 INTRODUCTION

Magnetic fluids are stable dispersions of magnetic nanoparticles in an organic or aqueous medium. Magnetic nanoparticles are solid-state particles that are affected by magnetic fields. The term "nano" indicates particles that are in the size range below 100 nm. Magnetic nanoparticles occur in the form of ferrites with the general formula MFe_2O_4, where M is a divalent metal cation (nickel, cobalt, manganese, zinc or iron). Ferrites crystallize in the spinel crystal structure.[1–3]

The most important characteristic of magnetic nanoparticles is superparamagnetism. Superparamagnetism relates to nanoparticles whose magnetic moments are oriented irregularly and do not show any magnetic properties in the absence of an applied magnetic field. However, even when these nanoparticles are exposed to a small external magnetic field, dipole moments are formed within the particles. The dipole moments are directed in accordance with the source of the magnetic field.[4]

There are several techniques for the preparation of magnetic nanoparticles. The most common are: co-precipitation, sol-gel synthesis, hydrothermal synthesis and synthesis in microemulsions. When magnetic nanoparticles are obtained it is better if the resulting particles are crystalline, have a narrow size distribution and have the same shape.[1,3]

The developing product must be stabilized so it does not agglomerate due to the attractive forces between the particles. The techniques of stabilization are electrostatic, steric and electrosteric. Electrostatic stabilization is the mechanism in which the attractive forces are due to the Coulomb forces between the charged colloidal particles. The repulsion between the particles is achieved with an equally charged electric double layer surrounding the particles. Steric stabilization is accomplished by the adsorption of long-chained molecules called surfac-

tants on the particle's surface. These surfactants then form a coating that creates a repulsive force and separates one particle from another particle. Electrosteric stabilization is a combination between electrostatic and steric stabilization. The repulsion between the particles is achieved by the adsorption of charged polymeric molecules on the nanoparticle's surface.[4,5]

The applications of magnetic fluids are primarily in engineering and medicine as seals for rotating mechanical parts, as in the heat dissipation system in speakers and as a contrast agent in imaging with the nuclear magnetic resonance technique.[6,7]

2 EXPERIMENTAL

The main goal of this study was to prepare magnetic nanoparticles based on cobalt ferrite or magnetite, and stabilize the obtained product in an aqueous suspension. The product was quantitatively and qualitatively analysed with a Rietveld analysis and morphologically described using scanning electron microscopy. The cobalt ferrite and magnetite were prepared by co-precipitation at 90 °C and pH = 13. The magnetite was also synthesized with the Massart method, where the product is instantaneously precipitated at room temperature with vigorous stirring. The product was stabilized with polyvinylpyrrolidone K in an aqueous medium.

2.1 Synthesis of cobalt ferrite and magnetite at elevated temperature

A solution of Co^{2+} and Fe^{3+} ions or a solution of Fe^{2+} and Fe^{3+} ions was mixed in a laboratory reactor with a reflux condenser using a magnetic stirrer (**Figure 1**). Then, in deionized water dissolved sodium hydroxide was added, which allows the progress of the synthesis at pH = 13. The stirring was continued. Immediately after the addition of sodium hydroxide the dark precipitate was formed.

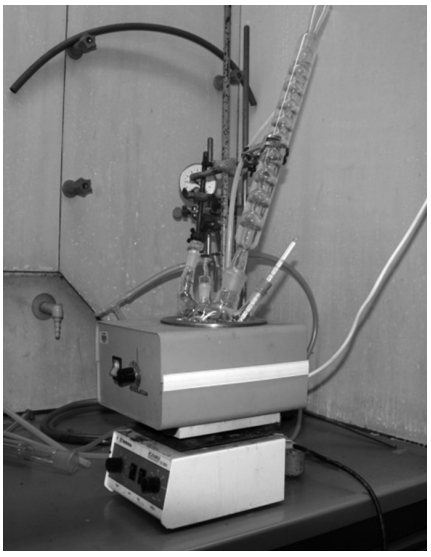

Figure 1: Laboratory reactor used for co-precipitation at elevated temperature
Slika 1: Laboratorijski reaktor za koprecipitacijo pri povišani temperaturi

The chemical reaction for the cobalt ferrite preparation is as follows:

$$8\ NaOH_{(aq)} + CoSO_{4(aq)} + Fe_2(SO_4)_{3(aq)} \rightarrow CoFe_2O_{4(s)} + +\ 4\ Na_2SO_{4(aq)} + 4\ H_2O \quad (1)$$

The chemical reaction for the magnetite preparation is as follows:

$$8\ NaOH_{(aq)} + 2\ FeCl_{3(aq)} + FeCl_{2(aq)} \rightarrow Fe^{2+}O \cdot Fe_2^{3+}O_{3(s)} + 8\ NaCl_{(aq)} + 4\ H_2O \quad (2)$$

Next, the oleic acid was added to the reaction mixture and it was heated up to 90 °C. This temperature was regulated until the end of the reaction. Following the synthesis the pH of the precipitate was reduced from 13 to 5.5, after which the mixture was filtered and the obtained nanoparticles were re-dispersed and stabilized in an aqueous medium with the addition of a surfactant.

2.2 Synthesis of magnetite using the Massart method

Aqueous solutions of Fe^{2+} and Fe^{3+} ions were mixed in a beaker. During vigorous stirring ammonia was added. This leads to the formation of a black, magnetic precipitate. After the reaction, when all the ingredients are well mixed, the mixture was filtered and the nanoparticles were re-dispersed and then stabilized in an aqueous medium with the addition of a surfactant.

The chemical reaction of the magnetite prepared with the Massart method can be described by Eqs. (3) and (4):

$$NH_{3(l)} + H_2O \rightarrow NH_4^+{}_{(aq)} + OH^-{}_{(aq)} \quad (3)$$

$$8\ NH_4^+{}_{(aq)} + 8\ OH^-{}_{(aq)} + FeCl_{2(aq)} + 2\ FeCl_{3(aq)} \rightarrow FeO \cdot Fe_2O_{3(s)} + 8\ NH_4Cl_{(aq)} + 4\ H_2O \quad (4)$$

2.3 Stabilization of the magnetic fluids

The first level of stabilization was achieved with the addition of oleic acid during the development of the synthesis. Oleic acid is an unsaturated fatty acid (between the carbons atoms there is at least one double bond) with the molecular formula $C_{18}H_{34}O_2$. The oleic acid surrounds the nanoparticles and prevents their further growth and agglomeration during the synthesis.

The second level of stabilization was realized after the purification of the product. The resulting cake of particles was necessary to re-disperse and stabilize in an aqueous medium. Steric stabilization with polyvinylpyrrolidone $[(C_6H_9NO)_n]$ label K was used. Its molecular weight is 30000 g/mol. Polyvinylpyrrolidone is freely soluble in polar solvents, where it creates films that can serve as a coating for the particles.

2.4 X-ray powder diffraction and Rietveld analysis

X-ray diffraction shows whether the desired product (cobalt ferrite or magnetite) is formed. A subsequent Rietveld analysis determines the amount of amorphous phase in a sample.

X-ray powder analysis provides information about the chemical composition, the degree of crystallinity and the size or symmetry of the crystal unit cell. With this method an X-ray beam is irradiated at the sample's surface at an angle Θ. During the operation the sample is synchronously rotated by half the speed of the detector so that the angle between the source of radiation and the sample is always equal to the angle between the sample and the detector. At every Θ the X-rays are apparently deducted from the samples surface. If the phase shift between the various parallel X-rays is equivalent to a multiple of the wavelength (peak of one wave coexists with the top of the second wave) then the X-rays are strengthened, otherwise they override.[8,9]

The samples were recorded on X-ray diffractometer PANalytical X'Pert PRO using Cu-Kα1 radiation with a wavelength of 1.5406×10^{-10} m.

Using the Rietveld method the sample was quantitatively analysed. The relative proportions of the individual crystal phases within the sample are determined. Measured and calculated powder patterns are compared using the Rietveld analysis. Also, the contribution of the individual phases in multiphase samples can be detected, including amorphous components or an unknown phase (with the addition of a crystalline or amorphous standard with a known mass fraction).[10]

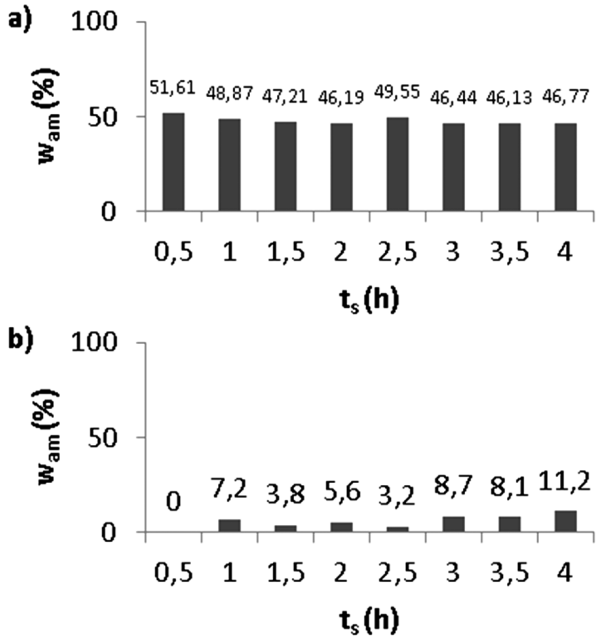

Figure 2: Dependence of the proportion of amorphous phase vs. time for the synthesis of: a) cobalt ferrite and b) magnetite

Slika 2: Odvisnost deleža amorfne faze od časa sinteze za: a) kobaltov ferit in b) magnetit

2.5 Scanning electron microscopy (SEM)

The microstructure of the samples was characterized with scanning electron microscopy (SEM). The microstructure of the materials is related to their properties (mechanical, electrical, optical and magnetic) and thus their usefulness and purpose. SEM is used to observe the surface of non-volatile solid samples. This technique allows the interaction of electrons with the surface atoms and gives information about the shape, size, grain size distribution, elemental composition and the proportion of each element in the sample.[9,11]

For a nanostructure analysis a Zeiss Ultra Plus (FE-SEM) scanning electron microscope equipped with an EDS detector SDD Oxford was used. From SE images the morphological characteristics of the prepared products, especially the particle size, were defined.

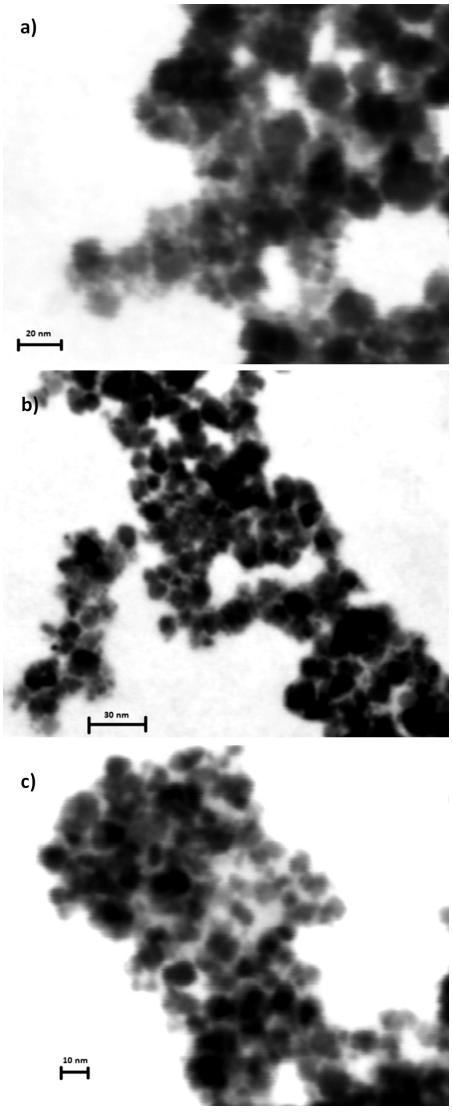

Figure 3: SE images of cobalt ferrite after: a) 0.5 h, b) 2 h and c) 4 h of co-precipitation

Slika 3: SE-posnetki kobaltovega ferita po: a) 0,5 h, b) 2 h in c) 4 h koprecipitacije

3 RESULTS AND DISCUSSION

When preparing cobalt ferrite and magnetite at elevated temperature, we were interested in the proportion of amorphous phase in the sample during the synthesis in order to determine the optimal synthesis time. For this purpose we used the Rietveld method.

Figure 2a shows that the proportion of amorphous phase in the cobalt ferrite is in a high range of about 50 % for all 4 h of synthesis. The reason for such a high proportion may be an incomplete reaction, old reactants or very fast precipitation. If the degree of supersaturation is high, then the precipitation is finished extremely quickly. Therefore, the particles do not have sufficient time to organize into a proper structure, which leads to the formation of an amorphous phase. This mechanism is quite possible as the average particle size varies very little after 30 min during the reaction. This means that the majority of the precipitation has come to an end much before 30 min. After 30 min of reaction the amount of amorphous phase is 51.61 % and then it is slightly decreasing for another hour and a half, when it reaches a value of 46.19 %. After 2 hours of synthesis the amount of amorphous phase varies. The minimum value is reached after 3.5 h, i.e., 46.13 %, but due to possible method errors, very small values deviation and economic reasons (long-term progress of the synthesis results in higher costs) it is enough to conduct the synthesis of the cobalt ferrite for 2 h or at least one hour. Because cobalt ferrite has a relatively high content of amorphous phase, the material has poor superparamagnetic properties as the particles react quite slowly on the magnet.

Figure 2b reveals a slight increase in the proportion of amorphous phase with the time of synthesis for the magnetite. Since after 30 min of reaction there is no amorphous phase in the magnetite, we have further operated with synthesis for just as long. Due to the lower levels of amorphous phase the superparamagnetic properties of the material are much better.

A Rietveld analysis was also performed for the magnetite synthesized using the Massart method. The proportion of amorphous phase was 4.3 %.

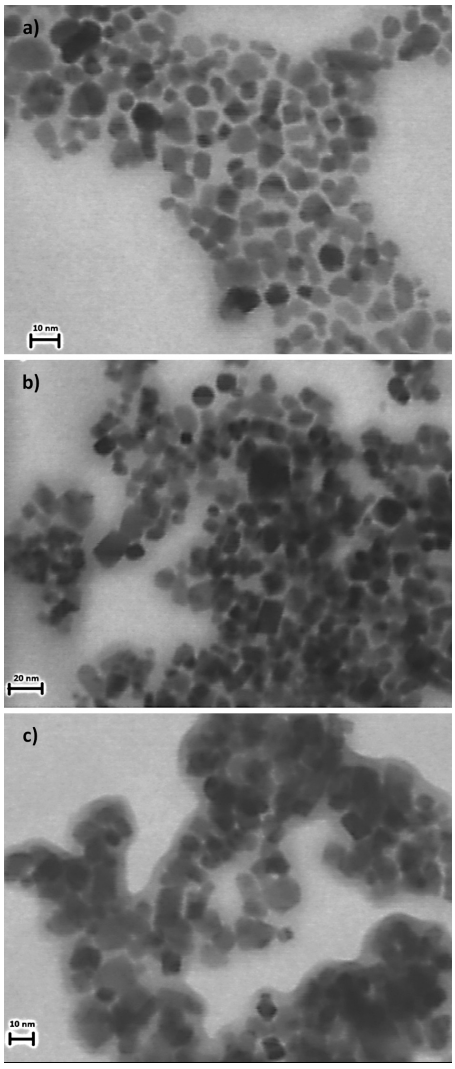

Figure 4: SE images of magnetite after: a) 0.5 h, b) 2 h and c) 4 h of co-precipitation

Slika 4: SE-posnetki magnetita po: a) 0,5 h, b) 2 h in c) 4 h koprecipitacije

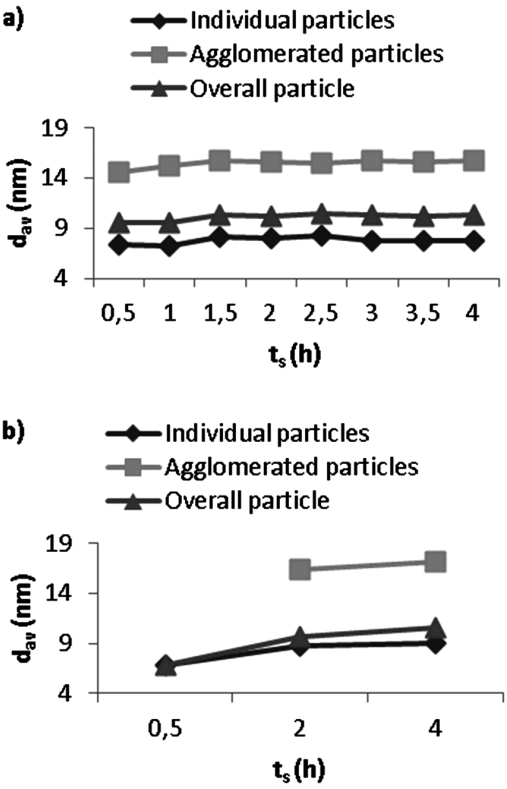

Figure 5: Average diameter changes of individual particles, agglomerated particles and overall particle for the synthesis of: a) cobalt ferrite and b) magnetite

Slika 5: Spreminjanje nadomestnega povprečnega premera posameznih delcev, aglomeriranih delcev in vseh delcev s časom sinteze za: a) kobaltov ferit in b) magnetit

SE images (**Figures 3** and **4**) were used to determine the morphological characteristics of the prepared products. The developing cobalt ferrite particles have predominantly a spherical shape, while the magnetite particles have a cubic shape.

The average size of the cobalt ferrite's individual particles after the first hour is approximately 7.3 nm, which then increases to about 8 nm. The same trend is also visible for the overall particle (individual and agglomerated), where the average size is in the range 9.46 nm to 10.37 nm (**Figure 5a**). The proportion of cobalt ferrite agglomerated particles is about 30 % for all 4 h of synthesis. A slight increase in the size of the individual particles is due to the co-precipitation mechanism, which in this case is not so definite. After 0.5 h the proportion of smallest particles (less than 4 nm) is about 20 % and after 1 h it dropped to 10 %. The conclusion from the morphological analysis of the cobalt ferrite particles is that in a time interval of 0.5 h to 1 h the formation of a new crystal nucleus is significantly reduced, but the particles are still growing. After 1 h of synthesis there are no noticeable changes so the crystal growth must have decelerated. The same trend was also observed for the agglomerated particles.

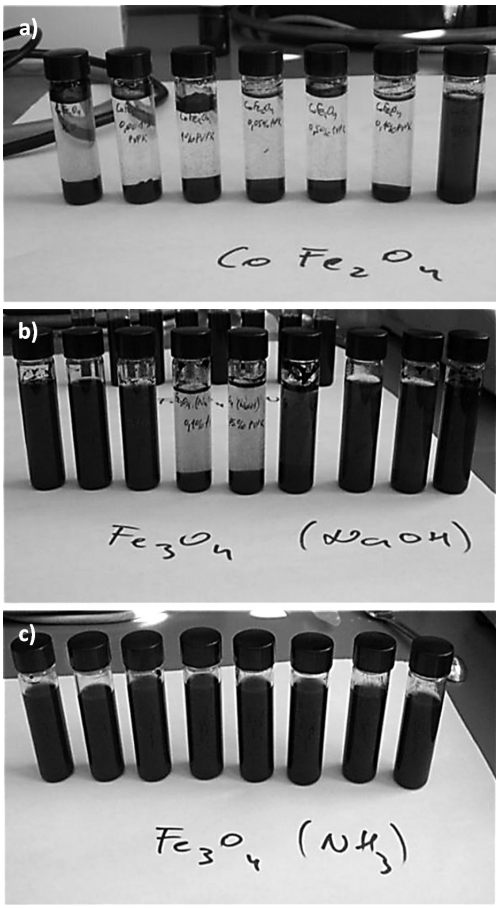

Figure 6: Magnetic suspensions with different mass fractions (*w*/%) addition of PVP K for: a) cobalt ferrite, b) magnetite obtained at an elevated temperature and c) magnetite synthesized with the Massart method

Slika 6: Magnetne suspenzije z različnimi masnimi deleži (*w*/%) PVP K-ja: a) kobaltov ferit, b) magnetit, pridobljen pri povišani temperaturi in c) magnetit, sintetiziran z Massartovo metodo

The size of the individual, agglomerated and overall particles of magnetite is slowly increasing with the synthesis time. The average individual particle grows from 6.84 nm to 8.97 nm and the overall average particle (individual + agglomerated) grows from 6.84 nm to 10.49 nm (**Figure 5b**). The overall average particle size increases much more than the individual particle because the proportion of agglomerated particles increases considerably with the synthesis time (from 2.86 % to 21.36 %). When the magnetite was precipitated, typical mechanisms of co-precipitation were observed. After 30 min there are no agglomerated particles in the system. With the extension in the synthesis time the amount of the smallest particles decreases, which implies a decline in the formation of the crystallization nucleus. However, the particles are growing more noticeably and consequently agglomerating with an increase of the synthesis time. The observed behaviour of the Fe_3O_4 system during the synthesis where the magnetite particles are growing slowly, while slowly increasing the proportion of amorphous phase with synthesis time, indirectly indicates the mechanism of formation of the solid phase magnetite in two stages. The first stage is relatively fast and results in magnetite nanoparticles with a number of defects higher than equilibrium. The second stage is substantially slower. On the initially precipitated Fe_3O_4 surface new, smaller magnetite grains with an equilibrium number of defects should re-precipitate.

The magnetite synthesized by the Massart method has a low proportion of agglomerated particles (4.6 %) so the possibility of their stabilization is extensive. The average individual particle size is 6.1 nm, and the overall particle size is 6.4 nm.

The last stage of the research was to stabilize the magnetic fluid with PVP K. The addition of a surfactant should take care of the steric stabilization in an aqueous medium.

A range of the mass fractions w = 0.001 % to 1 % PVP K was added in the polar aqueous medium and 1 % in decane. **Figure 6a** shows that cobalt ferrite is not stabilized in an aqueous medium with PVP K, irrespective of the quantity of added PVP K. Poorly stabilized, whereas the precipitate is settling, is the cobalt ferrite in a non-polar decane on the far right of **Figure 6a**. Despite everything, the settling of the particles was noticeably slower in the suspensions with a higher mass fraction of PVP K and faster in those with a lower mass fraction of PVP K.

In **Figure 6b** the suspensions of magnetite are shown. The stability of the suspensions is evidently improved compared to the cobalt ferrite, but the suspensions are still far from ideal. Again, 0.001 % to 1 % of PVP K was added and once again we observed an improved stability for a larger addition of PVP K.

In the case of the magnetite synthesized using the Massart method stable suspensions were prepared. In stable suspensions the particles do not settle and are distributed throughout the volume (**Figure 6c**). All the reconstituted suspensions are stable, regardless of the amount of added PVP K.

The stability of the suspensions can be related to the particle size and the proportion of agglomerated particles. Cobalt ferrite has an average particle size of 7.45 nm, but it also has 26 % of agglomerated particles. A high proportion of agglomerated particles implies a larger number of particles with greater mass that settle smaller particles below and thus destabilize the suspension. Magnetite has an average particle size of 8.17 nm, but only about 17 % of agglomerated particles. The number of magnetite particles with higher mass is much lower, so the particles settle slowly, but eventually they all settle. Magnetite synthesized with the Massart method has a particle size of 6.37 nm and only 4.5 % of agglomerated particles. These suspensions are very stable due to the particles' small size and because the contact between the particles was prevented by the addition of the surfactant.

4 CONCLUSIONS

The synthesis of cobalt ferrite operating for 4 h at 90 °C ensures a relatively constant average size of overall particles equal to about 10 nm during the synthesis. The proportion of amorphous phase in the samples was approximately constant throughout synthesis, i.e., high ≈ 50 %. The proportion of agglomerated particles within the suspension was around 30 %. An optimal synthesis time of 2 h was determined. After 2 h of synthesis the average particle size was 10.22 nm, the sample has 46.19 % of amorphous phase and the proportion of agglomerated particles was 30.44 %.

The synthesis of magnetite, which lasted for 4 h at 90 °C, exhibited a growth of the average particle size, an increase in the amount of amorphous phase and the proportion of agglomerated particles during the synthesis. The optimal time for the magnetite synthesis was 30 min when the particle size is 6.84 nm, the amount of the amorphous phase is 0 % and the proportion of agglomerated particles is 3 %.

Magnetic suspensions are stable when the particles are not agglomerated, dispersed all over the liquid volume and do not settle. For the stabilization of the magnetic fluids the surfactant polyvinylpyrrolidone K ($M \approx$ 30000 g/mol) was used. PVP K is freely soluble in water. When the nanoparticles are re-dispersed in liquid + PVP K the magnetite particles synthesized using the Massart method are more stable than the magnetite particles synthesized at 90 °C, which are more stable than the cobalt ferrite particles. Cobalt ferrite has an average particle size of 7.45 nm, but has 26 % of agglomerated particles. A high proportion of agglomerated particles implies a larger number of particles with greater mass that settle smaller particles below and thus destabilize the suspension. Magnetite has an average particle size of 8.17 nm, but only about 17 % of agglomerated particles. Because the number of particles with a higher mass is much smaller, the particles settle moderately, but eventually they all settle. Magnetite synthesized with the Massart method has a particle size of 6.37 nm and only 4.5 % of agglomerated particles. These suspensions are very stable due to the particles' small size and because the contact between the particles has been prevented by the addition of surfactant.

5 REFERENCES

[1] V. K. Varadan, K. Chen, X. J. Linfeng, Nanomedicine: Design and Applications of magnetic nanomaterials, nanosensors and nanosystems, Wiley, Chichester 2009, 38–39

[2] M. Remškar, Nanodelci in nanovarnost, Ministrstvo za zdravje, Urad RS za kemikalije, Ljubljana 2009, 14–17

[3] A. Goldman, Modern Ferrite Technology, Second edition, Springer, Boston 2006, 51–58, 172–174

[4] R. E. Rosensweig, Ferrohydrodynamics, Dover, New York 1997, 7, 32–38, 46, 55–63

[5] M. N. Rahaman, Ceramic processing and sintering, Second edition, Marcel Dekker, New York 2003, 190–191

[6] D. Makovec, Magnetne tekočine in njihova uporaba v tehniki, Življenje in tehnika, 58 (**2007**) 12, 60–64

[7] D. Makovec, Uporaba magnetnih nanodelcev v medicini, Življenje in tehnika, 60 (**2009**) 2, 39–42

[8] W. Clegg et al., Crystal stucture analysis: Principles and practice, Second edition, Oxford University Press, New York 2009, 251–253

[9] F. Zupanič, I. Anžel, Gradiva, Fakulteta za strojništvo, Maribor 2007, 53–59

[10] http://www.ki.si/fileadmin/user_upload/datoteke-L09/nzl/Kristalografija-NZL-POGL4.pdf 29. 6.2012

[11] M. Marinšek, Electron microscopy: Application of scanning electron microscope for observation and analysis of the solid samples surface, Literature on the subject of Materials, Faculty of chemistry and chemical technology, Ljubljana 1999

UDK 621.74.047:519.61/.64
Original scientific article/Izvirni znanstveni članek

ISSN 1580-2949
MTAEC9, 48(2)281(2014)

SIMULATION OF CONTINUOUS CASTING OF STEEL UNDER THE INFLUENCE OF MAGNETIC FIELD USING THE LOCAL-RADIAL BASIS-FUNCTION COLLOCATION METHOD

SIMULACIJA KONTINUIRNEGA ULIVANJA JEKLA POD VPLIVOM MAGNETNEGA POLJA NA PODLAGI METODE KOLOKACIJE Z RADIALNIMI BAZNIMI FUNKCIJAMI

Katarina Mramor[1], Robert Vertnik[2,3], Božidar Šarler[1,3,4]

[1]CO BIK, Tovarniška c. 26, 5270 Ajdovščina, Slovenia
[2]Štore Steel, Železarska c. 3, 3220 Štore, Slovenia
[3]University of Nova Gorica, Vipavska 13, 5000 Nova Gorica, Slovenia
[4]Institute of Metals and Technology, Lepi pot 11, 1000 Ljubljana, Slovenia
katarina.mramor@cobik.si

Prejem rokopisa – received: 2013-12-30; sprejem za objavo – accepted for publication: 2014-01-13

The initial results obtained with the local-radial basis-function collocation method (LRBFCM) for a two-dimensional (2D), simplified model of continuous casting of steel with an externally applied magnetic field are presented. The multiphysics model is composed of turbulent-solidification equations (mass, momentum, energy, turbulent kinetic energy, turbulent dissipation rate) and Maxwell's equations that are numerically solved for the non-uniform node arrangement. The numerical procedure is structured using the explicit time stepping and local collocation with multiquadric radial basis functions (MQ RBF) on the overlapping five-node subdomains. The pressure-velocity coupling follows the fractional-step method (FSM) and the convection is treated with adaptive upwinding.
The novel LRBFCM has been already verified in several benchmark test cases, such as the natural convection in a cavity with a magnetic field, the lid-driven cavity, and the flow over the backward-facing step with a transverse magnetic field.

Keywords: continuous casting of steel, turbulent flow, solidification, magnetohydrodynamics

Namen članka je predstavitev prvih rezultatov s poenostavljenim 2D-modelom za kontinuirano ulivanje jekel pri zunanjem magnetnem polju, izračunanih z metodo kolokacije z radialnimi baznimi funkcijami. Numerični model združuje Navier-Stokesove in Maxwellove enačbe, ki jih rešujemo na neenakomerni porazdelitvi točk. V numeričnem postopku je uporabljena eksplicitna časovna shema na pettočkovnih poddomenah, na katerih so uporabljene multikvadrične radialne bazne funkcije. Sklopitev tlaka in hitrosti se rešuje z metodo delnih korakov.
Omenjeno metodo smo poprej verificirali za izračun različnih preizkusov, kot so naravna konvekcija v kotanji z magnetnim poljem, kotanja z vsiljenim tokom ter tok preko stopnice v kanalu z magnetnim poljem. Dobljeni rezultati kažejo dobro ujemanje z drugimi numeričnimi postopki, kot je npr. metoda končnih volumnov.

Ključne besede: kontinuirano ulivanje jekla, turbulenten tok, strjevanje, magnetohidrodinamika

1 INTRODUCTION

The production of continuously cast steel[1] has greatly expanded in recent years. Continuous casting of billets, blooms and slabs is the most common process of steel production.[2] The continuously growing demand for cast steel has fueled the need to produce the steel of even better quality. Although the process of continuous casting of steel is cost efficient, exhibiting a high yield and good quality of the products, it can be further improved by introducing the electromagnetic (EM) field into it. The EM force, which is a result of an applied magnetic field, affects the velocity and temperature fields. By adjusting the magnetic field, the amount of defects in the material can be significantly reduced.

The magnitudes of the velocity, the temperature and magnetic fields are all crucial to the final quality of a product. As all these quantities are difficult or impossible to measure, numerical models help us to better understand and further improve the process. A number of different numerical models[3] have so far been used in the simulations of the problem. They include the finite-volume method (FVM),[4–8] the finite-element method (FEM)[9] and some more advanced meshless methods like the local-radial basis-function collocation method (LRBFCM).[10]

2 GOVERNING EQUATIONS

The system of governing equations that describes the turbulent heat transfer and the fluid flow as well as the magnetic field in the continuous casting of steel, is based on the Reynolds time-averaging approach to modeling a turbulent flow[11] and a mixture-continuum model, first introduced by Bennon and Incropera.[12] The system consists of five time-averaged mixture equations:

$$\nabla \cdot \mathbf{v} = 0 \tag{1}$$

$$\rho\frac{\partial \mathbf{v}}{\partial t}+\rho\nabla(\mathbf{vv})=-\nabla p+\nabla\left[(\mu_{\mathrm{L}}+\mu_{\mathrm{t}})[\nabla\mathbf{v}+(\nabla\mathbf{v})^{T}]\right]- \\ -\frac{2}{3}\rho\nabla k-\frac{\mu_{\mathrm{L}}(1-f_{\mathrm{L}})^{2}}{Cf_{\mathrm{L}}^{3}}(\mathbf{v}-\mathbf{v}_{\mathrm{s}})+\rho\beta_{\mathrm{T}}g(T-T_{ref})+\mathbf{F}_{\mathrm{m}} \quad (2)$$

$$\rho\frac{\partial h}{\partial t}+\rho\nabla(\mathbf{v}h)=\nabla(\lambda\nabla T)+\rho\nabla(\mathbf{v}h-f_{\mathrm{S}}\mathbf{v}_{\mathrm{S}}h_{\mathrm{S}}- \\ -f_{\mathrm{L}}\mathbf{v}_{\mathrm{L}}h_{\mathrm{L}})+\nabla\left(f_{\mathrm{L}}\frac{\rho_{\mathrm{L}}\nu_{\mathrm{t}}}{\sigma_{\mathrm{t}}}\nabla h_{\mathrm{L}}\right) \quad (3)$$

$$\rho\frac{\partial k}{\partial t}+\rho\nabla(\mathbf{v}k)=\nabla\left[\left(\mu_{\mathrm{L}}+\frac{\mu_{\mathrm{t}}}{\sigma_{\mathrm{k}}}\right)\nabla k\right]+P_{\mathrm{k}}+G_{\mathrm{k}}- \\ -\rho\varepsilon+\rho D-\mu_{\mathrm{L}}\frac{(1-f_{\mathrm{L}})^{2}}{Cf_{\mathrm{L}}^{3}}k \quad (4)$$

$$\rho\frac{\partial \varepsilon}{\partial t}+\rho\nabla(\mathbf{v}\varepsilon)=\nabla\left[\left(\mu_{\mathrm{L}}+\frac{\mu_{\mathrm{t}}}{\sigma_{\varepsilon}}\right)\nabla\varepsilon\right]+\rho E- \\ -\mu_{\mathrm{L}}\frac{(1-f_{\mathrm{L}})^{2}}{Cf_{\mathrm{L}}^{3}}\varepsilon+\left[c_{1\varepsilon}f_{1}(P_{k}+c_{3\varepsilon}G_{k})-c_{2\varepsilon}f_{2}\rho\varepsilon\right]\frac{\varepsilon}{k} \quad (5)$$

where $\mathbf{v}$ is the velocity of the mixture, $\rho = \rho_{\mathrm{S}} = \rho_{\mathrm{L}}$ is the density of the mixture, assumed to be constant; t stands for the time and p for the pressure; μ_{t} is the turbulent viscosity and μ_{L} is the dynamic viscosity; k represents the turbulent kinetic energy and K is the permeability of the porous matrix. β_{T}, g, T, and T_{ref} represent the thermal-expansion coefficient, the gravitational acceleration, the temperature and the reference temperature, respectively. $\mathbf{F}_{\mathrm{m}}$ stands for the Lorentz force, h for the enthalpy and λ for the thermal conductivity. f_{S}, f_{L}, $\mathbf{v}_{\mathrm{S}}$, $\mathbf{v}_{\mathrm{L}}$, h_{S}, and h_{L} represent the solid-volume fraction, the liquid-volume fraction, the velocity of the solid phase, the velocity of the liquid phase, the enthalpy of the solid phase and the enthalpy of the liquid phase, while ν_{t} is the turbulent kinematic viscosity. Symbols ε and C stand for the dissipation rate and the morphology constant of the porous media. Symbols σ_{t}, σ_{k}, σ_{ε}, $c_{1\varepsilon}$, f_1, $c_{2\varepsilon}$ and f_2 are the closure coefficients of the turbulence model. P_{k}, G_{k}, D and E are the shear production of the turbulent kinetic energy, the generation of turbulence due to the buoyancy force, the source term in the k equation and the source term in the ε equation, respectively. The closure relations defined by Abe, Kondoh and Nagano[13] are used in the present work. A detailed description of the closure coefficients, source terms and damping functions are given in the paper by Šarler et al[14]. The Lorentz force is defined as:

$$\mathbf{F}_{\mathrm{m}} = \mathbf{j} \times \mathbf{B} \quad (6)$$

where $\mathbf{j}$ and $\mathbf{B}$ are the current density and the magnetic-flux density. Maxwell's equations are used to calculate the current density:

$$\mathbf{j} = \sigma(-\nabla\phi + \mathbf{v} \times \mathbf{B}) \quad (7)$$

where σ is the fluid electric conductivity, ϕ is the fluid electric potential and B is the externally applied magnetic field. The induced magnetic field is assumed negligible in comparison with the applied magnetic field.

2.1 Initial and boundary conditions

The governing equations are strongly coupled. For the steady solution of a problem it is, therefore, very important how the initial conditions are chosen in order to minimize the required iterations to reach the steady state. Five different boundaries are chosen: the inlet, free surface, wall, outlet and symmetry of the present model. A detailed description of the initial and boundary conditions are given in the article by Šarler at al[14]. The model of the domain is presented in **Figure 1** and the computational domain is depicted in **Figure 2**.

3 SOLUTION PROCEDURE

The solution of the governing equations is obtained with the LRBFCM employing the explicit time stepping. The fractional-step method (FSM)[15] is used to solve the pressure-velocity coupling and an upwinding scheme is used to stabilize the highly convective situation.[16]

The solution procedure begins by calculating the initial Lorentz force (equation (6)). Afterwards, the intermediate velocity is calculated, without a pressure gradient. The pressure is then calculated from the Poisson equation[14] by assembling and solving a sparse matrix.[17] The calculated pressure gradient is afterwards used to correct the intermediate velocities. After the solution of the velocity field, the equations for the turbulent kinetic energy and dissipation rate are solved. This is followed

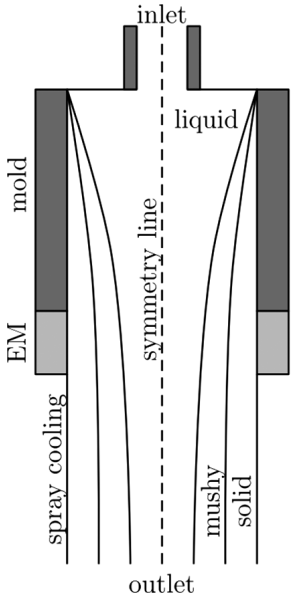

Figure 1: Simplified 2D model of continuous casting of steel
Slika 1: Poenostavljeni 2D-model kontinuirnega ulivanja jekla

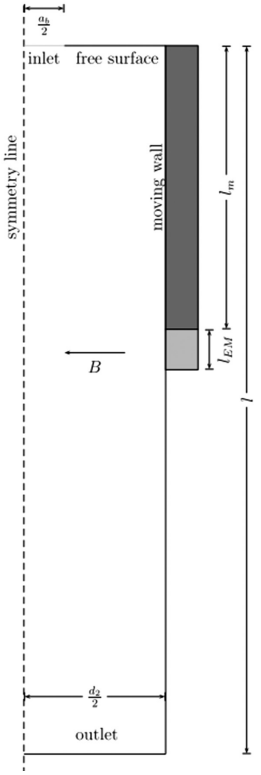

Figure 2: Scheme of the computational domain
Slika 2: Shema računske domene

by the solution of the enthalpy equation. The temperature is calculated from the enthalpy, using the temperature-enthalpy constitutive relation.[17,18] Finally, the turbulent viscosity, velocity, temperature, turbulent kinetic energy and dissipation rate are updated and the solution is ready for the next time step.

The LRBFCM is structured in the following way: Approximation function θ is represented on each of the subdomains as a linear combination of the radial basis functions (RBFs) as:

$$q({}_l\mathbf{p}_n) = \sum_{i=1}^{M} {}_l\psi_i({}_l\mathbf{p}_n)\,{}_l\gamma_i \tag{8}$$

where ${}_l\psi_i$, ${}_l\gamma_i$, and M represent the RBF shape functions, centred in points ${}_l\mathbf{p}_n$, the expansion coefficients, and the number of shape functions, respectively. The most commonly used RBF is the multiquadric RBF:[19,20]

$${}_l\psi_i(\mathbf{p}) = \sqrt{{}_l r_i^2(\mathbf{p}) + c^2} \tag{9}$$

where c stands for the dimensionless shape parameter, set to 32 in all the calculations, and the distance between the nodes:

$${}_l r_i^2(\mathbf{p}) = \sqrt{\left(\frac{x - x_i}{{}_l x_{i\max}}\right)^2 + \left(\frac{y - y_i}{{}_l y_{i\max}}\right)^2} \tag{10}$$

is scaled with ${}_lx_{i\max}$ and ${}_ly_{i\max}$, the scaling parameters of subdomain l in the x and y directions, respectively (**Figure 3**).

A subdomain is formed around each of the calculation points consisting of the ${}_lM - 1$ nodes nearest to node ${}_l\mathbf{p}_n$. For the purpose of this work, five-node overlapping subdomains are used. By considering the collocation condition of:

$${}_l\theta({}_l\mathbf{p}_n) = \theta_{i(l,n)} \tag{11}$$

a linear system of equations is obtained. To solve the partial differential equations (PDEs), the first and second derivatives of function ${}_l\theta(\mathbf{p})$ have to be calculated:

$$\frac{\partial^j}{\partial\chi^j}\,{}_l\theta(\mathbf{p}) = \sum_{i=1}^{M} \frac{\partial^j}{\partial\chi^j}\,{}_l\psi_i(\mathbf{p})\,{}_l\gamma_i \tag{12}$$

where index j = 1,2 is used to denote the order of the derivative and $\chi = x,y$. A detailed explanation of the solution procedure is given in the paper by Vertnik et al.[17,18] The schematics of the discretization scheme is shown in **Figure 3**.

4 NUMERICAL IMPLEMENTATION

The sparse-pressure matrices, used for the solution of the pressure and the flux-density Poisson equations, are solved by applying the Pardiso routine and Intel Math Kernel Library 11. The OpenMP Library is used for the parallelization. The post processing is performed in PGPlot, Gnuplot 4.4 and Octave 3.6.1. The results were calculated on an HP Proliant DL380 G/7 server running on 64 bit MS Windows.

5 NUMERICAL EXAMPLES

The numerical procedure has so far been verified on the following benchmark test cases: the lid-driven cavity,[21] the natural convection in a cavity,[22] and the backward-facing step.[23] The lid-driven test case was used

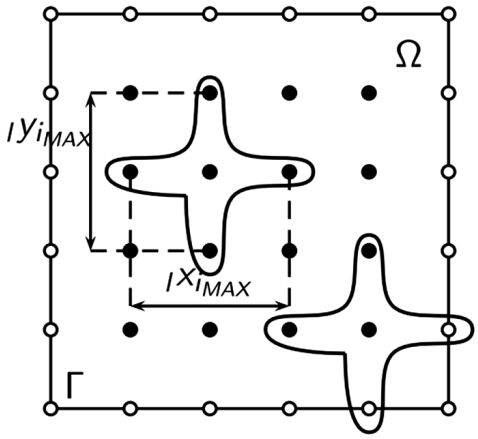

Figure 3: Discretization scheme. Γ, Ω, ${}_lx_{i\mathrm{MAX}}$ and ${}_ly_{i\mathrm{MAX}}$ represent the boundary, domain and scaling parameters in the x and y directions, respectively. The circles represent the boundary nodes, whereas the black dots represent the domain nodes.
Slika 3: Diskretizacijska shema. Γ, Ω, ${}_lx_{i\mathrm{MAX}}$ in ${}_ly_{i\mathrm{MAX}}$ označujejo rob, območje ter skalirna parametra v smeri x in y. Robne točke so označene s krogci, območne točke pa s pikami.

to verify the coupling between the mass and momentum equations.[21] In the natural-convection case, the energy-conservation equation was added.[22] For the backward-facing step problem, the boundary conditions for the inflow and outflow problems were tested. The natural-convection and backward-facing-step problems were first tested without a magnetic field and then with an external magnetic field. The results of all of the test cases are in good agreement with the reference results, calculated with a commercial code or obtained from several published sources. Since the results of our calculations, mentioned in the above history of test cases, are in good agreement with the reference results, the method is subsequently applied to the simplified problem of continuous casting of steel with a magnetic field, as defined in the paper by Šarler et al.[14]

5.1 Continuous-casting geometry and material properties

The simplified 2D continuous-casting model geometry is shown in **Figure 1** and the elements of the discretization are presented in **Figure 2**. The computational domain coincides with a half of the longitudinal section of the billet, taken to be 1.8 m long and 14 cm wide. The SEN diameter is 3.5 cm, the mold height is 0.8 m and the EM-coil height is 10 cm. The material properties of steel are temperature and steel grade dependent. However, for the purpose of the present simplified model, constant values are used. The values are given in **Table 1**.

Table 1: Simplified material properties of steel
Tabela 1: Poenostavljene snovne lastnosti jekla

Property	Value
ρ	7200 kg/m^3
λ	30 W/(m K)
c_p	700 J/(kg K)
T_S	1680 K
T_L	1760 K
h_m	250000 J/kg
μ	0.006 Pa s
β_T	$1 \cdot 10^{-4}$ K^{-1}
C	$1.6 \cdot 10^8$ m^{-2}

The results of the numerical simulation are represented in the following sections of the paper.

5.2 Convergence of the method and a comparison with the reference results for the continuous-casting process

First the convergence of the method was tested for the node arrangements with 20 220, 50 951, 73 940, 100 089, 131 452, 165 426 non-uniformly arranged nodes. The convergence was tested for the velocity and the temperature fields. The vertical and horizontal components of the velocity were compared for three different vertical cross-sections: just before the application of the magnetic field, just after the application of the magnetic field and at the end of the computational domain, as can be seen in **Figure 4** (left). The temperature was verified at two different vertical directions, the one at the center of the domain and the one at the outside wall, as shown in **Figure 4** (right).

As can be seen in **Figures 5** to **12**, the smallest appropriate node arrangement is 100 089. The results were also compared with the results obtained with the commercial code based on the FVM (Fluent[23]). The smallest appropriate amount of the finite volumes in the commercial code for reaching a reasonable convergence was 169 169. The agreement of the velocity profiles with the commercial code (the solid line denoted with F) is similarly good for the horizontal as well as vertical velocities. The largest differences occur at the positions closer to the inlet. At the positions closer to the end of the computational domain, where a fully developed flow and a partial solidification take place, the agreement between the results obtained with the LRBFCM and FVM is excellent. In the early stages of the flow, slightly larger differences can be observed. The differences between the commercial-code results and the results obtained with the in-house built LRBFCM are reasonably small. The exact cause for the differences is

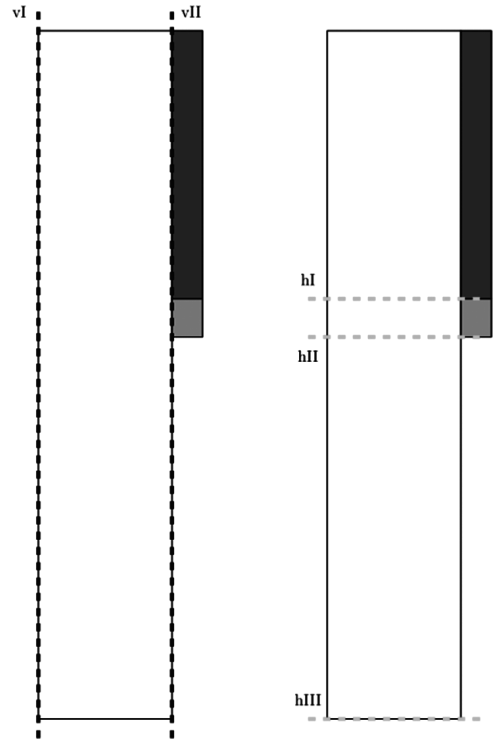

Figure 4: Left: the positions of the velocity-field comparison lines; hI = –0.8 m, hII = –0.9 m, hIII = –1.8 m. Right: the positions of the temperature-field comparison lines; vI = 0.0 m (centreline), vII = 0.07 m (surface).
Slika 4: Levo: Položaj linij, kjer je primerjano hitrostno polje; hI = –0,8 m, hII = –0,9 m, hIII = –1,8 m. Desno: Položaj linij, kjer je primerjano temperaturno polje; vI = 0,0 m (sredina), vII = 0,07 m (površina).

not known; however, several reasons why the results are not identical might be identified: the solution procedure, e.g., the energy equation in the commercial code is solved iteratively and the temperature is obtained directly from the equation, whereas in our method, the enthalpy equation is solved first and the temperature is obtained by solving the enthalpy-temperature relationship. Another reason might lie in the differences between the methods, e.g., in the commercial code a second-order upwind technique is used, whereas in our case an adap-

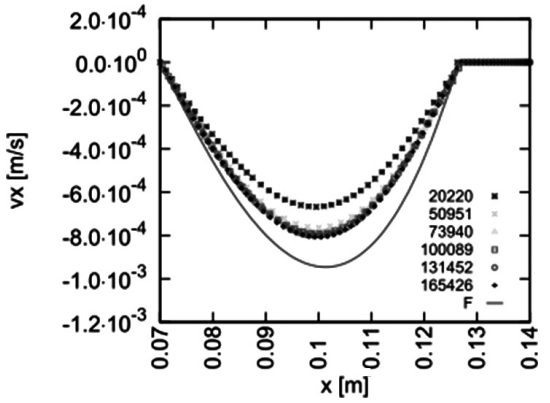

Figure 5: Horizontal-velocity profiles at vertical position hI = –0.8 m, at the top boundary of the magnetic field

Slika 5: Profili horizontalne hitrosti na mestu hI = –0,8 m na zgornji meji magnetnega polja

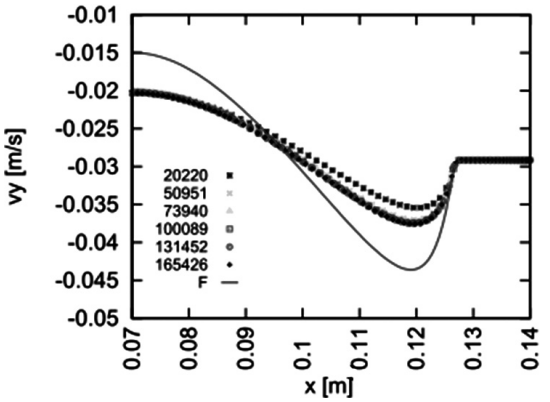

Figure 6: Horizontal-velocity profiles at vertical position hI = –0.8 m, at the top boundary of the magnetic field

Slika 6: Profili horizontalne hitrosti na mestu hI = –0,8 m na zgornji meji magnetnega polja

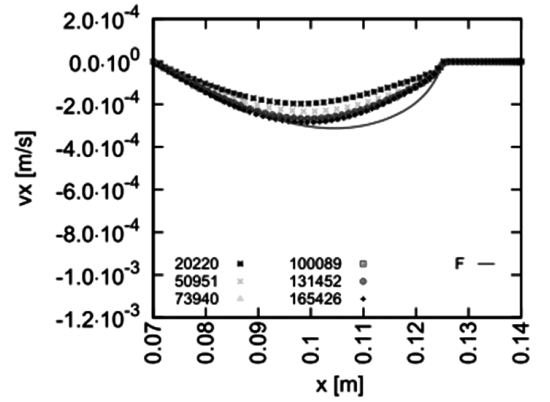

Figure 7: Horizontal-velocity profiles at vertical position hII = –0.9 m, at the bottom boundary of the magnetic field

Slika 7: Profil horizontalne hitrosti na mestu hII = –0,9 m na spodnji meji magnetnega polja

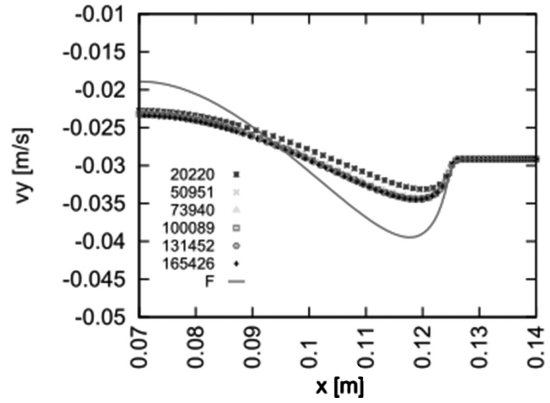

Figure 8: Horizontal-velocity profiles at vertical position hII = –0.9 m, at the bottom boundary of the magnetic field

Slika 8: Profili horizontalne hitrosti na mestu hII = –0,9 m na spodnji meji magnetnega polja

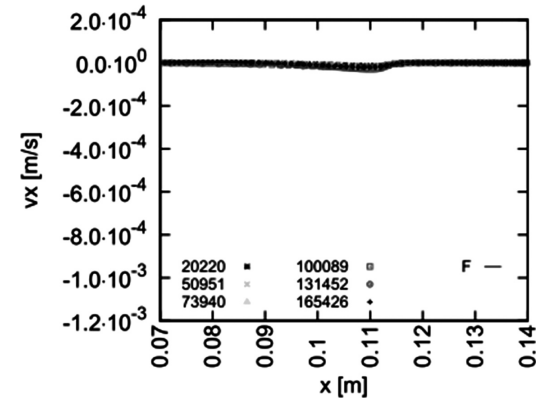

Figure 9: Horizontal-velocity profiles at vertical position hIII = –1.8 m, at the end of the computational domain

Slika 9: Profili horizontalne hitrosti na mestu hIII = –1,8 m na koncu računske domene

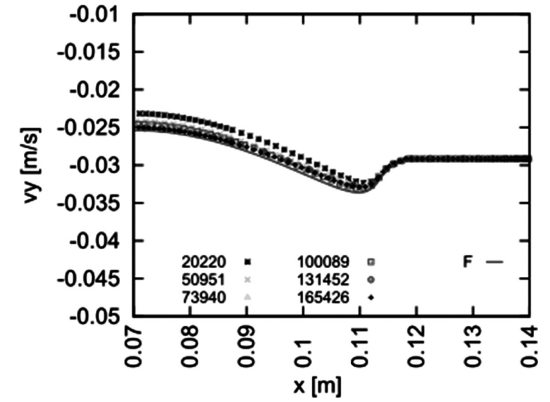

Figure 10: Horizontal-velocity profiles at vertical position hIII = –1.8 m, at the end of the computational domain

Slika 10: Profili horizontalne hitrosti na mestu hIII = –1,8 m na koncu računske domene

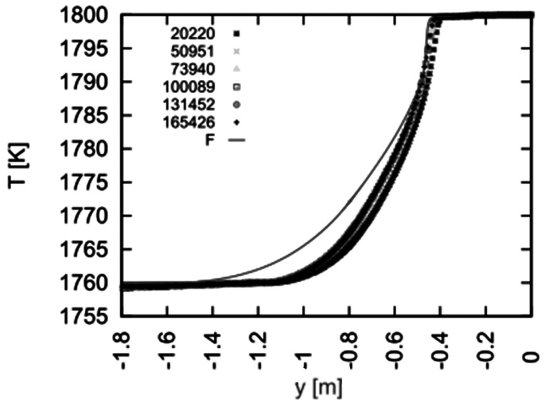

Figure 11: Temperature layout at position vI = 0.0 m, at the centre of the mold

Slika 11: Potek temperature na mestu vI = 0,0 m v središču kokile

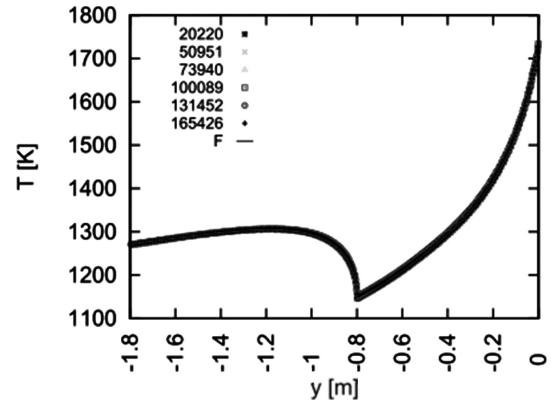

Figure 12: Temperature layout at position vII = 0.07 m, at the mold wall

Slika 12: Potek temperaturnega polja na mestu vII = 0,07 m na steni kokile

tive upwind technique is used. Despite the differences in the formulation, identical results are obtained in very simple test cases; however, slight differences appear when the examples become very complicated, like in the case of continuous casting of steel, where the turbulent-flow, heat-transfer and magnetic-field equations are strongly coupled.

The agreement between the temperature fields calculated with the commercial code and those calculated with the LRBFCM is better for the outer wall, where the shell has already solidified, than for the centre of the billet, where the liquid metal has not yet solidified.

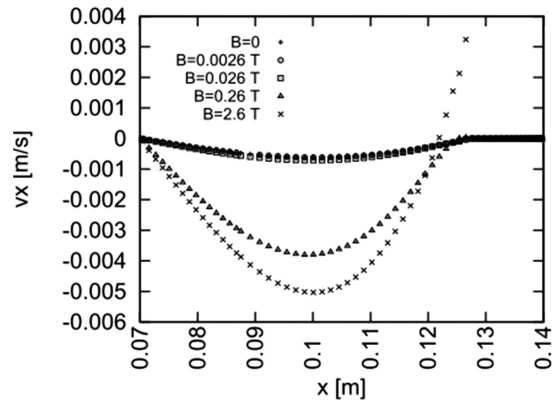

Figure 13: Velocity layout at position vI = –0.8 m, at the top edge of the applied magnetic field

Slika 13: Potek hitrostnega polja na mestu vI = –0,8 m na zgornjem robu apliciranega magnetnega polja

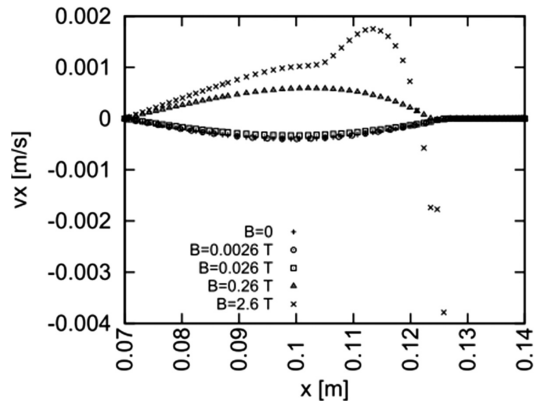

Figure 14: Velocity layout at position vI = –0.8 m

Slika 14: Potek hitrostnega polja na mestu vI = –0,8 m

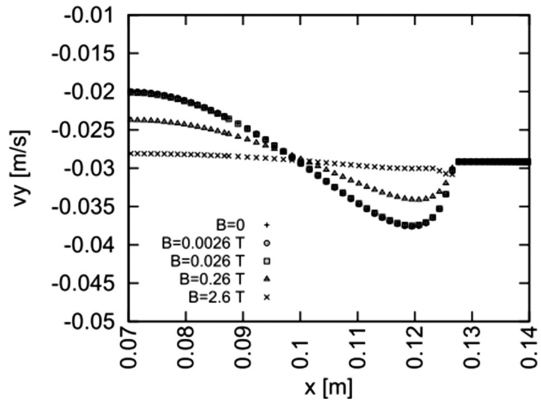

Figure 15: Temperature layout at position hII = –0.9 m, at the centre of the mold

Slika 15: Potek temperature na mestu hII = –0,9 m, v središču kokile

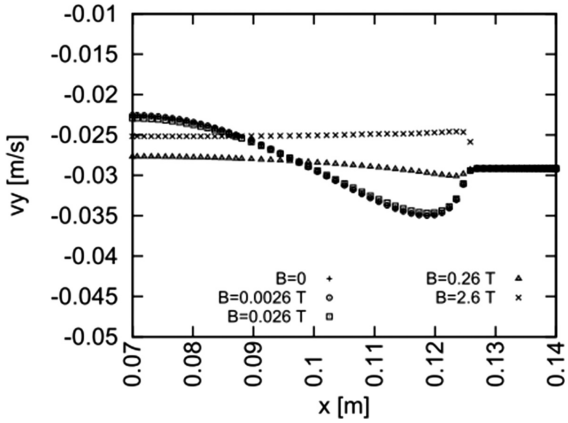

Figure 16: Velocity layout at position hIII = –1.8 m, at the centre of the mold

Slika 16: Potek hitrosti na mestu hIII = –1,8 m na spodnjem robu apliciranega magnetnega polja

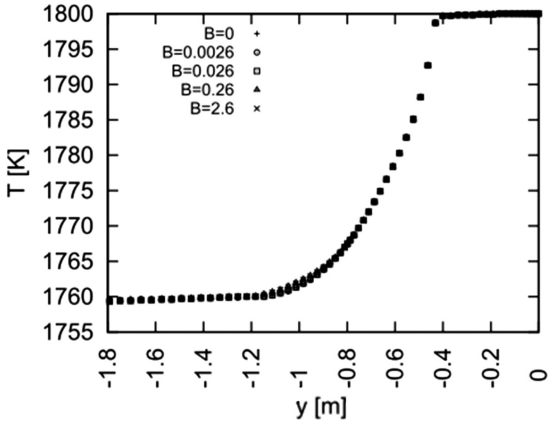

Figure 17: Temperature layout at position vI = 0.0 m, at the centre of the mold

Slika 17: Potek temperaturnega polja na mestu vI = 0,0 m v središču kokile

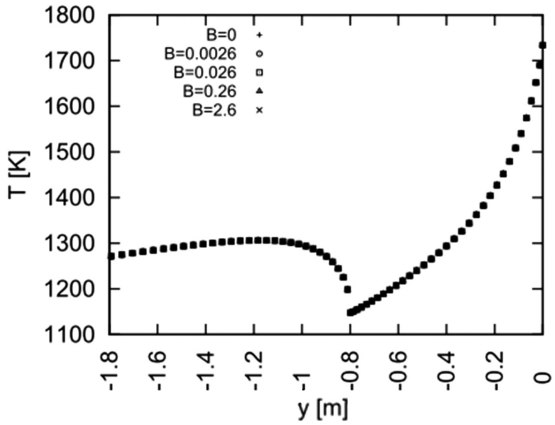

Figure 18: Temperature layout at position vII = 0.07 m, at the mold wall

Slika 18: Potek temperaturnega polja na mestu vII = 0,07 m na steni kokile

Finally, the velocity and temperature profiles were compared for different magnetic-field strengths at different vertical (velocity) and horizontal (temperature) positions. As can be seen in **Figures 13** to **16**, velocity profiles do not change much, when a weak magnetic field (0.0026 T or 0.026 T) is applied, being only slightly different from the velocity profiles obtained with no magnetic field. An application of a weak magnetic field in the *x* direction causes the velocity in the *x* direction to increase (**Figures 13** and **14**) and the velocity in the *y* direction to decrease (**Figures 15** and **16**). However, an application of a strong magnetic field (0.26 T or 2.6 T) alters the velocity profiles and can even change the direction of the flow.

The effect of the externally applied magnetic field on the temperature field is less pronounced. As can be seen in **Figures 17** and **18**, the temperature is slightly raised in the area of the application of the magnetic field.

6 CONCLUSIONS

In this paper, the initial numerical calculations of continuously cast steel under the influence of a magnetic field are presented and compared to the commercial FVM-based computational fluid-dynamics (CFD) code Fluent.[23] The LRBFCM method gives similar results as the commercial code; it is fully flexible, requiring no mesh generation, and enabling a straightforward inclusion of different turbulence models and constitutive equations. In the future, a more realistic magnetic field will be incorporated into the model and a realistic curved geometry of the caster will be assumed. Several sensitivity studies, in terms of the magnitude of an externally applied magnetic field and the position of the coils producing the magnetic field, will be performed. Finally, the species-conservation equation will be added in order to account for the macro-segregation.

Acknowledgements

The research in this paper was sponsored by the Centre of Excellence for Biosensors, Instrumentation and Process Control (COBIK) and the Slovenian Grant Agency under programme group P2-0357 and project L2-3651. This paper forms a part of a doctoral study of the first author that is partly co-financed by the European Union and the European Social Fund. The co-financing is carried out within the Human resources development operational programme for years 2007–2013, 1. Developmental priorities: Encouraging entrepreneurship and adaptation; Preferential directives, 1.3: Scholarship schemes.

7 REFERENCES

[1] W. R. Irwing, Continuous Casting of Steel, The Institute of Materials, London 1993

[2] Steel Statistical Yearbook 2013, World Steel Association, Brussels 2013

[3] B. Šarler, R. Vertnik, A. Z. Lorbiecka, I. Vušanović, B. Senčič, Anwendung eines Stranggieß-Simulationsmodells bei Štore Steel–II, BHM Berg- und Hüttenmännische Monatshefte, (**2013**), 1–9, doi: 10.1007/s00501-013-0147-7

[4] B. Zhao, B. G. Thomas, S. P. Vanka, R. J. O'Malley, Metall. Mater. Trans. B, 36 (**2005**) 6, 801–823

[5] M. R. Aboutalebi, M. Hasan, R. I. L. Guthrie, Metall. Mater. Trans. B, 26 (**1995**) 4, 731–744

[6] D. S. Kim, W. S. Kim, K. H. Cho, ISIJ Int., 40 (**2000**) 7, 670–676

[7] K. G. Kang, H. S. Ryou, N. K. Hur, Numer. Heat Trans. A, 48 (**2005**) 5, 461–481

[8] N. Kubo, T. Ishii, J. Kubota, T. Ikagawa, ISIJ Int., 44 (**2004**) 3, 556–564

[9] C. H. Moon, S. M. Hwang, Int. J. Numer. Meth. Eng., 57 (**2003**) 3, 315–339

[10] B. Šarler, R. Vertnik, Comput. Math. App., 51 (**2006**) 8, 1269–1282

[11] D. C. Wilcox, Turbulence Modeling for CFD, DCW Industries, Inc., California 1993

[12] W. D. Bennon, F. P. Incropera, Numer. Heat Transf. A-Appl., 13 (**1988**) 3, 277–96

[13] K. Abe, T. Kondoh, Y. Nagano, Int. J. Heat Mass Transf., 37 (**1994**) 1, 139–51
[14] B. Šarler, R. Vertnik, K. Mramor, IOP Conference Series: Mater. Sci. Eng., 33 (**2012**) 1, 12012–12021
[15] A. Chorin, Math. Comput., 22 (**1968**) 104, 745–762
[16] H. Lin, S. N. Atluri, CMES (Comput. Model. Eng. Sci.), 1 (**2000**) 2, 45–60
[17] R. Vertnik, B. Šarler, Int. J. Cast Metal. Res., 22 (**2009**) 1–4, 311–313
[18] R. Vertnik, B. Šarler, EABE [online] 2014 [cited 2014-01-02]. Available from World Wide Web: http://dx.doi.org/10.1016/j.enganabound.2014.01.017
[19] M. D. Buchmann, Radial Basis Function: Theory and Implementations, Cambridge University Press, Cambridge 2003
[20] R. Franke, Math. Comput., 38 (**1982**) 157, 181–200
[21] K. Mramor, R. Vertnik, B. Šarler, CMES (Comput. Model. Eng. Sci.), 92 (**2013**) 4, 327–352
[22] K. Mramor, R. Vertnik, B. Šarler, CMC (Comput. Mater. & Continua), 36 (**2013**) 1, 1–21
[23] ANSYS® Fluent, 6.1, ANSYS, Inc.

UDK 669.721.5:621.793
Professional article/Strokovni članek

ISSN 1580-2949
MTAEC9, 48(2)289(2014)

THE APPLICABILITY OF SOL-GEL OXIDE FILMS AND THEIR CHARACTERISATION ON A MAGNESIUM ALLOY

UPORABNOST SOL-GEL OKSIDNIH TANKIH PLASTI IN NJIHOVA KARAKTERIZACIJA NA MAGNEZIJEVI ZLITINI

Ekrem Altuncu[1,2], Hasan Alanyali[2]

[1]Sakarya University, Dept. Metallurgical and Materials Eng., Esentepe Campus, 54187 Sakarya, Turkey
[2]Kocaeli University, Machine-Metal Technology, Hereke Borusan Campus, Vocational School of Asim Kocabiyik, 41800 Kocaeli, Turkey
altuncu@sakarya.edu.tr

Prejem rokopisa – received: 2012-08-09; sprejem za objavo – accepted for publication: 2013-06-07

Magnesium and its alloys are widely used in many industrial applications because of their high specific strength (strength/density) ratio. However, these applications are still restricted by the relatively poor surface resistance of these materials. To overcome the inherent drawbacks a useful solution is to deposit a protective coating on the magnesium alloys. The sol-gel process is an effective method for fabricating oxide films on a magnesium alloy in order to produce a higher corrosion resistance. The objective of this study is to comparatively investigate the process and properties of repeated sol–gel oxide (ZrO_2, Al_2O_3) coatings. The coatings were characterized by SEM, XRD, ellipsometry and the effects of the process on their properties were comparatively analysed.

Keywords: sol-gel, oxide films, magnesium alloy

Magnezij in njegove zlitine se uporabljajo v vrsti industrij zaradi visoke specifične trdnosti (razmerje trdnost – gostota). Vendar pa je industrijska uporaba omejena zaradi njihove slabe odpornosti površine. Da bi to pomanjkljivost odpravili, je uporabna rešitev varovalni nanos na površini magnezijevih zlitin. Sol-gel postopek je učinkovita metoda za izdelavo oksidnih tankih plasti na magnezijevi zlitini za povečanje njihove korozijske obstojnosti. Namen te študije je primerjava postopka in ugotavljanje lastnosti ponavljajočih se sol-gel nanosov ZrO_2 in Al_2O_3. Nanosi so bili ovrednoteni s SEM, XRD in elipsometrijo, izvršena pa je bila tudi primerjava vpliva procesa na njihove lastnosti.

Ključne besede: sol-gel, oksidni nanosi, magnezijeva zlitina

1 INTRODUCTION

Magnesium and its alloys have a high specific strength, excellent mechanical properties, a good damping capacity and a high electromagnetic shielding capability. They can be used for a variety electronic and many automotive parts.[1,2] However, corrosion protection is one of the main obstacles to the application of magnesium alloys in real environments. Conversion coating, anodizing, plating, laser surface alloying and plasma electrolyte oxidation have been applied on magnesium alloys. Material designers attempted to improve the corrosion resistance of the surface.[3–5] However, with these technologies the protection of magnesium alloys it is hard to achieve a good cost-to-benefit ratio or there is a higher energy consumption or environmentally adverse effects. The sol–gel thin-film deposition method is described as a practical, environmentally friendly and cost-effective way to produce magnesium alloy surfaces. It is well known that Al_2O_3 thin films have been extensively used as an isolator, oxidation barrier, for anti-corrosion and for anti-wear.[6–8] However, sol–gel ZrO_2 thin films, owing to their chemical stability, have important applications as corrosion-resistant coatings on metal surfaces.[9] Thin (0.2–10 μm), dense, sol–gel oxide coatings exhibited significant advantages in overcoming metallic surface-corrosion problems. From the point of view of synthesis, the sol–gel route offers versatile ways to synthesize effective coatings with specific properties. Surface functionality can be optimized by varying experimental parameters such as the chemical structure, the composition and the ratio of precursors and complexing agents, the rate and conditions of hydrolysis, the synthesis media, the aging and curing conditions, and the deposition procedure.[10–14] The objective of this study is to comparatively investigate the process and properties of repeated sol-gel ZrO_2 and Al_2O_3 coatings. The coatings were characterized and the effects of the process on their properties were analysed.[15–17]

2 EXPERIMENTAL

AM60 magnesium alloy plates were used as the substrates. The specimens were cut into pieces of 20 mm × 20 mm × 2 mm and their surfaces were ground and degreased ultrasonically in acetone and then dried with hot air. The deposition steps were as follows: sol preparation, gelation and heat treatment (**Figure 1**). Initially, deionized water was heated in a glass beaker until it reached 80 °C. Aluminium sec-butoxide (ASB) was added to the water with continuous mixing. The molar

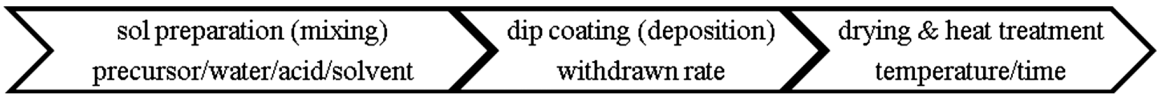

Figure 1: Flow chart for the preparation of coatings
Slika 1: Postopek priprave nanosa

ratio of ASB to water was 1 : 25. As hydrolysis took place, the temperature of the solution rose to 90 °C, at which it was maintained for 3 min. Then, acetoacetate (AcAc) was added to the mixture. The molar ratio of AcAc to water was fixed at 1 : 25. After stirring for 2 min, nitric acid was added to the solution stepwise, with stirring until it was transformed into a transparent solution. The pH value of the as-synthesized sol was about 3. The Al_2O_3 sol–gel film was deposited onto the magnesium substrate via the dip-coating method and withdrawing at a constant rate of 2 cm/min. The coated substrate was dried in a clean cabinet at 130 °C for 10 min to produce the alumina gel film. Then, the supported gel films were subjected to a thermal treatment at 500 °C for 1 h in an oxygen atmosphere. Zirconium n-propoxide (ZrNP) was diluted in n-propanol as the source of zirconia, and then acetylacetone AcAc and deionized water (diluted with n-PrOH) were added. The molar ratio of $Zr(n\text{-}OPr)_4$: AcAc : H_2O : n-PrOH was 1 : 2 : 2 : 60. After stirring for 3 h at room temperature, a clear precursor solution was obtained.[16] The ZrO_2 coatings were deposited by dipping the substrate into the sol and withdrawing it at a constant rate of 5 cm/min. Thin layers were prepared by repeating the dip coating and after every deposition there was a heat treatment of the sample at 500 °C for 1 h in an air atmosphere. The thicker films were produced by repeating the dipping process four times, followed by a thermal treatment.

The deposited films were studied by using scanning electron microscopy (SEM), while the film thicknesses and the refractive indices were measured using the ellipsometry method (Jobin Yvon, UVISEL HR 460). The structures of the resulting films were examined by grazing-incidence X-ray diffraction (XRD) with Cu K_α radiation using a thin-film apparatus. The electrochemical measurements were performed on a EG&G 273A-type potentiostat, using Pt as an auxiliary electrode, a saturated calomel electrode (SCE) as a reference electrode and 3.5 % NaCl solution as an aggressive medium. The potential was scanned from –1.8 V to 0.7 V (vs. SCE) at a scanning rate of 0.5 mV/s.

3 RESULTS AND DISCUSSION

3.1 Morphology and Thickness

Different viscosities of sols were created by the addition of the required amounts of nitric acid to the synthesis mixture of aluminium sec-butoxide and AcAC in n-propanal, which allowed us to control the rate of the condensation reactions. Uniform, mesoporous alumina coatings were obtained for the solvent-withdrawal rates below 10 cm/min. The limiting withdrawal rate increases as the solvent evaporation rate increases and it decreases as the sol viscosity increases. The cross-sectional morphologies indicate a mean thickness of approximately 1.6 μm and 2.3 μm for the repeated sol-gel coating for

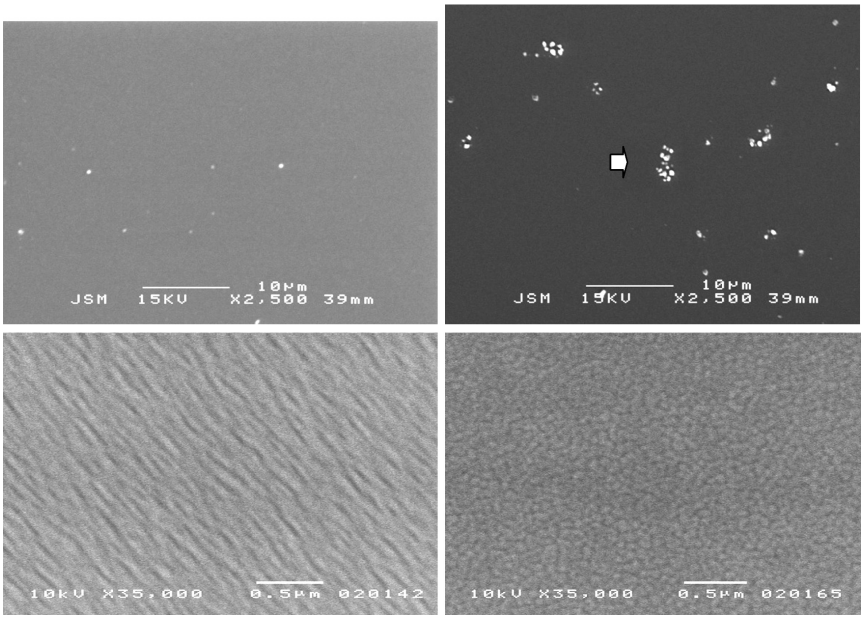

Figure 2: Surface morphology of sol-gel coatings using the dip-coating method (SEM micrographs)
Slika 2: Morfologija površine sol-gel nanosa s potapljanjem (SEM)

ZrO_2 and Al_2O_3, respectively (**Table 1**). The deposition efficiency is higher in the Al_2O_3 than in the ZrO_2 sol-gel coating. The porosity level of the alumina coating is lower than the zirconia coating.

Table 1: Thicknesses of the coatings
Tabela 1: Debeline nanosov

Composition	Average bilayer thicknesses (nm) for 9 measurement		
	Min	Average	Max
ZrO_2	63.42	65.2 ± 5	68.72
Al_2O_3	82.33	87.2 ± 4	90.14

It is clear from **Figure 2** that both films were smooth, compact and crack-free, and the thicknesses were between 60 nm and 95 nm. In addition, a lot of bumps and small pores were observed in this film.

3.2 Crystal Structure

Figure 3 illustrates the structure of the coatings formed on the AM60 alloy substrate. Both of the coatings have an amorphous structure. A small quantity of crystallite structures were observed, depending on the heat-treatment temperature and the time. However, the crystallisation growth was inadequate for both coatings. At higher temperatures than 600 °C for 1 h the crystallites started to produce strong peaks in the XRD pattern for the Al_2O_3 film. The characteristic peaks of γ-Al_2O_3 and δ-Al_2O_3 that were observed imply the existence of crystallized γ-Al_2O_3 and δ-Al_2O_3, which were transferred from the alumina sol annealed at 500 °C in the amorphous coating. The repeated sol-gel coating, which indicates a more crystallized α-Al_2O_3 phase, is due to the direct introduction of Al_2O_3 particles. These results are similar to those in Wang's study.[18] The zirconia coatings are made up of m-ZrO_2 (monoclinic crystal structure) and t-ZrO_2 (tetragonal crystal structure) after a heat treatment at 600 °C for 4 h (**Figure 3**). Partial spinodal decomposition was observed in the ZrO_2 coating.

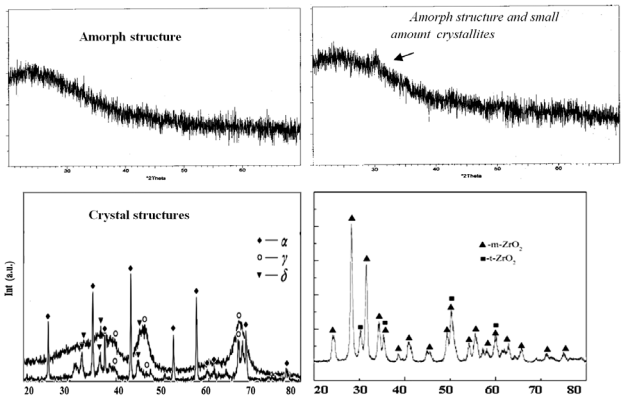

Figure 3: XRD patterns of the sol–gel coatings
Slika 3: XRD-posnetki sol-gel nanosov

3.3 Optical Properties

Figure 4 shows the reflective spectra of a glass substrate, alumina bi-layer coatings with 1.5 and 1.625 refractive indices in the region 300–800 nm. The refractive index is changing between 1.9 and 2.2 for the zirconia coating. The magnitude of the refractive index decreases with the heat-treatment temperature and the refractive indices of the Al_2O_3 and ZrO_2 thin films decrease with the increasing coating thickness. With an increase in the crystallinity there is a decrease in the refractive index of the thin films. The refractive index of the films depends strongly on their morphology. Up to the heat-treatment temperature, limiting the amorphous and crystallized phase, it increases steadily, probably in relation to an increasing densification of the layer. The lowering of the refractive index for the crystallized films is probably related to a lower densification of the films. The decrease of light intensity is strongly lowered for amorphous layers.

3.4 Corrosion Properties

In both cases, the polarization curves of the sol-gel-coated substrates were appreciably different from that of the bare substrates. The corrosion test showed a smooth surface with no appreciable delamination or cracking of the coating on the magnesium alloy substrates. The open-circuit potential, E_{oc}, of the sol-gel-coated substrates was significantly lower than that of the bare surfaces

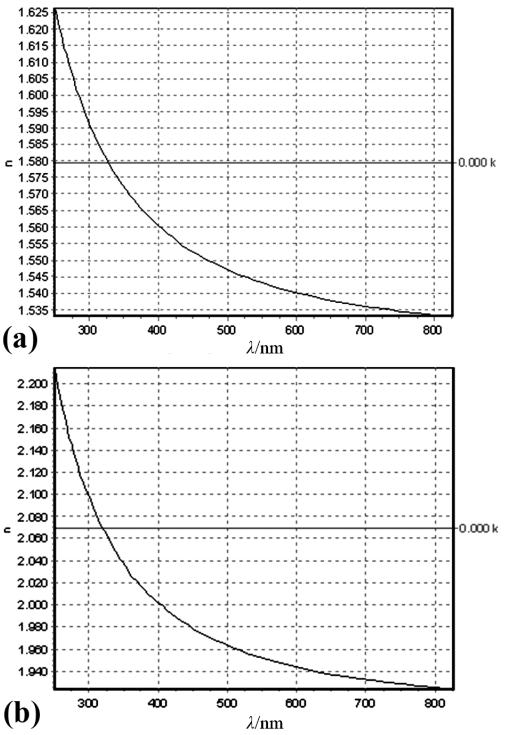

Figure 4: Refractive index (n) versus the wavelength λ/nm change for the coatings
Slika 4: Spremembe lomnega količnika (n) v odvisnosti od valovne dolžine λ/nm pri nanosih

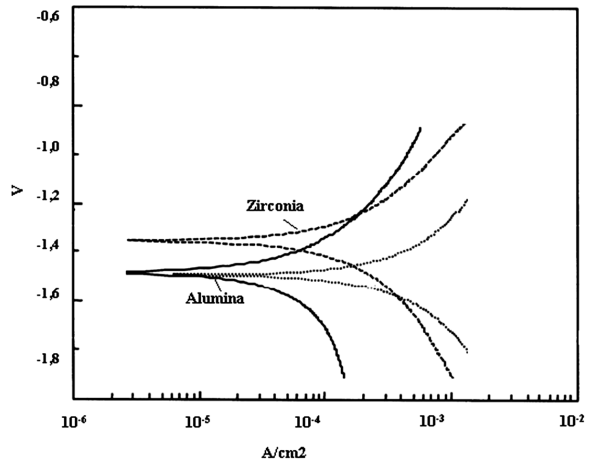

Figure 5: Polarization curves for the thin oxide films: ZrO_2 and Al_2O_3
Slika 5: Polarizacijski krivulji za tanek oksidni nanos ZrO_2 in Al_2O_3

(**Figure 5**). In addition, a distinct passivation region was present for the coated substrates. The corrosion-protection properties of the sol–gel-derived coatings are strongly dependent on the processing conditions. As evident from **Figure 5**, the alumina (Al_2O_3) film corrosion protection is better than the zirconia (ZrO_2) films.

4 CONCLUSIONS

The sol-gel-deposited oxide films formed with these compounds had good adhesion, reflectivity or UV protection. After the appropriate deposition and heat treatment the oxide films were formed with very favourable properties, such as high adhesion, homogeneity and density. The sol-gel alumina coatings developed on the magnesium alloy surface provide superior corrosion protection. After the heat treatments the XRD patterns revealed crystalline structures. With a controlled heat treatment a slight increase in the corrosion resistance was observed. However, both of the alumina- and zirconia-based coatings can be used for optical applications with suitable heat-treatment conditions. The refractive index of the alumina film was lower than that of the zirconia films. This depends on the crystallite structure and the surface morphology, such as bubbles and the porosity effect.

Acknowledgements

The authors would like to thank İstanbul Technical University, Metal. and Mat. Eng. Laboratory, JOBIN YVON Lab. Also, thanks go to the Researchers Céline Marchand and Michel Stchakovsky, Researcher Stefan Winter, Metallic Mat. Dept. of Universität Des Saarlandes for their experimental support.

5 REFERENCES

[1] E. F. Emley, Principle of magnesium technology, Pergamon Press, London 1966, 297
[2] M. M. Avedsian, H. S. Baker, Magnesium and magnesium alloys, ASM International, New York 1999, 138
[3] J. E. Gray, B. Luan, Protective coating on magnesium and its alloys, A critical review, Journal of Alloys and Compounds, 336 (**2002**) 1–2, 88–113
[4] R. Arrabal, E. Matykina, F. Viejo, P. Skeldon, G. E. Thompson, Corrosion resistance of WE43 and AZ91D magnesium alloys with phosphate PEO coatings, Corrosion Sci., 50 (**2008**) 6, 1744–1752
[5] Z. M. Liu, W. Gao, Electroless nickel plating on AZ91 Mg alloy substrate, Surface and Coatings Technology, 200 (**2006**) 16–17, 5087–5093
[6] Y. Tamar, D. Mandler, Corrosion inhibition of magnesium by combined zirconia silica sol-gel films, Electrochim Acta, 53 (**2008**), 5118–5127
[7] Y. Kobayashi, T. Ishizaka, Y. Kurokawa, Preparation of alumina films by the sol-gel method, J Mater Sci., 40 (**2005**), 263–283
[8] X. K. Zhong, Q. Li, B. Chen, J. P. Wang, J. Y. Hu, W. Hu, Effect of sintering temperature on corrosion properties of sol-gel based Al_2O_3 coatings on pre-treated AZ91D magnesium alloy, Corrosion Sci., 51 (**2009**), 2950–2958
[9] Q. Li, B. Chen, S. Xu, H. Gao, L. Zhang, C. Liu, Structural and electrochemical behavior of sol–gel ZrO_2 ceramic film on chemically pre-treated AZ91D magnesium alloy, Journal of Alloys and Compounds, 478 (**2009**), 544–549
[10] M. L. Zheludkevich, I. M. Miranda Salvado, M. G. S. Ferreira, Sol-Gel Coatings for Corrosion Protection of Metals, J. of Materials Chemistry, 15 (**2005**), 5099–5111
[11] A. Atkinson, D. L. Segal, Some recent developments in aqueous sol-gel processing, J. Sol–Gel Sci. Technol., 13 (**1998**), 133–139
[12] D. Niznansky, J. L. Rehspringer, Infrared study of SiO_2 sol to gel evolution and gel aging, J. Sol–Gel Sci. Technol., 180 (**1995**), 191–196
[13] L. Nicole, C. Boissiere, D. Grosso, A. Quach, C. Sanchez, Meso structured hybrid organic-inorganic thin films, J. Mater. Chem., 15 (**2005**), 3598–3627
[14] F. Mammeri, E. Le Bourhis, L. Rosez, C. Sanchez, Mechanical properties of hybrid organic-inorganic materials, J. Mater. Chem., 15 (**2005**), 3787–3811
[15] E. Altuncu, Practicability of a ceramic thin film formation technique in order to improve the surface properties of magnesium and its alloys, Kocaeli University, Metallurgical and Materials Engineering, Master Thesis, 2004
[16] H. Li, K. Liang, L. Mei, S. Gu, S. Wang, Oxidation protection of mild steel by zirconia sol–gel coatings, Materials Letters, 51 (**2001**), 320–324
[17] C. Jing, X. Zhao, Y. Zhang, Sol–gel fabrication of compact, crack-free alumina film, Materials Research Bulletin, 42 (**2007**), 600–608
[18] Z. L. Wang, R. C. Zeng, Comparison in characterization of composite and sol-gel coating on AZ31 magnesium alloy, Trans. Nonferrous Met. Soc. China, 20 (**2010**), 665–669

UDK 669.131.6:531.43:620.178.1
Professional article/Strokovni članek

ISSN 1580-2949
MTAEC9, 48(2)293(2014)

TESTING THE TRIBOLOGICAL CHARACTERISTICS OF NODULAR CAST IRON AUSTEMPERED BY A CONVENTIONAL AND AN ISOTHERMAL PROCEDURE

PREIZKUŠANJE TRIBOLOŠKIH LASTNOSTI NODULARNE LITINE, MEDFAZNO KALJENE PO KONVENCIONALNEM IN IZOTERMIČNEM POSTOPKU

Dušan Golubović[1], Pavel Kovač[2], Borislav Savković[2], Dušan Ješić[3], Marin Gostimirović[2]

[1]Faculty of Mechanical Engineering, Vuka Karadzica 30, 71213 East Sarajevo, Bosnia and Herzegovina
[2]Faculty of Technical Science, Trg D. Obradovica 6, 21000 Novi Sad, Serbia
[3]University of Banja Luka, Faculty of Engineering, V. Stepe Stepanovica 75, 7800 Banja Luka, Bosnia and Herzegovina
pkovac@uns.ac.rs

Prejem rokopisa – received: 2013-03-01; sprejem za objavo – accepted for publication: 2013-07-15

In this paper the heat treatment of ductile iron and the tribological properties of contact pairs (pin and disk) were investigated. Two types of nodular cast iron, EN-GJS-500-7 and EN-GJS-700-2, austempered using an isothermal and a conventional procedure, were tested. The friction-and-wear test was carried using a PIN on DISC Tribometer and the PQ test. The methodology of the classical and nodular cast-iron isothermal austempering and the methodology for the examination are also described. From analysing the results it was concluded that the tribological characteristics depend on the structural characteristic of the nodular cast iron, which are determined by heat treatment. The tested sample, austempered using a classic approach, gives the best performance in terms of friction, but it also showed the worst performance in terms of wear. In the same heat-treatment regime EN-GJS-500-7 is characterized by better tribological characteristics compared to the EN-GJS-700-2. The obtained results can be used for the proper selection of the type and regime of the nodular cast iron's heat treatment, with the aim of improving the exploitation characteristics of the contact pairs.

Keywords: nodular cast iron, heat treatment, friction, wear

Članek obravnava preizkušanje nodularne litine s toplotno obdelavo in tribološke lastnosti kontaktnih parov (klin in disk). Preizkušeni sta bili dve vrsti nodularne litine EN-GJS-500-7 in EN-GJS-700-2, medfazno kaljeni po konvencionalnem in izotermičnem postopku. Preizkus trenja in obrabe je bil izveden s "pin-on-disk" tribometrom in PQ-preizkusom. Prikazana je metodologija izotermnega poboljšanja klasične in nodularne litine ter metodologija preiskave. Analiza rezultatov je pokazala, da so tribološke lastnosti odvisne od značilnosti strukture nodularne litine, ki je določena z vrsto nodularne litine in toplotno obdelavo. Preizkusni vzorec, klasično medfazno kaljen, izkazuje najboljše rezultate glede trenja, hkrati pa največjo obrabo. V istem režimu toplotne obdelave ima EN-GJS-500-7 boljše tribološke lastnosti v primerjavi z EN-GJS-700-2. Dobljeni rezultati se lahko uporabijo pri izbiri primernega režima toplotne obdelave nodularne litine, z namenom izboljšanja lastnosti kontaktnih parov med rabo.

Ključne besede: nodularna litina, toplotna obdelava, trenje, obraba

1 INTRODUCTION

Modern materials used to create the elements of machinery, equipment and vehicles (cars, trucks, tractors, etc.) must possess, in addition to a high hardness, a good toughness and a high fatigue strength, as well as a more satisfactory resistance to friction and wear.[1,2] The first three properties of metallic materials are determined by standard methods. Information about them can be found in the relevant literature and standards, as well as in the technical documentation of the manufacturer of the materials.

The resistance to abrasive wear, as the tribological characteristic of materials, depends not only on their physical and chemical properties, but also on the conditions under which the contact between the elements of the tribomechanical system is achieved, as well as the properties of the other elements in the contact.[3] The measurement of the tribological properties of these two materials is carried out, usually on tribometers that fulfil one of the three possible geometries of contact (touch at a point on the line or on the surface). The paper presents the results achieved for a linear contact.[4,5]

In this paper, using a realized tribomechanical system with a geometric line contact, we examine the basic tribological properties of materials in terms of friction and wear. Part of the results of the tribological characteristics of the two types of nodular cast iron, isothermal and the improved classical procedure, obtained in laboratory conditions and presented in this study, indicate the importance of heat treatment on the resistance to friction and wear.[6–8]

The use of ductile iron in scientific research has a strong presence, so the paper[9] also considers the microstructures and tribological behaviour of different roller mill specimens, having basically nodular cast iron compositions, produced by conventional static and vertical centrifugal casting methods. Also, in the research work,[10] the initiative was taken to improve the surface hardness as well as the wear resistance of the as-received nodular

cast iron using the pack-carburizing technique. The objective of the paper[11] is to evaluate the fatigue life of the nodular cast iron EN-GJS-500-7, which is used for railway brake discs. In the paper[12] the results of the abrasive and adhesive wear resistance of selected grades of nodular cast iron with carbides are presented. The materials of the friction pairs, tested at the stand and subjected to heat treatment and chemical processing in order to attain specific parameters of their surface layers, were studied in the work.[13] The studies conducted enabled a determination of the abrasive wear values for the material samples tested, having entailed the surface-layer parameters and the factors related to the operation of actual structural components used in automotive engineering.

Through a literature review we can see what has already been done in terms of the wear resistance of ductile iron.[14–16] The abrasion wear rates of two-step austempered ductile cast iron (ADI) were investigated.[17] The wear resistance of the ductile cast iron can be improved through a different heat-treatment procedure and surface engineering techniques, each having some limitations and drawbacks.[17,18]

A microstructure of lower bainite consisting of acicular (needle) bainite stable ferrite and carbon-enriched retained austenite, is provided if the isothermal transformation is carried out at low temperatures. The microstructure of the upper bainite, which consists of ferrite-tile bainite and stable carbon-enriched retained austenite is obtained if the isothermal transformation is carried at a temperature of 390 °C.

With isothermal transformation temperature the distance between the ferrite tile bainite increases while reducing the remaining shares, i.e., the volume fraction of retained austenite was increased.

The impact strength and the fracture toughness can be strongly reduced. The light microscope, however, does not show the difference in the microstructure. Therefore, for a detailed correlation of the mechanical properties depending on the microstructure it is necessary to apply a high-resolution transmission electron microscope (TEM).

For ductile iron of a ferrite base it is strongly recommend to use an isothermal transformation temperature of 350 °C.[19]

The objectives of the research were to prove that for a variety of thermal processing on the same material, a different value for the level of material wear is obtained. In addition, they want to show that the same level of heat treatment applied to different materials, for some sizes that represent the level of friction and wear, are of great importance and influence, whereas for some they are not.

2 EXPERIMENTAL PROCEDURE

2.1 Material

In all the experiments we used a hardened carbon steel (C40E) pin of guaranteed chemical composition and a hardness of 52 HRC. The test program includes two types of nodular cast iron, EN-GJS-500-7 and EN-GJS-700-2, austempered by an isothermal and conventional procedure.[19,20]

The melting of the material was carried out in a network frequency induction furnace pot with an acid coating capacity of 2.5 t in a foundry. After this the desulfurization was carried out in a batch nodulation closed pot using a "sandwich" method with a simultaneous modification at a temperature of 1500 °C. A secondary modification was made before the actual casting. The as-prepared metal was poured into a total 11 Y tube to BS 2789.

All the Y tubes were covered by two tube sections, 25 mm diameter and length 250 mm. Attention was also given to two tubes by tensile tests in the irons JUS C.J2.022 and three tubes with V-notch toughness testing JUS C.A4.004.

The isothermal austenitising was performed in a muffle furnace in a protective atmosphere at 900 °C for 90 min prior to preheating at 520 °C for 60 min. The austempering was carried out in a solar bath (made specifically for this purpose) at a temperature of 390 °C with a hold time of 30 min at a speed of movement for the salts of 0.6 m/s.

Their basic characteristics are listed in **Table 1**.[19] We present the chemical composition, the conventional austempering regimes, the isothermal austempering and the hardness of the tested parts.[21]

Figure 1 shows the metallographic structure of the nodular cast iron used in the test. It is important to mention that the EN-GJS-500-7 is ferrite-pearlite structure

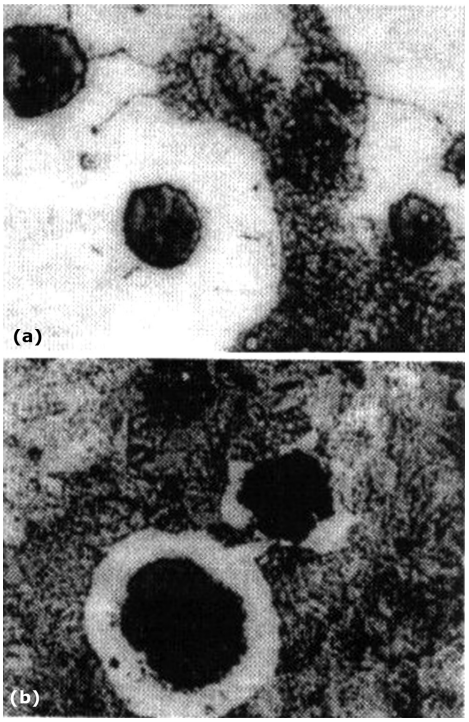

Figure 1: Microstructures of: a) EN-GJS-500-7 and b) EN-GJS-700-2
Slika 1: Mikrostruktura: a) EN-GJS-500-7, b) EN-GJS-700-2

Table 1: The chemical composition and heat-treatment regimes of nodular cast iron EN-GJS-500-7 and EN-GJS-700-2
Tabela 1: Kemijska sestava in režimi toplotne obdelave nodularne litine EN-GJS-500-7 in EN-GJS-700-2

Material of Disk	Heat Treatment		Hardness HB	Legend	Structure
	T_a/°C	T_p/°C / t/min			
EN-GJS-500-7	900	390/30	355	EN-GJS-500-7-30	ferrite-pearlite
		520/60	302	EN-GJS-500-7-k	
EN-GJS-700-2		520/60	320	EN-GJS-700-2-k	mostly pearlitic
		390/30	365	EN-GJS-700-2-30	

	Chemical composition, *w*/%							
	C	Si	Mn	Mg	P	S	Cu	Ni
EN-GJS-500-7	3.85	2.9	0.076	0.035	0.02	0.004		1.5
EN-GJS-700-2	3.76	2.35	0.51		0.02	0.004	1.48	1.5

based (50 % ferrite and 50 % pearlite and more than 90 % of graphite-type-K size 3) and the EN-GJS-700-2 is predominantly pearlitic-structure based. During the structural test of the nodular cast iron the etching was performed with 2 % HNO_3 and increased 500-times. **Figure 1** shows that the black parts have a pearlitic structure, and the white parts are a softer ferrite structure. In the middle are the visible graphite nodules surrounded by a highly visible ferrite structure.[4]

Figure 2 shows the austempered ductile iron microstructure. The mechanical properties depend on the structure of the material. One pearlitic ductile cast iron has, before the isothermal treatment, an improved microstructure consisting of pearlite, and in it are the graphite nodules. After the isothermal improvement the material microstructure consists of bainite and retained austenite. The amount of retained austenite is relatively high (aged between 20 % and 40 %). The austenite contributes to the high toughness and the ductility of the austempered ductile iron.

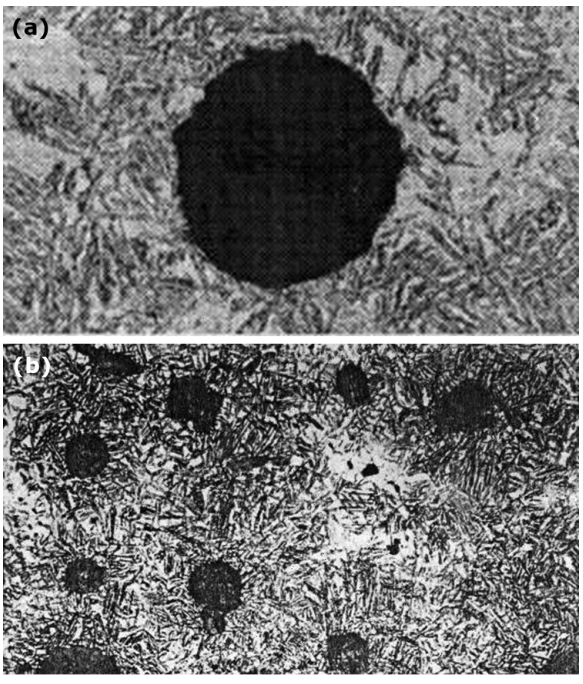

Figure 2: Microstructure of austempered ductile iron: a) EN-GJS-500-7 and b) EN-GJS-700-2
Slika 2: Mikrostruktura izotermno poboljšane nodularne litine: a) EN-GJS-500-7, b) EN-GJS-700-2

Irons that were improved during a low-temperature isothermal transformation have a structure of lower bainite and about 400 HB hardness (HRC about 43), and are suitable for first gear and applications that must be resistant to high pressures.

Irons that were improved at higher temperatures of isothermal transformation have an upper bainite structure and a hardness from 260 HB to 350 HB (HRC 27 to 38), and have a particularly high ductility, impact strength and fatigue strength.

Figure 3 shows a diagram of the classical austempering procedure of nodular cast iron.[14] The process of austempering conventional materials was achieved by heating up to a temperature of 900 °C, where it is held for about 90 min and then by rapid cooling (water or air) to room temperature. After this it is heated to a temperature of 520 °C and is then cooled to room temperature.

Figure 4 shows a diagram of the discs' isothermal austempering, made of an EN-GJS-500-7 ferrite-pearlite base and an EN-GJS-700-2 made of a very pearlite base. The austempering is done by heating the disks to a tem-

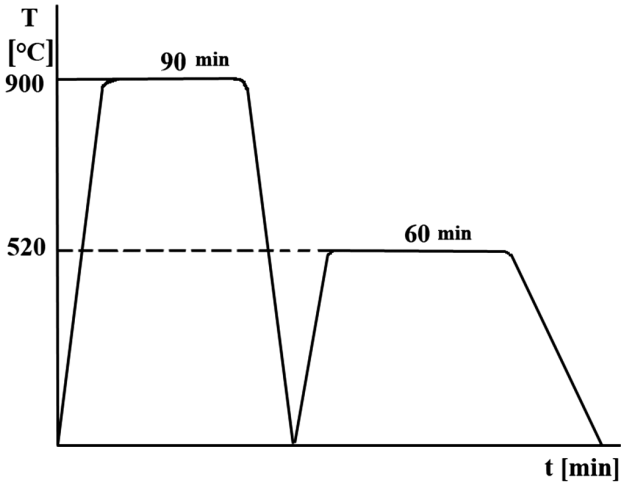

Figure 3: Diagram of conventional discs' austempering
Slika 3: Diagram klasičnega poboljšanja ploščic

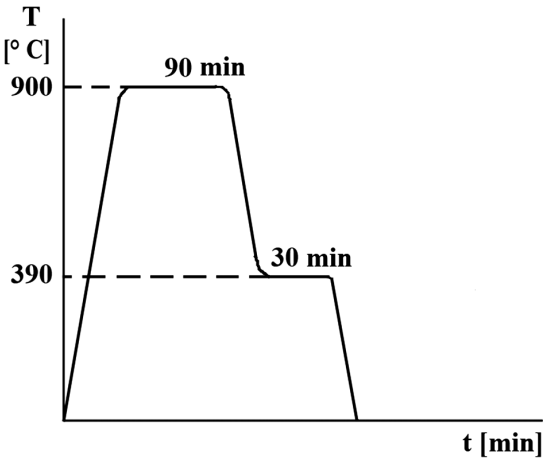

Figure 4: Diagram isothermal discs' austempering
Slika 4: Diagram izotermičnega poboljšanja ploščic

perature of 900 °C, at which it is held for about 90 min, and then fast cooled to a temperature of 390 °C.

The discs of EN-GJS-500-7 and EN-GJS-700-2 were kept for 90 min and 30 min at the temperature of 390 °C. In this way we get a bainite structure (upper or lower bainite) that enables improved toughness, and in this case the wear resistance (abrasion of discs).

2.2 Method

Figure 5 provides a schematic view of the contact pair (pin and disk) and an image using the Tribometer TPD-93 where the coefficient of friction is measured for the inline contact.[5] With this equipment it is possible to measure the friction force, the normal force, the coefficient of friction, the acoustic emission temperature of the oil and the contact temperature. The characteristics of the tribometer are: normal load 1–500 N, sliding speed 0.1–5 m/s, the motor power A is 1.5 kW, the motor power B is 0.37 kW, and the overall dimensions are 1 200 mm × 600 mm × 1 300 mm.

By measuring the normal and friction forces at different levels of load and sliding speed v = 1.3 m/s, the friction coefficients for a given combination of contact pairs are determined. In the given range of load F_n = 1–3 N the differences in friction coefficients are less than 5 %, so the comparison is the heat-treated nodular cast iron EN-GJS-500-7 and EN-GJS-700-2 derived for the adopted level of load F_n = 2 N. This force was set on the tribometer.

To determine the *PQ* index we used the *PQ* 2000 Particle quantifier shown in **Figure 6**. According to the procedure methodology the value of the *PQ* index is directly proportional to the quantity of the wear products (greater than 5–10 μm) that are contained in the oil used for lubrication of the contact zone, during the disk sliding along the pin. For this purpose the used oil was Polar INA 55-K.

The *PQ* index is the average value obtained from several measurements. The average measurements of the

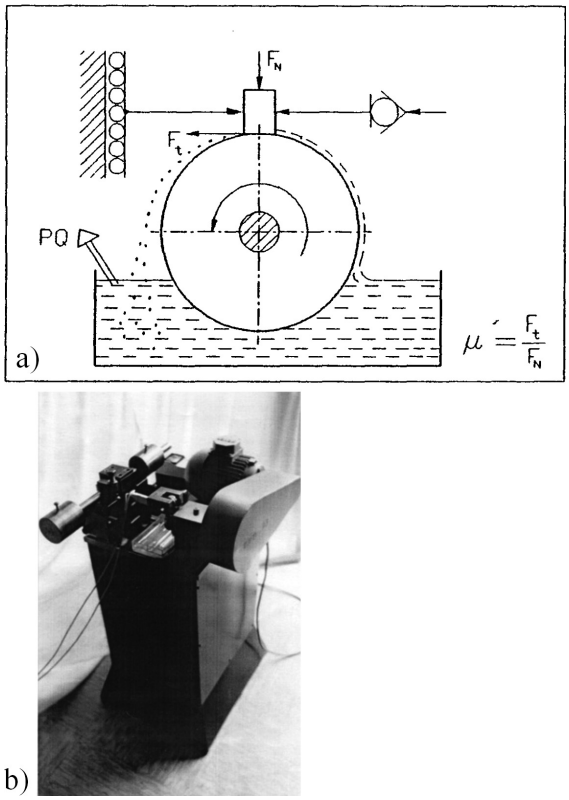

Figure 5: a) Schematic view of the contact pair (pin and disk) and b) image of Tribometer TPD-93
Slika 5: a) Shematski prikaz kontakta para (pin in disk) in b) tribometer TPD-93

PQ index for a sample of oil containing products in the research conducted was 10. In most cases the measurement error did not exceed 10 %.

The duration of the contact in the experimental operations was about 30 min. The friction force was measured at the beginning and at the end of the actual contact (t_p = 1 min, t_k = 29 min). There was a line contact

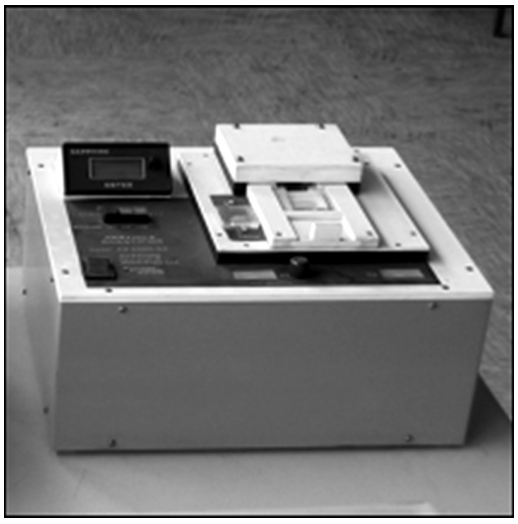

Figure 6: PQ 2000 Particle quantifier
Slika 6: Kvantifikator delcev PQ 2000

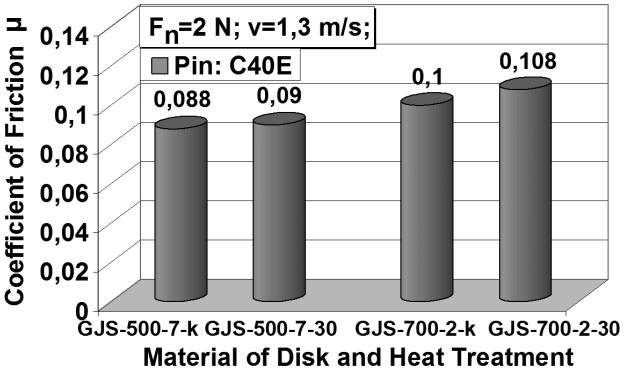

Figure 7: Histogram of the obtained friction coefficients for the tested materials

Slika 7: Histogram prikazuje dobljene koeficiente trenja preizkušanih materialov

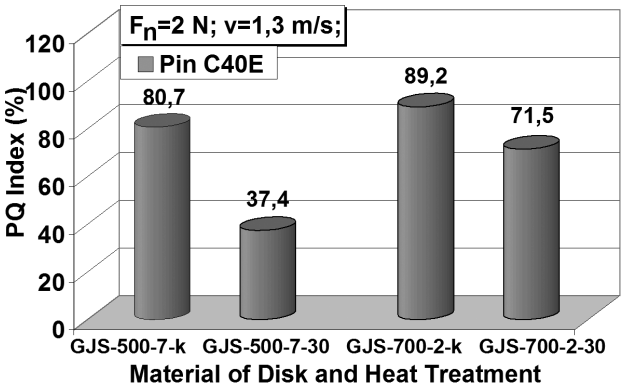

Figure 8: Histogram values of PQ index

Slika 8: Histogram prikazuje dobljene vrednosti PQ-indeksov

between the pin and the disc. The measurement of the *PQ* indices in a sample of oil in which there are wear products was performed 3 times on 10 samples.

The *PQ* index was determined based on the quantity of wear products per mg of oil produced during the sliding of one element of the tribomechanical system over the other for t = 30 min. The different values of the *PQ* index indicate the amount of wear product for the samples in contact in the lubricant are a direct consequence of the greater or lesser intensity of the wear of the contact pair. The test covered above thermally austempered discs of nodular cast iron EN-GJS-500-7 and EN-GJS-700-2. The wear of the pins for 30 min was carried out under the same contact conditions and based on samples of oil particle quantifiers over the levels of the *PQ* indices.

3 RESULTS AND DISCUSSION

3.1 Experimental results

3.1.1 According to the experimental results

In order to determine the influence of the heat-treatment type on the tribological properties of ductile iron, on two types of ductile iron EN-GJS-500-7 and EN-GJS-700-2, the test of the friction and wear according to a pre-defined methodology of experimental research was conducted. **Figure 7** shows the histogram displaying values of the friction coefficients at the line of contact for the disc and pin, obtained from the derived values of forces, recorded by the measuring instrumentation. The histogram shows that the heat treatment of the ductile iron EN-GJS-500-7 has a small (approximately 2 %), practically negligible, impact on the value of the friction coefficient. Simultaneously, the EN-GJS-700-2 ductile iron isothermally improved by about 8 % higher coefficient of friction than the same nodular cast iron improved using the classical procedure. On the other hand, the coefficient of friction in a ductile iron EN-GJS-700-2 increased by 15–20 % more than the values that were obtained for ductile iron EN-GJS-500-7.

Figure 8 shows a histogram of the *PQ* index values for the observed contact pairs (pin and disk), the load level of 2 N and the slip velocity v = 1.3 m/s. The histogram displays the values of the *PQ* index, different than the coefficient of friction, which shows that the treatment regimens have a very large impact on the aspects of wear. In both nodular irons the *PQ* index is higher for iron improved by the classical procedure, especially for EN-GJS-500-7 (approx. 115 %). On the other hand, the ductile iron EN-GJS-500-7, improved the isothermal and classic approach, has a significantly lower *PQ* index for iron EN-GJS-700-2 (approx. 10–90 %).

Figure 9 shows a comparative review of the tribological characteristics of the tested discs, in terms of friction and wear, i.e., by the indicators $P_t = \mu_r/\mu_x$ and $P_h = PQ_r/PQ_x$. Here, μ_r and PQ_r are the values of the friction coefficient and the wear index of the reference contact pairs (it was a material austempered using the classical procedure), whereas μ_x and PQ_x are the values of the investigated contact pair. In doing so, for the reference a contact couple with the lowest coefficient of friction and wear is chosen, which receives the same indicator value for the maximum of 100 %.

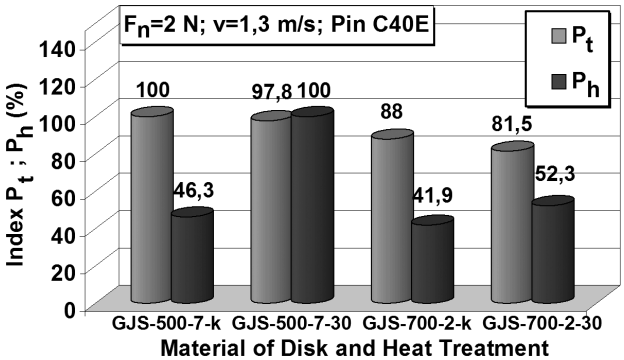

Figure 9: Histogram P_t, P_h index of the tested materials with different heat treatments

Slika 9: Histogram P_t, P_h-indeksov preizkušenih materialov z različno toplotno obdelavo

3.2 Discussion

By analysing the results obtained, it can be concluded that ductile iron, austempered using the classic approach, has different tribological properties in terms of friction and wear.[6,7,14–17] The tribological characteristics significantly depend on the type of nodular cast iron, and the heat treatment.

By comparing the tribological characteristics of the tribomechanical system elements, made of some kind of ductile iron, some coefficients of friction lead to the conclusion that the thermal treatment has no practical impact. Differences in the tribological characteristics of the same elements, however, are very large if the tribological characteristics are determined by the size of their wear, which occurs after a specified duration of the contact.

The difference in the coefficients of friction is slightly higher when comparing the two studied materials. The coefficient of friction of the ductile iron EN-GJS-700-2 is slightly larger than the coefficient of friction of the material EN-GJS-500-7.

The *PQ* index is higher in the material EN-GJS-700-2. Both classical materials' heat-treated *PQ* index is greater than the isothermally processed material. Based on this we can conclude that the higher wear is in the conventionally heat-treated material. The isothermal heat treatment helps to reduce the wear of these materials

The indicator of the friction coefficient between the investigated disks P_t is higher for the classical heat-treated material. Also, the indicator P_t is significantly lower for the material EN-GJS-700-2, which suggests that the friction is less for this material. The values of the parameters P_h are higher for the materials EN-GJS-500-7, whether it is a classic procedure or isothermally processed. It is confirmed that the materials that are isothermally processed have less contact wear than the classically heat-treated materials.

4 CONCLUSIONS

The tested sample, a disc made of EN-GJS-500-7 austempered using the classic approach, gives the best performance in terms of friction, but it also showed the worst in terms of wear. The disc made of a hardened EN-GJS-500-7 and isothermally austempered has excellent features from the point of view of friction and wear. In the same heat-treatment regime EN-GJS-500-7 is characterized by better tribological characteristics than the EN-GJS-700-2.

The laboratory studies of the improved tribological properties of nodular cast iron can be used during the selection of materials and heat treatment in order to reduce the friction and wear in the contact pairs' exploitation conditions. Further research is planned to follow the tribological properties of selected materials in specific industrial conditions.

5 REFERENCES

[1] J. Zimba, D. J. Simbi, E. Navara, Austempered ductile iron: an alternative material for earth moving components, Cement & Concrete Composites, 25 (**2003**) 6, 643–649

[2] K. S. Vinoth, R. Subramanian, S. Dharmalingam, B. Anandavel, Mechanical and tribological characteristics of Stir-Cast Al-Si10Mg and Self-Lubricating Al-Si10Mg/MoS_2 Composites, Mater. Tehnol., 46 (**2012**) 5, 497–501

[3] B. Ivkovic, D. Jesic, B. Tadic, Tribological Characteristics of Nodular Cast Iron, INTERTRIBO'93, Bratislava, 1993

[4] D. Golubovic, P. Kovac, D. Jesic, M. Gostimirovic, Tribological properties of adi material, Journal of the Balkan Tribological Association, 18 (**2012**) 2, 165–173

[5] M. Demirel, M. Muratoglu, The friction and wear behavior of Cu-Ni3Al composites by dry sliding, Mater. Tehnol., 45 (**2011**) 5, 401–406

[6] M. N. Ahmadabadi, H. M. Ghasemi, A. M. Osia, Effects of successive austempering on the tribological behavior of ductile cast iron, Wear, 231 (**1999**) 2, 293–300

[7] Y. Kharlamov, V. Dal, I. Mamuzić, L. Lopata, G. S. Pisarenko, The selection and development of tribological coatings, Mater. Tehnol., 44 (**2010**) 5, 283–287

[8] D. Jesic, Einfluss der Warmebedehandlungsart des Gusseisens mit Kugelgrapit auf seine Tribologisch Charakteristika, Tribologie und Schmierungstechnik, 40 (**1993**) 2

[9] O. Birbaşar, E. Türedi, S. H. Atapek, M. Zeren, Wear Behavior of Roller Materials produced by Static and Centrifugal Casting Methods, International Iron & Steel Symposium, Karabük, Turkey, 2012, 136–142

[10] N. Fatima, M. A. Islam, Wear Behaviour of Nodular Cast Iron, International Conference on Mechanical Engineering 2009 (ICME2009), Dhaka, Bangladesh, 2009, ICME09-RT-17, 1–5

[11] B. Šamec, I. Potrc, M. Šraml, Low cycle fatigue of nodular cast iron used for railway brake discs, Engineering Failure Analysis, 18 (**2011**), 1424–1434

[12] G. Gumienny, Wear resistance of nodular cast iron with carbides, Archives of Foundry Engineering, 11 (**2011**) 3, 81–88

[13] R. Burdzik, P. Folega, B. Lazarz, Z. Stanik, J. Warczek, Analysis of the Impact of Surface Layer Parameters on Wear Intensity of Friction pairs, Archives of Metallurgy and Materials, 57 (**2012**) 4, 987–993

[14] M. J. Perez, M. M. Cisneros, H. F. Lopez, Wear resistance of Cu-Ni-Mo austempered ductile iron, Wear, 260 (**2006**) 7–8, 879–885

[15] R. Arabi Jeshvaghani, M. Shamanian, M. Jaberzadeh, Enhancement of wear resistance of ductile iron surface alloyed by stellite 6, Materials and Design, 32 (**2011**) 4, 2020–2033

[16] N. Rebasa, R. Dommarco, J. Sikora, Wear resistance of high nodule count ductile iron, Wear, 253 (**2002**) 7, 855–861

[17] P. Silawong, A. Panitchagul, S. Inthidech, N. Akkarapattanagoon, U. Kitkamthorn, Improvement of Abrasion Wear Resistance of Ductile Iron by Two-Step Austempering, Advanced Materials Research, 567 (**2012**), 58–61

[18] B. Podgornik, J. Vizintin, I. Thorbjornsson, B. Johannesso, J. T. Thorgrimsson, M. Martinez Celis, N. Valle, Improvement of ductile iron wear resistance through local surface reinforcement, Wear, 274–275 (**2012**), 267–273

[19] D. Ješić, Tribological Properties of Nodular Cast Iron, Monography, Journal of the Balkan Tribological Association, Sofia, 2000, 125

[20] K. Brandenburg, Machining Austempered Ductile Iron, Manufacturing Engineering, 128 (**2002**), 5

[21] A. R. Ghaderi, M. N. Ahmadabadi, H. M. Ghasemi, Effect of graphite morphologies on the tribological behavior of austempered cast iron, Wear, 255 (**2003**) 1–6, 410–416

UDK 669.715:536.7
Professional article/Strokovni članek

ISSN 1580-2949
MTAEC9, 48(2)299(2014)

QUANTIFICATION OF THE COPPER PHASE(S) IN Al-5Si-(1–4)Cu ALLOYS USING A COOLING CURVE ANALYSIS

UPORABA ANALIZE OHLAJEVALNE KRIVULJE ZA OCENO KOLIČINE BAKROVIH FAZ V ZLITINAH Al-5Si-(1-4)Cu

Mile B. Djurdjevic[1], Srecko Manasijevic[2], Zoran Odanovic[1], Natalija Dolic[3], Radomir Radisa[2]

[1]IMS Institute, Bulevar Vojvode Misica 43, 11 000 Belgrade, Serbia
[2]Lola Institute, Kneza Viseslava 70a, 11 000 Belgrade, Serbia
[3]University of Zagreb, Faculty of Metallurgy, Aleja narodnih heroja 3, 44 103 Sisak, Croatia
srecko.manasijevic@li.rs

Prejem rokopisa – received: 2013-04-02; sprejem za objavo – accepted for publication: 2013-06-18

The aim of this paper is to demonstrate that it is possible to characterize the development and quantify the area percentage of Cu-enriched phases in Al-5Si-(1-4)Cu alloys by applying a cooling-curve analysis. It is shown that several distinct Cu-enriched phases are manifested as peaks on the first derivative of the cooling curve. The total area percentage of the Cu-enriched phases is defined as the ratio of the area between the first derivative of the cooling curve and the hypothetical solidification path of the Al-Si-Cu eutectic to the total area between the first derivative of the cooling curve and the base line. These calculations, based on the cooling curve analyses, are compared with the image-analysis and chemical-analysis results in order to verify the proposed method. There is a good correlation between the measured and calculated values for the area of the Cu-rich phase in Al-5Si-(1–4)Cu alloys.

Keywords: aluminum alloys, thermal analysis, cooling-curve analysis, image analysis

Namen tega članka je predstaviti možnost ocene nastanka in količinsko določiti področja s Cu bogatih faz v zlitinah Al-5Si-(1-4)Cu z analizo ohlajevalne krivulje. Pokazano je, da se več ločenih, s Cu bogatih faz kaže v obliki vrhov v prvem odvodu krivulje ohlajanja. Skupni delež območja s Cu bogatih faz je določen kot razmerje površin med prvim odvodom krivulje ohlajanja in hipotetične poti strjevanja Al-Si-Cu-evtektika ter celotno površino prvega odvoda krivulje ohlajanja in osnovno linijo. Izračuni, ki temeljijo na analizi ohlajevalnih krivulj, so bili primerjani z analizo slik in rezultati kemijske analize, da bi potrdili predlagano metodo. Obstaja dobra korelacija med izmerjenimi in izračunanimi vrednostmi področij s Cu bogatih faz v zlitini Al-5Si-(1–4)Cu.

Ključne besede: aluminijeve zlitine, termična analiza, analiza ohlajevalne krivulje, analiza slik

1 INTRODUCTION

The automotive industry makes frequent use of the Al-Si-Cu series of aluminum alloys. In order to ensure that cast components have good mechanical properties, their as-cast microstructures must be closely monitored. Two eutectic microconstituents are primarily responsible for defining the microstructures of Al-Si-Cu series alloys: Al-Si and Al-Cu. Both of these eutectics can be detected on a thermal-analysis (TA) cooling curve, or more precisely, on its first derivative. The solidification of Al-Si-Cu series alloys and the formation of Cu-enriched phases can be described, according to many authors, as follows:[1–4]

1. A primary α-aluminum dendritic network forms between 580–610 °C. The exact temperature depends mainly on the amounts of Si and Cu in an alloy. This leads to an increase in the concentration of Si and Cu in the remaining liquid.
2. Between 570–555 °C (the Al-Si eutectic temperature), a eutectic mixture of Si and α-Al forms, leading to a further localized increase in the Cu content of the remaining liquid.
3. At approximately 540 °C, Mg_2Si and $Al_8Mg_3FeSi_6$ phases begin to precipitate.
4. At approximately 525 °C, a "massive" or "blocky" Al_2Cu phase (containing approximately w = 40 % Cu) forms together with β-Al_5FeSi platelets.
5. At approximately 507 °C, a fine Al-Al_2Cu eutectic phase forms (containing mass fractions approximately 24 % Cu). If the melt contains more than 0.5 % Mg, an ultra-fine $Al_5Mg_8Cu_2Si_6$ eutectic phase also forms at this temperature. This phase grows from either of the two previously mentioned Al_2Cu phases.

A metallographic analysis of the TA test samples, presented in **Figure 1**, combined with an X-ray micro-analysis has confirmed that Cu-enriched phases appear with three main morphologies: the blocky type, the eutectic type and the fine eutectic type.[3,5,6]

The Al-5Si-(1–4)Cu alloys are characterized by the presence of the two eutectics (Al-Si and Al-Si-Cu) that are primarily responsible for the mechanical properties of these alloys. Both eutectic temperatures can be detected on a TA cooling curve, or more precisely, on its first derivative. The eutectic-formation temperatures can

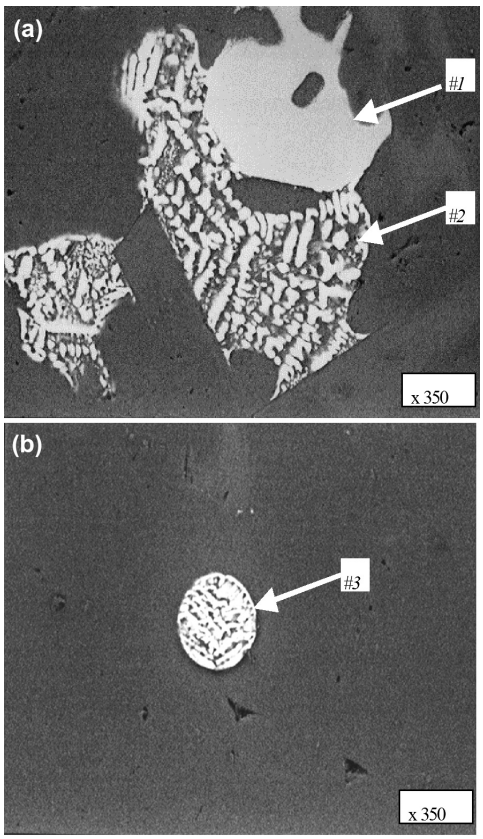

Figure 1: SEM micrographs (BSE images) with the characteristic morphologies of Cu-enriched phases found in the investigated alloys: a) the blocky (#1) and eutectic types (#2), b) the fine eutectic type (#3)[6]

Slika 1: SEM-posnetka (BSE-posnetka) z značilno morfologijo s Cu bogatih faz v preiskovih zlitinah: a) kockasta (#1), evtektik (#2), b) drobni evtektik (#3)[6]

help to define the maximum temperature, to which castings can be exposed during a solution treatment (i.e., by defining the temperature, at which incipient melting will take place). Unfortunately, the total amount of the Cu-enriched phases present in an as-cast part can, so far, only be measured using a metallographic analysis. This information is critical because these Cu-rich phases play a significant role in the heat-treatment process and can have a negative influence on the mechanical properties of the Al-5Si-(1–4)Cu alloys. The goal of this paper is to demonstrate that it is possible to quantify and characterize the development of the Cu-enriched phases in the Al-5Si-(1–4)Cu alloys using the TA system. This estimation is verified using quantitative metallography (an image analysis (IA)) and a chemical analysis (optical emission spectroscopy (OES)).

2 EXPERIMENTAL PROCEDURES

Three Al-Si-Cu alloys with the chemical compositions presented in **Table 1** were produced. Their chemical compositions were determined using the OES.

Liquid test samples with the masses of approximately 300 g were poured into thermal-analysis steel test cups. The weight of a steel test cup was 50 g. Two K-type thermocouples were inserted into the melt and the temperatures between 700–400 °C were recorded. The tip of a thermocouple was always kept at the constant height, 15 millimeters from the bottom of the crucible. The accuracy of a thermocouple was ± 0.5 °C. The data for TA was collected using a high-speed data-acquisition system linked to a personal computer. The cooling conditions were kept constant during all the experiments and the cooling rate was approximately 6 K min^{-1}. The cooling rate was calculated as the ratio of the temperature difference between the liquidus and solidus temperatures to the total solidification time between these two temperatures. Each TA trial was repeated three times. Consequently, a total of nine samples were gathered. In all the cases, the masses of the thermal-analysis test samples were virtually identical.

The samples for the microstructural analysis were cut from the TA test samples, close to the tips of the thermocouples. The cross-sections of the specimens were ground and polished on an automatic polisher using standard metallographic procedures. The samples were observed with a scanning electron microscope (SEM) using the magnifications between 200-times and 5000-times. Qualitative and quantitative assessments of the chemical compositions of the Cu-enriched phases were done using an energy dispersive spectrometer (EDS). The area fractions of the Cu-enriched phases were calculated using image-analysis software linked to a microscope, under a magnification of 500-times. Twenty-five analytical fields were measured for each sample and the final area fraction was expressed as the mean value.

3 RESULTS AND DISCUSSION

3.1 Thermal-analysis results

Three representative TA cooling curves obtained for the Al-5Si-1Cu, Al-5Si-2Cu and Al-5Si-4Cu alloys are presented in **Figure 2**. The cooling rate for all three curves was approximately 6 K min^{-1}. **Figure 3** shows that the increasing Cu amount of the melt lowers all the

Table 1: Chemical compositions (mass fractions, *w*/%) of the synthetic alloys
Tabela 1: Kemijska sestava (masni deleži, *w*/%) sintetičnih zlitin

Alloy	Si	Cu	Fe	Mg	Mn	Zn	Ni	Al
Al-5Si-1Cu	4.85	1.03	0.09	0.14	0.01	0.01	0.007	residual
Al-5Si-2Cu	5.01	2.06	0.10	0.26	0.01	0.01	0.007	residual
Al-5Si-4Cu	4.89	3.85	0.09	0.16	0.01	0.01	0.009	residual

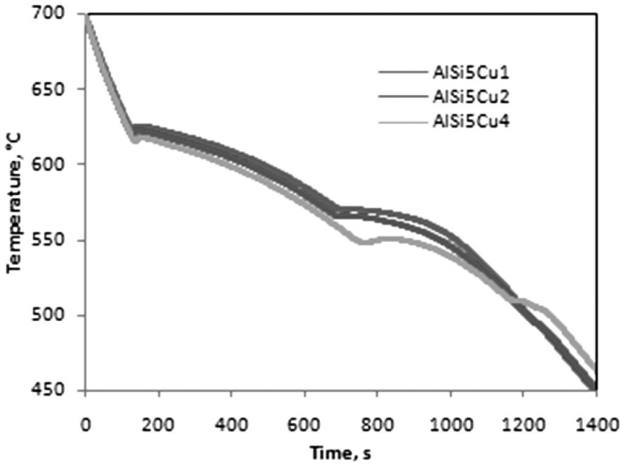

Figure 2: Cooling curves of the investigated Al-5Si-(1–4)Cu alloys
Slika 2: Ohlajevalne krivulje preiskovanih zlitin Al-5Si-(1-4)Cu

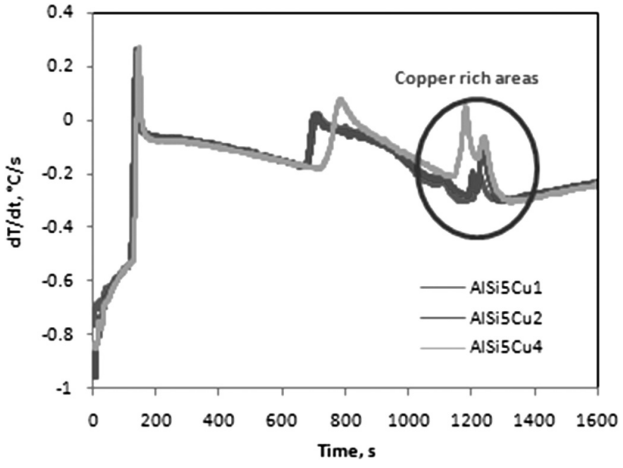

Figure 4: First derivatives of the Al-5Si-(1–4)Cu cooling curves
Slika 4: Prvi odvod ohlajevale krivulje zlitin Al-5Si-(1-4)Cu

characteristic solidification temperatures (T_{LIQ}, T_{COH}, T_{EUT}^{Al-Si} and $T_{EUT}^{Al-Si-Cu}$) except the solidus temperature that is almost constant for all the investigated alloys.

The first derivatives of the cooling curves are presented in **Figure 4**. It is apparent that the shapes of the first derivative curves strongly depend on the Cu amount in the melt. The Cu-rich area is particularly affected by different Cu amounts.

The numbers and shapes of the peaks visible in the Cu-enriched region of the first-derivative curves show a strong relationship with the amount of Cu present in the alloy. It can also be observed in **Figure 5** that an increase in the Cu amount increases the solidification time of the Cu-rich eutectic phase. The precipitation temperature of the Cu-enriched phases decreases when Cu increases from mass fractions 1 % to 4 %. The Cu-enriched phase represented by the first peak on the cooling curve in **Figure 5** (5 % Si, 1 % Cu in the alloy) began to precipitate at 542.7 °C and the Cu-enriched phase represented by the second peak precipitated at 503.2 °C. For the alloy with 5 % Si and 2 % Cu, three peaks precipitated at various temperatures, (530.4, 505.4 and 498.1) °C, respectively. The increasing amount of Cu to 4 % (5 % Si) further changes the shapes of the Cu-enriched phase peaks (**Figure 5**). The precipitation temperatures were also altered. The Cu-enriched phase represented by the first peak of the Al-Si5-Cu4 alloy begins to precipitate at 514.4 °C, while the second peak appears at 507.2 °C. The increasing Cu amount from 1 % to 4 % slightly increased the total solidification time from 1167 s (for the Al-5Si-1Cu alloy) to 1211 seconds (for the Al-5Si-4Cu alloy), increasing also the total solidification temperature interval of the Cu-rich phase(s) from 31.4 °C (for the Al-5Si-1Cu alloy) to 65.4 °C (for the Al-5Si-4Cu alloy).

These results of the experiments (**Figures 2** to **5**) indicate that the Cu-enriched phases precipitate at different temperatures depending on the amount of Cu pre-

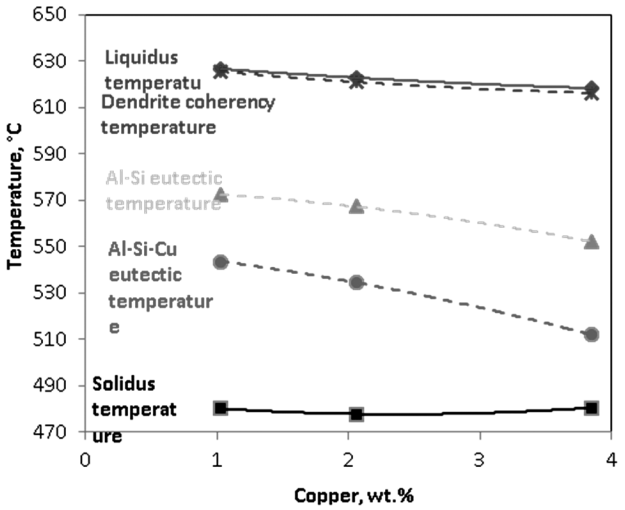

Figure 3: Impacts of different Cu amounts on the characteristic temperatures of Al-5Si-(1–4)Cu alloys
Slika 3: Vpliv različnih vsebnosti Cu na značilne temperature v zlitinah Al-5Si-(1-4)Cu

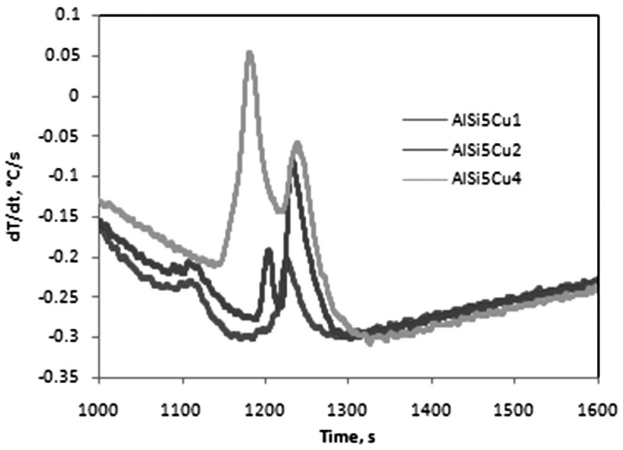

Figure 5: First derivatives of the Al-Si5-Cu(1–4) cooling curves related to the Cu-enriched region
Slika 5: Prvi odvod ohlajevalnih krivulj Al-5Si-Cu(1-4) glede na z bakrom bogato področje

sent in the particular Al-Si5-Cu(1-4) alloy. The nucleation temperature of the Cu-enriched phases can be accurately read from the first derivatives of the cooling curves and used to define the maximum temperatures that the castings can be exposed to during the conventional solution-treatment process. However, before the solution-treatment routines can be "tailored" to specific alloys and applications, it is also necessary that the volume fractions of the Cu-enriched phases are known. This data enables the researchers to predict the mechanical properties of the castings and design components according to the predetermined specifications and requirements. To date, a volume-fraction assessment has only been possible through a metallographic analysis.

3.2 Metallography, the cooling curve and image-analysis results

Light optical microscopy (LOM) observations combined with the IA showed that the area fractions of the Cu-enriched phases increased with additions of Cu. A Cu increase from 1 % to 4 % caused the area fraction of the Cu-enriched phases to increase from about 0.55 % to about 2.42 % (**Table 2**).

Table 2: Comparison of the Cu-enriched-phase area fractions detected by the IA system and determined with the TA
Tabela 2: Primerjava deleža področij s Cu bogatih faz, ugotovljenih z IA-sistemom in določenih s TA

Alloy	Area of Cu-rich phase, (TA) %	Area of Cu-rich phase, (IAS) %	*w*(Cu)/%
Al-5Si-1Cu	0.90	0.55	1.03
Al-5Si-2Cu	2.55	1.65	2.06
Al-5Si-4Cu	4.30	2.42	3.85

An additional SEM observation, combined with an X-ray spot microanalysis for the investigated alloy (Al-5Si-4Cu) was performed to identify the morphologies and stoichiometries of the observed Cu-enriched phases. This analysis confirmed the earlier assertion that Cu-enriched phases appear with three main morphologies: the blocky type, the eutectic type and the fine eutectic type (**Figure 6**). The quantitative X-ray microanalysis of the revealed stoichiometries of the Cu phases (**Table 2**) is presented in **Figure 6**.

It should be noted that a complete evaluation of the morphologies and the corresponding stoichiometries of the Cu-enriched phases is beyond the scope of the present paper. Quenching experiments will be necessary to establish the crystallization sequences of the Cu-enriched phases and the corresponding stoichiometries with respect to the TA results.

The imperfect agreement between these two measurements can be explained with two factors: First, the IA measurements do not take into account the small Si crystals that cannot be resolved with the LOM or the Si that is dissolved in the aluminum matrix. Second, because the cast samples are heterogeneous and due to the fact that only a finite number of regions were evaluated using the IA, these measurements may not be representative of all the test samples.

A determination of the total Cu-enriched-phase area fraction with metallography is a time-consuming and laborious procedure; therefore, it cannot be used as an on-line measurement tool, or as a method of controlling the casting quality in a foundry environment.

The TA approach developed by Kierkus and Sokolowski[5] was used in this work for determining the area fractions of individual phases that precipitate during

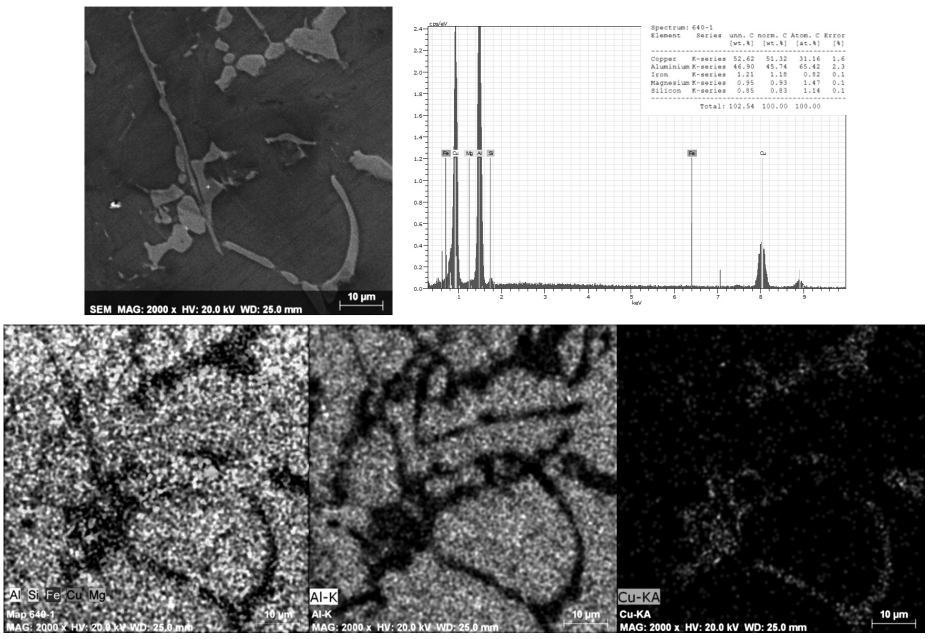

Figure 6: SEM micrographs of the characteristic morphologies of Cu-enriched phases and their EDX elemental maps
Slika 6: SEM-posnetki značilne morfologije s Cu bogatih faz in njihova elementna EDS-analiza

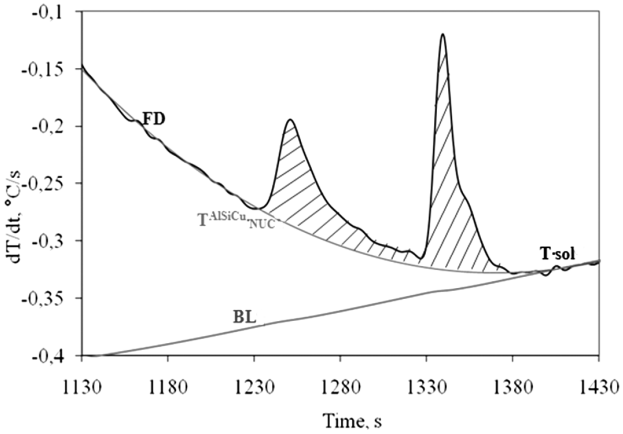

Figure 7: Part of the first-derivative curve (FD) related to the Cu-rich phase[5]
Slika 7: Del prvega odvoda krivulje (FD) glede na s Cu bogate faze[5]

solidification of Al-Si-Cu alloys. In their work, the integrated area of the Cu-enriched phases is defined as the ratio of the area between the first derivative (FD) of the cooling curve and the hypothetical solidification path of the Al-Si-Cu eutectic (the hatched area in **Figure 7**) to the total area between the first derivative of the cooling curve and the base line (BL). The rationale of this assumption is based on:[5]

1. The IA results, which permit one to postulate that the solidification of the Al-Si eutectic continues until the solidus temperature is reached.
2. The total latent energy evolved during the alloy solidification is the sum of the energy released by all of the phases involved in the process.

This concept is briefly demonstrated in **Figures 7** and **8**, which present the FD of the cooling curve and the BL curve. The area between the two curves, from the liquidus state (T_{LIQ}) to the solidus state (T_{SOL}), is proportional to the latent heat of the solidification of the alloy. If the two aforementioned assumptions are correct,

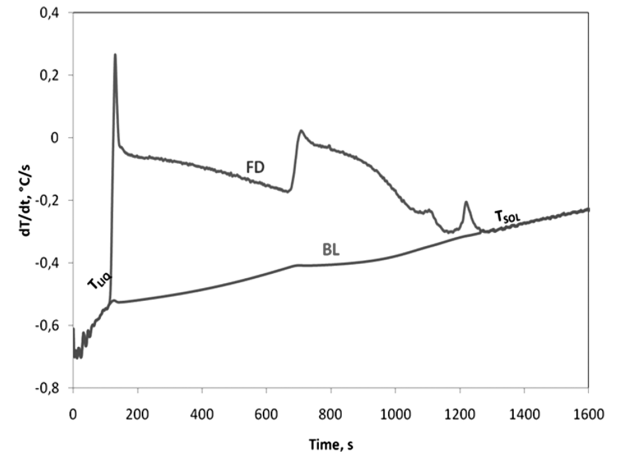

Figure 8: Relationship between IA and TA measurements and the chemical compositions of the investigated alloys
Slika 8: Odvisnost med IA- in TA-meritvami ter kemijsko sestavo preiskovanih zlitin

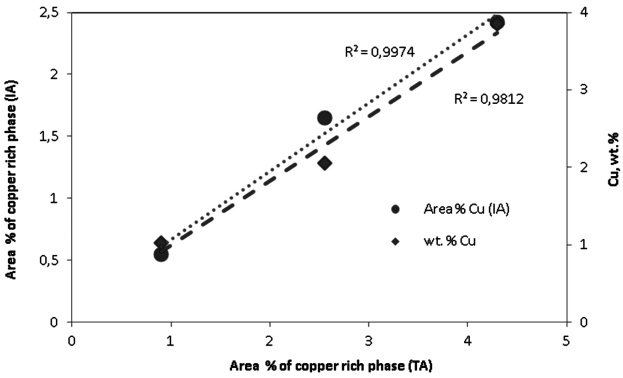

Figure 9: Relationship between IA and TA measurements and the chemical compositions of the investigated alloys
Slika 9: Odvisnost med IA- in TA-meritvami ter kemijsko sestavo preiskovanih zlitin

then the regression line between the arbitrarily selected state ($T_{NUC}^{Al\text{-}Si\text{-}Cu}$) and the solidus state (T_{SOL}) is a part of the solidification path of the Al-Si-Cu eutectic (the hatched area). Therefore, it is evident that the area between the path ($T_{NUC}^{Al\text{-}Si\text{-}Cu} - T_{SOL}$) and the FD of the cooling curve should be proportional to the latent heat of the solidification of the Cu-enriched phases. The proportionality is constant in both cases; the total latent heat of the alloy solidification and the latent heat of the solidification associated with the Cu-enriched phases are the "apparent specific heat" of the alloy.

A comparison of the total area fraction of the Cu-enriched phases determined using the IA with the integrated area (the hatched area in **Figure 7**) of the Cu-enriched phase of each alloy tested shows that the two measurements are almost perfectly correlated (**Figure 9**).

The imperfect agreement between these two measurements can be explained with two factors: First, the IA measurements do not take into account the small Si crystals that cannot be resolved with the LOM or the Si that is dissolved in the aluminum matrix. Only TEM investigations under a very high magnification would be able to reveal the presence of ultra-fine Al-Cu eutectics. Second, because the cast samples are heterogeneous and because only a finite number of regions were evaluated using the IA, these measurements may not be precisely representative of all the samples.

The results of the Cu-enriched-phase determinations are presented in **Table 2** and in **Figure 9**. A high correlation observed on the regression plots (**Figure 9**) shows that it is possible to estimate the volume fraction of the Cu-enriched phases from the TA analysis experiments without resorting to the IA.

4 CONCLUSIONS

A comprehensive understanding of the melt quality is of a paramount importance for the control and prediction of actual casting characteristics. The thermal analysis is

an already used tool for the melt-quality control in an aluminum casting plant. It has been used routinely for assessing the master-alloy additions to an aluminum melt. In addition, its application can be extended to quantify the total volume fraction of the Cu-enriched phases of the Al-Si-Cu aluminum alloys. Future work should confirm that an on-line quantitative control of the Cu-enriched phases is also possible for the other series of Al-Si alloys using TA.

5 REFERENCES

[1] L. Bäckerud, G. Chai, J. Tamminen, Solidification Characteristics of Aluminum Alloys, Vol. 2: Foundry Alloys, AFS/ScanAluminum, Oslo 1990

[2] C. H. Caceres, M. B. Djurdjevic, T. J. Stockwell, J. H. Sokolowski, The effect of Cu content on the level of microporosity in Al-Si-Cu-Mg Casting Alloys, Scripta Materialia, 40 (**1999**), 631–637

[3] M. B. Djurdjevic, T. Stockwell, J. Sokolowski, The effect of strontium on the microstructure of the Al-Si and Al-Cu eutectics in the 319 aluminum alloy, International Journal of Cast Metals Research, 12 (**1999**), 67–73

[4] H. W. Doty, A. M. Samuel, F. H. Samuel, Factors controlling the type and morphology of Cu-Containing phases in the 319 aluminum alloy, 100th AFS Casting Congress, Philadelphia, Pennsylvania, USA, 1996, 1–30

[5] W. T. Kierkus, J. H. Sokolowski, Recent advances in cooling curve analysis: A new method of determining the "base line" equation, AFS Transactions, 66 (**1999**), 161–167

[6] M. B. Djurdjevic, W. Kasprzak, C. A. Kierkus, W. T. Kierkus, J. H. Sokolowski, Quantification of Cu enriched phases in synthetic 3XX aluminum alloys using the thermal analysis technique, AFS Transactions, 24 (**2001**), 1–8

UDK 621.762:621.762.5
Professional article/Strokovni članek

ISSN 1580-2949
MTAEC9, 48(2)305(2014)

INVESTIGATION OF INDUCTION AND CLASSICAL-SINTERING EFFECTS ON POWDER-METAL PARTS WITH THE FINITE-ELEMENT METHOD

PRIMERJAVA VPLIVA INDUKCIJSKEGA IN KONVENCIONALNEGA SINTRANJA NA DELCE KOVINSKEGA PRAHU Z UPORABO METODE KONČNIH ELEMENTOV

Göksan Akpınar, Can Çivi, Enver Atik

Celal Bayar University, Engineering Faculty, Mechanical Engineering Department, 45040 Manisa, Turkey
goksanakpinar105@hotmail.com

Prejem rokopisa – received: 2013-04-29; sprejem za objavo – accepted for publication: 2013-06-13

Induction sintering provides large time and energy savings because the components heat up rapidly and the sintering time is lower than in classical sintering in a furnace. Therefore, induction sintering is an important alternative to classical sintering. In this study, mechanical properties of induction-sintered Fe-based components including Cu and carbon (graphite) were compared with those sintered in a classical furnace. For this purpose, microstructure photographs of both samples were taken. A tensile analysis of the sintered powder-metal samples was carried out with the finite-element method, and the micro-stress values were found to change depending on the amount and distribution of the porosity.

Keywords: powder metallurgy, sintering, induction sintering, classical furnace, microstructure analysis, finite-element method

Indukcijsko sintranje omogoča velike prihranke pri času in energiji, saj se komponente ogrejejo hitro in je čas sintranja krajši, kot pri klasičnem sintranju v pečeh. Zato je indukcijsko sintranje pomembna alternativa klasičnemu sintranju. V tej študiji so bile primerjane mehanske lastnosti indukcijsko sintrane komponente z Fe-osnovo in dodatki Cu ter grafita s komponentami, sintranimi v klasičnih pečeh. V ta namen so bili napravljeni posnetki mikrostrukture obeh vzorcev. Izvršena je bila analiza nateznih preizkusov sintranih kovinskih vzorcev z metodo končnih elementov. Ugotovljeno je bilo, da so vrednosti mikronapetosti odvisne od količine in porazdelitve poroznosti.

Ključne besede: metalurgija prahov, sintranje, indukcijsko sintranje, klasična peč, analiza mikrostrukture, metoda končnih elementov

1 INTRODUCTION

Powders with different compositions are pressed and then sintered with the powder-metallurgy (P/M) method. Sintering is one of the most important issues of powder metallurgy because it causes a significant increase in the strength of the pressed powders. The sintering process is generally performed in sintering furnaces. It is done in a protective atmosphere of batch or continuous furnaces.[1] In addition, rapid sintering methods such as induction sintering, microwave sintering, plasma sintering, laser sintering and discharge sintering are important alternatives to conventional sintering methods.[2] Sintering and additional heat treatments of powder mixtures cause the microstructure to meet the performance requirements.[3]

Mixtures of elemental iron and graphite powders are commonly used for P/M applications. A small amount of copper powder is always added to further strengthen the sintered alloys owing to its relative ease of dissolving and diffusing in an iron matrix upon sintering.[4]

Almost all low-alloy steel powders contain copper. The mass fractions of copper varies between approximately 1 % and 8 % depending upon the desirability of end products. A small amount of copper is added to provide strength by age hardening, while the purpose of higher concentrations is to promote liquid-phase sintering causing a faster densification and homogenization.[5] An addition of carbon to iron powder increases the sintering kinetics as it dissolves into the iron lattice, changing the melting point, surface tension and viscosity of the iron melt formed. Small areas of martensite and tempered martensite are also formed. [6]

The most important feature of the induction-heating system is a rapid heating of the material because heating occurs directly on the metal parts. In general, induction sintering is used for surface heating of materials.[7] If the frequency increases, eddy currents will occur on the region close to the surface.[8] The heat transfer is 3.000 times better than in the other heating systems.[7] This allows a much faster completion of the warm-up process, reducing the time spent for this period and, thus, shortening the sintering time.

In addition, sintered ferrous P/M components have emerged as attractive candidates to replace wrought alloys in many applications due to their low cost, high performance and the ability to be processed to the near-net shape. Sintered materials are typically characterized by the residual porosity after sintering, which is quite detrimental to the mechanical properties of these materials.[9–17] The nature of the porosity is controlled with

several processing variables such as green density, sintering temperature and time, alloying additions, and the particle size of the initial powders.[10] In particular, the fraction, size, distribution and morphology of the porosity have a profound impact on mechanical behavior. Alloying elements such as copper, nickel and graphite affect the sintering parameters leading to the formation of a heterogeneous internal structure. Thus, the heterogeneous nature of the microstructures of P/M steels will certainly play a role in the onset and evolution of damage under an applied stress.[11–17] Under a monotonic tensile loading, the porosity reduces the effective load-bearing cross-sectional area acting as a stress-concentration site for the strain localization and damage, decreasing both strength and ductility.[11] Interconnected porosity causes an increase in the localization of the strain on the relatively smaller sintered regions between the particles, while isolated porosity results in a more homogeneous deformation. It is also not uncommon for the porosity distribution in a material to be inhomogeneous. In this case, the strain localization will take place at the "pore clusters". Thus, for a given amount of porosity, the interconnected porosity is more detrimental, reducing the macroscopic ductility to a greater extent than the isolated porosity.[17]

Porosity affects the mechanical properties of materials. Many studies have been conducted on this topic. N. Chawla and X. Deng[17] investigated the effects of mechanical properties, the shape and size factors of the porosity of sintered Fe–0.85Mo–Ni steels. They systematically examined the effect of porosity on the tensile and fatigue behaviors of the Fe–Mo–Ni steel. The steels of three densities were studied: 7.0 g/cm^3, 7.4 g/cm^3 and 7.5 g/cm^3. A quantitative analysis of the microstructure was performed to determine the pore-size distribution and the pore shape as functions of the sintered density. Holmes and Queeney[18] proposed that the relatively high stress concentration at pores, particularly the surface pores, is responsible for the localized slip leading to a crack initiation. Christian and German[19] showed that the fraction of porosity, pore size, pore shape and pore spacing are all important factors controlling the fatigue behavior of P/M materials. In general, more irregular pores exhibit a higher stress than perfectly round pores.[10] Polasik et al.[15] showed that small cracks nucleate from the pores during the fatigue and coalesce to form a larger crack leading to a fatigue fracture. Here, the heterogeneous nature of the microstructure played an important role by contributing to the crack tortuosity. Crack arrest and crack deflection were observed due to microstructural barriers such as particle boundaries, fine pearlite, and nickel-rich regions.[15]

In this study, the microstructures of classically sintered and induction-sintered metal-powder parts with a medium/low frequency (30 kHz) obtained with the experimental studies were compared. The effects of the sintering time on the mechanical properties were identified with image processing and the finite-element method. The micro-stresses around the internal spaces in the microstructures were investigated.

2 MATERIALS AND METHODS

In this study, the Högenas ASC 100.29 iron powder (2 % Cu, 0.5 % graphite and 1 % Zn Stereat lubricant by mass) was used. Powder-metal bushings were produced by Toz Metal Inc. with a dual-axis press under a 600 MPa pressure. The sieve analysis of the iron powder is shown in **Table 1.**[20] Induction and classical sintering mechanism are indicated in **Figure 1**. Powder-metal bushings with the dimensions of Φ16/14 mm × 36 mm are shown in **Figure 2**.

Table 1: Sieve analysis of the metal powder[20]
Tabela 1: Sejalna analiza kovinskega prahu[20]

Iron powder	Sieve analysis (%)			
ASC 100.29	< 45 μm	45–150 μm	150–180 μm	> 180 μm
	23	69	8	0

The powder-metal bushings were sintered in an environment atmosphere in an electric-resistance furnace

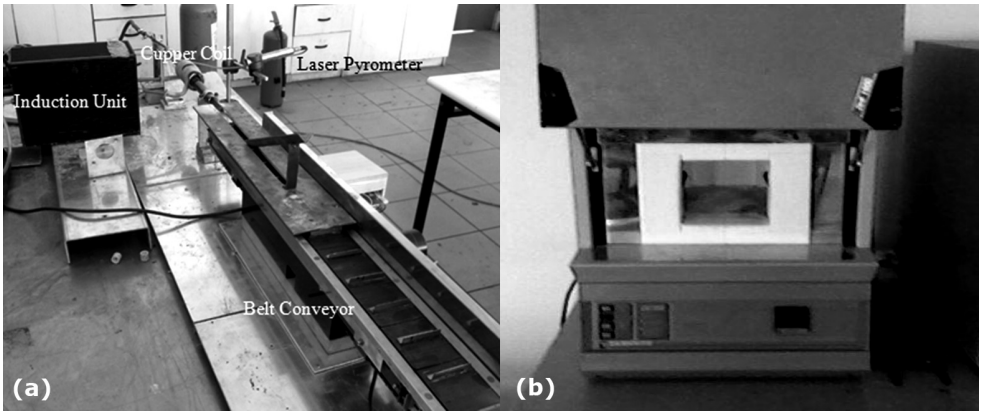

Figure 1: a) Induction-sintering mechanism, b) classical resistance furnace
Slika 1: a) Naprava za indukcijsko sintranje, b) klasična uporovna peč

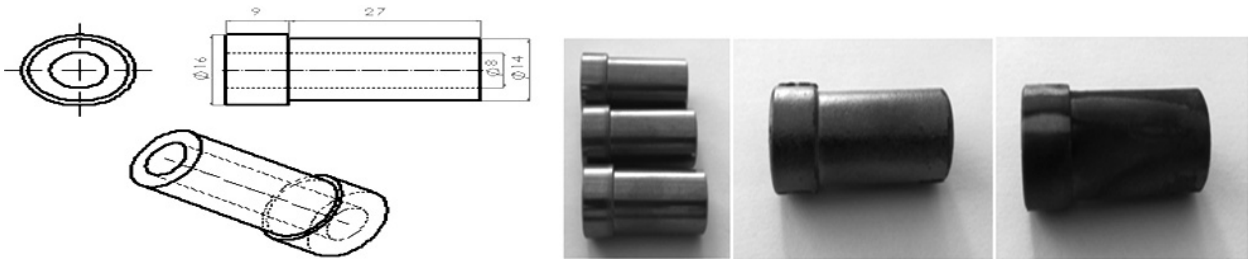

Figure 2: Sintered bushings
Slika 2: Sintrane puše

for 30 min at 1120 °C and they were also sintered by induction sintering for 8.4 min and 15 min at 1120 °C in the environment atmosphere. Induction sintering was carried out in a heat-resistant glass in a copper coil. The microstructural mechanical properties of these samples sintered for different periods and in different furnaces are compared with each other.

The induction sintering was carried out in a heat-resistant glass in a 36 mm diameter copper coil. The conveyor belt system is suitable for a mass production. The sintering temperature of 1120 °C was recorded on a pyrometer with laser and it was kept constant with the induction-mechanism unit. The sintered powder-metal bushings were cut and the microstructure images of the specimens were investigated using a Nikon Eclipse LV100 microscope. The cross-sections of the steel specimens were ground, polished and etched with a 2 % Nital solution (2 % HNO_3 and 98 % alcohol). The images of the polished surfaces of the cross-sections were taken.

The microstructures of the samples (40 μm) were processed by image processing. A tensile stress was applied to the samples with the finite-element method and the micro-stress values were obtained for the samples. The solution was made with an adoption of the mechanical properties of the steel containing 0.6 % graphite.

3 RESULTS

3.1 Microstructural analysis

A microstructural investigation was applied to the sintered bushings after polishing the surface with alumina and acid etching with a 3 % Nital solution. The microstructural photos are shown in **Figures 3** to **5**.

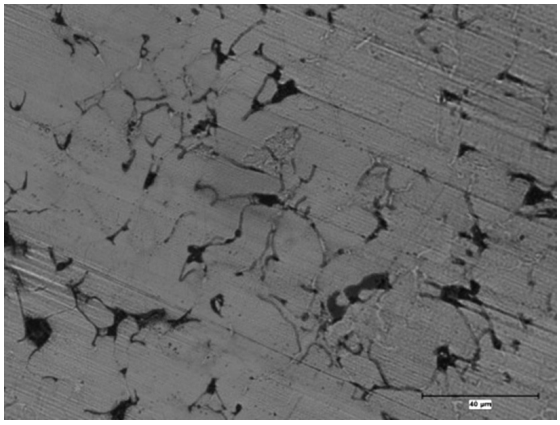

Figure 4: Microstructure of an induction-sintered powder-metal bushing (sintered at 1120 °C for 8.4 min), light microscope (LM), a 100-times magnification
Slika 4: Mikrostruktura indukcijsko sintrane puše iz kovinskega prahu (sintrano pri 1120 °C za 8,4 min), svetlobni mikroskop, povečava 100-krat

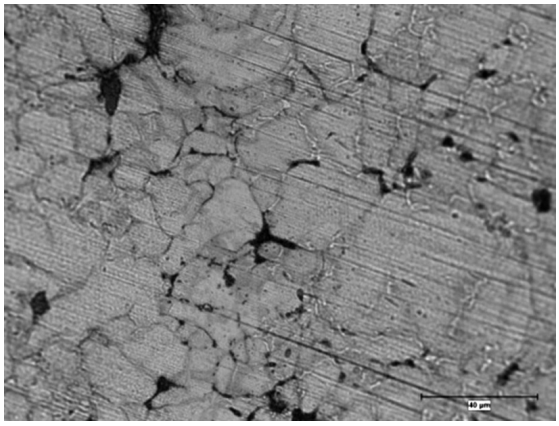

Figure 3: Microstructure of a classically sintered powder-metal bushing (1120 °C/30 min in the furnace), light microscope (LM), a 100-times magnification
Slika 3: Mikrostruktura klasično sintrane kovinske puše (1120 °C/30 min v peči), svetlobni mikroskop, povečava 100-krat

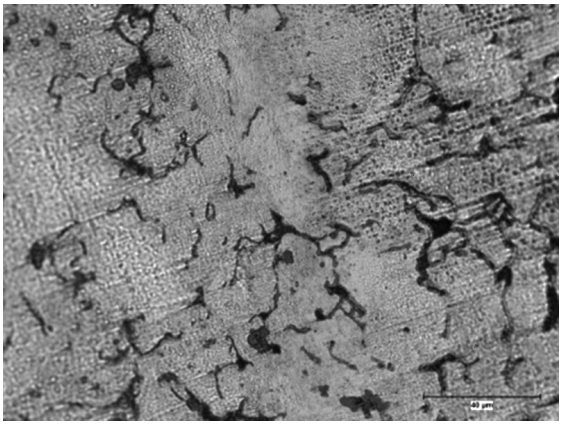

Figure 5: Microstructure of an induction-sintered powder-metal bushing (sintered at 1120 °C for 15 min), light microscope (LM), a 100-times magnification
Slika 5: Mikrostruktura indukcijsko sintrane kovinske puše (sintrano pri 1120 °C za 15 min), svetlobni mikroskop, povečava 100-krat

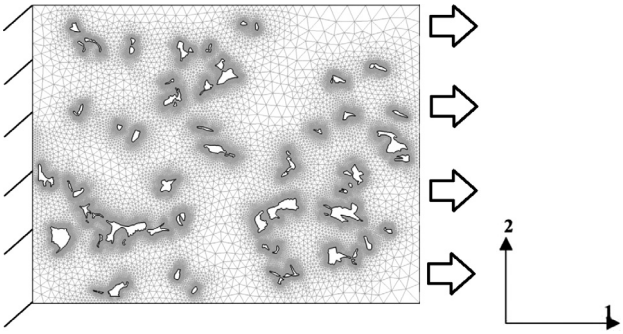

Figure 6: Finite-element boundary conditions of the real-microstructure image of a powder-metal part
Slika 6: Robni pogoji za analizo z metodo končnih elementov na realni mikrostrukturi sintranega kovinskega dela

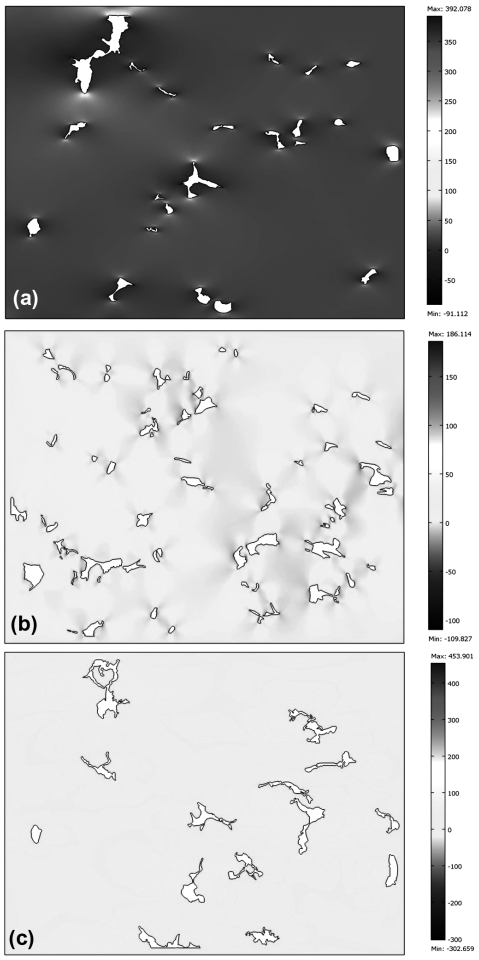

Figure 7: a) Microstructure of a powder-metal bushing classically sintered for 30 min in the furnace, a finite-element model of microstructure images with normal stress (MPa), b) microstructure of a powder-metal bushing induction sintered for 8.4 min, a finite-element model of microstructure images with normal stress, c) microstructure of a powder-metal bushing induction sintered for 15 min, a finite-element model of microstructure images with normal stress
Slika 7: a) Mikrostruktura klasično sintrane kovinske puše 30 min v peči; model mikrostrukture z metodo končnih elementov z normalno napetostjo (MPa), b) mikrostruktura indukcijsko sintrane kovinske puše (8,4 min); model mikrostrukture z metodo končnih elementov z normalno napetostjo, c) mikrostruktura indukcijsko sintrane kovinske puše (15 min); model mikrostrukture z metodo končnih elementov z normalno napetostjo

3.2 Image processing and FEM Analyses of microstructure pictures

The mechanical properties of the materials are shown in **Table 2**. The porosity values obtained from the image analysis of the samples are shown in **Table 3**. The maximum and minimum micro-stresses of the static tensile strength acting horizontally (1 direction) on the internal pores were found and compared with each other. The results of the study using the finite-element method are shown in **Figures 6** to **10**.

Table 2: Mechanical properties of the iron-based sintered material with 0.6 % graphite added and the loading conditions of the samples
Tabela 2: Mehanske lastnosti sintranega materiala z dodatkom 0,6 % grafita in razmere pri obremenitvi vzorcev

Poisson's ratio (an approximation)	Thermal-expansion coefficient (1/K)	F_x – Edge load, 1-direction (N/m²)
0.3	11.8 E–6	20 E6

4 DISCUSSION

It is well known that porosity decreases the Young's modulus of a material.[10] We use the approach of Ramakrishnan and Arunachalam (R–A)[21] to model the effect of the porosity on the Young's modulus. The Young's modulus of a material, E, with a given fraction of porosity, p, is given by:

$$E = E_0 \left[(1 - p)^2 / (1 + \kappa E_p)\right] \quad (1)$$

where E_0 is the Young's modulus of a fully dense steel (obtained by extrapolating the experimental data to the zero porosity, yielding a value of approximately 200 GPa), and κE is the constant in terms of the Poisson's ratio of a fully dense material, v_0:

$$\kappa E = 2 - 3v_0 \quad (2)$$

For a fully dense steel, the Poisson's ratio is approximately 0.3. This is supported by the analysis of Ramakrishnan and Arunachalam,[21] who compared the bulk modulus of porous materials with the spherical-versus-angular-pore geometry using FEM. An analytical solution was made to show that, depending on the density and porosity, the samples of the microstructures were

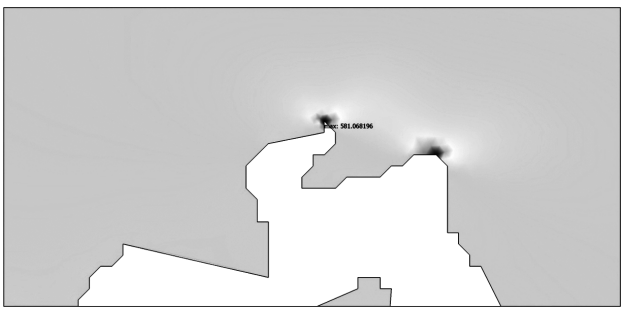

Figure 8: Induction-sintered sample 15 min, the maximum stress (MPa) in the area of the porosity of the microstructure
Slika 8: Indukcijsko sintran vzorec 15 min, največja napetost (MPa) na območju poroznosti v mikrostrukturi

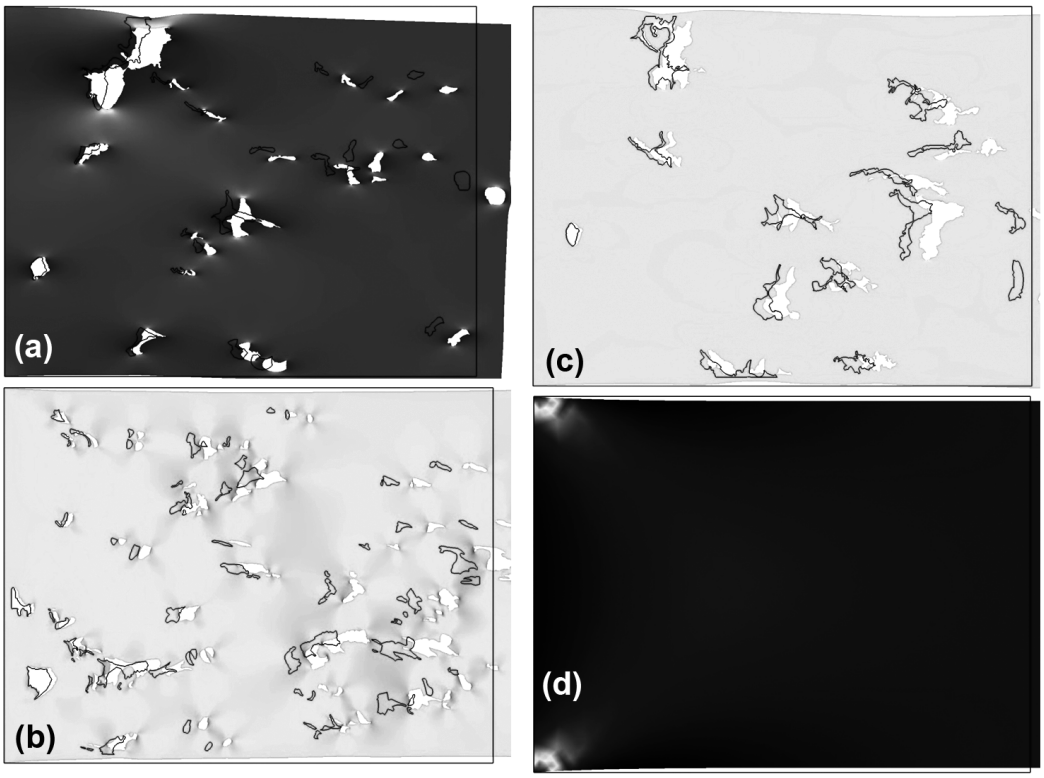

Figure 9: Finite-element investigation of the microstructures of the samples with both deformed and undeformed shapes: a) powder-metal bushing classically sintered for 30 min in the furnace, b) powder-metal bushing induction sintered for 8.4 min, c) powder-metal bushing induction sintered for 15 min, d) bulk material

Slika 9: Preiskava mikrostrukture z metodo končnih elementov vzorcev v deformiranem in nedeformiranem stanju: a) klasično sintrana kovinska puša (30 min v peči), b) indukcijsko sintrana kovinska puša (8,4 min), c) indukcija sintrana kovinska puša (15 min) in d) osnovni material

Table 3: Porosity, stresses and total-displacement values obtained from the image-processing analysis

Tabela 3: Poroznost, napetosti in skupen pomik, dobljeni iz analize slik

Samples	Porosity from image analysis (%)	Density (kg/m³)	Maximum stress around a pore (MPa)	Minimum stress around a pore (MPa)	Total displacement (μm)	Young's modulus (GPa)
Average of the samples induction sintered for 8.4 min	3.5411	7270	794.128	–234.780	2.31 E–2	185.684
Average of the samples induction sintered for 15 min	3.1846	7352	581.068	–473.677	3.186 E–2	187.077
Average of the samples classically sintered for 30 min	2.4004	7474	708.883	–228.570	2.774 E–2	190.177
Bulk sample	0	7860	34.171	17.967	1.691 E–2	200.000

affected by micro-stresses. The Young's modulus values of the samples are given in **Table 3**.

Although the finite-element analysis was used to study the mechanical behaviors of powder-metallurgy materials,[16,22–24] the pores are generally modeled as perfect spheres. But, at critical values of strain the imperfections cause localization of plastic flow.[24] In the R-A model a single spherical pore is surrounded by a spherical matrix shell, causing an intensification of the pressure on the pore surface due to the interaction of the pores in the material.[25] The material behavior is controlled by the microstructure of steel, in particular, the nature of the porosity.[17]

In this study we used two-dimensional microstructures as the basis for the finite-element simulations of the samples induction sintered for 8.4 minutes and 15 min, and the samples classically sintered for 30 min in a furnace. **Figure 6** shows the actual microstructure version of the uniaxial loading, boundary conditions and the mesh. A quadratic triangular mesh modeling was deemed appropriately. A finer mesh was used in the regions of pore clusters. In order to yield accurate simulation results, we used an entire picture of the microstructure simulation. The 2D analysis presented here shows the qualitative effects of the pore microstructure on the localized plastic strain and stress initiation around the pores. The porosity values of the samples, the maximum and minimum normal stresses, the Young's modulus, the total displacement, thermal-expansion coefficient values,

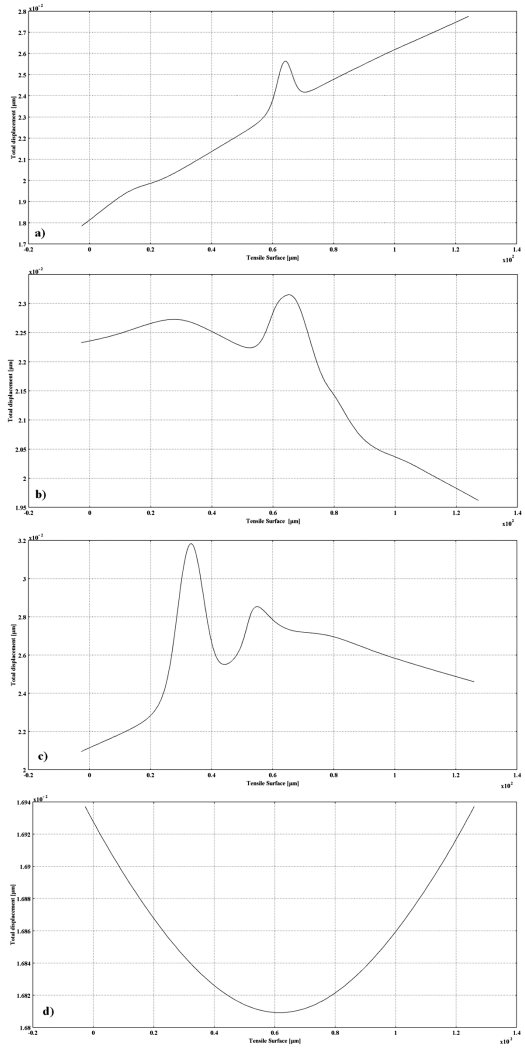

Figure 10: Total displacement curves of the tensile surfaces: a) powder-metal bushing classically sintered for 30 min in the furnace, b) powder-metal bushing induction sintered for 8.4 min, c) powder-metal bushing induction sintered for 15 min, d) bulk material

Slika 10: Skupni premik natezno obremenjene površine: a) klasično sintrana kovinska puša (30 min v peči), b) indukcijsko sintrana kovinska puša (8,4 min), c) indukcija sintrana kovinska puša (15 min) in d) osnovni material

the Poisson's ratio and the edge 1-direction loads are shown in **Tables 2** and **3**.

The normal stress around the pores, the total displacement, the deformed and undeformed shapes of the microstructures of the samples are shown in **Figures 7** and **9**. These figures show that the porosity was caused by an inhomogeneous deformation. The modeling also shows that the plastic-strain intensification begins at the tips of the irregular pores in the microstructure. This means that the more irregular the porosity, the more damage can be seen in the microstructure. For a regular deformation, as well as the porosity shape, the distribution of porosity in a structure is also important. Vedula and Heckel[9] investigated the mechanisms of a damage of flat and angular pores in a microstructure. They observed the forming of local shear bands at the ends of the pores, creating unstable tensions around the angular pores.

A mesh view and the finite-element boundary conditions of a real-microstructure image of a powder-metal part is shown in **Figure 6**. The solutions for each sample were compared by applying the same boundary conditions. Also, the local plastic strain acting around the micropores was found to be a result of the two-dimensional analysis. Each sample of the tensile surface is taken to have a value of $F_1 = 20$ N/m^2 for the stress-edge 1-direction load.

The stress equation of the modeling is as follows:[25]

$$F(\sigma_{ij} - \xi_{ij}) - h(\lambda h) = 0 \qquad (3)$$

where σ_{ij} is the symmetric stress index, ξ_{ij} is the first cycle of the yield surface, lh is the scalar function of the plastic strain and $h(\lambda$h) refers to the amount of expansion of the yield surface.

The stress concentrations at the tips of irregular pores in the microstructure are shown in **Figure 7**. Also, for the area around the pores of the sintered samples, the normal-stress FE-analysis results are given.

The maximum stress around the pores of the sample induction sintered for 8.4 min was 794.1 MPa. For the sample induction sintered for 15 min, a relatively lower value of 581.5 MPa for the maximum stress was obtained. On the basis of these results, it can be concluded that the maximum-stress value around the pores decreases with an increase in the density. As you can see in **Figure 8**, the maximum stress in the area of porosity depends not only on the density but also on the pore shape. The maximum stress for the microstructure of the sample induction sintered for 15 min is also shown in **Figure 8**. However, we have a difficulty here: although the sample induction sintered for 15 min showed the lowest tensile stress, the maximum stress value in the opposite direction is –473.7 MPa, which is higher than the other values. This result shows that the pore shape of a microstructure plays a key role in the micro-tensile stress.

The non-deformed and deformed shapes of the samples were analyzed. Despite having the lowest density, the induction-sintered sample 8.4 min showed a more uniform deformation than the other porosity samples. According to these results, smaller and regular pores contribute to a uniform deformation. When comparing the amounts of deformation in the porosity samples and the bulk sample, the porosity samples are found to be more deformed than the bulk sample. It can be said that the deformation amount of the samples depends on the pore shape as well as on the density.

The strain curves of the tensile surfaces of the samples are given in **Figure 10**. These strain curves appear to be quite different. The reasons for this difference are the rate, the shape and the pore density of the samples. As expected, the bulk sample has a symmetric deformation curve. When the inner tensile surface of the pores

increases, the surface-deformation-curve peak increases as well.

5 CONCLUSIONS

In this study, Fe-based powder-metal bushings were sintered with the classical-furnace and induction-sintering mechanisms. The microstructures of the classically sintered and induction sintered powder-metal bushings with a low to medium frequency (30 kHz) were compared. The effects of the sintering time on the mechanical properties were investigated with image processing and the finite-element method. The results show the following:

- The stresses that occurred around the pores in the microstructures of the samples were investigated numerically, showing how the stresses and displacement of the pores related to the sintering methods and parameter changes. Besides, it was also found that the mechanical properties of porous materials and the bulk material are quite different.
- Numerical results are shown in the **Table 3**. The maximum and minimum stresses for the samples classically sintered for 30 min are 708.9 MPa and –228.6 MPa, respectively. The maximum and minimum stresses for the sample induction sintered for 8.4 min are 794.1 MPa and –234.8 MPa, respectively. The maximum and minimum stresses for the samples induction sintered for 15 min are 581.5 MPa and –473.7 MPa, respectively, while the maximum and minimum stresses for the bulk samples are 34.2 MPa and 18 MPa, respectively.
- The pore sizes decrease with the increasing sintering time as illustrated in **Figure 7**. With the increasing induction-sintering time, large pores become relatively small, small pores disappear and the sintered density increases. On the other hand, when the induction-sintering time in the microstructures increases, lower and more homogenized tensile stresses occur around the pores.
- When looking at the values for the porosity obtained with the image analysis shown in **Table 3**, the minimum porosity value (2.4 %) is found for the samples classically sintered in the furnace for 30 min and, as expected, this porosity causes a smaller displacement than the other porosities. It is seen that the sample induction sintered for 8.4 min has a smaller displacement than the one induction sintered for 15 min. A more regular deformation is also shown in **Table 3** and **Figure 8**. According to this result, smaller and more regular pores of the sample induction sintered for 8.4 min are thought to cause a more regular deformation.
- The porosity samples were also compared to the bulk sample. It was seen that considerable internal stresses were formed around the pores of the porosity samples. This means that the material is exposed to tension, and the micro-stress concentrating around the pores can cause damage in a much shorter time. As a precaution, smaller and more regular pores should be formed in the microstructure and the microstructures of the materials should be concentrated.
- The microstructure-based FEM modeling showed that smaller, more regular and more clustered pores cause a more regular displacement and a reasonable micro-stress. So, the micro-stress and micro-strain depend on the pore shape and the loading condition as well as on the pore density.
- In our previous study, it was found that the strength values of the samples sintered with induction were increased by increasing the sintering time.[26] Due to more uniform and smaller pores in our current study, the micro-stress values of the sintered samples decreased. This also proves that the strength of the samples increases with a decrease in the micro-stress values.
- Another aim of this study was to investigate how the pores affect the micro-stress and micro-deformation. It was found that the strength of a porous material depends on the shape, the size and the density of the pores.

Acknowledgments

We would like to thank Toz Metal Inc. and Mr. Aytaç Ataş for providing the metal powder and pressing the powder-metal bushings.

6 REFERENCES

[1] R. M. German, Powder Metallurgy and Particulate Materials Processing, MPIF, New Jersey 2005

[2] E. Atik, U. Rye, Traditional and Fast Sintering Methods, CBU Soma Vocational School of Technical Sciences Journal, 1 (**2011**) 15

[3] K. S. Narasimhan, Sintering of powder mixtures and the growth of ferrous powder metallurgy, Materials Chemistry and Physics, 67 (**2001**) 1–3, 56–65

[4] W. F. Wang, Effect of alloying elements and processing factors on the microstructure and hardness of sintered and induction-hardened Fe–C–Cu alloys, Materials Science and Engineering, 402 (**2005**) 1–2, 92–97

[5] G. S. Upadhyaya, Effect of copper and VCN additions on sintering of low alloy steel, Materials & Design, 22 (**2001**) 5, 359–367

[6] A. Simchi, Effect of C and Cu addition on the densification and microstructure of iron powder in direct laser sintering process, Materials Letters, 62 (**2008**) 17–18, 2840–2843

[7] R. M. German, Sintering Theory and Practice, The Pennsylvania State University Park, Pennsylvania, A Wiley-Interscience Publication, Jon Wiley & Sons, Inc, USA 1996, 313–362, 373–400, 403–420

[8] A. H. Demırcı, Engineering Materials, Important Industrial Materials and Heat Treatment, Alfa Aktüel Press, 2004

[9] K. M. Vedula, R. W. Heckel, Modem Developments in Powder Metallurgy, Metal Powder Industries Federation, Princeton, NJ, 1981, 759

[10] A. Salak, Ferrous Powder Metallurgy, Cambridge International Science Publishing, Cambridge 1997

[11] A. Hadrboletz, B. Weiss, Int. Mater. Rev., 42 (**1997**), 1

[12] N. Chawla, S. Polasik, K. S. Narasimhan, M. Koopman, K. K. Chawla, Int. J. Powder Metall., 37 (**2001**), 49
[13] N. Chawla, T. F. Murphy, K. S. Narasimhan, M. Koopman, K. K. Chawla, Mater. Sci. Eng. A, 308 (**2001**), 180
[14] N. Chawla, D. Babic, J. J. Williams, S. J. Polasik, M. Marucci, K. S. Narasimhan, Advances in Powder Metallurgy and Particulate Materials, Metal Powder Industries Federation, 2002, 104
[15] S. J. Polasik, J. J. Williams, N. Chawla, Metall. Mater. Trans. A, 33 (**2002**), 73
[16] N. Chawla, B. Jester, D. T. Vonk, Mater. Sci. Eng. A, 346 (**2003**), 266
[17] N. Chawla, X. Deng, Microstructure and mechanical behavior of porous sintered steels, Materials Science and Engineering A, 390 (**2005**), 98–112
[18] J. Holmes, R. A. Queeney, Powder Metall., 28 (**1985**), 231
[19] K. D. Christian, R. M. German, Int. J. Powder Metall., 31 (**1995**), 51
[20] K. Widanka, Effect of Compacting Pressure on Interconnected Porosity in Iron PM Compacts, Powder Metallurgy Progress, 8 (**2008**) 1, 63–70
[21] N. Ramakrishnan, V. S. Arunachalam, J. Am. Ceram. Soc., 76 (**1993**), 2745
[22] R. Becker, J. Mech. Phys. Solids, 35 (**1987**), 577
[23] R. J. Bourcier, R. E. Smelser, O. Richmond, D. A. Koss, Inter. J. Fract., 24 (**1984**), 289
[24] R. J. Bourcier, D. A. Koss, R. E. Smelser, O. Richmond, Acta Metall., 34 (**1986**), 2443
[25] S. Suresh, Fatigue of Materials, second ed., Cambridge University Press, Cambridge 1998
[26] C. Çivi, E. Atik, AIP Conference Proceedings, 1476 (**2012**), 119–122